Λ_c^+ baryon production measurements with the ALICE detector at the LHC in pp and p–Pb collisions at $\sqrt{s_{NN}} = 5.02$ TeV

Thesis submitted in accordance with the requirements of
the University of Liverpool for the degree of Doctor in Philosophy by

Christopher Hills

September 2022

Contents

Abstract

This thesis presents new measurements of the production of prompt charmed baryon, Λ_c^+ in pp and p-Pb collisions at the energy of $\sqrt{s_{\rm NN}} = 5.02$ TeV made with the ALICE detector at the Large Hadron Collider (LHC). These measurements provide important information on how charm quarks hadronise in collisions involving protons and nuclei, and provide a vital reference for future measurements in Pb–Pb collisions.

The $p_{\rm T}$-differential cross section for the $\Lambda_c^+ \rightarrow {\rm pK}^-\pi^+$ decay channel has been measured in the transverse momentum ranges $1 < p_{\rm T} < 12$ GeV/c in pp collisions and $2 < p_{\rm T} < 24$ GeV/c in p–Pb collisions at $\sqrt{s_{\rm NN}} = 5.02$ TeV. The Λ_c^+ candidates were reconstructed from tracking information from the Inner Tracking System and Time Projection Chamber, and from the particle identification information obtained by the Time-Of-Flight detector. The signal extraction was performed by fitting the invariant mass distributions in each $p_{\rm T}$ interval after the number of background candidates had been reduced by the application of topological cuts and a Bayesian particle identification algorithm. Subsequently, the appropriate corrections for the reconstruction and selection efficiencies and the contribution from feed-down were applied to the measured Λ_c^+ yield.

The measured cross sections in both pp and p-Pb collisions are shown to be underestimated by theoretical model predictions calculated with perturbative Quantum Chromodynamics. The measured baryon-to-meson ratio $\Lambda_c^+/{\rm D}^0$ is found to be larger than that of previous measurements in e^+e^- experiments and any theoretical model predictions tuned on e^+e^- data. A better agreement with the new measurements is obtained with models that include an additional enhancement mechanism for charmed baryons, although greater precision is needed to discriminate between the models.

Finally the nuclear modification factor $R_{\rm pPb}$, the ratio of the measured Λ_c^+ yield in p–Pb to the corresponding Λ_c^+ yield in pp collisions scaled by the number of binary nucleon-nucleon collisions, was extracted. The uncertainty on the

measurement was reduced by the increased statistics and measurement of both collision systems at the same energy. The measured values were compared against those obtained from D-meson measurements and theory predictions, although greater precision is needed to determine the contribution of cold nuclear matter effects or hot-medium effects.

Future measurements of the Λ_c^+ baryon and other charmed baryons planned during the upcoming Run 3 data taking period of the LHC will hopefully provide further insight with the enhanced precision of the newly upgraded ALICE detector and shed light on the nature of hadronisation.

Chapter 1

Introduction

This thesis presents new measurements made with the ALICE detector at the Large Hadron Collider (LHC) in pp and p–Pb collisions. Production of the prompt charmed baryon Λ_c^+ (udc) was measured in the $\Lambda_c^+ \to pK^-\pi^+$ channel at the energy of $\sqrt{s_{NN}} = 5.02$ TeV in both collision systems. Heavy flavour particles (particles that contain a bottom (b) or charm (c) quark), such as the Λ_c^+, act as a valuable probe of the Quark-Gluon Plasma (QGP) generated in relativistic heavy-ion collisions. This is because heavy quarks are created, in the earliest moments of the collision, in perturbatively calculable hard quantum chromodynamic processes, and participate in the entire evolution of the QGP medium.

This chapter includes a brief history of Quantum Chromodynamics (QCD) and the characteristics that drive the study of the QGP in heavy-ion collisions at the LHC and other particle accelerators. Additionally, theoretical background is given for the measurement of heavy-flavour hadron production.

1.1 Quantum Chromodynamics

In the 1960s, there were a large number of newly discovered hadrons (particles that experience the strong nuclear force), but there was no overall theory explaining how these particles and their properties were linked. A successful scheme to classify these particles would be produced by Gell-Mann and Ne'eman using a SU(3) symmetry [1, 2]. This would later be developed into the quark model, only including the up (u), down (d), and strange (s) quarks [3, 4]. Evidence for the physical existence of quarks, beyond being a mathematical tool, came from electron-proton experiments at SLAC [5]. The full set of quarks (listed in Table

1.1) that we know today would not be completely observed until the discovery of the top quark in 1995 [6].

Name	Mass	Charge (e)	Discovered (year)
Up	$2.16^{+0.49}_{-0.26}$ MeV	2/3	1969
Down	$4.67^{+0.48}_{-0.17}$ MeV	-1/3	1969
Strange	93^{+11}_{-5} MeV	-1/3	1969
Charm	1.27 ± 0.02 GeV	2/3	1974
Bottom	$4.18^{+0.03}_{-0.02}$ GeV	-1/3	1977
Top	172.76 ± 0.30 GeV	2/3	1995

TABLE 1.1: List of quark mass, charge and discovery date. Mass values taken from [7]

Quantum Chromodynamics (QCD) and Quantum Electrodynamics (QED) are gauge field theories that each describe the behaviour and interactions of particles that carry their respective quantum properties, colour and electric charge. Notably, the massless force carrier of QED, the photon, is electrically neutral. However, the massless force carrier of QCD, the gluon, carries both a colour and anti-colour charge. This gives eight possible colour anti-colour combinations for gluons and the ability to participate in strong interactions as well as mediate them. The coupling strength of QCD and QED can be explored through the vacuum polarisation effect. In QED, the placement of a charge into a "vacuum" (a space filled with only virtual particles) leads to the polarisation of virtual electron-positron pairs leading to a reduced or screened charge observed at a distance away from the bare charge. This causes the observed charge to depend on distance (or energy). In QCD, when a bare colour charge is placed into the vacuum, a similar screening effect occurs via virtual quark-antiquark pairs. However, due to the gluon also possessing a colour charge and being capable of self interacting, an overall net anti-screening effect occurs. This means that at large distances (or low energies) the observed charge diverges, while at small distances (or high energies) the observed charge decreases. The relative strength of the interaction, denoted as α_s, can be seen in Figure 1.1.

1.2 The Quark-Gluon Plasma

This observed trend of the strong coupling constant seen in Figure 1.1 becoming smaller at higher energy scales, as well as the observation of increasing numbers of

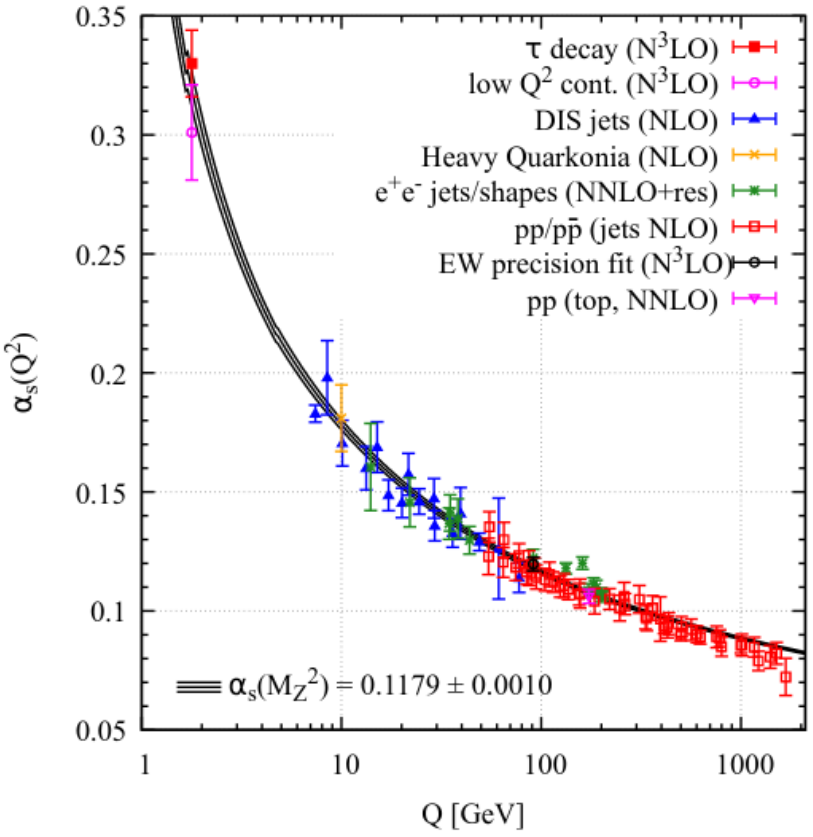

FIGURE 1.1: Summary of measurements of the strong coupling constant α_s, as a function of energy scale Q, from [7]. The order to which perturbative QCD is applied is given in the brackets.

resonances at higher temperatures [8] led to the idea of a transition from hadronic matter to a deconfined medium called the Quark-Gluon Plasma (QGP).

1.2.1 Exploring the phase diagram of hadronic matter

At the LHC and other relativistic heavy-ion colliders, this state of matter can be investigated in the high temperature and low net baryon density region of hadronic matter (see Figure 1.2). Net baryon density represents the excess of quarks over antiquarks. At lower collision energies which relate to lower temperatures, the initial baryon number gives a greater contribution, thus increasing net baryon density. This allows experiments performed at different particle accelerators with different collision energies to scan different regions of the phase diagram.

Alternatively, on the phase diagram there is a region defined by high net baryon density and low temperature. The centre of neutron stars provide the

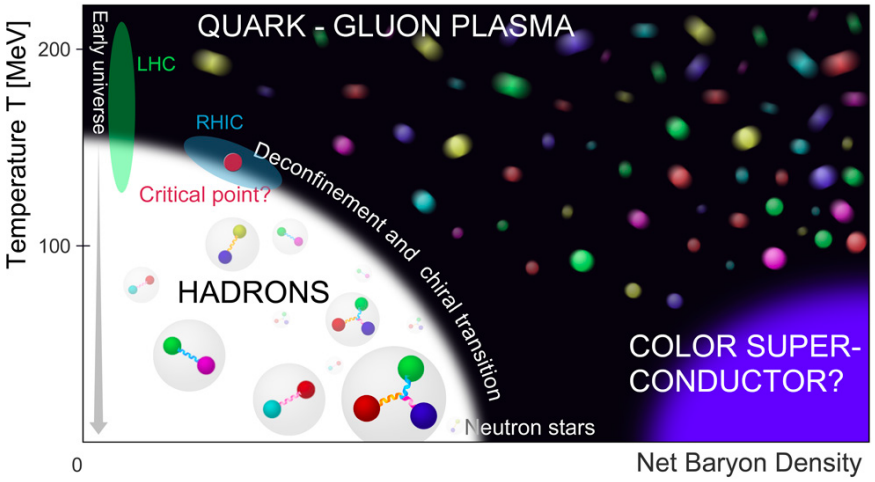

FIGURE 1.2: Phase diagram of QCD matter in the temperature vs net baryon density plane.

best candidate for this environment. Future measurements by collaborations such as LIGO and VIRGO [9] alongside X-ray measurements may be able to provide insights into the transport mechanisms of cold dense quark matter, if it exists in neutron stars.

1.2.2 Probes of the QGP

The QGP can be studied in ultra-relativistic collisions at particle accelerators such as the LHC, where a droplet of QGP is generated for a brief moment [10]. The particles produced in the collision can interact with the QGP medium and provide information about its properties. In ultra-relativistic collisions of heavy ions, the collision undergoes the following evolution (shown in Figure 1.3):

1. Initial collisions between the two Lorentz-contracted nuclei
2. Generation and thermalisation of the QGP medium
3. Expansion and cooling of the QGP medium
4. Hadronisation
5. Chemical freezeout (hadron yields freeze)
6. Kinetic freezeout (momenta spectra freezes)

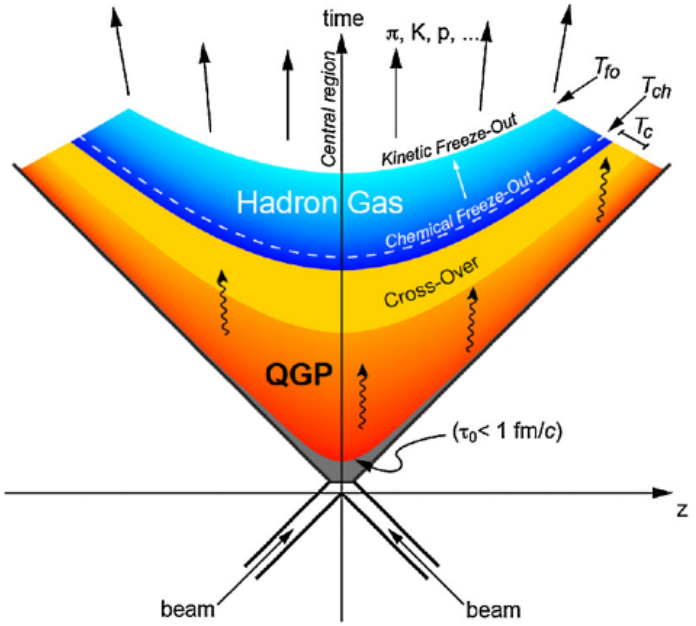

FIGURE 1.3: Space-time diagram of a heavy-ion collision between two nuclei, from [11].

Heavy-ion collisions provide a wide variety of probes that are generated at different stages of the collision and that subsequently interact with the QGP medium, providing the means to measure its properties.

Some of the measurements presented include some terms or observables that shall be explained here. The momenta of an observed particle is split into components either in the direction of the beam line, p_z (defined as the z-axis) or perpendicular to it, p_{T} (in the x-y plane). The rapidity of a particle, y, can be expressed by

$$y = \frac{1}{2} \ln \left(\frac{E + p_z}{E - p_z} \right), \tag{1.1}$$

where E denotes the energy of the particle.

This quantity changes additively under Lorentz boosts along the beam line. When shifting from one frame of reference to another along the direction of the beam line the rapidity distribution remains the same and is simply shifted. Another commonly used quantity for describing the spatial properties of particles produced in collisions and regions covered by a detector is pseudorapidity. This is denoted by

$$\eta = -\ln \left(\tan \left(\frac{\theta}{2} \right) \right), \tag{1.2}$$

where θ is the angle between the direction of the momentum vector and the beam axis. In the limit of high-energy particles, rapidity, y and pseudorapidity, η are equivalent.

Some of the measurements presented here occur at different centralities. Centrality is linked to the geometry of the collision and is typically given as a percentage of the impact parameter, the offset between the centres of the two colliding nuclei in the transverse direction, with respect to the combined radii of the two colliding nuclei. A centrality of 0% corresponds to a perfectly head-on collision and 100% to a perfectly peripheral collision where the nuclei just graze each other.

To highlight the effects caused by the QGP medium, the observable called nuclear modification factor, R_{AA}, is useful as it compares the yield from Pb–Pb collisions (dN_{AA}/dp_T) to the cross section observed in pp collisions ($d\sigma_{pp}/dp_T$), where $\frac{1}{<T_{AA}>}$ scales the result based on the mean nuclear thickness,

$$R_{\mathrm{AA}}(p_{\mathrm{T}}) = \frac{1}{< T_{AA} >} \frac{\mathrm{d}N_{AA}/dp_{\mathrm{T}}}{\mathrm{d}\sigma_{pp}/\mathrm{d}p_{\mathrm{T}}}. \tag{1.3}$$

Likewise the hydrodynamic behaviour of the medium can be determined by the measurement of an observable called elliptic flow. Elliptic flow, most prominent in non-central collisions, originates from the elliptically shaped region formed by the overlap of the two colliding nuclei. Pressure gradients cause the spatial asymmetry to translate into a momentum anisotropy as the medium expands. The anisotropy is measured by the azimuthal momentum-dependent distribution of identified particles in the reaction plane. The varying patterns of anisotropic flow can be quantified by the coefficients from the Fourier transform of the azimuthal distribution,

$$\frac{\mathrm{d}N}{\mathrm{d}(\phi - \phi_R)} = \frac{N_0}{2\pi}(1 + 2\sum_{n\geq 1} v_n \cos n(\phi - \phi_R)), \tag{1.4}$$

where ϕ_R is the orientation with respect to the reaction plane of the collision and N_0 is the azimuthally intergrated yield. In the case of elliptic flow, this is given by the second coefficient, v_2.

To probe the initial state of the collision, high transverse momentum (p_{T}) photons, and massive Z bosons act as good probes due to the fact they are produced during the earliest part of the collision, are well described by perturbative QCD calculations in pp collisions, and interact only weakly with the QGP medium. These measurements act as a clean baseline for other measurements where the probes are expected to interact strongly with the the medium. In Figure 1.4,

measurements of the nuclear modification factor of high p_{T} photons are consistent with unity and are best described by calculations that include nuclear parton distribution functions (nPDFs) [12]. Similarly, measurements of the nuclear modification factor for Z bosons as a function of rapidity show better agreement with PDFs that include nuclear modification than those based solely on free nucleon PDFs [13].

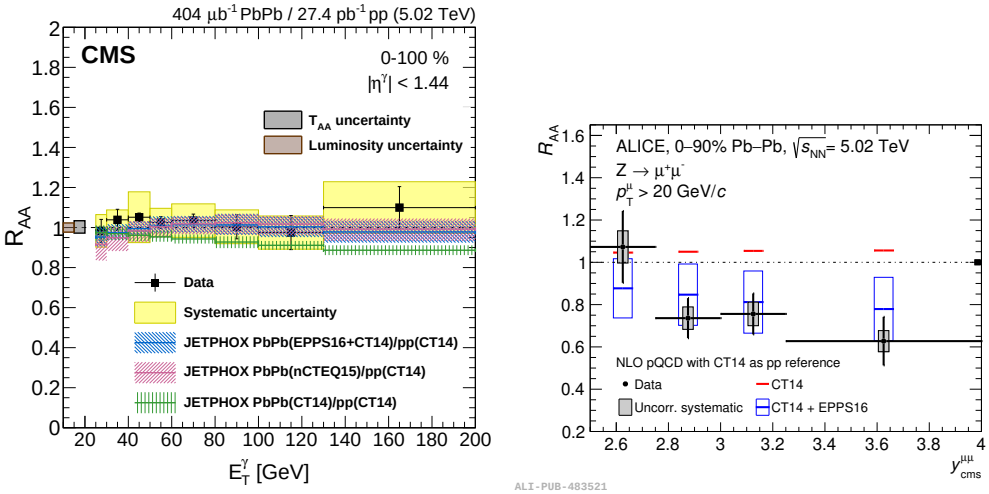

FIGURE 1.4: The R_{AA} measured for high-p_{T} photons vs energy of the photon compared to JETPHOX calculations using three different PDFs (left) [12] and Z^0 bosons vs rapidity, y (right) [13] in Pb-Pb collisions at $\sqrt{s_{\mathrm{NN}}}$ =5.02 TeV.

The species of quarkonia present were once thought to act as a simple thermometer for the produced QGP due to a supposed screening of the the heavy quark potential in a colour deconfined medium. With increasing temperature more tightly bound states would sequentially melt and give an indication of the temperature. However at collision energies in the LHC, the R_{AA} that can be seen in Figure 1.5 does not show the same level of suppression to that of collisions at lower energies at the PHENIX experiment and suggests a competing regeneration mechanism at LHC energies. This matches well with predictions by transport models and the statistical hadron models that include this regeneration mechanism at low p_{T} [14].

Jets and heavy flavour hadrons are produced in the initial hard partonic scatterings at the start of the collision. These probes that do interact strongly with the hot medium can provide insights into the energy loss and transport mechanisms present in the medium. For jets, the energy loss to the QGP medium is referred to as jet quenching, where coloured objects (quarks or gluons, which

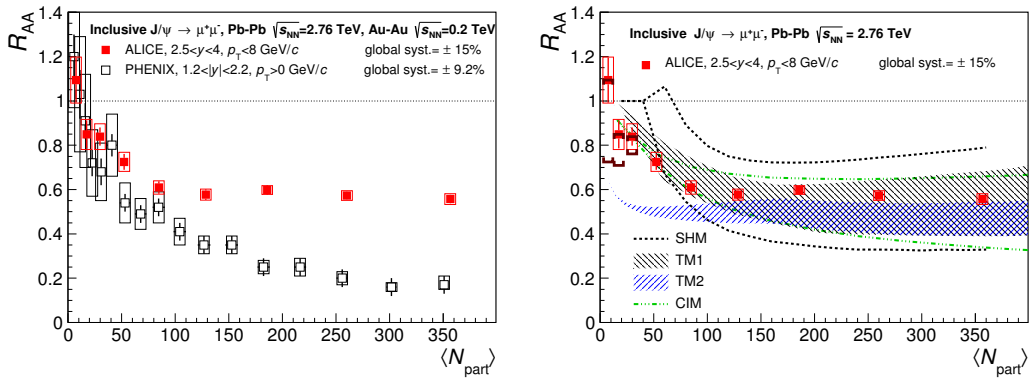

FIGURE 1.5: Inclusive J/Ψ R_{AA} as a function of the number of participant nucleons measured in Pb-Pb collisions at $\sqrt{s_{\mathrm{NN}}}$ =2.76 TeV, compared to the PHENIX measurement in Au-Au collisions at $\sqrt{s_{\mathrm{NN}}}$ =0.2 TeV (left) and to theoretical models, which all include a J/Ψ regeneration component (right). From [14].

can be generally referred to as partons) interact with the hot medium and lose energy, resulting in a suppression of high p_{T} hadrons. In Figure 1.6, R_{AA} less than unity of charged particles indicates this suppression and provides evidence of jet quenching. The plot on the right compares the R_{AA} and R_{pPb} values to help elucidate whether the observed suppression effect is caused by an effect of the hot medium.

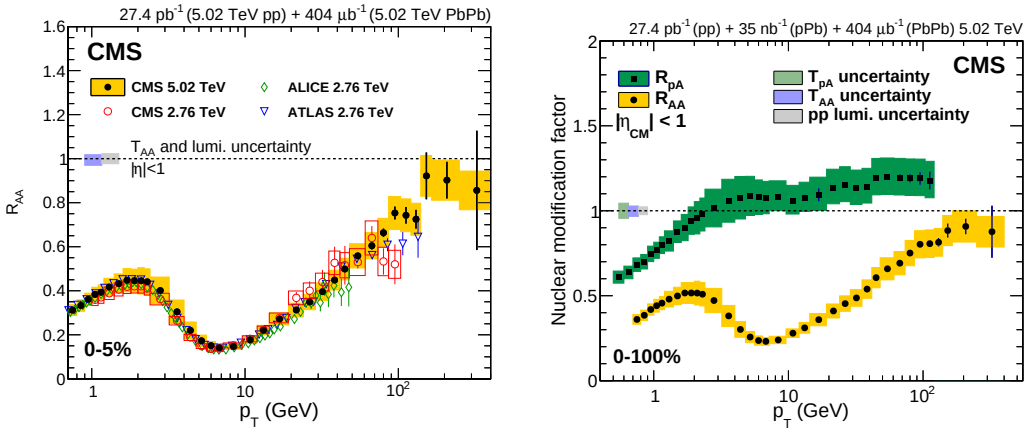

FIGURE 1.6: Charged-particle R_{AA} measured in the 0-5% centrality class from CMS in Pb–Pb collisions at $\sqrt{s_{\mathrm{NN}}}$ = 5.02 TeV with measurements from CMS, ALICE, and ATLAS in Pb–Pb collisions at $\sqrt{s_{\mathrm{NN}}}$ = 2.76 TeV (left). A comparison of charged-particle R_{AA} and R_{pPb} in collisions at $\sqrt{s_{\mathrm{NN}}}$ = 5.02 TeV (right), from [15]

Energy loss for heavy flavour probes focuses on the effects of differing parton mass and colour charge on in-medium energy loss. This can be via collisional or

radiative processes, causing a diffusion process where heavy quarks partially thermalise with the medium. This diffusion can be parameterised by the heavy quark spatial diffusion coefficent D_s which is closely linked to fundamental properties of the QGP such as the coupling strength of the medium. A energy-loss hierarchy is expected where gluons are expected to lose the most energy and the charm and beauty quarks lose less energy by virtue of their large masses ($E_g > E_c > E_b$). In Figure 1.7, several similarities are shown between the measured D meson R_{AA}

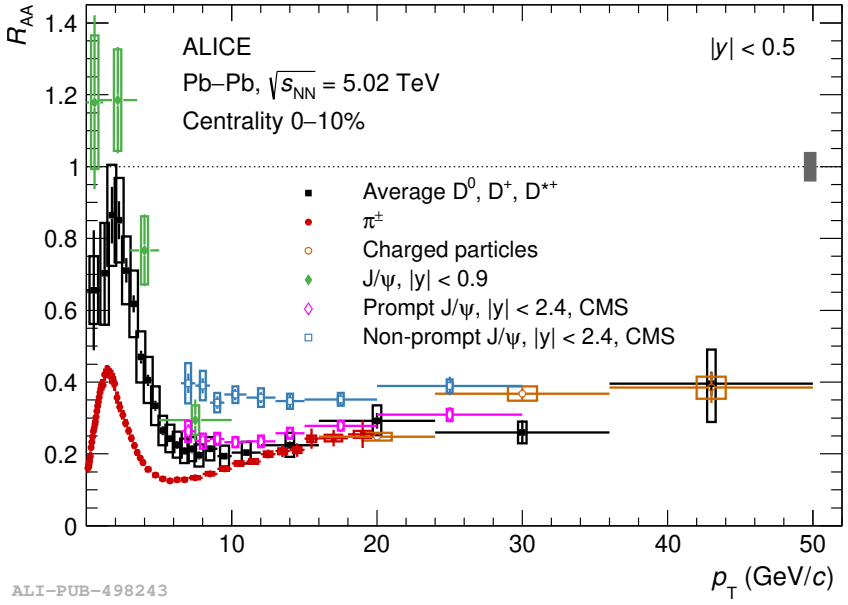

FIGURE 1.7: Average R_{AA} of D mesons in the 0-10% centrality class compared to the R_{AA} of charged pions, charged particles, inclusive J/Ψ, measured by ALICE, and to prompt and non-prompt J/Ψ measured by CMS in Pb–Pb collisions at $\sqrt{s_{\mathrm{NN}}} = 5.02$ TeV, from [16].

and those of the inclusive and prompt J/Ψ. The R_{AA} for D mesons is lower than the R_{AA} for non-prompt J/Ψ from beauty decays. At low p_{T} the D meson R_{AA} is higher than the pion R_{AA} before converging at about 10 GeV/c.

Despite these observations, it is important to note the R_{AA} shown for the different particle species cannot necessarily be simply intepreted as the energy loss to the medium due to a variety of other factors (such as flow or hadronisation) that contribute to the measured R_{AA}. In order to get a greater understanding of the energy loss and transport mechanisms at play, a comparison to theoretical models in both R_{AA} and v_2 measurements are needed. These are shown in Figure 1.8.

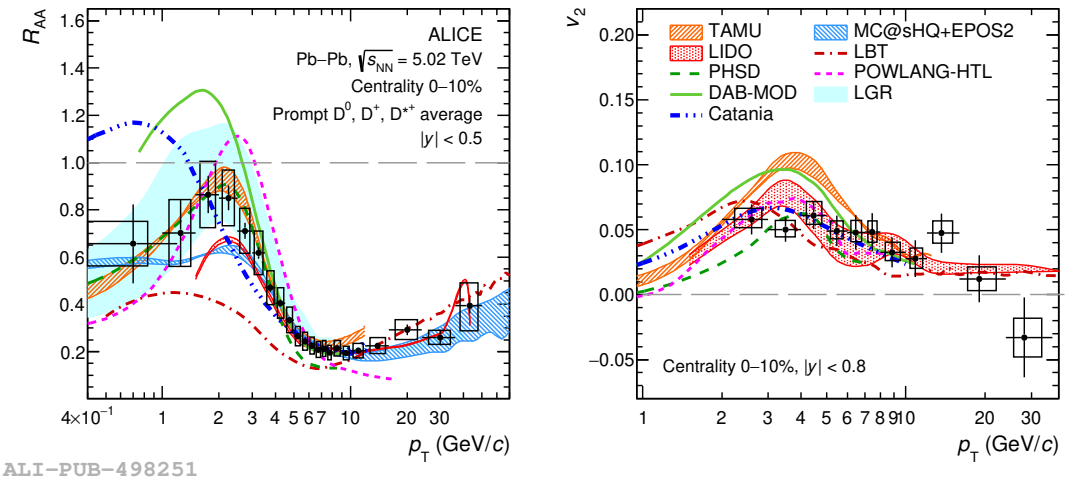

FIGURE 1.8: Average R_{AA} (left) and v_2 of D mesons in the 0-10% centrality class compared to multiple transport models in Pb–Pb collisions at $\sqrt{s_{\mathrm{NN}}}$ = 5.02 TeV, from [16].

Making simultaneous descriptions for both R_{AA} and v_2 is difficult for models and allows the data to give constraints on the ingredients and parameters used. The models compared differ in terms of the charm interaction with the medium, evolution of the medium, initial nuclear PDFs, and hadronisation mechanism. The models that give the best description of both the R_{AA} and v_2 measurements appear to use a similar range of values for the heavy-quark spatial diffusion coefficient,D_s.

One important way to understand the thermalisation and hadronisation of heavy quarks in the medium is the measurement of the relative production rates of baryons and mesons, i.e. baryon-to-meson ratios. The process of hadronisation may modify the momentum of the final state hadron with respect to the initial charm quark which hadronises, and this modification is very different depending on how the quark hadronises, and differs for baryons (which contain three quarks) and mesons (which contain two quarks). The production of baryons relative to mesons as a function of the hadron momentum is therefore a sensitive probe of how hadrons form from quarks, and as such can distinguish between different hadronisation scenarios. This makes the measurements of charmed baryons, such as the Λ_{c}^{+}, very important for understanding the underlying hadronisation mechanisms present in heavy-ion collisions.

In heavy-ion collisions, the major hadronisation mechanisms in Pb–Pb are:

- **Fragmentation:** This is the assumed mechanism of hadronisation for partons in the vacuum. In this process, quarks or diquarks are generated from the vacuum and combine with the heavy quark to form a hadron, and some fraction of the parton's momentum is transferred to the produced hadron. This is predicted to be the dominant process at high-p_{T}.

- **Coalescence/recombination:** The QGP is a dense system of deconfined quarks and gluons, and hadronisation occurs when the QGP has cooled sufficiently. It is predicted [17, 18] that in this case, quarks that are close to each other in position and momentum space can 'coalesce' to form hadrons. The hadron momentum is then the sum of the individual quark momenta. This is expected to be the dominant process at low p_{T}, and an enhancement of the baryon-to-meson ratio is expected where coalescence is dominant.

An enhancement of both the proton/pion and Λ/K^0_S ratios with respect to pp collisions at RHIC [22] and the LHC [23, 24] were interpreted to be due to hadronisation via coalescence as well as radial flow. Recently the Λ_{c}^+ baryon has become experimentally accessible for the first time and allowed for the measurement of the $\Lambda_{\mathrm{c}}^+/\mathrm{D}^0$ ratio. Measurements of the $\Lambda_{\mathrm{c}}^+/\mathrm{D}^0$ ratio in Pb–Pb collisions at $\sqrt{s_{\mathrm{NN}}}$ = 5.02 TeV with the CMS [19], [20], and ALICE [21] detectors are presented in Figure 1.9. At midrapidity in the ALICE measurements (Figure 1.9 bottom), the $\Lambda_{\mathrm{c}}^+/\mathrm{D}^0$ ratio is enhanced with respect to measurements in pp and p–Pb collisions. When attempting to replicate the data, the Catania model performed best when only including the coalescence mechanism. Similarly, the Shao-Song model required a higher value of $R_{BM} = 1.2$, a parameter for determining the relative production of singly charmed baryon and mesons, than the the value used (0.425) to replicate the behaviour seen in pp and p–Pb collisions. However, the uncertainties in this first measurement are very large and increased precision is needed to further constrain these models. The CMS results also measured at midrapidity (Figure 1.9 top left), seem to show no significant difference in the $\Lambda_{\mathrm{c}}^+/\mathrm{D}^0$ ratio measured in pp and Pb–Pb collisions in the p_{T} range shared by the two measurements, indicating that fragmentation is the dominant hadronisation mechanism at $p_{\mathrm{T}} > 10$ GeV/c. Measurements by STAR (Figure 1.9 top right) in Au–Au collisions at $\sqrt{s_{\mathrm{NN}}} = 200$ GeV show similarities between the $\Lambda_{\mathrm{c}}^+/\mathrm{D}^0$ ratio and light flavour baryon-to-meson ratios and models that implement coalescence give the best description of the data.

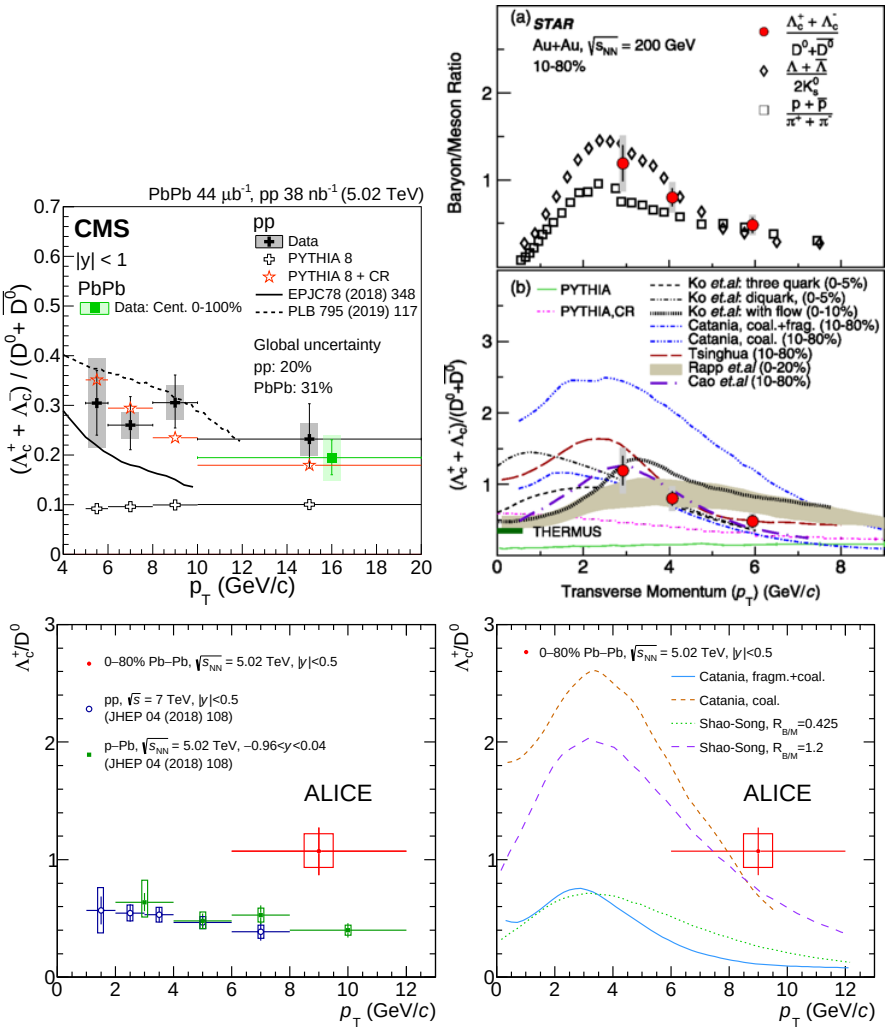

FIGURE 1.9: The measured Λ_c^+/D^0 ratio from CMS in pp and Pb–Pb collisions at $\sqrt{s_{NN}} = 5.02$ TeV (top left). The measured Λ_c^+/D^0 ratio from STAR in Au–Au collisions at $\sqrt{s_{NN}} = 200$ GeV (top right). The measured Λ_c^+/D^0 ratio from ALICE in Pb–Pb collisions at $\sqrt{s_{NN}} = 5.02$ TeV compared with the measured Λ_c^+/D^0 ratio in pp collisions at $\sqrt{s} = 7$ TeV and p–Pb collisions at $\sqrt{s_{NN}} = 5.02$ TeV (bottom left), and with theoretical models (bottom right). From [19], [20] and [21], respectively.

1.2.3 Heavy-flavour production in pp collisions

The measurements detailed in this thesis are of the production of heavy-flavour hadrons, in particular the charmed baryon, Λ_c^+. The production of heavy-flavour hadrons can be described by the factorisation theorem [25]. This is a convolution of three terms:

- The parton distribution functions of the two colliding protons (or nuclei).

- The hard scattering cross sections of partons to produce a charm-anticharm pair.

- The fragmentation functions that determine the probability of a charm quark fragmenting into a given hadron species

While the partonic hard-scattering cross sections may be calculated perturbatively, the parton distribution functions and fragmentation functions are non-perturbative and require input from experimental data. Typically, the data is taken from Deep Inelastic Scattering (DIS) and e^+e^- experiments, respectively. The measurement of heavy flavour hadrons in pp collisions provides a good test of pQCD calculations, tests the validity of fragmentation functions measured in e^+e^- collisions, and acts as a vital reference for corresponding measurements made in heavy-ion collisions. Measurements in p–Pb collisions are needed to understand the cold nuclear matter effects which could also modify the production of heavy-flavour hadrons.

Predictions of heavy quark production come in three broad categories:

1. The first category of predictions are pQCD calculations. The assumptions made as part of the calculation can change the p_{T} range where these predictions are applicable. Calculations such as general-mass variable-flavour-number-scheme (GM-VFNS) [26] and fixed-order + next-leading-logarithms (FONLL) [27] are suitable over a large p_{T} range and are regularly compared against measurements of heavy-flavour hadrons.

2. The second category are Monte Carlo generators that generate their predictions through the simulation of many particle collisions. They also use QCD to calculate the heavy quark production cross section. However, the final state is generated by simulating the parton shower that includes string fragmentation. The fragmentation is tuned to fragmentation functions measured in e^+e^- and e^-p collisions. Some Monte Carlo generators such as PYTHIA include mechanisms by which the the production of baryons can be altered. When colour reconnection [28] (a process that is suppressed in e^+e^- collisions) is included, this allows for colour connections between quarks in initially uncorrelated parton interactions, pictured in Figure 1.10 (top). Figure 1.10 (bottom) shows the possible cluster configuration that would lead to baryon reconnection.

3. The third category are predictions from theorists that implement hadronisation via specific mechanisms. For instance, the Catania model [29] assumes coalescence in small systems and the model by He and Rapp [30] assumes currently unobserved high-mass charmed baryon states. These models include FONLL calculations for the charm quark production cross section, but the subsequent method by which hadronisation of the charm quarks is handled is specific to the particular model. Catania implements a combination of coalescence and fragmentation, with coalescence dominant at low p_{T} and fragmentation dominant at high p_{T}, while the He and Rapp model uses the statistical hadronisation model with an enhanced list of high-mass charmed baryon states that strongly decay to the Λ_{c}^{+}.

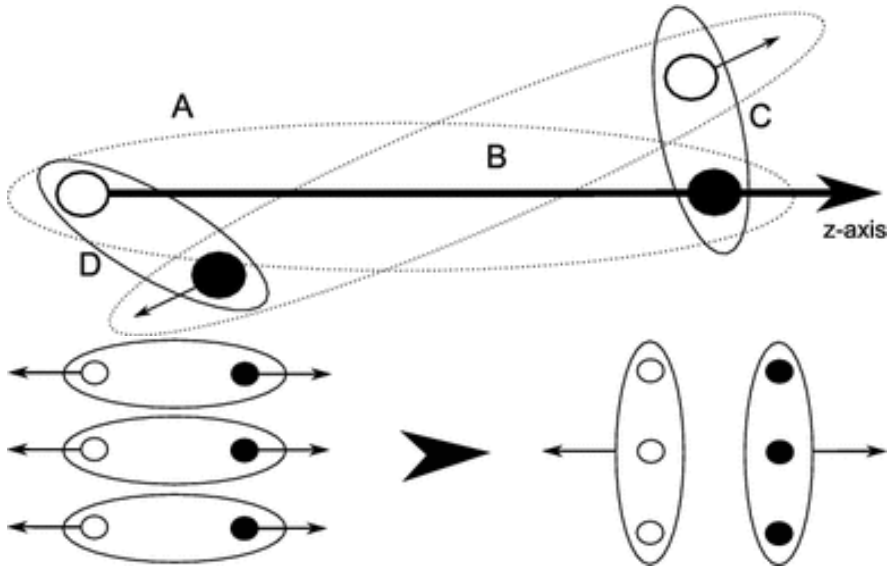

FIGURE 1.10: Representation of initially correlated quarks denoted by A and B, and the newly colour connected quarks denoted by C and D (top). Representation of a possible cluster configuration that could lead to baryonic reconnection (bottom), from [31].

In the previous data-taking period of the LHC (Run 1), a first measurement of the Λ_{c}^{+} baryon production cross section at ALICE for pp and p–Pb collisions [32], was much higher than model predictions which used fragmentation functions tuned on $e^{+}e^{-}$ data, that had previously provided good descriptions for charmed meson production, but were unable to accurately describe the Λ_{c}^{+} measurement. This result has implied that the fragmentation functions tuned on $e^{+}e^{-}$ data may not be universal between collision systems and led to the development of models [29, 30] that aim to explain the Λ_{c}^{+} enhancement.

1.2.4 The measurements detailed in this thesis

This thesis presents new measurements of the production of prompt charmed baryon, Λ_c^+ in pp and p-Pb collisions at the energy of $\sqrt{s_{\rm NN}} = 5.02$ TeV made with the ALICE detector at the LHC during the Run 2 data taking period. This analysis benefits greatly from the greater data sample, allowing the analysis to cover a wider $p_{\rm T}$ range in smaller $p_{\rm T}$ intervals than the previous analysis. Additionally, the change in the collision energy studied for pp collisions to match that used in p–Pb and Pb–Pb collisions reduces the uncertainties on observables that rely on comparisons between collision systems.

The contents of the rest of thesis is as follows. A general description of the ALICE detector is included and further information is given on the sub-detectors relevant to the analysis in Chapter 2. The next two chapters include excerpts from analysis notes that I coauthored and that are specific to the analysis of the $\Lambda_c^+ \rightarrow {\rm pK}^-\pi^+$ decay channel in pp and p–Pb collisions, respectively. The fifth and sixth chapters incorporate published materials I have cowritten based on my work on the $\Lambda_c^+ \rightarrow {\rm pK}^-\pi^+$ decay channel and the work of fellow collaborators and analysers of the $\Lambda_c^+ \rightarrow {\rm pK}^0_{\rm S}$ decay channel. These chapters will show the results and some further theoretical background for the measurements presented. Finally, conclusions on the presented work are given and the future of similar measurements are discussed. This thesis is primarily my own work. The sources of other materials are declared.

References

[1] Murray Gell-Mann. "Symmetries of Baryons and Mesons". In: *Phys. Rev.* 125 (3 1962), pp. 1067–1084. DOI: 10.1103/PhysRev.125.1067. URL: https://link.aps.org/doi/10.1103/PhysRev.125.1067.

[2] Y. Ne'eman. "Derivation of strong interactions from a gauge invariance". In: *Nuclear Physics* 26.2 (1961), pp. 222–229. ISSN: 0029-5582. DOI: https://doi.org/10.1016/0029-5582(61)90134-1. URL: https://www.sciencedirect.com/science/article/pii/0029558261901341.

[3] G Zweig. *An SU_3 model for strong interaction symmetry and its breaking; Version 1.* Tech. rep. Geneva: CERN, 1964. URL: http://cds.cern.ch/record/352337.

[4] M. Gell-Mann. "A schematic model of baryons and mesons". In: *Physics Letters* 8.3 (1964), pp. 214–215. ISSN: 0031-9163. DOI: https://doi.org/10.1016/S0031-9163(64)92001-3. URL: https://www.sciencedirect.com/science/article/pii/S0031916364920013.

[5] Martin Breidenbach et al. "OBSERVED BEHAVIOR OF HIGHLY INELASTIC ELECTRON-PROTON SCATTERING". In: *Physical Review Letters* 23 (1969), pp. 935–939.

[6] S. Abachi et al. "Observation of the Top Quark". In: *Phys. Rev. Lett.* 74 (14 1995), pp. 2632–2637. DOI: 10.1103/PhysRevLett.74.2632. URL: https://link.aps.org/doi/10.1103/PhysRevLett.74.2632.

[7] P.A. Zyla et al. "Review of Particle Physics". In: *PTEP* 2020.8 (2020), p. 083C01. DOI: 10.1093/ptep/ptaa104.

[8] Rolf Hagedorn. "Statistical thermodynamics of strong interactions at high energies". In: *Nuovo Cimento, Suppl.* 3 (1965), pp. 147–186. URL: http://cds.cern.ch/record/346206.

[9] B. P. Abbott et al. "GW170817: Observation of Gravitational Waves from a Binary Neutron Star Inspiral". In: *Phys. Rev. Lett.* 119 (16 2017), p. 161101. DOI: 10.1103/PhysRevLett.119.161101. URL: https://link.aps.org/doi/10.1103/PhysRevLett.119.161101.

[10] C. Aidala et al. "Creation of quark–gluon plasma droplets with three distinct geometries". In: *Nature Phys.* 15.3 (2019), pp. 214–220. DOI: 10.1038/s41567-018-0360-0. arXiv: 1805.02973 [nucl-ex].

[11] Peter Braun-Munzinger and Benjamin DÃűnigus. "Loosely-bound objects produced in nuclear collisions at the LHC". In: *Nuclear Physics A* 987 (2019), pp. 144–201. ISSN: 0375-9474. DOI: https://doi.org/10.1016/j.nuclphysa.2019.02.006. URL: https://www.sciencedirect.com/science/article/pii/S0375947419300405.

[12] Albert M Sirunyan et al. "The production of isolated photons in PbPb and pp collisions at $\sqrt{s_{\mathrm{NN}}} = 5.02$ TeV". In: *JHEP* 07 (2020), p. 116. DOI: 10.1007/JHEP07(2020)116. arXiv: 2003.12797 [hep-ex].

[13] Shreyasi Acharya et al. "Z-boson production in p-Pb collisions at $\sqrt{s_{\mathrm{NN}}} = 8.16$ TeV and Pb-Pb collisions at $\sqrt{s_{\mathrm{NN}}} = 5.02$ TeV". In: *JHEP* 09 (2020), p. 076. DOI: 10.1007/JHEP09(2020)076. arXiv: 2005.11126 [nucl-ex].

[14] Jaroslav Adam et al. "Differential studies of inclusive J/ψ and ψ(2S) production at forward rapidity in Pb-Pb collisions at $\sqrt{s_{\mathrm{NN}}} = 2.76$ TeV". In: *JHEP* 05 (2016), p. 179. DOI: 10.1007/JHEP05(2016)179. arXiv: 1506.08804 [nucl-ex].

[15] Vardan Khachatryan et al. "Charged-particle nuclear modification factors in PbPb and pPb collisions at $\sqrt{s_{\mathrm{N\,N}}} = 5.02$ TeV". In: *JHEP* 04 (2017), p. 039. DOI: 10.1007/JHEP04(2017)039. arXiv: 1611.01664 [nucl-ex].

[16] Shreyasi Acharya et al. "Prompt D^0, D^+, and D^{*+} production in Pb-Pb collisions at $\sqrt{s_{\mathrm{NN}}} = 5.02$ TeV". In: (Oct. 2021). arXiv: 2110.09420 [nucl-ex].

[17] V. Greco, C. M. Ko, and P. Lévai. "Partonic coalescence in relativistic heavy ion collisions". In: *Phys. Rev. C* 68 (3 2003), p. 034904. DOI: 10.1103/PhysRevC.68.034904. URL: https://link.aps.org/doi/10.1103/PhysRevC.68.034904.

[18] R. J. Fries et al. "Hadron production in heavy ion collisions: Fragmentation and recombination from a dense parton phase". In: *Phys. Rev. C* 68 (2003), p. 044902. DOI: 10.1103/PhysRevC.68.044902. arXiv: nucl-th/0306027.

[19] Albert M Sirunyan et al. "Production of Λ_{c}^{+} baryons in proton-proton and lead-lead collisions at $\sqrt{s_{\mathrm{NN}}} = 5.02$ TeV". In: *Phys. Lett. B* 803 (2020), p. 135328. DOI: 10.1016/j.physletb.2020.135328. arXiv: 1906.03322 [hep-ex].

[20] Jaroslav Adam et al. "First measurement of Λ_c baryon production in Au+Au collisions at $\sqrt{s_{\mathrm{NN}}} = 200$ GeV". In: *Phys. Rev. Lett.* 124.17 (2020), p. 172301. DOI: 10.1103/PhysRevLett.124.172301. arXiv: 1910.14628 [nucl-ex].

[21] Shreyasi Acharya et al. "Λ_c^+ production in Pb-Pb collisions at $\sqrt{s_{\mathrm{NN}}} = 5.02$ TeV". In: *Phys. Lett. B* 793 (2019), pp. 212–223. DOI: 10.1016/j.physletb.2019.04.046. arXiv: 1809.10922 [nucl-ex].

[22] K. Adcox et al. "Centrality dependence of pi+ / pi-, K+ / K-, p and anti-p production from s(NN)**(1/2) = 13-=GeV Au+Au collisions at RHIC". In: *Phys. Rev. Lett.* 88 (2002), p. 242301. DOI: 10.1103/PhysRevLett.88.242301. arXiv: nucl-ex/0112006.

[23] Betty Bezverkhny Abelev et al. "K^0_S and Λ production in Pb-Pb collisions at $\sqrt{s_{NN}} = 2.76$ TeV". In: *Phys. Rev. Lett.* 111 (2013), p. 222301. DOI: 10.1103/PhysRevLett.111.222301. arXiv: 1307.5530 [nucl-ex].

[24] Shreyasi Acharya et al. "Production of charged pions, kaons, and (anti-)protons in Pb-Pb and inelastic *pp* collisions at $\sqrt{s_{NN}} = 5.02$ TeV". In: *Phys. Rev. C* 101.4 (2020), p. 044907. DOI: 10.1103/PhysRevC.101.044907. arXiv: 1910.07678 [nucl-ex].

[25] John C. Collins, Davison E. Soper, and George F. Sterman. "Factorization of Hard Processes in QCD". In: *Adv. Ser. Direct. High Energy Phys.* 5 (1989), pp. 1–91. DOI: 10.1142/9789814503266_0001. arXiv: hep-ph/0409313.

[26] B. A. Kniehl et al. "Collinear subtractions in hadroproduction of heavy quarks". In: *Eur. Phys. J. C* 41 (2005), pp. 199–212. DOI: 10.1140/epjc/s2005-02200-7. arXiv: hep-ph/0502194.

[27] Matteo Cacciari, Mario Greco, and Paolo Nason. "The P(T) spectrum in heavy flavor hadroproduction". In: *JHEP* 05 (1998), p. 007. DOI: 10.1088/1126-6708/1998/05/007. arXiv: hep-ph/9803400.

[28] Jesper R. Christiansen and Peter Z. Skands. "String Formation Beyond Leading Colour". In: *JHEP* 08 (2015), p. 003. DOI: 10.1007/JHEP08(2015)003. arXiv: 1505.01681 [hep-ph].

[29] Salvatore Plumari et al. "Charmed Hadrons from Coalescence plus Fragmentation in relativistic nucleus-nucleus collisions at RHIC and LHC". In: *Eur. Phys. J.* C78.4 (2018), p. 348. DOI: 10.1140/epjc/s10052-018-5828-7. arXiv: 1712.00730 [hep-ph].

[30] Min He and Ralf Rapp. "Charm-Baryon Production in Proton-Proton Collisions". In: *Phys. Lett.* B795 (2019), pp. 117–121. DOI: 10.1016/j.physletb.2019.06.004. arXiv: 1902.08889 [nucl-th].

[31] Stefan Gieseke, Patrick Kirchgaeßer, and Simon Plätzer. "Baryon production from cluster hadronisation". In: *Eur. Phys. J. C* 78.2 (2018), p. 99. DOI: 10.1140/epjc/s10052-018-5585-7. arXiv: 1710.10906 [hep-ph].

[32] Shreyasi Acharya et al. "Λ_c^+ production in pp collisions at $\sqrt{s} = 7$ TeV and in p–Pb collisions at $\sqrt{s_{NN}} = 5.02$ TeV". In: *JHEP* 04 (2018), p. 108. DOI: 10.1007/JHEP04(2018)108. arXiv: 1712.09581 [nucl-ex].

Chapter 2

ALICE Experimental Setup

2.1 The Large Hadron Collider

The LHC is a double-ring hadron accelerator located under the French-Swiss border. It was built in the 26.7 km circumference tunnel that originally housed the CERN LEP machine. It has four crossing points, each corresponding to the four main experiments (ALICE, ATLAS, CMS and LHCb). It was built with the aim to produce the high-energy proton-proton collisions necessary in which to study the proposed Higgs Boson, discovered by both ATLAS [1] and CMS [2] experiments in 2012. The ATLAS and CMS detectors are general-purpose detectors able to study a large range of physics topics, including supersymmetry, extra dimensions, and dark matter. LHCb and ALICE are more specialised. LHCb studies CP violation and the observation of rare decays B hadrons. ALICE focuses on Heavy-Ion collisions and measures the properties of the QGP.

Figure 2.1 shows a schematic of the LHC. The ring is separated into eight straight sections of approximate length 528 m joined by eight arcs. The straight sections can house experimental or utility installations. The ATLAS and CMS experiments are located in opposing interaction regions 1 and 5, respectively. ALICE and LHCb are located at interaction regions 2 and 8, where the injection systems for each beam are also located. Interaction regions 3 and 7 contain collimation systems designed to clean the beam of particles with either high momentum offset or high betatron amplitudes, respectively. Interaction region 4 contains the radio frequency systems and LHC beam instrumentation and interaction region 6 contains the beam abort systems for both beams, where the beams are kicked and deflected out of the ring into absorbers in a separate tunnel.

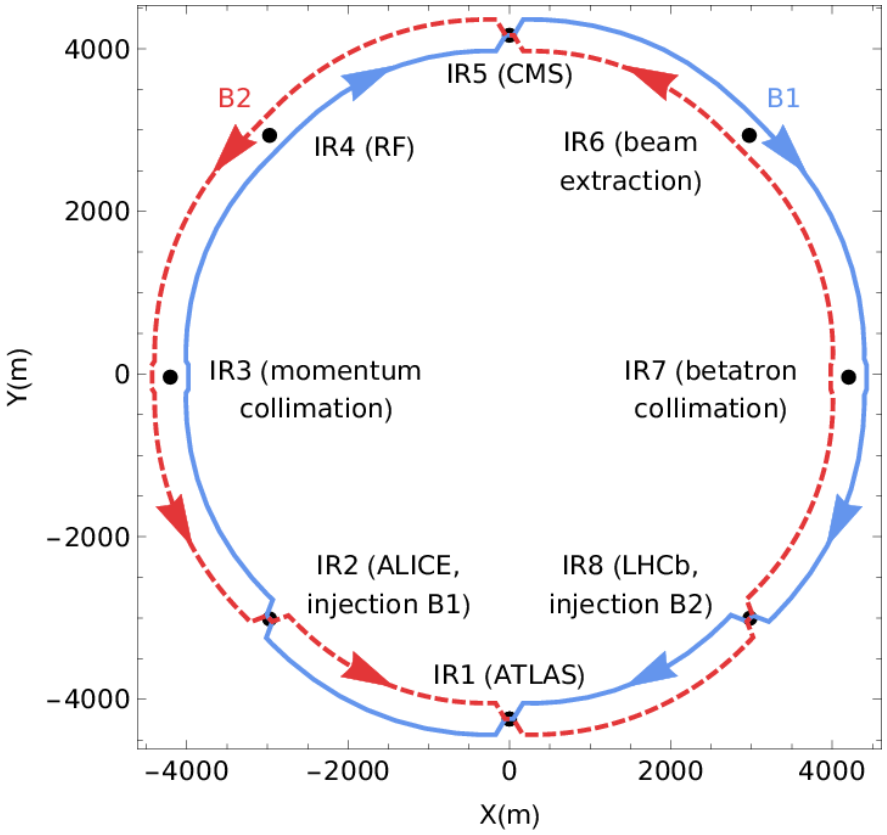

FIGURE 2.1: Schematic layout of the LHC showing the locations of experimental and instrumentation installations, from [3].

2.2 The ALICE detector

The ALICE detector is a general-purpose detector specialising on studying strongly interacting matter and the quark-gluon plasma generated, at high-energy densities, in the collisions of heavy nuclei. Although all of the main detectors at the LHC each have their own heavy-ion programmes, ALICE is differentiated by its capability to reconstruct and identify particle tracks in the high multiplicity environment seen in these collisions. To achieve this, the ALICE detector includes a variety of tracking and Particle Identification (PID) detectors that will be described in the rest of this chapter [4]. The detectors can be separated into two main groups: the central barrel that encloses the interaction point and provides measurements of hadrons, electrons, and photons at mid-rapidity, and the forward arm that measures muons and the global characteristics of the events.

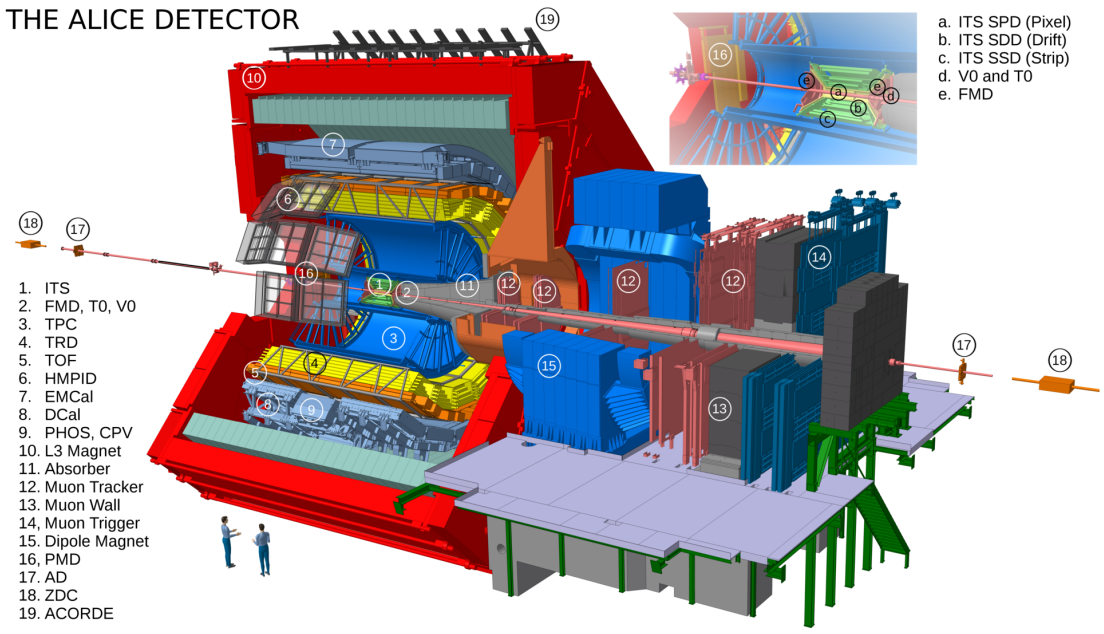

FIGURE 2.2: Schematic of the ALICE detector. Subdetectors are labelled. [5]

2.2.1 The Central Barrel

The central barrel contains detectors that are primarily dedicated to vertexing, tracking, or the particle identification (PID) of hadrons, electrons, and photons produced at mid-rapidity. The central barrel detectors are enclosed by the L3 solenoid magnet [6] in a magnetic field of $B = 0.5$ T. Moving outwards from the interaction point, the first four detectors cover a pseudorapidity of $-0.9 \leq \eta \leq 0.9$ in the full azimuth. From the interaction point outwards, the detectors are the:

- **Inner Tracking System (ITS)** - Consisting of six silicon layers, it performs the reconstruction of the primary and secondary vertices, provides tracking and PID of low momenta particles, and supplements the tracking in the Time Projection Chamber.

- **Time-Projection Chamber (TPC)** - Acts as the primary tracking detector, used in the vertexing, and can provide $\mathrm{d}E/\mathrm{d}x$ information for PID.

- **Time-Of-Flight detector (TOF)** - Array of Multigap Resistive Plate Chambers (MRPCs) that provides time-of-flight measurements used in PID of charged tracks.

- **Transition Radiation Detector (TRD)** - Specialised PID detector for electrons over $p_{\mathrm{T}} < 1$ GeV/c using transition radiation and specific energy

loss ($\mathrm{d}E/\mathrm{d}x$) measurements as well as providing tracking and a fast trigger for charged particles.

- **Photon Spectrometer (PHOS)** - A high-resolution electromagnetic spectrometer that operates in a limited acceptance ($-0.12 \leq \eta \leq 0.12$) at central rapidity. PHOS contributes to the study of thermal and dynamic properties through the measurement of low p_{T} direct photons and jet quenching through the measurements of π^0 and γ-jet correlations.

- **Electro-Magnetic Calorimeter (EMCal)** - A large Pb-scintillator that acts as a large-acceptance ($-0.7 \leq \eta \leq 0.7$), moderate resolution electromagnetic calorimeter focused on the study of jet quenching. The EMCal provides a fast and efficient trigger for hard jets, photons and electrons.

- **High-Momentum Particle Identification Detector (HMPID)** - Specialised PID detector for hadrons over $p_{\mathrm{T}} > 1$ GeV/c using ring imaging Cherenkov counters. Additionally, the HMPID can perform PID for light nuclei at hight p_{T} at central rapidity.

2.2.2 The Forward Arm and Trigger detectors

The forward arm of the ALICE detector primarily focuses on the tracking of muons, triggers, and the global characteristics of an event. The magnetic field ($B = 0.67$ T) is provided by a dipole magnet placed 7m from the interaction vertex. There are also detectors that characterise the global properties of events and trigger on those of interest. The detectors located in the forward arm that are used for triggers include:

- **Muon Spectrometer** - The measurement of muons is performed by the muon spectrometer in the pseudorapidity range $-4.0 < \eta < -2.5$ allowing for the study of open heavy flavour and the complete spectrum of heavy-flavour vector-meson resonances via e-μ coincidence and $\mu^+\mu^-$ decay measurements, respectively.

- **Zero Degree Calorimeter (ZDC)** - Composed of hadronic calorimeters at 116 m either end of the interaction point and electromagnetic calorimeters located at 7 m away from the interaction point opposite the muon spectrometer. It measures the energy carried in the forward direction by spectator nucleons and gives information on the centrality class of the event.

- **Photon Multiplicity Detector (PMD)** - Two planes of gas proportional counters that are used to estimate the reaction plane of the collision and transverse electromagnetic energy from measurements of the multiplicity and spatial distributions of photons in the forward pseudorapidity region ($2.3 \leq \eta \leq 3.7$).

- **Forward Multiplicity Detector (FMD)** - Provides charged-particle multiplicity in the pseudorapidity ranges $-3.4 \leq \eta \leq -1.7$ and $1.7 \leq \eta \leq 5.0$.

- **V0** - Two arrays of scintillator counters installed on either end of the ALICE interaction point that cover the pseudorapidity ranges $-3.4 \leq \eta \leq -1.7$ and $2.8 \leq \eta \leq 5.1$. This detector alongside the Silicon Pixel Detector provides the minimum bias trigger for the central barrel, and is additionally used to provide centrality information and elimate background events caused by interactions between protons and residual gas in the beam pipe.

- **T0** - Two arrays of Cherenkov counters covering the pseudorapidity ranges $-3.28 \leq \eta \leq -2.97$ and $4.61 \leq \eta \leq 4.92$ that provide a start time for the time-of-flight detector and supplies the main signals for the L0 trigger (Information about triggers in Sect. 2.2.6).

- **ALICE Cosmic Ray Detector(ACORDE)** - Two stacked scintillator arrays, operating in coincidence, located above the L3 solenoid magnet. It provides a L0 trigger for alignment and calibration procedures. It is also used in the study of cosmic rays through the detection of single atmospheric and multi-muon events.

2.2.3 The Inner Tracking System

The ITS consists of six cylindrical layers of silicon detectors that cover a pseudorapidity range $|\eta| < 0.9$ and extend from an inner radius of 3.9 cm to an outer radius of 43 cm. The inner and outer radii of the the detector are dictated by the dimensions of the beam pipe and ensuring a good track matching efficiency with the TPC, respectively. The ITS can be divided into smaller sub-detectors based on the type of silicon layers used. The Silicon Pixel Detector (SPD) corresponds to the two innermost layers, the Silicon Drift Detector (SDD) to the middle two layers, and the Silicon Strip Detector (SSD) to the two outermost layers. The SPD module is comprised of a 2D sensor matrix bump bonded to five readout chips.

The sensor matrix consists of 256 × 160 cells to give an active area of 12.8 mm ($r\phi$) × 70.7 mm (z). The SDD was produced from homogeneous high-resistivity neutron transmutation doped silicon with a sensitive area of 70.17($r\phi$)×75.26(z) mm^2. The sensitive region is split in two drift by a central cathode strip. The drift regions each contain 256 collection anodes, and three rows of 33 MOS injectors that monitor drift velocity. The SSD sensors are 300 μm thick and have 768 strips on each side. The sensors are mounted so that the strips are in parallel to magnetic field to optimise the resolution in the bending direction. The role of the ITS is to determine the primary vertex to a resolution better than 100 μm, reconstruct the secondary vertices of strange and heavy flavour particles, and to track and identify low momenta particles below 200 MeV/c. The choice and the position of the silicon detector types is largely dependent on the ability to fufill these roles while minimising the amount of material in the active volume and being suitable for the expected particle density (50 particles per cm^2 for the inner layer and less than 1 particle per cm^2 for the outer layers). The SPD has high granularity, important for the high-particle density. The SDD has very good multitrack capability and provides the first two of the dE/dx measurements necessary for PID. The SSD provides the latter two dE/dx measurements and provides a two dimensional measurement of the track position crucial for the matching of tracks with the TPC.

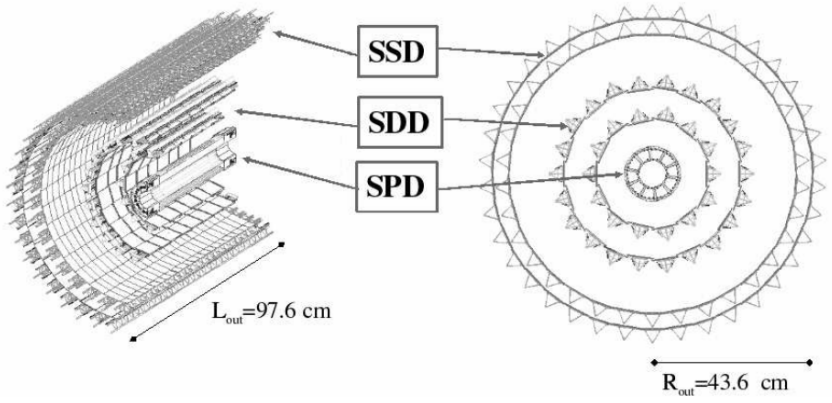

FIGURE 2.3: Schematic of the ITS layout showing the positions of the different silicon layers. From the inside outwards, there is the Silicon Pixel Detector, the Silicon Drift Detector, and Silicon Strip Detector. [4]

Detector Type	Acceptance	Radial position (cm)	Area (m^2)
SPD	± 2, ± 1.4	3.9, 7.6	0.07, 0.14
SDD	± 0.9, ± 0.9	15.0, 23.9	0.42, 0.89
SSD	± 0.97, ± 0.97	38.0, 43.0	2.20, 2.80

TABLE 2.1: Table showing the Acceptance and dimensions of the different ITS layers. From [4]

2.2.4 The Time Projection Chamber

The Time Projection Chamber (TPC) is the main tracking detector of the experiment and is designed to match tracks in the ITS and TRD. It has an active volume extending from an inner radius of about 85 cm to an outer radius of 250 cm and a length of 500 cm, covering a pseudorapidity range $|\eta| < 0.9$. The inner radius was decided by the maximum acceptable hit density (tracking). Whereas, the outer radius was determined by the length necessary to achieve a specific energy loss resolution of 5-7%, allowing the TPC to also identify particles up to approximately 50 GeV/c. The design of the ALICE TPC follows typical design principles for a TPC. It contains an active volume of gas in a uniform electric field and multi-wire proportional chambers (MWPCs) along the endplates. Any charged particle passing through the gas leaves a track of ionised gas, the electrons follow the electric field and their locations are directly measured by the MWPCs in r and ϕ. The z-coordinate is determined by the drift time. It is able to provide measurements of particles in a wide range of transverse momentum, from 0.1 GeV/c to 100 GeV/c. The TPC provides up to 159 space points to reconstruct the particle trajectory and determine its momentum, and provides charged PID via the measurement of the specific energy loss $\mathrm{d}E/\mathrm{d}x$.

2.2.5 The Time-Of-Flight Detector

The TOF detector is an array of Multi-gap Resistive Plate Chambers (MRPCs) that covers the full azimuth in the pseudorapidity range $|\eta| < 0.9$. These chambers contain an array of strips 1220 mm long and 100 mm wide.These chambers hold several advantages over other parallel plate designs such as: they can be operated at atmospheric pressure; the signal is summed from multiple gaps which removes any late tail and gives a peak well separated from zero; the resistive plates enable operation at high gain by quenching streamers. The MRPC strips are tilted as to minimise the transversal path of particles through the strips. This mitigates

signal being shared among adjacent pads, reducing occupancy and the time jitter of measured signals. The TOF detector provides PID for pions and kaons in the range $p_{\mathrm{T}} < 2.5$ GeV/c, and $p_{\mathrm{T}} < 4$ GeV/c for protons, providing π/K and K/p separation better than 3σ.

2.2.6 Triggers

The ALICE Central Trigger Processor (CTP) generates three levels of hierarchical hardware triggers: L0, L1, and L2. By operating at these different levels the CTP can satisfy the varied timing requirements of the different sub-detectors. A pretrigger activates electronics in the TRD at < 900 ns from information given by the T0, V0 and TOF detectors, then at 1.2 μs the L0 recieves some of the fast trigger inputs with the remaining fast trigger inputs being collected by the L1 signal at 6.5 μs. For pp collisions, these fast triggers include signals from the T0, PHOS, EMCAL, TOF, V0, TRD, ZDC, ACORDE and SPD. The final trigger L2 is sent at 88 μs to include the input from the TPC. This L2 trigger also corresponds to the past-future protection interval. ALICE implements this protection to ensure that selected events are not spoilt by pile-up. The protection is programmable and can be implemented differently depending on the the collision type to account for the widely differing multiplicity and luminosity in pp and Pb–Pb collisions. The software-based High-Level Trigger (HLT) is used to mitigate the large discrepancy between the data rate and the archiving rate. To do this, events are rejected or selected based on further online analysis. Further reductions can be achieved by passing only data related to a physics region of interest from an event, and compression of the event data. When there are multiple triggers corresponding to events of differing rarity, downscaling can be applied to the more common events. In addition to the downscaling, common trigger classes can be temporarily disabled when the occupied temporary storage exceeds some preset level to keep bandwidth available for rare processes.

2.2.7 Vertex and Track Reconstruction

The reconstruction of the primary vertex is a vital requirement for multiple levels of data processing in ALICE. The primary vertex is needed at the online level to monitor the beam position and spread. This is provided by the SPD due to its proximity to the interaction point, response time, and excellent resolution

due to high granularity. The primary vertex, as given by clusters in the SPD, is taken by the Kalman filter algorithm as an input at the reconstruction level. The primary vertex can be determined either locally from tracklets in the SPD or via reconstructed tracks. The primary vertex and tracks are reconstructed by information in the ITS, TPC, and TRD in the following steps [7]:

1. The first estimate of the the primary vertex is given by the local determination in the SPD. If a position in 3D space cannot be determined only the z coordinate will be passed to the next step.

2. Track reconstruction occurs from the TPC inwards using a Kalman filtering algorithm. Track candidates are created using the location of the primary vertex and information from the outermost rows in the TPC.

3. The track reconstruction moves inwards from the TPC into the outermost layer of the ITS and the tracks are then matched. The reconstruction continues to the innermost pixel layer. This is done with and without vertex information from the SPD to maximise the efficiency for primary tracks and to find tracks displaced from the vertex, respectively.

4. Back-propagation outwards through both the ITS and TPC where the tracks are then extrapolated to the TRD. Further extrapolation matches hits on the PID detectors.

5. A final pass inwards, now with the full PID information, is performed.

6. The primary vertex is determined now using the reconstructed tracks. The tracks and (their corresponding vertex) are stored for later analysis.

2.2.8 Particle Identification

For the analyses presented, only the PID from the TPC and TOF was used. Further details of how these PID signals are combined are given in Chapter. 3.

Energy Loss in the TPC

The TPC provides PID from simultaneous measurements of the specific energy loss ($\mathrm{d}E/\mathrm{d}x$), the charge, and the momentum of the particle. The energy loss is

described by the Bethe-Bloch formula, parameterised as

$$f(\beta\gamma) = \frac{P_1}{\beta^{P_4}} \cdot \left(P_2 - \beta^{P_4} - ln\left(P_3 + \frac{1}{(\beta\gamma)^{P_5}} \right) \right) \tag{2.1}$$

by the ALEPH collaboration [8], where β is the velocity of the particle as a fraction of the speed of light c, γ is the Lorentz factor, and $P_1, P_2, ...P_5$ correspond to fit parameters based on the gas mixture. A truncated mean is taken over the maximum of 159 clusters. PID of charged hadrons occurs on a track-by-track basis up to 1-2 GeV/c. In the relativistic region, a statistical approach is used to increase the range on charged hadron PID to p_{T} of tens of GeV/c. The specific energy loss (dE/dx) for the TPC in p–Pb collisions is shown in 2.4.

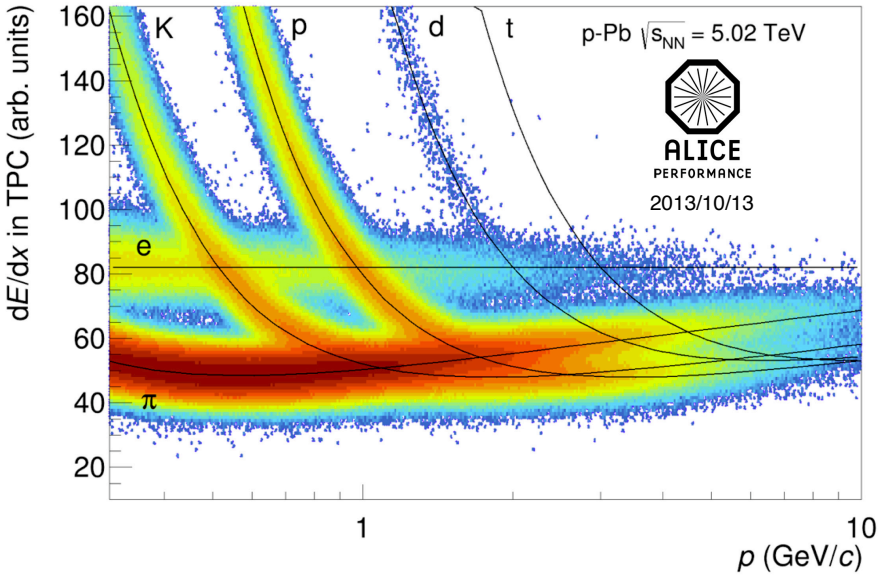

FIGURE 2.4: The plot shows the specific energy loss (dE/dx) of charged particles vs their momentum measured by the TPC in p–Pb collisions. The lines are a parameterization of the detector response based on the Bethe-Bloch formula.

Time-of-flight

Charged hadrons of intermediate momentum (up to a few GeV/c) are identified using the TOF detector. This is achieved by the combination of the measurement of the time of flight from the TOF t_{TOF}, and momentum measurements p from

the ITS and TPC detectors to calculate the mass of the particle m.

$$m = \frac{p}{\beta\gamma} = p\sqrt{\frac{ct_{TOF}^2}{L} - 1} \tag{2.2}$$

L is the track length. All other symbols retain their definitions made for Eq. 2.1. t_{TOF} is given as the difference between the time of the collision T_{coll} and the arrival time of a particle in the TOF detector T_{arr}. The T0 detector is dedicated to determining T_{coll}. However, due to the limited acceptance of the T0 detector, it is not possible to measure T_{coll} for all events. In this case, the TOF detector can provide an estimate of T_{coll} using tracks with an associate TOF signal and an χ^2-minimisation process that considers all possible mass combinations. The measured particle velocity by the TOF detector is shown in figure 2.5.

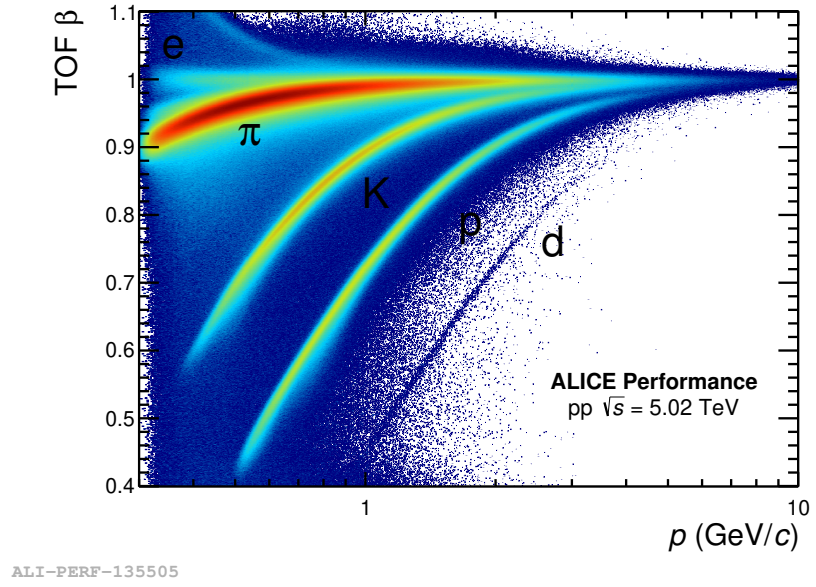

FIGURE 2.5: TOF Beta vs Momentum performance plot in pp collisions at 5.02 TeV

The ALICE detector is a powerful general purpose detector able to reconstruct and identify particle tracks even in the high multiplicity environment of heavy-ion collisions due to its wide range of sub-detectors. The ITS, TPC and TOF detectors are located the central barrel and provide the necessary tracking and PID to measure charmed baryons like the Λ_c^+. In the next section, the procedure to extract the Λ_c^+ baryon cross section will be explained.

References

[1] G. Aad et al. "Observation of a new particle in the search for the Standard Model Higgs boson with the ATLAS detector at the LHC". In: *Physics Letters B* 716.1 (2012), pp. 1 –29. ISSN: 0370-2693. DOI: https://doi.org/10.1016/j.physletb.2012.08.020. URL: http://www.sciencedirect.com/science/article/pii/S037026931200857X.

[2] S. Chatrchyan et al. "Observation of a new boson at a mass of 125 GeV with the CMS experiment at the LHC". In: *Physics Letters B* 716.1 (2012), pp. 30 –61. ISSN: 0370-2693. DOI: https://doi.org/10.1016/j.physletb.2012.08.021. URL: http://www.sciencedirect.com/science/article/pii/S0370269312008581.

[3] R. Bruce et al. "Reaching record-low Îš* at the CERN Large Hadron Collider using a novel scheme of collimator settings and optics". In: *Nuclear Instruments and Methods in Physics Research Section A: Accelerators, Spectrometers, Detectors and Associated Equipment* 848 (Dec. 2016). DOI: 10.1016/j.nima.2016.12.039.

[4] K. Aamodt et al. "The ALICE experiment at the CERN LHC". In: *JINST* 3 (2008), S08002. DOI: 10.1088/1748-0221/3/08/S08002.

[5] Arturo Tauro. "ALICE Schematics". General Photo. 2017. URL: https://cds.cern.ch/record/2263642.

[6] Guy von Dardel et al. "L3 Technical Proposal". In: (May 1983).

[7] E Bruna et al. "Vertex reconstruction for proton-proton collisions in ALICE". In: (2009). URL: https://cds.cern.ch/record/1225497.

[8] Walter Blum, Luigi Rolandi, and Werner Riegler. *Particle detection with drift chambers*. Particle Acceleration and Detection. 2008. ISBN: 978-3-540-76683-4, 978-3-540-76684-1. DOI: 10.1007/978-3-540-76684-1.

Chapter 3

Data Analysis: $\mathbf{\Lambda_c^+ \to pK^-\pi^+}$ in pp collisions at $\sqrt{s}$= 5.02 TeV

3.1 Declaration

This work was written up as an Analysis Note and peer reviewed internally by the ALICE collaboration. The subsequent paper containing this analysis is presented in Chapter 5. This work that I coauthored details the analysis of the $\Lambda_c^+ \to pK^-\pi^+$ and $\Lambda_c^+ \to pK_S^0$ decay channels in pp collisions at $\sqrt{s} = 5.02$ TeV using data taken during LHC Run 2. My specific contribution to this work was the analysis of the $\Lambda_c^+ \to pK^-\pi^+$ decay channel in pp collisions at $\sqrt{s} = 5.02$ TeV using data taken during LHC Run 2. The excerpt shown only includes details of the analysis in the $\Lambda_c^+ \to pK^-\pi^+$ decay channel and was written primarily by myself in collaboration with J. Norman.

Permission to include this excerpt from the Analysis Note with identification reference ALICE-ANA-844 entitled "Measurement of prompt Λ_c^+ production via hadronic decay channels, in pp collisions at $\sqrt{s} = 5.02$ TeV (Run 2 data)" was given by all the data-analysers who co-authored this document, as well as by the ALICE Collaboration Physics Coordinator and the co-chairs of the ALICE Collaboration Editorial Board. Their consent declaration can be found in Appendix A.

3.2 Introduction

The inclusive open heavy-flavour hadronic cross section can be calculated under the factorisation theorem as a convolution of the (perturbative) partonic cross section, the parton distribution function describing the probability distribution of parton fractional momentum within the proton, and the fragmentation function, describing the probability of a heavy quark fragmenting into a given hadron. While the partonic cross section can be calculated within perturbative QCD, the fragmentation function and parton distribution are non-perturbative and rely on experimental input. The measurement of the relative production of charmed hadrons in proton-proton collisions is a sensitive to fragmentation parameters determined from e^+e^- collisions, and can give insight into hadronisation mechanisms. The charmed baryon-to-meson ratio (e.g. Λ_c^+/D^0) is a particularly sensitive probe of how baryons and mesons hadronise. A measurement in pp collisions at $\sqrt{s} = 5.02$ TeV also provides a reference for a measurement in Pb-Pb collisions, where baryon production is expected to be further enhanced if coalescence plays a role in hadronisation [1, 2, 3].

The measurement of the production cross sections of D mesons (and the relative production of different D meson species) in pp collisions [4] are described well by perturbative-QCD-based calculations (e.g. FONLL [5, 6], GMVFNS [7, 8]) which take fragmentation parameters from e^+e^- collision data. D meson production measured in minimum bias p-Pb collisions [9] shows minimal modification with respect to the binary-scaled pp expectation, indicating minimal cold-nuclear-matter effects in minimum bias p-Pb collisions. However, the Λ_c^+ production cross section measured by ALICE [10] is higher than all expectations. In particular, the baryon-to-meson ratio (Λ_c^+/D^0) in pp collisions was measured in $1 < p_T < 8$ GeV/c at mid-rapidity to be 4-5 times higher than previous measurements in different collision systems (e^+e^-, e^-p), at different centre-of-mass collision energies and in different kinematic regimes. Theoretical predictions from PYTHIA [11, 12], DIPSY [13, 14] and HERWIG [15] all underestimate the Λ_c^+/D^0 ratio, while PYTHIA with enhanced colour reconnection, which is a phenomenological model which allows additional colour reconnections between initially uncorrelated scattered partons, brings the prediction closer to data. This model also gives a reducing trend with p_T.

During Run 2 of the LHC, ALICE has collected around 1 billion minimum-bias pp collisions at $\sqrt{s} = 5.02$ TeV - 2.5 times that collected in Run 1 at $\sqrt{s} =$

7 TeV. This new dataset will extend the kinematic range of the measurement and will allow for the uncertainties on the Λ_c^+/D^0 measurement to be significantly reduced. It will also provide a reference for the Pb–Pb measurement expected to be made with the Pb–Pb data taken at the end of 2018. This note presents the measurement of the Λ_c^+ in pp collisions at $\sqrt{s} = 5.02$ TeV collisions.

3.3 $\Lambda_c^+ \to pK^-\pi^+$ analysis

The following sections outline the measurement of the Λ_c^+ baryon in pp collisions via the decay channel $\Lambda_c^+ \to pK^-\pi^+$. The event and track selection is described in Section 3.4. The PID and topological selection strategy is described in Section 3.5. The signal extraction is described in Section 3.6. The efficiency and acceptance corrections are described in Section 3.7. The systematic uncertainty sources and the methods used to estimate them are described in Section 3.8.

The Λ_c^+ is the lightest charmed baryon with a rest mass of 2286.46 ± 0.14 MeV/c^2. The golden channel of its measurement is the the decay $\Lambda_c \to pK\pi$ with a BR of 6.28 $\pm$0.23%, which includes 4 decays that are indistinguishable in this measurement. This includes three resonant decays and one non-resonant decay. These are shown in Table 3.1.

Λ_c^+ decay mode	branching ratio (Γ_i/Γ_{total})	Γ_i/Γ_1	q(MeV/c)
$pK^-\pi^+$	$(6.28 \pm 0.32)\%$	1	823
$p\bar{K}^*(892)^0$	$(1.96 \pm 0.27)\%$	0.31 ± 0.05	685
$\Delta(1232)^{++}K^-$	$(1.08 \pm 0.25)\%$	0.17 ± 0.04	710
$\Lambda(1520)\pi^+$	$(2.2 \pm 0.5)\%$	0.35 ± 0.08	628
$pK^-\pi^+$ nonresonant	$(3.5 \pm 0.4)\%$	0.55 ± 0.06	823

TABLE 3.1: Λ_c^+ decay channels considered in this analysis. Values taken from [16]

Λ_c^+ decay mode	branching ratio (Γ_i/Γ_{total})	q(MeV/c)
$\bar{K}^*(892)^0 \to K^-\pi^+$	(66.6)%	289
$\Delta(1232)^{++} \to p\pi^-$	(100)%	229
$\Lambda(1520) \to pK^-$	$(22.5 \pm 0.5)\%$	243

TABLE 3.2: Λ_c^+ resonant decay channels and branching ratios, in the case where the Λ_c^+ ends up in the pKπ final state. Values taken from [16]

The signal extraction strategy is based on particle identification of single tracks, an invariant mass analysis of resonant states created in the decay of Λ_c^+ and an invariant mass analysis of the Λ_c^+ itself from decay candidates. Having the three candidates of Λ_c^+ daughters (a proton, kaon and pion) the invariant mass can be calculated as follows:

$$M^2_{\Lambda_c^+} = (E_p + E_K + E_\pi)^2 - (|\vec{P}_p + \vec{P}_K + \vec{P}_\pi|)^2, \tag{3.1}$$

where

- E_p,E_K, and E_π are the energy of protons, kaons and pions, respectively.
- $\vec{P}_p$, $\vec{P}_K$ and $\vec{P}_\pi$ are the momentum vectors of protons, kaons and pions, respectively.

The invariant mass of the candidates has a peak in the Λ_c^+ invariant mass region. However, events containing Λ_c^+ are relatively few compared to light flavour physics. As a consequence, the combination of random particles generates significant background. The measurement requires a good study of its decay topology and particle identification. An analysis based on standard 'rectangular' topological selection will be shown.

The identification of the Λ_c^+ is only possible for Λ_c^+ at moderate to high momenta ($\Lambda_c^+ p_{\rm T} > 1$ GeV/c), due to its decay topology with the secondary vertex typically less than 100 μm from the primary (collision vertex) and the current pointing resolution of the ALICE ITS (Inner tracking System) for single tracks. In this note, the analysis of Λ_c^+ in pp collisions with the ALICE experiment will be shown in the $p_{\rm T}$ bins 1-2, 2-3, 3-4, 4-5, 5-6, 6-8, 8-12, 12-16, 16-24 GeV/c.

3.4 Data samples, Event and Track selection

3.4.1 Data samples

The presented Λ_c^+ analyis is performed using pp collisions at $\sqrt{s_{\rm NN}} = 5.02$ TeV data, recorded in 2017 composed of minimum bias events. Where the main trigger detectors are the SPD and V0 scintillator arrays. The minimum bias trigger selects all events with at least one hit in the SPD or in one of the two V0 counters, in coincidence with the signals from the beam pickup detectors.

Two Monte Carlo productions were used to compute the efficiencies and acceptance corrections. They were made with PYTHIA for events enriched by charm or beauty pairs forced to decay into either $\Lambda_c^+ \to pK^-\pi^+$ or $\Lambda_c^+ \to \mathrm{pK}_S^0$.

3.4.2 Event selection

For the event selection, any event passing the minimum bias trigger and physics selection were included. The primary vertex was required to be reconstructed with only tracks within 10 cm in the z direction from the interaction point. The reconstructed ITS and ITS+TPC vertices are required to be closer than 5 mm. Events with more than one interaction (pile-up) were removed.

3.4.3 Track selection

For a track to be included in the reconstruction of the secondary vertices of Λ_c^+ they were selected by requiring the conditions stated in Table 3.3:

Parameter	choice
n. of TPC clusters	≥ 70
TPCrefit	true
n. of ITS clusters	≥ 2
ITSrefit	true
$\lvert\eta\rvert$	< 0.8
p_T	> 0.4 GeV/c

TABLE 3.3: The track selection applied in this analysis.

3.4.4 Lego train Information and AliRoot Code Used

After event selection, the data sample is composed of 980 million minimum bias events. The MC simulations used for the efficiency corrections and tuning cut parameters is composed of 600 thousand minimum bias events. The code used to obtain the results in this analysis is available publicly at [17].

3.5 Particle identification and topological selection

3.5.1 Topological selection

For each reconstructed candidate, several cut variables are calculated based on primary and secondary vertex positions as well as the kinematics of the decay product tracks.

For the stage where pairs of opposite charge are constructed from the tracks that met the single track selection, a secondary vertex is calculated, and cuts are applied to:

- The distance of closest approach between the two tracks (DCA)
- The distance between the primary and secondary vertex reconstructed from the pair of tracks ($dist_{12}$)

A third track is then added to the pair to form a triplet which will be a Λ_c^+ candidate. The secondary vertex for this triplet is calculated and cuts are applied to:

- the quality of the reconstructed vertex. This is computed by summing in quadrature the distance of closest approach of each track to the calculated secondary vertex (σ_{vertex})
- The distance between the primary and secondary vertex (decay length)
- The cosine of the pointing angle. The pointing angle is the angle between the Λ_c^+ flight line, determined by the primary and secondary vertex, to the reconstructed Λ_c^+ momentum vector ($\mathrm{Cos}\theta_p$)
- The transverse momentum of the decay products $p_\mathrm{T}(p)$, $p_\mathrm{T}(K)$ and $p_\mathrm{T}(\pi)$.

The difference in the signal and background distributions for these cut parameters can be studied with the aforementioned Monte Carlo simulation. It was decided that imposing tighter topological selections did not improve the predicted significance. For this reason, 'loose' cuts (shown in Table 3.4 and) defined at the creation of the analysis dataset, referred to as 'production cuts', were chosen as the cuts for this analysis as they performed comparatively well in all p_T bins and the cuts were by definition constant with p_T.

p_T, Λ_c^+	p_T, p	p_T,K	p_T,π	DCA	dist12	σv	d^{length}	Cosθ_p
$2 < p_T < 3$	>0.5	>0.4	>0.4	<0.05	>0.01	<0.06	>0.005	>0
$3 < p_T < 4$	>0.5	>0.4	>0.4	<0.05	>0.01	<0.06	>0.005	>0
$4 < p_T < 6$	>0.5	>0.4	>0.4	<0.05	>0.01	<0.06	>0.005	>0
$6 < p_T < 8$	>0.5	>0.4	>0.4	<0.05	>0.01	<0.06	>0.005	>0
$8 < p_T < 12$	>0.5	>0.4	>0.4	<0.05	>0.01	<0.06	>0.005	>0
$12 < p_T < 24$	>0.5	>0.4	>0.4	<0.05	>0.01	<0.06	>0.005	>0
(GeV/c)	(GeV/c)	(GeV/c)	(GeV/c)	(cm)	(cm)	(cm)	(cm)	

TABLE 3.4: Corresponding cut parameter values for production cuts.

3.5.2 Particle identification

Particle identification of protons, pions and kaons, from which the Λ_c^+ candidates are reconstructed, is based on information on the specific ionisation, dE/dx in the TPC gas as well as the time-of-flight measurement from the TOF detector. TOF measurements help to identify particles where the TPC is no longer able to, such as at 0.6 GeV/c and 1.2 GeV/c where the kaon band merges with the pion and proton bands, respectively for TPC PID. However TOF measurements are not always available because tracks present in the TPC may not reach the TOF. A Bayesian approach of particle identification has been developed by ALICE [18] and is used in this analysis. In this analysis tracks are assigned the identity of the particle species with the highest posteriori probability (conditional probability given the PID measurement and prior knowledge of the expected particle abundances), the so-called 'maximum probability criterion'. The Bayesian approach was chosen over the nσ approach, since although it can result in a smaller efficiency, this approach gives a higher chance of correctly identifying a track, thus allowing for a higher purity in the sample of tracks passing the PID selection. This was previously shown to be the optimal approach for the $\Lambda_c^+ \rightarrow pK^-\pi^+$ analysis [18].

3.6 Signal extraction

In this section, the signal extraction results for the $\Lambda_c^+ \rightarrow pK^-\pi^+$ in pp data will be shown for the nine momentum bins: 1-2, 2-3, 3-4, 4-5, 5-6, 6-8, 8-12, 12-16, 16-24 GeV/c. The value for the signal (raw yield) are taken from the invariant mass plots of candidates containing p,K and π tracks, as described in equation 3.1.

The fit function to reproduce these distributions is the combination of a Gaussian for the Λ_c^+ peak and a second-order polynomial for the background. The fit is performed in two steps: The first estimates the background function parameters using the side bands; the second repeats this including the signal range, fitting the signal, leading to a final estimation of all fit parameters. The number of signal events are extracted by subtracting the background function from the total fit in the signal range within 3 standard deviations.

Figure 3.1 shows the peak mean and width values for data and Monte Carlo. Good agreement is observed between peak means of the invariant mass in data and Monte Carlo with the exception of the last p_T bin as shown in Figure 3.1 (top). A similar trend is also seen for the peak widths of the invariant fits of the combined dataset when compared to Monte Carlo in Figure 3.1 (bottom). It can also be seen that for 'Sample 1' and 'Sample 2' datasets (independent subdivisions of the total dataset based on their reconstruction strategy) there are several p_T bins where the widths are comparatively small, potentially caused by fitting to fluctuations in the mass spectra. Figure 3.2 shows invariant mass plots in each p_T bin for productions cuts with sigma values fixed to MC values. In Figure 3.2, it can be seen that we get good signal extraction in the p_T range 2-12 GeV/c. We also see hints of signal in the 1-2 and 12-24 GeV/c bins.

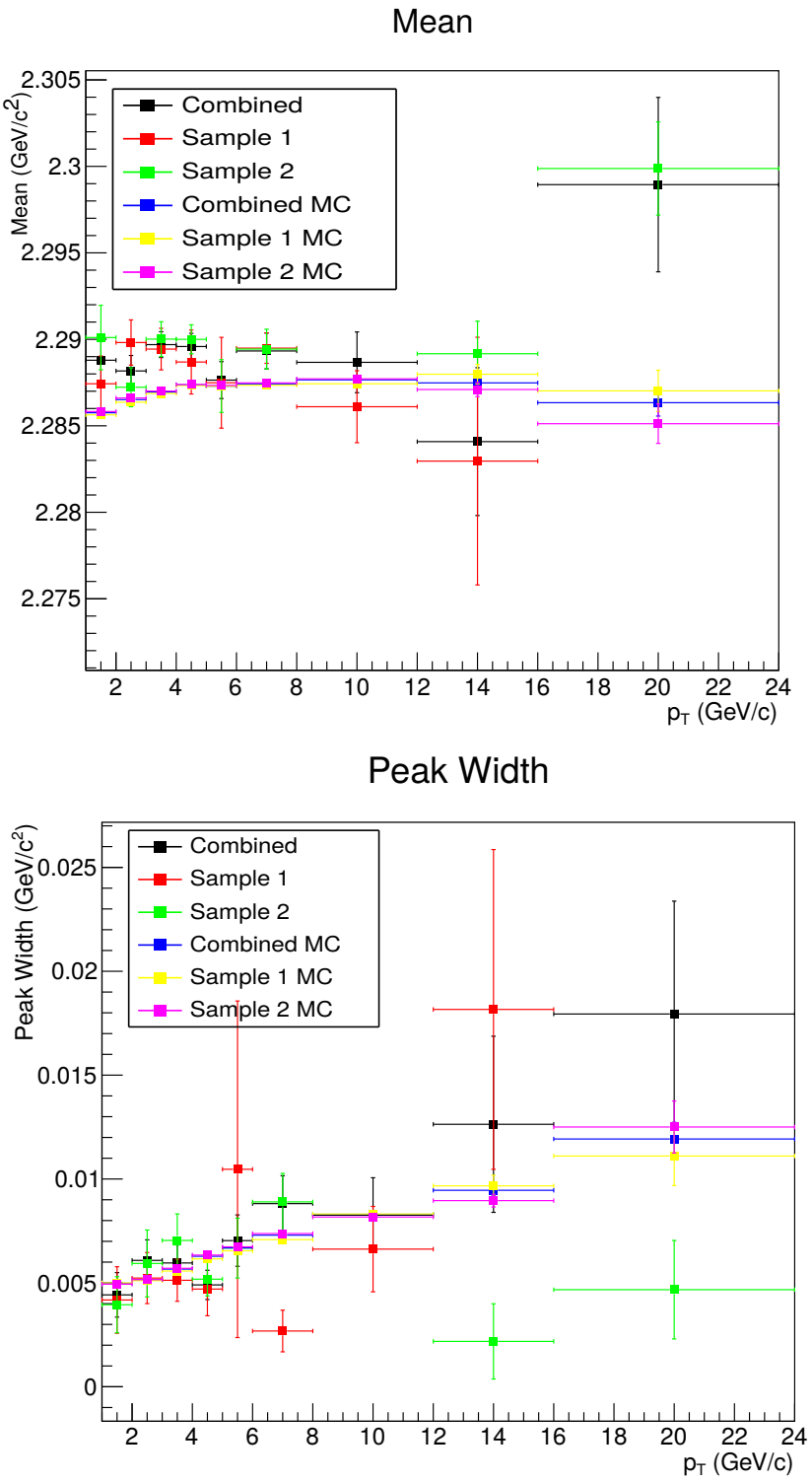

FIGURE 3.1: Top: Comparison of peak mean for data and MC, Bottom: Comparison of peak width for data and MC. Both the data and Monte Carlo have been split into two independent samples based on their reconstruction strategy.

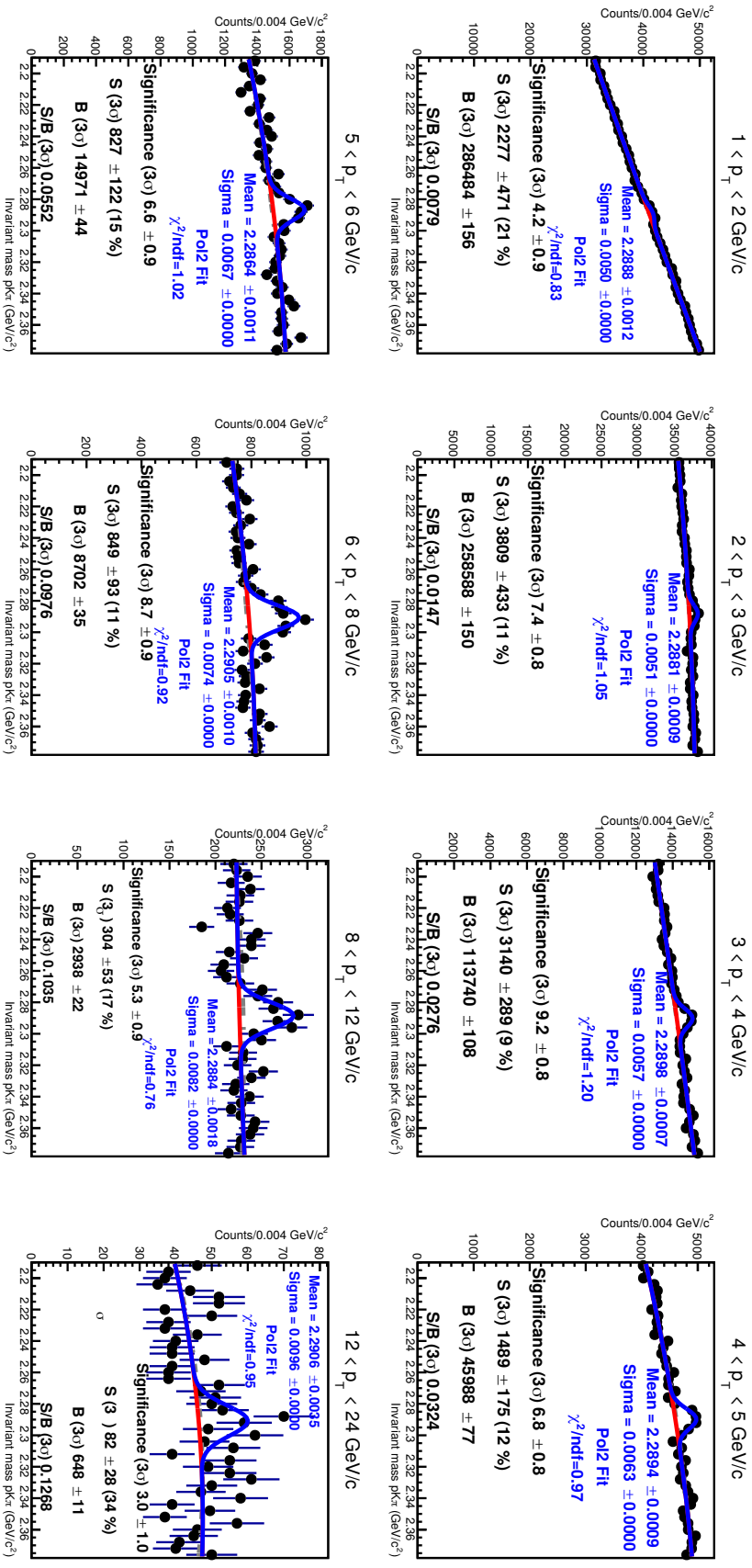

FIGURE 3.2: Invariant mass plots in each p_{T} bin for productions cuts with sigma values fixed to MC values.

3.7 Corrections to the raw yield

3.7.1 Efficiency and Acceptance correction

In order to obtain true productions yields of Λ_c^+, corrections are made to the raw yields extracted from the invariant mass spectra. The product of acceptance and efficiency corrections $Acc \times \epsilon$ is determined in each p_T bin using Monte Carlo simulated pp events. The efficiency of each intermediate $\Lambda_c^+ \rightarrow pK^-\pi^+$ resonant decay is different due the different kinematic properties, requiring the efficiency and acceptance to be determined individually for each decay. Both Pythia 6 and Pythia 8 are used to simulate the pp events, and Geant3 is used to simulate the detector response.

The Λ_c^+ Efficiency is calculated in 8 stages:

- MC particles in acceptance
- Vertex (event selection)
- Refit (number of hits in ITS and TPC detectors)
- Reconstructed candidates
- Reconstructed candidates in acceptance
- Passing minimum no. of ITS clusters
- Topological cuts
- PID

Figure 3.3 shows the prompt and non-prompt efficiencies of the Λ_c^+ which are given for the four different decay channels as well as the overall efficiency multiplied by the acceptance (shown separately in Figure 3.4). The efficiency is greater in general for non-prompt due to its displaced secondary vertex.

The acceptance factor is necessary to normalise the yield to the rapidity window, $|y| < 0.5$ where the cross-section is essentially flat. This is calculated using a toy Monte Carlo, as the acceptance is a purely geometric effect.

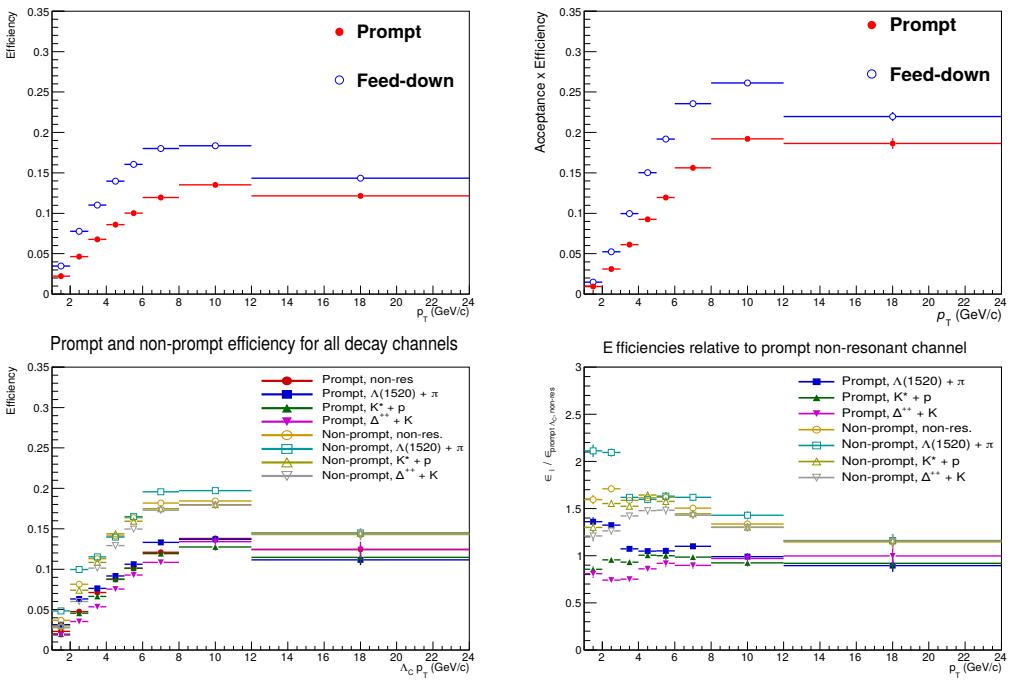

FIGURE 3.3: Top left: Prompt and non-prompt Λ_c^+ efficiencies, Top right: Acceptance x efficiency for prompt and non-prompt Λ_c^+, Bottom left: Efficiencies for each $\Lambda_c^+ \to pK^-\pi^+$ decay (prompt and non-prompt), Bottom right: Efficiencies relative to the prompt non-resonant decay.

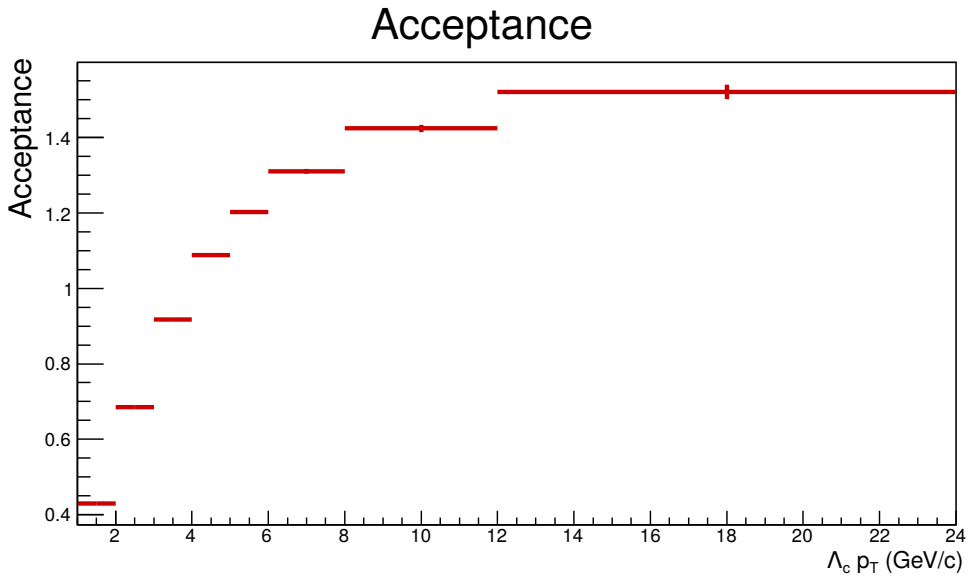

FIGURE 3.4: Acceptance factor as calculated in Toy Monte Carlo generated with Pythia.

3.7.2 Feed-down correction

To extract the raw yield $\mathrm{N}_{raw,prompt}^{\Lambda_c^+}$ corresponding to only prompt Λ_c^+, the contribution of feed-down $\mathrm{N}_{raw}^{\Lambda_b^0\to\Lambda_c^+ + \mathrm{X}}$ from $\Lambda_b^0 \to \Lambda_c^+ + \mathrm{X}$ decays is subtracted from the measured raw yield, $\mathrm{N}_{raw}^{\Lambda_c^+}$:

$$N_{raw,prompt}^{\Lambda_c^+} = N_{raw}^{\Lambda_c^+} - N_{raw}^{\Lambda_b^0\to\Lambda_c^+ + \mathrm{X}} \tag{3.2}$$

$$N_{raw,prompt}^{\Lambda_c^+} = N_{raw}^{\Lambda_c^+} \cdot (1 - \frac{N_{raw}^{\Lambda_b^0\to\Lambda_c^+ + \mathrm{X}}}{N_{raw}^{\Lambda_c^+}}) = N_{raw}^{\Lambda_c^+} \cdot f_{prompt}, \tag{3.3}$$

where f_{prompt} is the relative fraction of Λ_c^+ not from the $\Lambda_b^0 \to \Lambda_c^+ + \mathrm{X}$ decay. The method chosen to calculate the feed-down, referred to as the N_b method, uses the production cross section of Λ_b^0 calculated within FONLL multiplied by branching ratio to the decay channel $\Lambda_b^0 \to \Lambda_c^+ + \mathrm{X}$, the correction factors for the acceptance and reconstruction efficiency $\epsilon_{\Lambda_b^0\to\Lambda_c^+ + \mathrm{X}}$ of non-prompt Λ_c^+, and the integrated luminosity, $\mathcal{L}_{int}$:

$$f_{prompt} = 1 - \frac{1}{N_{raw}^{\Lambda_c^+}} \cdot \mathcal{L}_{int} \cdot BR_b \cdot \epsilon_{\Lambda_b^0\to\Lambda_c^+ + \mathrm{X}} \int_{\Delta y \Delta p_\mathrm{T}} \frac{d\sigma_{FONLL}^{\Lambda_b^0}}{dy dp_\mathrm{T}} \Delta y \Delta p_\mathrm{T} \tag{3.4}$$

The production cross section of Λ_c^+ from Λ_b^0-baryon decays, $\left(\frac{\mathrm{d}^2\sigma}{\mathrm{d}p_\mathrm{T}\mathrm{d}y}\right)_{\mathrm{feed-down}}^{\mathrm{FONLL}}$, was calculated using the b-quark p_T-differential cross section from FONLL calculations [5, 19], the fraction of beauty quarks that fragment into Λ_b^0 estimated from LHCb measurements [20], and the $\Lambda_b^0 \to \Lambda_c^+ + X$ decay kinematics modelled using PYTHIA 8 simulations [21], normalised according to the branching ratio $f(\Lambda_b^0 \to \Lambda_c^+ + \mathrm{X}) = 33\%$ [22]. This method has been updated since the previous measurement of the Λ_b^0, which used a fragmentation fraction determined from $\mathrm{e}^+\mathrm{e}^-$ collisions, and included a factor of two in the uncertainty to account for measurements of Λ_b^0 production in pp collisions. At that time, fragmentation fractions of beauty hadrons had not been measured at the LHC, but we now take advantage of the recent LHCb measurements [20, 23] to parameterise Λ_b^0 fragmentation in pp collisions.

The $\mathrm{b} \to \Lambda_b^0$ fragmentation was derived from the LHCb measurements of Λ_b^0-production fraction relative to $\overline{\mathrm{B}}^0$ and B^- mesons in pp collisions at $\sqrt{s} = 13$ TeV [20], which indicates that the fraction of b quarks hadronising into a Λ_b^0 baryon

is strongly p_T dependent in the measured range of $4 < p_T < 25$ GeV/c. The fits to the production fractions of $\overline{B}_s^0$ and Λ_b^0 hadrons normalised to the sum of B^- and $\overline{B}^0$ hadrons are presented in [20] as a function of the beauty-hadron p_T as

$$\frac{f_s}{f_u + f_d}(p_T) = A[p_1 + p_2 \times (p_T - < p_T >)] = X, \tag{3.5}$$

$$\frac{f_{\Lambda_b^0}}{f_u + f_d}(p_T) = C[q_1 + \exp(q_2 + q_3 \times p_T)] = Y, \tag{3.6}$$

where f_d, f_u, f_s and $f_{\Lambda_b^0}$ are the fractions of b quarks that hadronise into $\overline{B}^0$, B^-, $\overline{B}_s^0$ and Λ_b^0, respectively, and A, p_1, p_2, $< p_T >$, C, q_1, q_2 and q_3 are free parameters of the fits to the measured ratios. The LHCb paper defines $C = 1 \pm 0.061$, $q_1 = (7.93 \pm 1.41) \cdot 10^{-2}$, $q_2 = -1.022 \pm 0.047$ and $q_3 = -0.107 \pm 0.002$ GeV^{-1} for eq. 3.6, as well as $A = 1 \pm 0.043$, $p_1 = 0.119 \pm 0.001$, $p_2 = (-0.91 \pm 0.25) \cdot 10^{-3}$ GeV^{-1} and $< p_T >= 10.1$ GeV for eq. 3.5. Assuming $f_u = f_d$ and $f_u + f_d + f_s + f_{\Lambda_b^0} = 1$ the Λ_b^0 fragmentation fraction can then be defined as

$$f_{\Lambda_b^0}(p_T) = \frac{Y}{(X + Y + 1)}, \tag{3.7}$$

and, for completeness, the fragmentation fractions for the other species can be defined as

$$f_u(p_T) = f_d(p_T) = \frac{1}{2(X + Y + 1)}, \tag{3.8}$$

$$f_s(p_T) = \frac{X}{(X + Y + 1)}, \tag{3.9}$$

The parameterisation for $f_{\Lambda_b^0}$ is used to define the Λ_b^0 fragmentation, for $p_T >$ 5 GeV/c. For $p_T < 5$ GeV/c it was assumed that $f_{\Lambda_b^0} = 0.2$, since measurements of the ratio $\Lambda_b^0/\overline{B}^0$ in pp collisions at $\sqrt{s} = 7$ TeV and 8 TeV [23] are flat as a function of p_T in this interval within the experimental uncertainties.

The uncertainties for $f_{\Lambda_b^0}$ are defined by varying the free parameters independently within their uncertainties. Figure 3.5 (left) shows the fragmentation ratios with the fits and variations of the fits, where each free parameter is varied independently. Figure 3.5 (right) shows the $f_{\Lambda_b^0}$ fraction with the same variations.

Figure 3.6 (left) shows the measurements at different centre-of-mass energies as measured by LHCb. Figure 3.6 (right) shows the ratio of the different energies. An additional flat 20% uncertainty associated with the possible $\sqrt{s}$-dependence

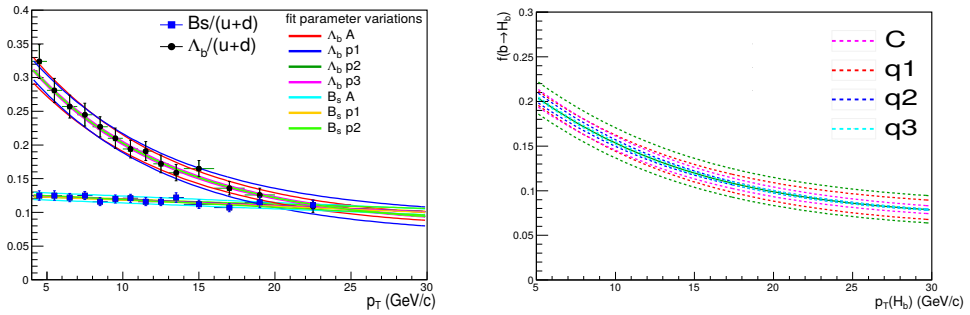

FIGURE 3.5: Left: The measured beauty fragmentation ratios by LHCb with the fit to the data, along with the variations of the free parameters of the fits. Right: The parameterisation of the fragmentation fraction $f_{\Lambda_b^0}$ and the variations from independent variations of the free parameters.

of the beauty baryon-to-meson ratios was added to the upper uncertainty of the Λ_b^0 fragmentation fraction, chosen conservatively to account for the additional possible $\sqrt{s}$-dependence between the ratios at 5 TeV and 7 TeV. It was assumed that there is no rapidity dependence of $f_{\Lambda_b^0}$ since the LHCb measurements of beauty-production ratios are flat as a function of rapidity in $2 < y < 5$ within the experimental uncertainties [23, 20].

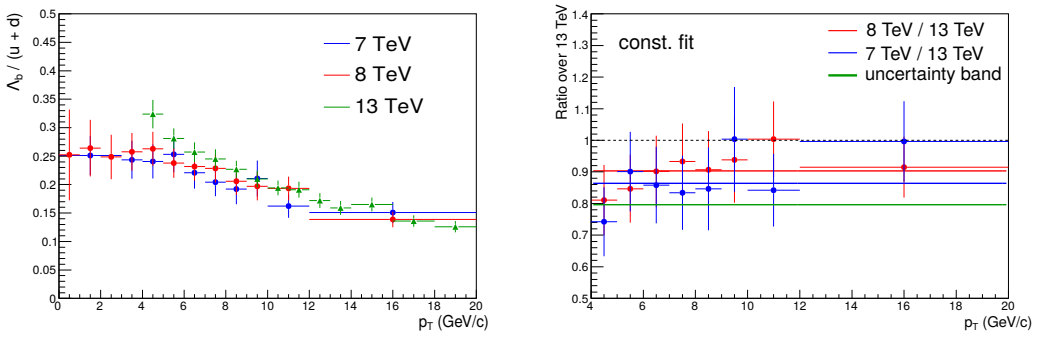

FIGURE 3.6: Left: Measurements of the Λ_b^0 / B production ratios at different energies by LHCb. Right: Ratios of the ratios.

Figure 3.7 shows the p_T-dependent fragmentation fractions that are used in this analysis. For $p_T = 5$ GeV/c, $f_{\Lambda_b^0}$ is around 0.2, and it decreases to a value of around 0.09 for $p_T > 20$ GeV/c. For $p_T(\Lambda_b^0) < 5$ GeV/c, the lower uncertainty bound of $f_{\Lambda_b^0}$ was taken to be equal to the lower bound of the fit at $p_T(\Lambda_b^0) = 5$ GeV/c, independent of p_T, while the upper uncertainty bound was taken to be equal to the p_T-dependent upper bound of the fit.

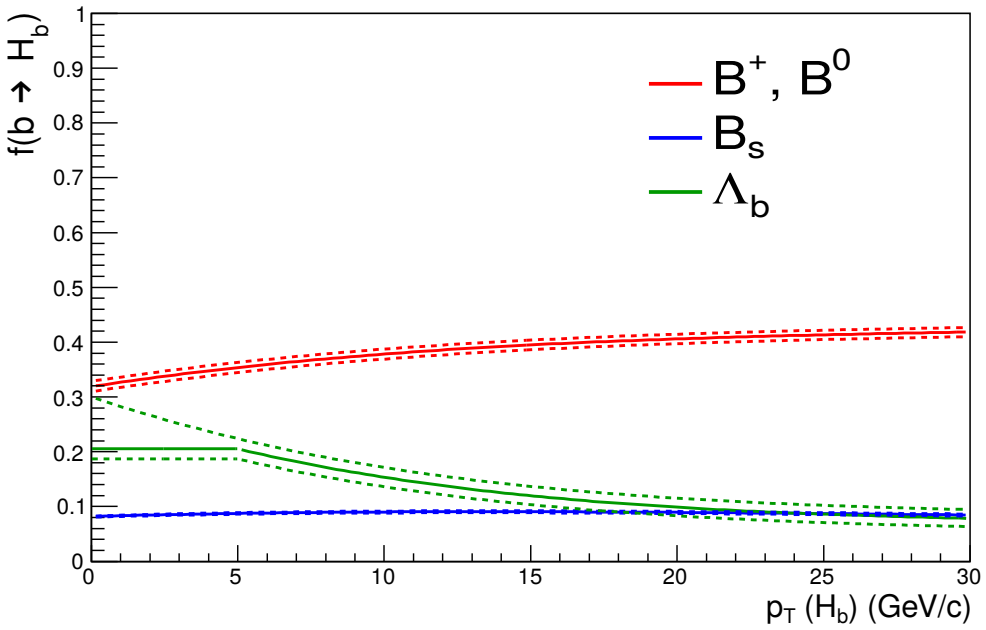

FIGURE 3.7: Parameterisation of the fragmentation fraction of beauty quarks into Λ_b^0 used in the feed-down estimation in this analysis.

Figure 3.8 shows the $\Lambda_b^0 \to \Lambda_c^+ + X$ cross section used in this analysis, taking the FONLL b cross section, the fragmentation parameterisation as described in the text, and the $\Lambda_b^0 \to \Lambda_c^+ + X$ decay kinematics from PYTHIA. The uncertainty components are also shown. It can be seen that the dominant uncertainty is that from the FONLL calculation.

Figure 3.9 shows the value of f_{prompt} for the $\Lambda_c^+ \to pK^-\pi^+$ analysis. The green box shows the f_{prompt} used in this analysis. It is also compared to the value used with the old feed-down method (without the factor of two as described above). Due to the increase in the fragmentation fraction at low p_T, the updated value of f_{prompt} is lower than the old value.

Figure 3.10 shows the new prompt fraction values after updating the branching fractions of beauty hadron to charmed hadron decays to those reported in the PDG 2020 [16]. The prompt fraction shown in this Figure is the one used in the publication.

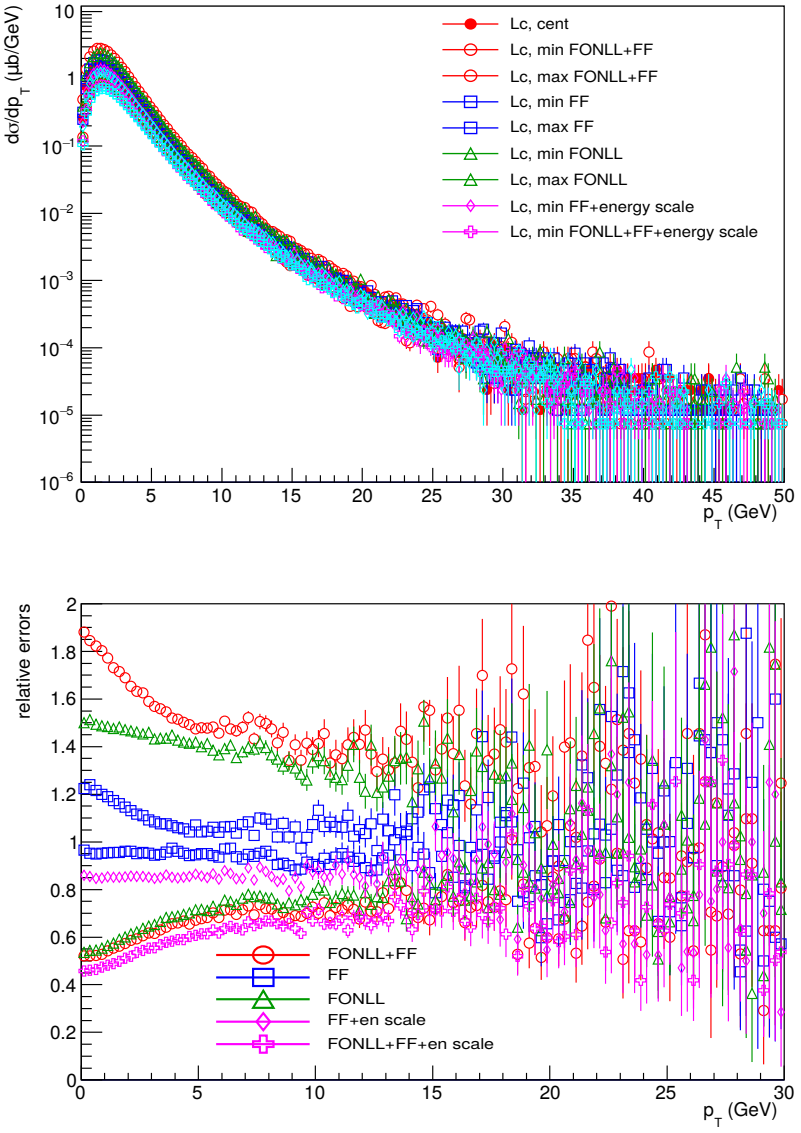

FIGURE 3.8: Top: The p_{T}-differential cross section of Λ_c^+ from Λ_b^0 decays, taking the FONLL b cross section, the fragmentation parameterisation as described in the text, and the $\Lambda_b^0 \to \Lambda_c^+ + \mathrm{X}$ decay kinematics from PYTHIA. Bottom: The uncertainty from each component of the cross section calculation.

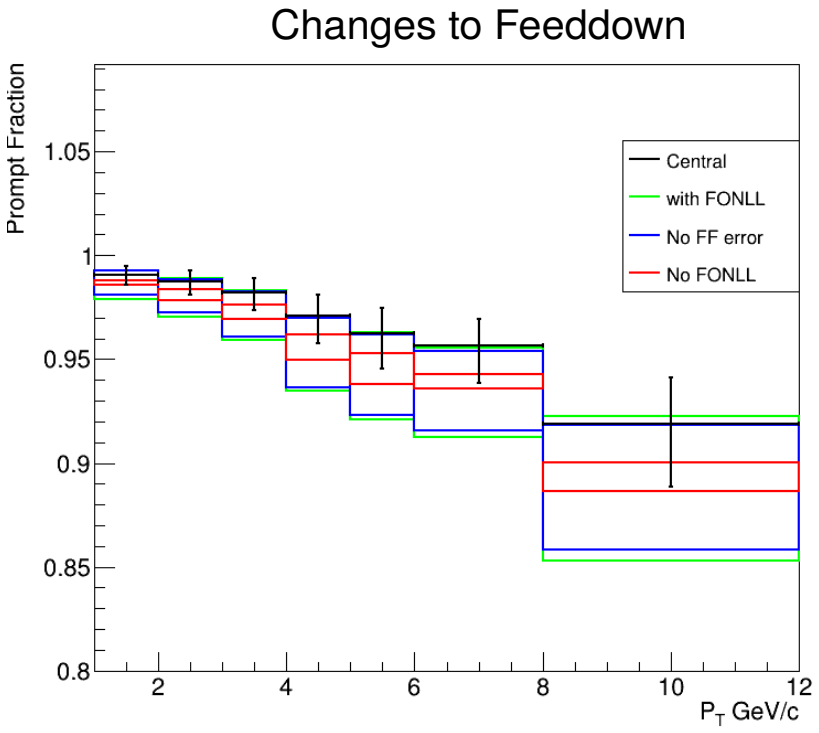

FIGURE 3.9: Relative fraction of Λ_c^+ estimated to be present in the the raw yield using N_b method. The 'Central' points are the values calculated using the Run 1 method, the boxes show the uncertainties of the new method including or not including the uncertainties from FONLL and the fragmentation fraction.

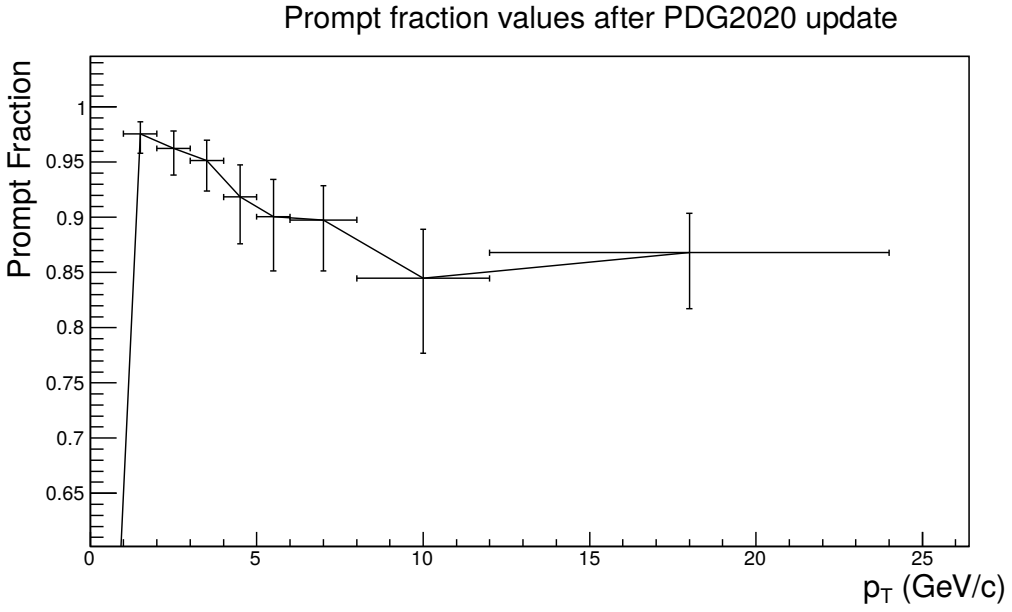

FIGURE 3.10: f_{prompt} for the $\Lambda_c^+ \to pK^-\pi^+$ analysis after an update with respect to the values in PDG 2020 [16].

3.8 Systematic uncertainties

This section summarizes the steps taken into account to determine the systematic errors present in the analysis.

3.8.1 Signal extraction

The systematic uncertainty on the extraction of the raw yield can be estimated by varying the various fitting and histogram parameters from the default used in the central cross section calculation. This is done in a loop, and the following fit and histogram parameters are changed from the default (defined in **bold** below):

- The function used to fit background. Four functions were used an exponential, linear, **2nd order polynomial** and a 3rd order polynomial.
- The mass window. Five upper limits were chosen (2.40, 2.39, **2.38**, 2.37 and 2.36 GeV/c) and five lower limits were chosen(2.17, 2.18, **2.19**, 2.20, 2.21 GeV/c).
- Three rebin steps: 2, **4** and 6 GeV/c.
- Four combinations of either free or fixed Sigma and free or fixed Mean. The default was fixed sigma and free mean. Where the values are fixed to values in the Monte Carlo.

The results of the fit variation systematic studies can be seen in figures 3.11 to 3.18, where shown is (from top left clockwise) the peak width of the fit as a function of the trial number, the raw yield as a function of the trial number, the χ^2/NDF as a function of the trial number, and the distribution of the raw yield. The red line indicates the raw yield of the 'central' cross section.

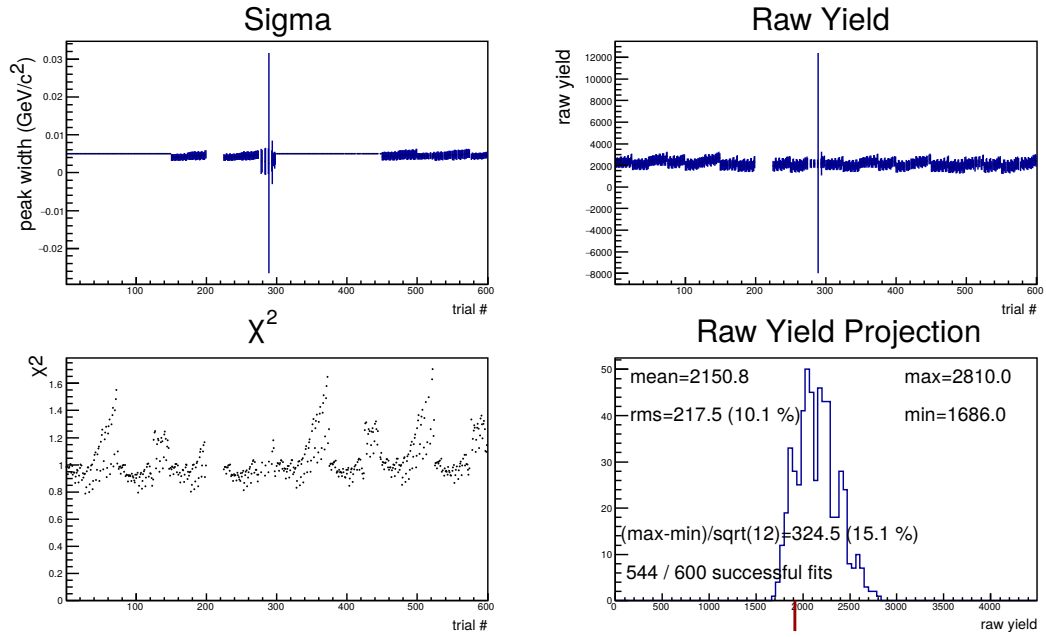

FIGURE 3.11: Multi-trial variation for 1< p_T <2 GeV/c. From top left clockwise: the peak width of the fit as a function of the trial number, the raw yield as a function of the trial number, the χ^2/NDF as a function of the trial number, and the distribution of the raw yield. The red line indicates the raw yield of the 'central' cross section.

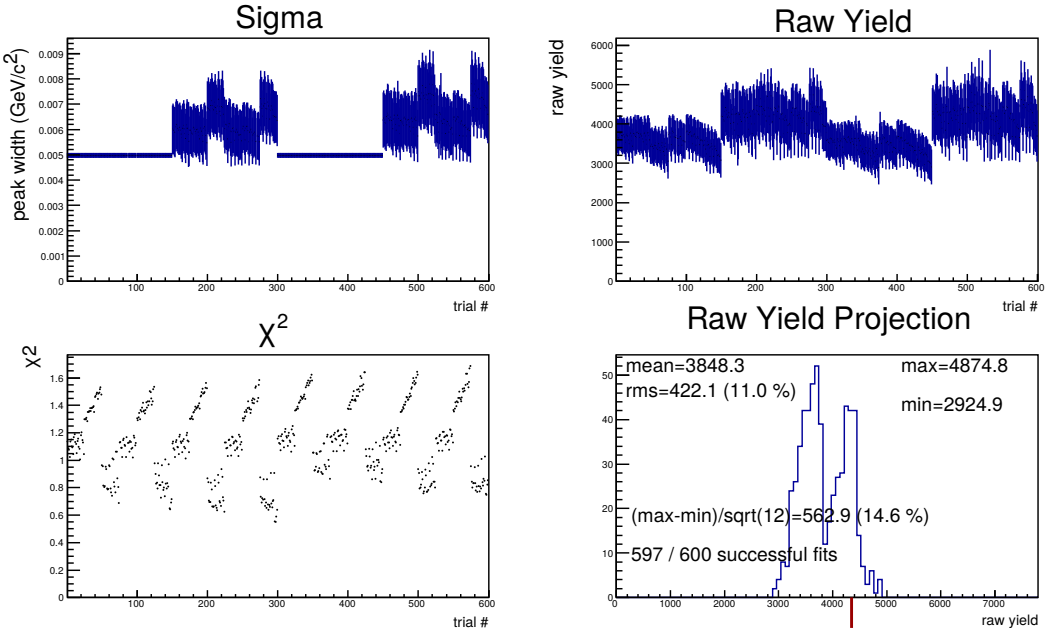

FIGURE 3.12: Multi-trial variation for 2< p_T <3 GeV/c. From top left clockwise: the peak width of the fit as a function of the trial number, the raw yield as a function of the trial number, the χ^2/NDF as a function of the trial number, and the distribution of the raw yield. The red line indicates the raw yield of the 'central' cross section.

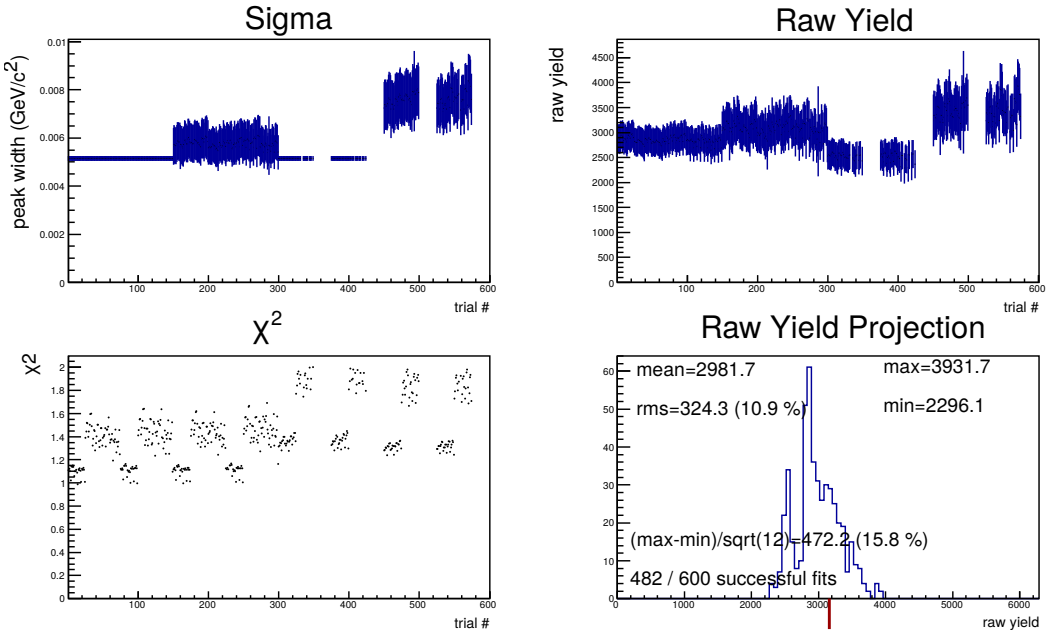

FIGURE 3.13: Multi-trial variation for 3< p_T <4 GeV/c. From top left clockwise: the peak width of the fit as a function of the trial number, the raw yield as a function of the trial number, the χ^2/NDF as a function of the trial number, and the distribution of the raw yield. The red line indicates the raw yield of the 'central' cross section.

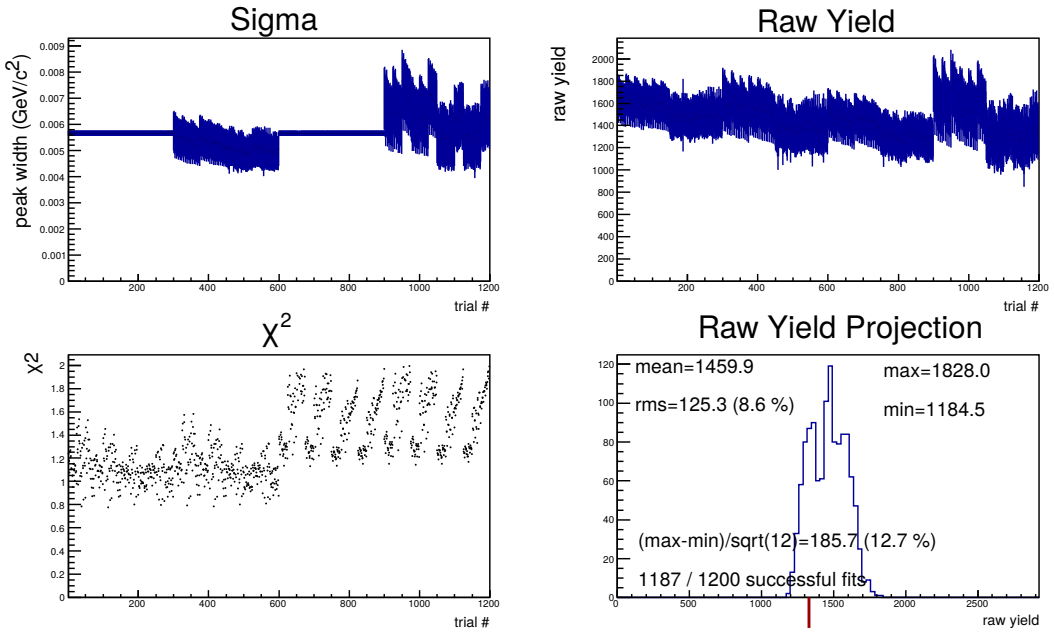

FIGURE 3.14: Multi-trial variation for 4< p_T <5 GeV/c. From top left clockwise: the peak width of the fit as a function of the trial number, the raw yield as a function of the trial number, the χ^2/NDF as a function of the trial number, and the distribution of the raw yield. The red line indicates the raw yield of the 'central' cross section.

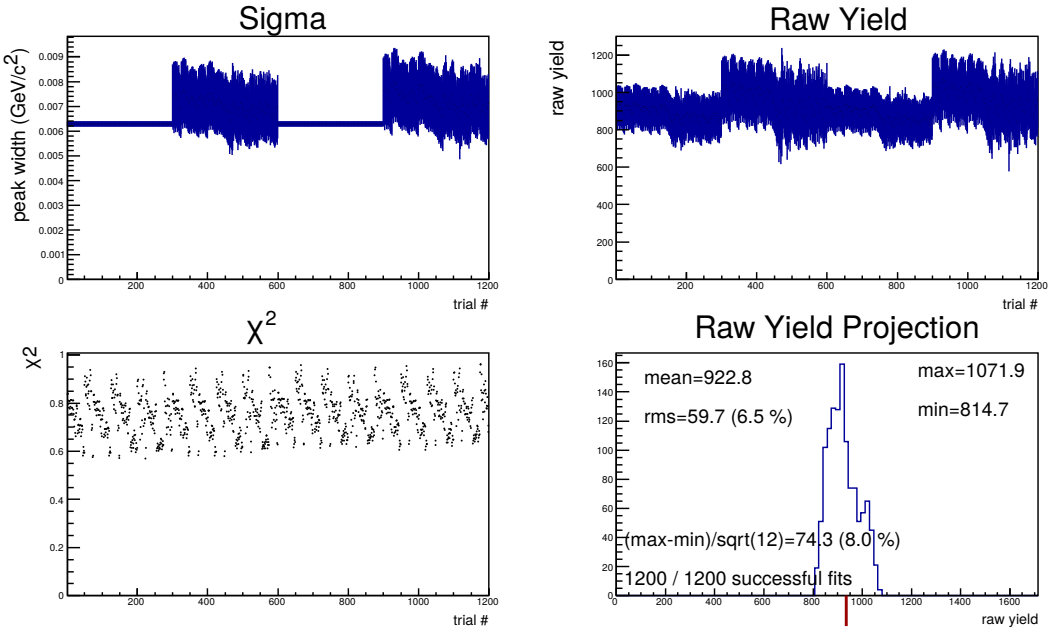

FIGURE 3.15: Multi-trial variation for 5< p_T <6 GeV/c. From top left clockwise: the peak width of the fit as a function of the trial number, the raw yield as a function of the trial number, the χ^2/NDF as a function of the trial number, and the distribution of the raw yield. The red line indicates the raw yield of the 'central' cross section.

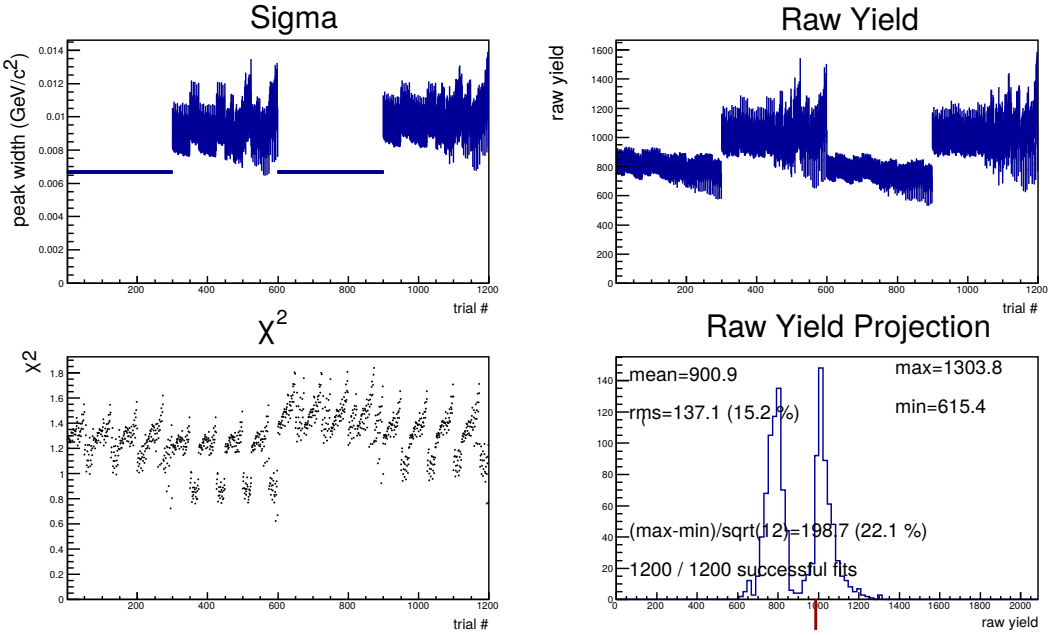

FIGURE 3.16: Multi-trial variation for 6< p_T <8 GeV/c. From top left clockwise: the peak width of the fit as a function of the trial number, the raw yield as a function of the trial number, the χ^2/NDF as a function of the trial number, and the distribution of the raw yield. The red line indicates the raw yield of the 'central' cross section.

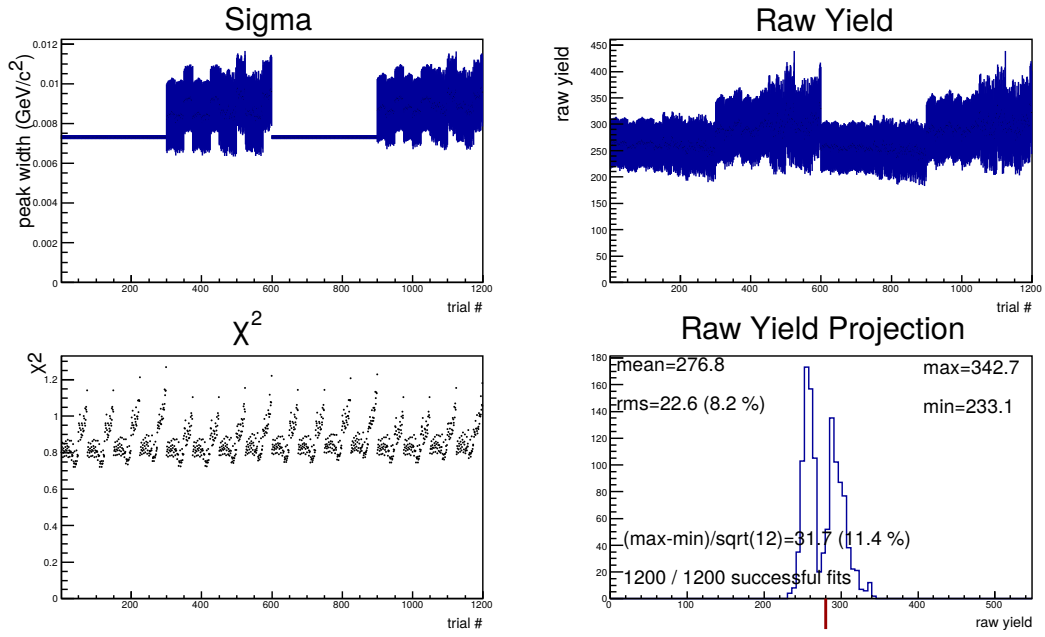

FIGURE 3.17: Multi-trial variation for 8< p_{T} <12 GeV/c. From top left clockwise: the peak width of the fit as a function of the trial number, the raw yield as a function of the trial number, the χ^2/NDF as a function of the trial number, and the distribution of the raw yield. The red line indicates the raw yield of the 'central' cross section.

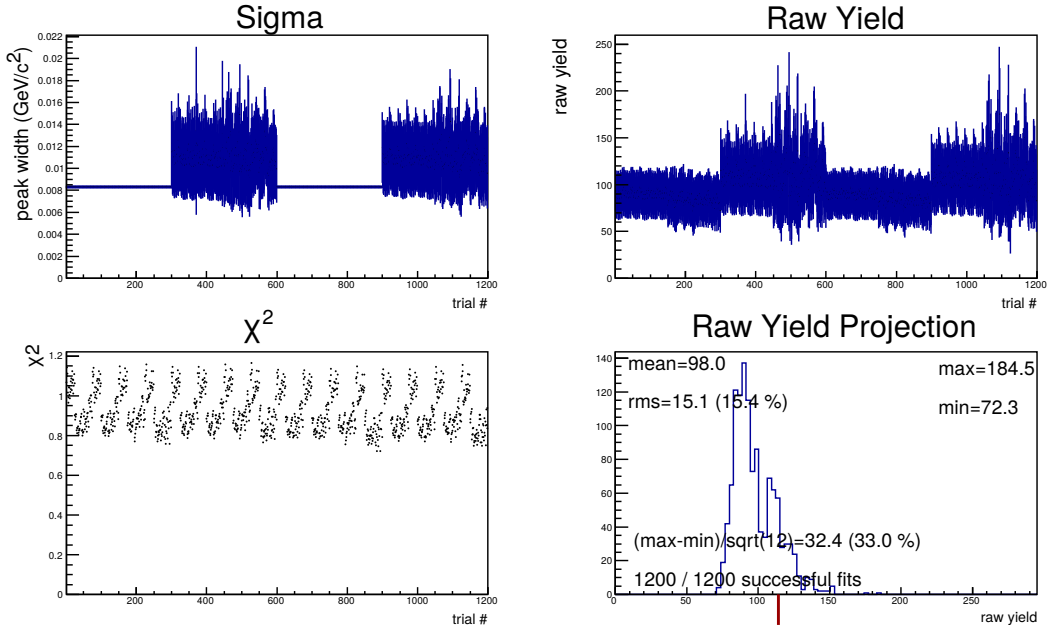

FIGURE 3.18: Multi-trial variation for 12< p_{T} <24 GeV/c. From top left clockwise: the peak width of the fit as a function of the trial number, the raw yield as a function of the trial number, the χ^2/NDF as a function of the trial number, and the distribution of the raw yield. The red line indicates the raw yield of the 'central' cross section.

3.8.2 Topological selection

The uncertainty due to the topological cuts is determined by varying the topological cuts. The production cuts (which were defined at creation of the analysis dataset) had been chosen as a result of the cut optimisation investigation. Due to this, the usual method of varying the cuts to be both tighter and looser than the central cut could only be done for tighter variations. The prompt Λ_c^+ efficiencies for different topological variations relative to the 'central' cut are shown in Figure 3.19 and the cross section for different topological variations relative to the 'central' cut are shown in Figure 3.20.

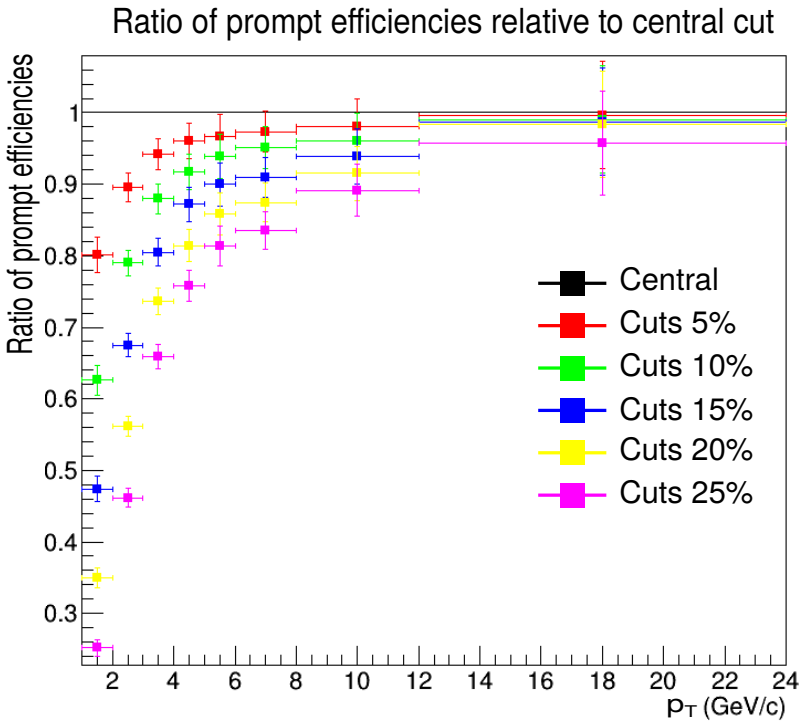

FIGURE 3.19: Ratio of prompt Λ_c^+ efficiencies for the different topological cuts (with range up to 25% change of cut parameters).

Two p_{T} bins (1-2 and 12-24 GeV/c) display a distinct shift in the value of the cross section for the variations relative to the 'central' cut. This trend is studied in more detail in the following subsections.

1-2 GeV/c p_{T} bin

One issue for the 1-2 bin particular is the large variation in efficiency (70%) covered with the current range set. Figure 3.21 shows the prompt Λ_c^+ efficiencies

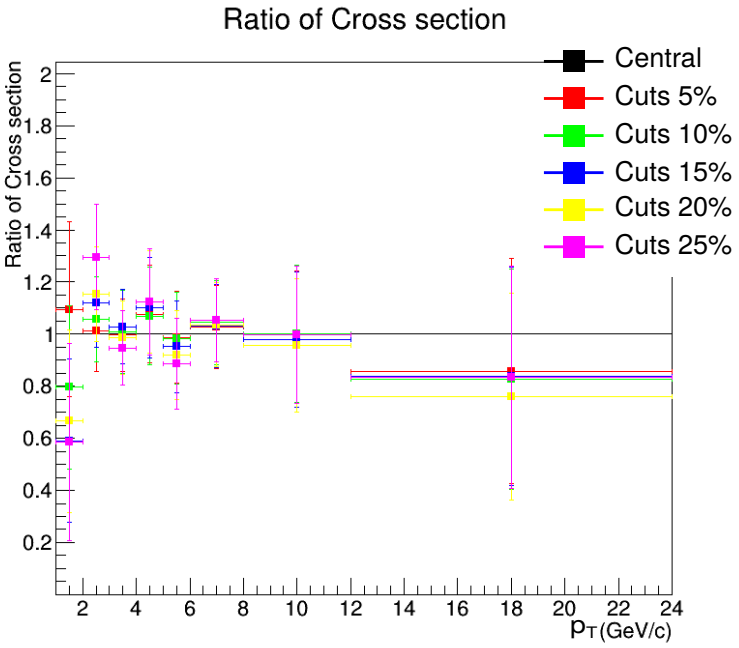

FIGURE 3.20: Ratio of Λ_c^+ cross section for the different topological cuts (with range up to 25% change of cut parameters).

where the cut variation is limited to 5%. Reducing the % change in cut variation from 25% to 5% still results in a reasonable variation of 20% in efficiency. This also reduces the effect of a drop in significance that occurs after a cut variation of 10% tighter than the standard value.

12-24 GeV/c p_{T} **bin**

In a cut study for the 12-24 GeV/c p_{T} bin, it was found applying a tighter standard cut on the p_{T} of the pion daughter increased the significance of the fit to above 3σ which systematically reduced the raw yield extracted in the previous cut variations. With this offset on the cut applied, when plotting the Λ_c^+ cross sections from the different variations relative to cross section from the 'central' cut (Figure 3.23), the variations are no longer systematically offset from the central cross section in the 12-24 GeV/c bin.

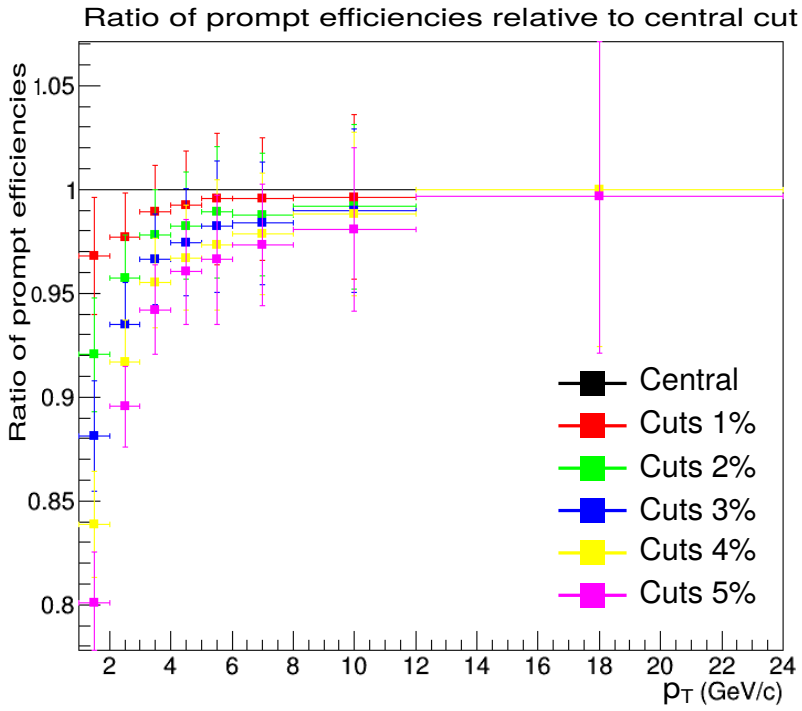

FIGURE 3.21: Ratio of prompt Λ_c^+ efficiencies for the different topological cuts (with range up to 5% change of cut parameters) for the study of the 1-2 GeV/c bin.

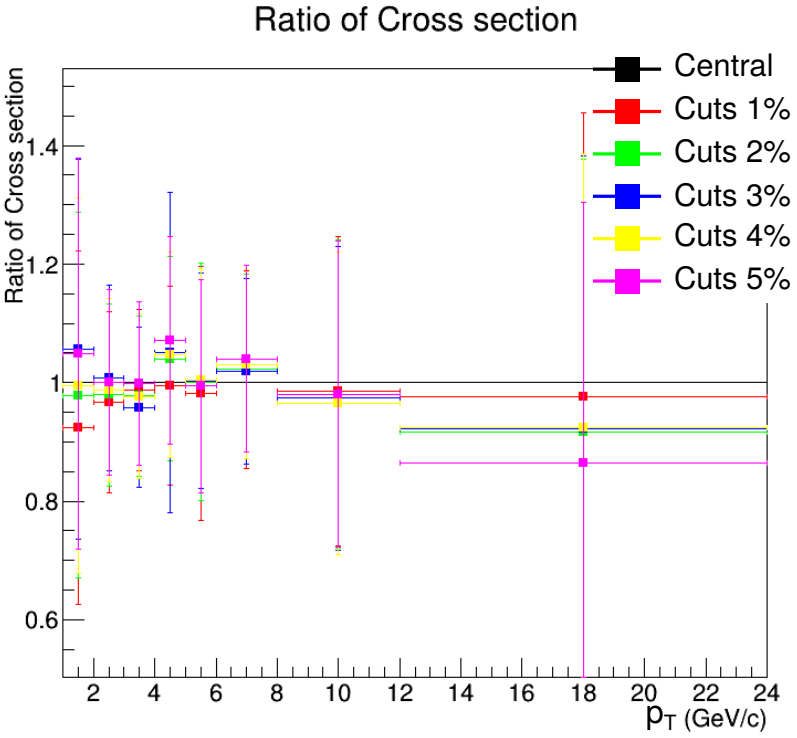

FIGURE 3.22: Ratio of Λ_c^+ cross section for the different topological cuts (with range up to 5% change of cut parameters) for the study of the 1-2 GeV/c bin.

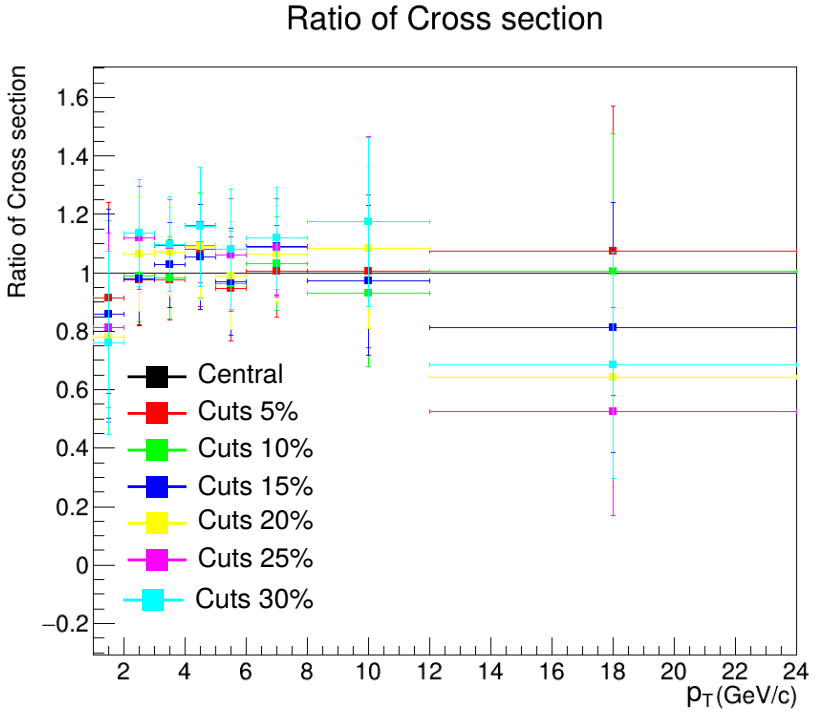

FIGURE 3.23: Ratio of Λ_c^+ cross section for the different topological cuts after applying the offset on the cut applied to the p_T of the pion daughter for the study of the 12-24 GeV/c bin.

3.8.3 PID

This analysis used the Bayesian approach with the maximum probability criteria for the PID. To estimate the systematic uncertainty due to PID, a varying probability threshold cut was placed on the three decay species (p,K,π) using the values in Table 3.5.

Prob. Threshold	Proton	Kaon	Pion
	30	30	30
	40	40	40
	50	50	50
	60	60	60
	70	70	70
	80	80	80

TABLE 3.5: Probability thresholds used.

Figure 3.24 shows the efficiencies for each of the different PID thresholds relative to the efficiency corresponding to the maximum probability criteria. As can be seen in Figure 3.24, when the probability thresholds are high (50-80%) the efficiences fall as a function of p_{T} and relative to the maximum probability criteria, and the opposite is true for low thresholds (30-40%). The corresponding Λ_c^+ cross sections for each PID threshold variation are shown relative to the 'central' cross section in Figure 3.25. A large variation seen in the cross section for the 12-24 GeV/c bin is taken to be due to low significance in the corresponding invariant mass distribution for that variation, and therefore is ignored when estimating a flat uncertainty. The average of the RMS/mean values for the remaining p_{T} bins gave a flat uncertainty of 5%.

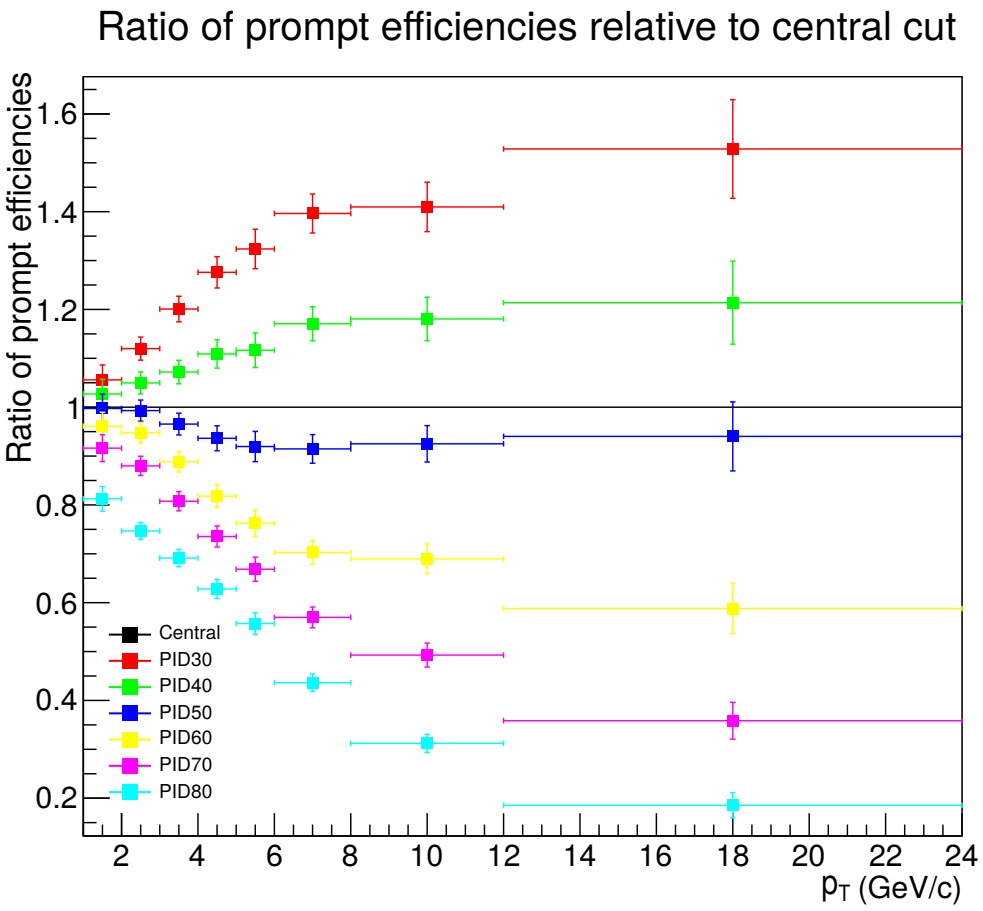

FIGURE 3.24: Ratio of prompt Λ_c^+ PID efficiencies for the different probability thresholds relative to the maximum probility criteria.

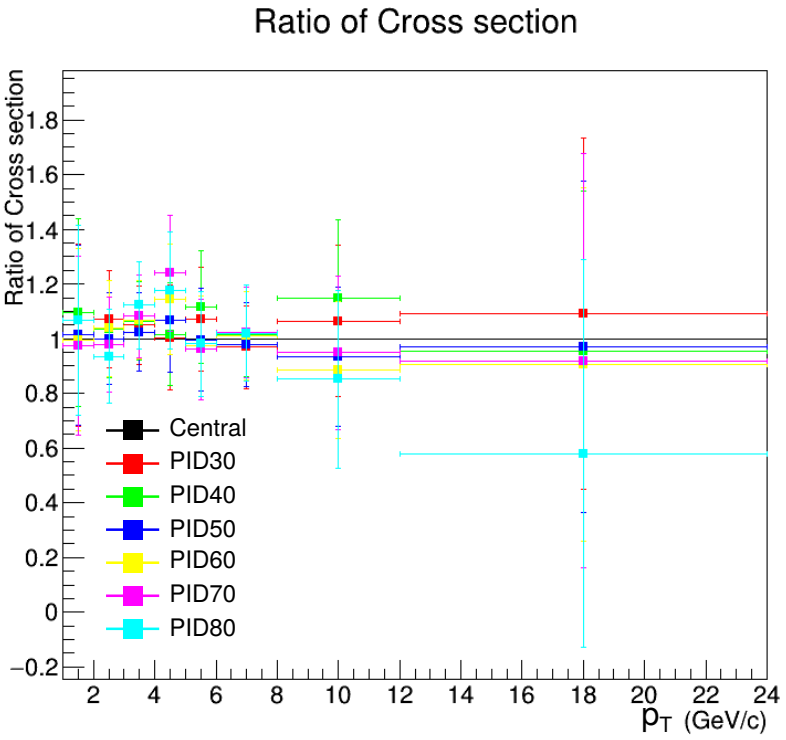

FIGURE 3.25: Variation of the Λ_c^+ cross section for the different PID probability thresholds relative to the maximum probility criteria.

3.8.4 MC p_T shape

Λ_c^+ generated in MC productions are generated with a certain p_T shape, given in PYTHIA. A discrepancy between the shape generated and the true shape of Λ_c^+ p_T shape will produce a systematic error in the calculated efficiences. To estimate this, the efficiency is calculated with the weights determined from different p_T hypotheses as predicted in FONLL. The weight used for comparison was w5LHC18a4a2 (p_T shape of D Meson spectra in the same dataset). In Figure 3.26, efficiencies corresponding to different p_T shapes are plotted relative to the efficiency corresponding to the Λ_c^+ p_T shape used in this analysis. The variation between the D meson and Λ_c^+ p_T shapes is neglible with the exception of the 1-2 GeV/c bin with a variation of about 2%.

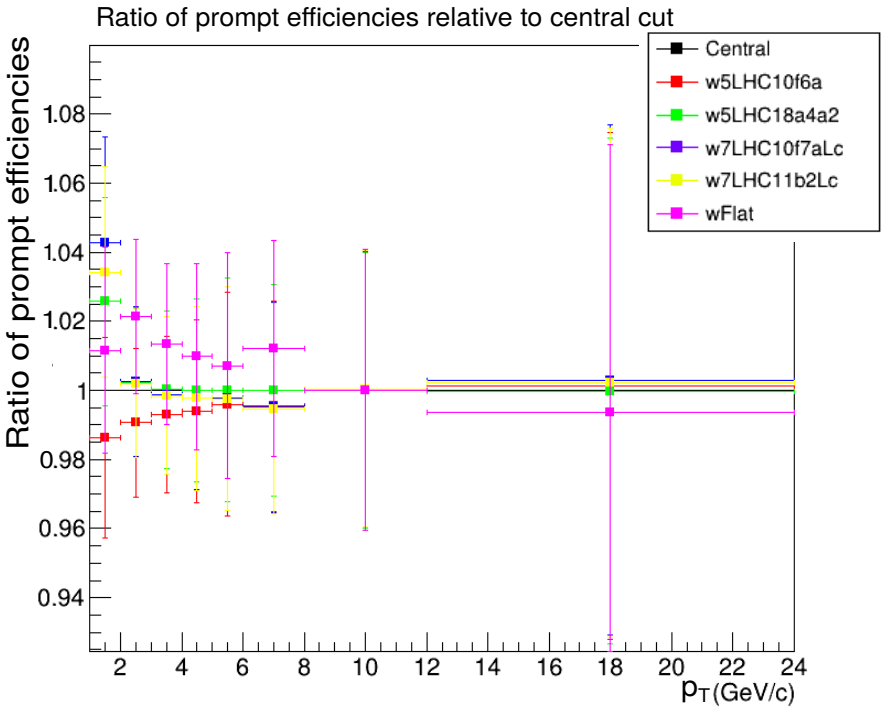

FIGURE 3.26: Ratio of prompt Λ_c^+ efficiencies for the different MC shapes. The statistical uncertainty was estimated by the variation between the Λ_c^+ p_T shape (Central) and the D meson p_T shape (w5LHC18a4a2).

3.8.5 Feed-down

The contribution to the uncertainties coming from the subtraction of Λ_c^+ baryons from Λ_b^0 was calculated as the envelope of the uncertainty bands obtained by varying the p_T-differential cross section of beauty hadrons within the FONLL , and the envelope of the variations of the Λ_b^0 fragmentation parameterisations. This is explained in detail in Section 3.7.

3.8.6 Tracking

Track selection variation

The Λ_c^+ raw yields, efficiency and corrected yields were evaluated with four different sets of track cuts selection. Each variation was compared to the standard value.

1. p_T dependent cut: number of TPC crossed rows > 120 - $(5/p_T)$
2. number of TPC clusters > 0.65 × number of TPC crossed rows
3. number of clusters with TPC dE/dx signal > 0.5 × number of TPC crossed rows
4. ratio of crossed rows over findable clusters in the TPC > 0.9

Matching efficiency

The values for the matching efficiency were previously determined as part of a previous D meson measurement. The systematics from both the track selection variation and matching efficiency were combined taking into account the decay kinematics of the Λ_c^+ to give the values shown in Figure 3.27.

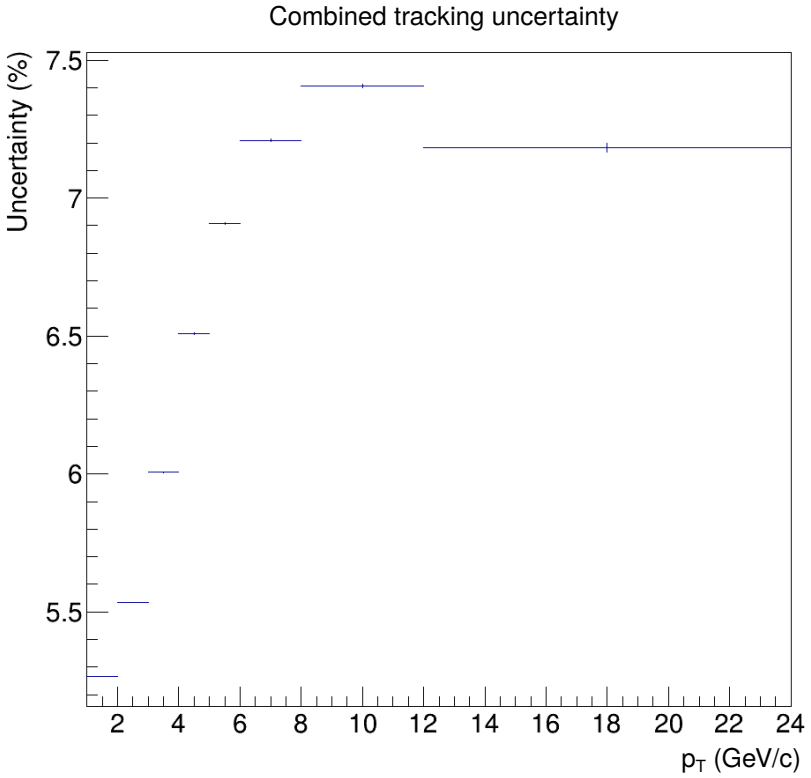

FIGURE 3.27: Combined tracking uncertainties vs p_T.

3.8.7 Summary

The total systematic uncertainties are summarized in Table 3.6, and include:

- Yield extraction: ranged 6-16%
- Cut efficiency: ranged 3-20%
- PID efficiency: considered flat at 5%
- Tracking: 5 to 7%
- MC p_{T} Shape: ranged 0-2%
- Feed-down: asymmetric, from around 1-4%

p_T interval (GeV/c)	1-2	2-3	3-4	4-5	5-6	6-8	8-12	12-24
Yield extraction (%)	10	10	10	10	6	8	8	16
Cut efficiency (%)	6	6	6	6	6	6	6	6
PID (%)	5 (flat uncertainty)							
Tracking (%)	5	6	6	7	7	7	7	
MC p_T Shape (%)	2	0	0	0	0	0	0	0
Feed-down (%)	+0.4 -0.5	+0.6 -0.8	+0.8 -1.1	+1.2 -1.4	+1.8 -2.2	+2.1 -2.6	+2.0 -2.9	+3.8 -4.3
Branching fraction (%)	+5.1							
Luminosity (%)	3.7							

TABLE 3.6: Summary of the systematic uncertainties assigned to each source.

References

[1] Su Houng Lee et al. "Λ_c enhancement from strongly coupled quark-gluon plasma". In: *Phys. Rev. Lett.* 100 (2008), p. 222301. DOI: 10.1103/PhysRevLett.100.222301. arXiv: 0709.3637 [nucl-th].

[2] Yongseok Oh et al. "Heavy baryon/meson ratios in relativistic heavy ion collisions". In: *Phys. Rev.* C79 (2009), p. 044905. DOI: 10.1103/PhysRevC.79.044905. arXiv: 0901.1382 [nucl-th].

[3] Salvatore Plumari et al. "Charmed Hadrons from Coalescence plus Fragmentation in relativistic nucleus-nucleus collisions at RHIC and LHC". In: *Eur. Phys. J.* C78.4 (2018), p. 348. DOI: 10.1140/epjc/s10052-018-5828-7. arXiv: 1712.00730 [hep-ph].

[4] Shreyasi Acharya et al. "Measurement of D-meson production at mid-rapidity in pp collisions at $\sqrt{s} = 7$ TeV". In: *Eur. Phys. J.* C77.8 (2017), p. 550. DOI: 10.1140/epjc/s10052-017-5090-4. arXiv: 1702.00766 [hep-ex].

[5] Matteo Cacciari, Mario Greco, and Paolo Nason. "The P(T) spectrum in heavy flavor hadroproduction". In: *JHEP* 05 (1998), p. 007. DOI: 10.1088/1126-6708/1998/05/007. arXiv: hep-ph/9803400.

[6] Matteo Cacciari et al. "Theoretical predictions for charm and bottom production at the LHC". In: *Journal of High Energy Physics* 2012.10 (2012), p. 137. ISSN: 1029-8479. DOI: 10.1007/JHEP10(2012)137. URL: https://doi.org/10.1007/JHEP10(2012)137.

[7] B. A. Kniehl et al. "Collinear subtractions in hadroproduction of heavy quarks". In: *Eur. Phys. J. C* 41 (2005), pp. 199–212. DOI: 10.1140/epjc/s2005-02200-7. arXiv: hep-ph/0502194.

[8] B. A. Kniehl et al. "Inclusive Charmed-Meson Production at the CERN LHC". In: *Eur. Phys. J.* C72 (2012), p. 2082. DOI: 10.1140/epjc/s10052-012-2082-2. arXiv: 1202.0439 [hep-ph].

[9] Jaroslav Adam et al. "D-meson production in p–Pb collisions at $\sqrt{s_{\mathrm{NN}}} = 5.02$ TeV and in pp collisions at $\sqrt{s} = 7$ TeV". In: *Phys. Rev.* C94.5 (2016), p. 054908. DOI: 10.1103/PhysRevC.94.054908. arXiv: 1605.07569 [nucl-ex].

[10] Shreyasi Acharya et al. "Λ_c^+ production in pp collisions at $\sqrt{s} = 7$ TeV and in p–Pb collisions at $\sqrt{s_{NN}} = 5.02$ TeV". In: *JHEP* 04 (2018), p. 108. DOI: 10.1007/JHEP04(2018)108. arXiv: 1712.09581 [nucl-ex].

[11] Peter Skands, Stefano Carrazza, and Juan Rojo. "Tuning PYTHIA 8.1: the Monash 2013 Tune". In: *Eur. Phys. J.* C74.8 (2014), p. 3024. DOI: 10.1140/epjc/s10052-014-3024-y. arXiv: 1404.5630 [hep-ph].

[12] Jesper R. Christiansen and Peter Z. Skands. "String Formation Beyond Leading Colour". In: *JHEP* 08 (2015), p. 003. DOI: 10.1007/JHEP08(2015)003. arXiv: 1505.01681 [hep-ph].

[13] Christian Bierlich and Jesper Roy Christiansen. "Effects of color reconnection on hadron flavor observables". In: *Phys. Rev.* D92.9 (2015), p. 094010. DOI: 10.1103/PhysRevD.92.094010. arXiv: 1507.02091 [hep-ph].

[14] Christoffer Flensburg, Gosta Gustafson, and Leif Lonnblad. "Inclusive and Exclusive Observables from Dipoles in High Energy Collisions". In: *JHEP* 08 (2011), p. 103. DOI: 10.1007/JHEP08(2011)103. arXiv: 1103.4321 [hep-ph].

[15] Johannes Bellm et al. "Herwig 7.0/Herwig++ 3.0 release note". In: *Eur. Phys. J. C* 76.4 (2016), p. 196. DOI: 10.1140/epjc/s10052-016-4018-8. arXiv: 1512.01178 [hep-ph].

[16] Particle Data Group et al. ""Review of Particle Physics"". In: *"Progress of Theoretical and Experimental Physics"* 2020.8 (Aug. 2020). 083C01. ISSN: 2050-3911. DOI: 10.1093/ptep/ptaa104. eprint: https://academic.oup.com/ptep/article-pdf/2020/8/083C01/34673722/ptaa104.pdf. URL: https://doi.org/10.1093/ptep/ptaa104.

[17] *ALISW/AliPhysics: Alice Analysis Repository.* URL: https://github.com/alisw/AliPhysics.

[18] Jaroslav Adam et al. "Particle identification in ALICE: a Bayesian approach". In: *Eur. Phys. J. Plus* 131.5 (2016), p. 168. DOI: 10.1140/epjp/i2016-16168-5. arXiv: 1602.01392 [physics.data-an].

[19] Matteo Cacciari et al. "Theoretical predictions for charm and bottom production at the LHC". In: *JHEP* 10 (2012), p. 137. DOI: 10.1007/JHEP10(2012)137. arXiv: 1205.6344 [hep-ph].

[20] Roel Aaij et al. "Measurement of b hadron fractions in 13 TeV pp collisions". In: *Phys. Rev.* D100.3 (2019), p. 031102. DOI: 10.1103/PhysRevD.100.031102. arXiv: 1902.06794 [hep-ex].

[21] Torbjorn Sjöstrand, Stephen Mrenna, and Peter Z. Skands. "A Brief Introduction to PYTHIA 8.1". In: *Comput. Phys. Commun.* 178 (2008), pp. 852–867. DOI: 10.1016/j.cpc.2008.01.036. arXiv: 0710.3820 [hep-ph].

[22] M. Tanabashi et al. "Review of Particle Physics". In: *Phys. Rev.* D98.3 (2018), p. 030001. DOI: 10.1103/PhysRevD.98.030001.

[23] R. Aaij et al. "Study of the production of Λ_b^0 and $\overline{B}^0$ hadrons in pp collisions and first measurement of the $\Lambda_b^0 \to J/\psi p K^-$ branching fraction". In: *Chin. Phys.* C40.1 (2016), p. 011001. DOI: 10.1088/1674-1137/40/1/011001. arXiv: 1509.00292 [hep-ex].

Chapter 4

Data Analysis: $\mathbf{\Lambda_c^+ \to pK^-\pi^+}$ in p–Pb collisions at $\sqrt{s}$= 5.02 TeV

4.1 Declaration

This work was written up as an Analysis Note and peer reviewed internally by the ALICE collaboration. The subsequent paper containing this analysis is presented in Chapter 5. This work that I coauthored details the analysis of the $\Lambda_c^+ \to pK^-\pi^+$ and $\Lambda_c^+ \to pK_S^0$ decay channels in p–Pb collisions at $\sqrt{s} = 5.02$ TeV using data taken during LHC Run 2. My specific contribution to this work was the analysis of the $\Lambda_c^+ \to pK^-\pi^+$ decay channel in p–Pb collisions at $\sqrt{s} = 5.02$ TeV using data taken during LHC Run 2. The excerpt shown only includes details of the analysis in the $\Lambda_c^+ \to pK^-\pi^+$ decay channel and was written primarily by myself in collaboration with J. Norman.

Permission to include this excerpt from the Analysis Note with identification reference ALICE-ANA-811 entitled "Measurement of prompt Λ_c^+ production via hadronic decay channels, in p–Pb collisions at $\sqrt{s_{NN}} = 5.02$ TeV (Run 2 data)" was given by all the data-analysers who co-authored this document, as well as by the ALICE Collaboration Physics Coordinator and the co-chairs of the ALICE Collaboration Editorial Board. Their consent declaration can be found in Appendix A.

4.2 Introduction

The following sections outline the measurement of the Λ_c^+ baryon in p-Pb collisions via the decay channel $\Lambda_c^+ \rightarrow pK^-\pi^+$. The event and track selection is described in Section 4.3. The PID and topological selection strategy is described in Section 4.4. The signal extraction is described in Section 4.5. The efficiency and acceptance corrections are described in Section 4.6. The systematic uncertainty sources and the methods used to estimate them are described in Section 4.7. The motivations for this measurement and details about the $\Lambda_c^+ \rightarrow pK^-\pi^+$ have been previously discussed in Sections 3.2 and 3.3, respectively.

4.3 Data samples, Event and Track selection

4.3.1 Data samples

The presented Λ_c^+ analysis is performed using p-Pb collisions at $\sqrt{s_{NN}} = 5.02$ TeV data, recorded in 2016 composed of minimum bias events. Where the main trigger detectors are the SPD and V0 scintillator arrays. The minimum bias trigger selects all events with at least one hit in the SPD or in one of the two V0 counters, in coincidence with the signals from the beam pickup detectors.

Two Monte Carlo productions were used to compute the efficiencies and acceptance corrections. They were made with a combination of HIJING for the background events and PYTHIA for events enriched by charm or beauty pairs forced to decay into either $\Lambda_c^+ \rightarrow pK^-\pi^+$ or $\Lambda_c^+ \rightarrow pK_S^0$.

4.3.2 Event selection

For the Event selection, any event passing the minimum bias trigger and physics selection were included. The primary vertex was required to be reconstructed with only tracks within 10 cm in the z direction from the interaction point. The reconstructed ITS and ITS+TPC vertices are required to be closer than 5 mm. Events with more than one interaction (pile-up) were removed.

4.3.3 Track selection

For a track to be included in the reconstruction of the secondary vertices of Λ_c^+ they were selected by requiring the conditions stated in Table 4.1:

Parameter	choice
n. of TPC clusters	≥ 70
TPCrefit	true
n. of ITS clusters	≥ 2
ITSrefit	true
$\|\eta\|$	< 0.8
p_{T}	> 0.4 GeV/c

TABLE 4.1: The track selection applied in this analysis.

4.3.4 Lego train Information and AliRoot Code Used

After event selection, the data sample is composed of 600 million minimum bias events. The MC simulations used for the efficiency corrections and tuning cut parameters is composed of 85 million minimum bias events. The code used to obtain the results in this analysis is available publicly at [1].

4.4 Particle identification and topological selection

4.4.1 Topological selection

For each reconstructed candidate, several cut variables are calculated based on primary and secondary vertex positions as well as the kinematics of the decay product tracks. These cut variables have been discussed previously in Section 3.5.1.

4.4.2 Particle identification

Particle identification of protons, pions and kaons, from which the Λ_c^+ candidates are reconstructed, is based on information on the specific ionisation, dE/dx in the TPC gas as well as the time-of-flight measurement from the TOF detector. TOF measurements help to identify particles where the TPC is no longer able to, such as at 0.6 GeV/c and 1.2 GeV/c where the kaon bands merges with the pion and proton bands, respectively for TPC PID. However TOF measurements are not always available because tracks present in the TPC may not reach the TOF. A Bayesian approach of particle identification has been developed by ALICE [2] and is used in this analysis. In this analysis tracks are assigned the identity of the particle species with the highest posteriori probability (conditional probability given the PID measurement and prior knowledge of the expected particle abundances), the so-called 'maximum probability criterion'. The Bayesian approach was chosen over the nσ approach, since although it can result in a smaller efficiency, this approach gives a higher chance of correctly identifying a track, thus allowing for a higher purity in the sample of tracks passing the PID selection. This was previously shown to be the optimal approach for the $\Lambda_c^+ \rightarrow \mathrm{pK}^-\pi^+$ analysis [2].

4.5 Signal extraction

In this section, the signal extraction results for the $\Lambda_c^+ \rightarrow \mathrm{pK}^-\pi^+$ in p-Pb data will be shown for the six momentum bins: 2-3, 3-4, 4-6, 6-8, 8-12, 12-24 GeV/c. The value for the signal (raw yield) are taken from the invariant mass plots of candidates containing p,K and π tracks, as described in equation 3.1. The fit function to reproduce these distributions is the combination of a Gaussian for the

Λ_c^+ peak and a second order polynomial for the background. The fit is performed in two steps: The first estimates the background function parameters using the side bands; the second repeats this including the signal range, fitting the signal, leading to a final estimation of all fit parameters. The number of signal events are extracted by subtracting the background function from the total fit in the signal range within 3 standard deviations.

A topological cut study was performed using the cut variables listed in Section 3.5.1. The main method for this was the use of several rectangular cut optimisation techniques from the Toolkit for Multivariate Data Analysis (TMVA) software package [3]. The two techniques were:

- **Genetic Algorithm**: In the first step, a group of individuals with randomised cut parameters values are generated. They are evaluated in terms of background rejection at specific signal efficiencies. Individuals with cut parameter values that produce a improvement in background rejection are stored. Individuals with good performance form the basis for the next generation of individuals that are produced by crossover (cut parameter values mixed into different combinations) and then mutation (some parameter values are changed randomly following a Gaussian distribution). This process is repeated until the improvement has fallen below a given value resulting an optimal set of cuts.

- **Simulated Annealing**: A well known minimisation problem solver, dealing with finding global minima even when local minima are present. Analogous to the heating and cooling of metal, with infinitesimal changes to temperature, this ultimately leads to the system finding its global energy minimum. The probability of the system recovering out of a local minima is given by Eq 4.1.

$$p(\Delta E) \propto e^{(-\frac{\Delta E}{T})} \tag{4.1}$$

  Where ΔE is the energy shift required and T is the temperature of the system. By allowing changes to cut parameters values that may initially reduce performance but increases access to more optimal solutions, simulated annealing can consistently provide the most optimal solutions.

Figure 4.1 shows the significance, signal/background ratio, peak mean and peak width for different topological cuts and the Monte Carlo simulation. As

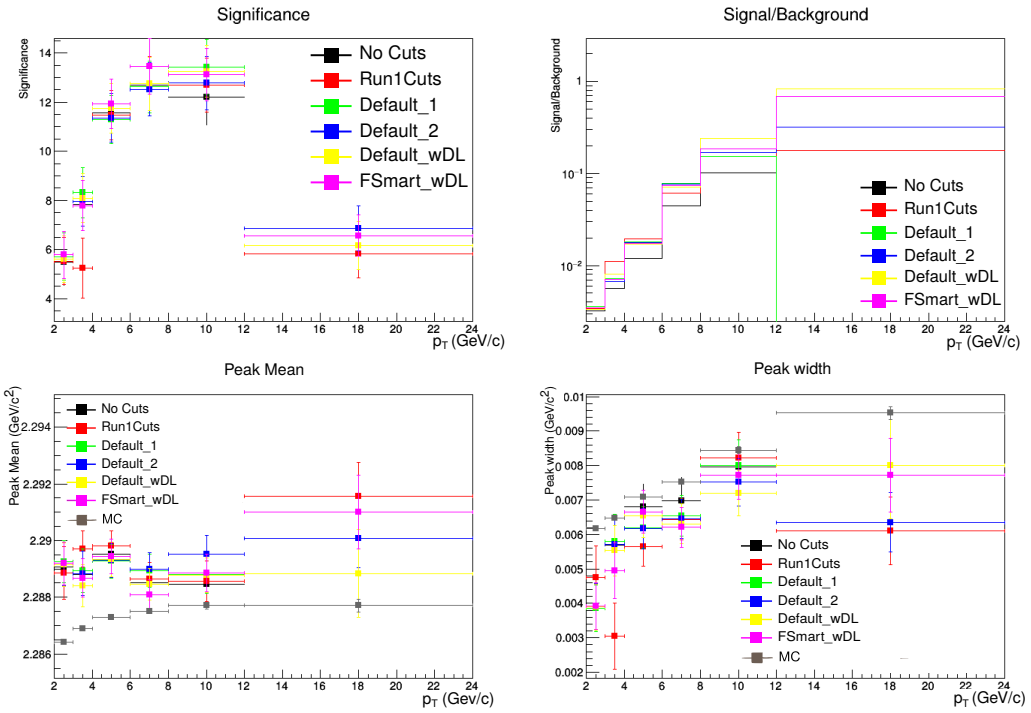

FIGURE 4.1: Top left: Comparison of significance, Top right: Comparison of the signal to background ratio, Bottom left: Comparison of peak mean with MC, Bottom right: Comparison of peak width with MC. Default and FSmart refers to how TMVA samples its cuts and the suffix 'wDL' corresponds to where the normalised decay length in the XY plane is used as an extra cut variable.

shown in Figure 4.1, several trials of cuts were done using different options available in the TMVA as well testing the effect of adding the normalised decay length in the XY plane as an extra cut variable. Despite these optimised cuts improving the signal to background ratio, they did not allow for a significant improvement in the significance which defines the statistical uncertainty of the signal extraction. For this reason, 'loose' cuts (shown in Table 4.2 and) defined at the creation of the analysis dataset, referred to as 'production cuts', were chosen as the cuts for this analysis as they performed comparatively well in all p_{T} bins and the cuts were by definition constant with p_{T}.

Figure 4.2 shows the fitted invariant mass distributions in the p_{T} bins considered for this analysis. In Figure 4.2, it can be seen that we get good signal extraction in the p_{T} range 2-24 GeV/c. This includes the new 12-24 GeV/c bin, extending the p_{T} range with respect to Run 1.

p_T, Λ_c^+	p_T, p	p_T,K	p_T,π	DCA	dist12	σv	d^{length}	Cosθ_p
$2 < p_T < 3$	>0.5	>0.4	>0.4	<0.05	>0.01	<0.06	>0.005	>0
$3 < p_T < 4$	>0.5	>0.4	>0.4	<0.05	>0.01	<0.06	>0.005	>0
$4 < p_T < 6$	>0.5	>0.4	>0.4	<0.05	>0.01	<0.06	>0.005	>0
$6 < p_T < 8$	>0.5	>0.4	>0.4	<0.05	>0.01	<0.06	>0.005	>0
$8 < p_T < 12$	>0.5	>0.4	>0.4	<0.05	>0.01	<0.06	>0.005	>0
$12 < p_T < 24$	>0.5	>0.4	>0.4	<0.05	>0.01	<0.06	>0.005	>0
(GeV/c)	(GeV/c)	(GeV/c)	(GeV/c)	(cm)	(cm)	(cm)	(cm)	

TABLE 4.2: Corresponding cut parameter values for production cuts

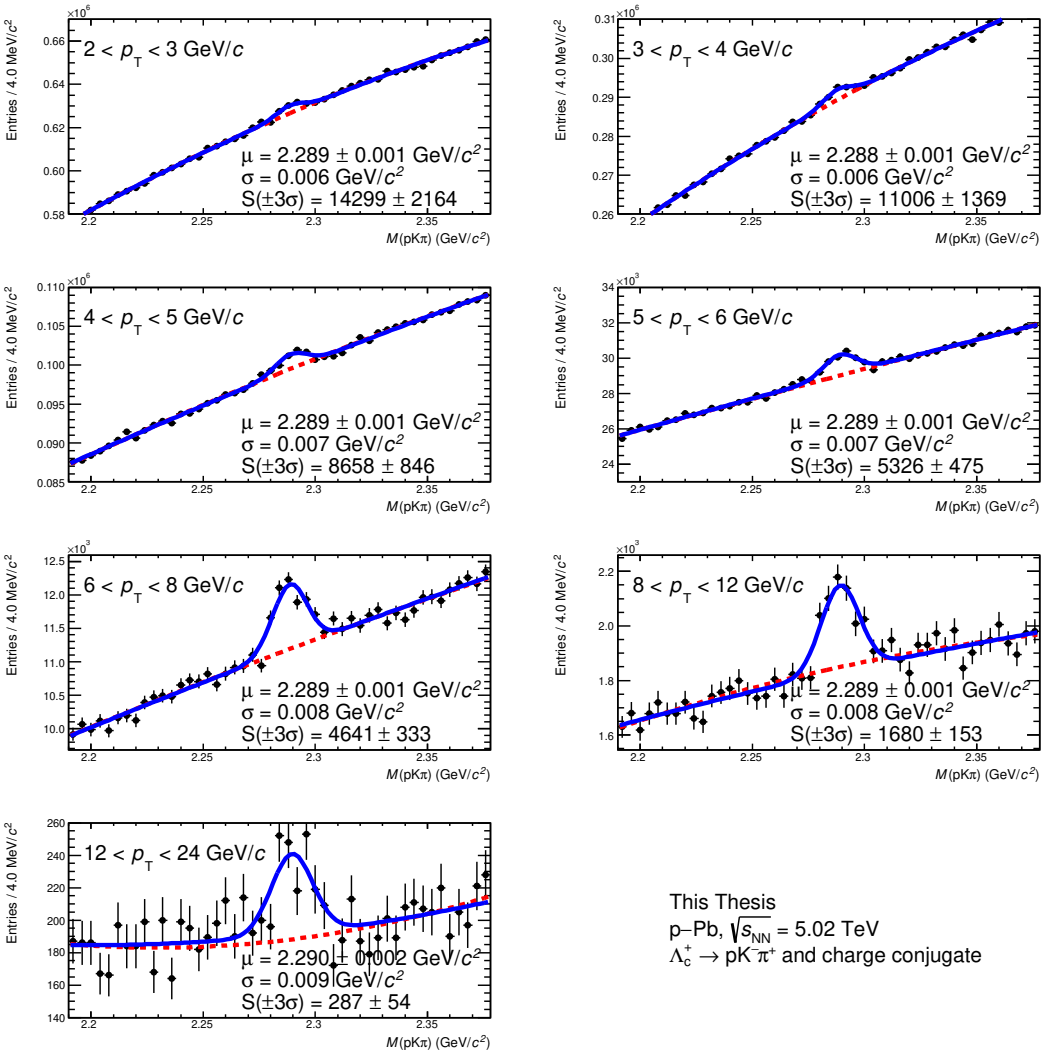

FIGURE 4.2: Invariant mass plots in each p_T bin for productions cuts.

4.6 Corrections to the raw yield

4.6.1 Efficiency and Acceptance correction

In order to obtain true productions yields of Λ_c^+, corrections are made to the raw yields extracted from the invariant mass spectra. The product of acceptance and efficiency corrections $Acc \times \epsilon$ is determined in each p_T bin using Monte Carlo simulated p-Pb events. The efficiency of each intermediate $\Lambda_c^+ \rightarrow pK^-\pi^+$ resonant decay is different due the different kinematic properties, requiring the efficiency and acceptance to be determined individually for each decay. Both Pythia 6 and Pythia 8 are used to simulate the pp events, and Geant3 is used to simulate the detector response.

The Λ_c^+ efficiency is calculated in 8 stages:

- MC particles in acceptance
- Vertex (event selection)
- Refit (number of hits in ITS and TPC detectors)
- Reconstructed candidates
- Reconstructed candidates in acceptance
- Passing minimum no. of ITS clusters
- Topological cuts
- PID

Figure 4.3 shows the prompt and non-prompt efficiencies of the Λ_c^+ which are given for the four different decay channels as well as the overall efficiency multiplied by the acceptance (shown separately in Figure 4.4). The efficiency is greater in general for non-prompt due to its displaced secondary vertex.

The acceptance factor is necessary to normalise the yield to the rapidity window, $|y| < 0.5$ where the cross section is essentially flat. This is calculated using a toy Monte Carlo, as the acceptance is a purely geometric effect.

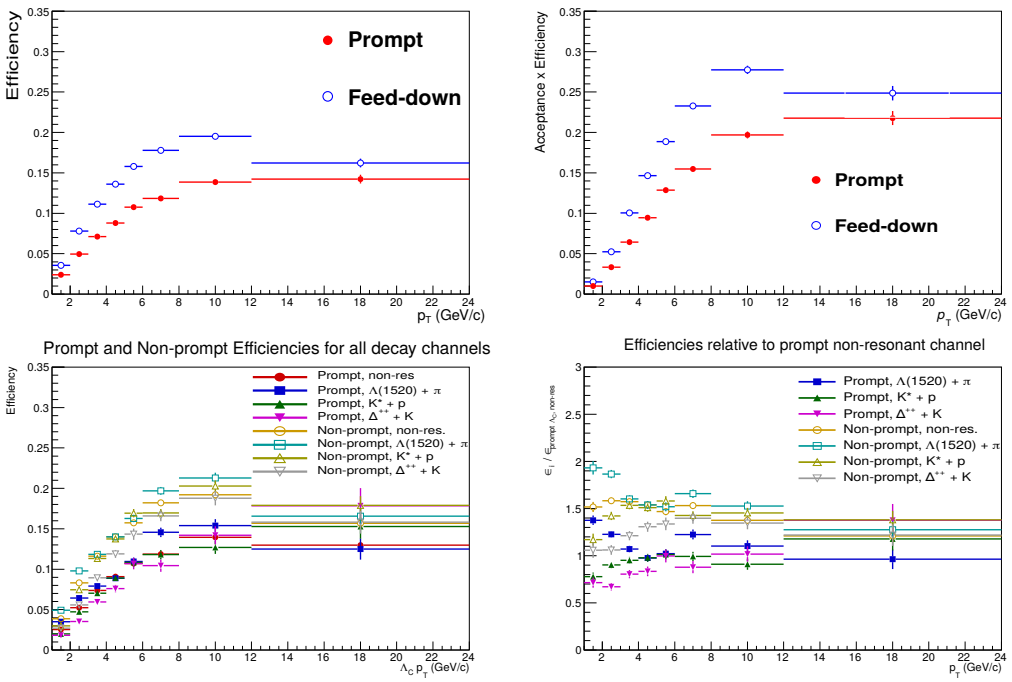

FIGURE 4.3: Top left: Prompt and non-prompt Λ_c^+ efficiencies, Top right: Acceptance x efficiency for prompt and non-prompt Λ_c^+, Bottom left: Efficiencies for each $\Lambda_c^+ \to pK^-\pi^+$ decay (prompt and non-prompt), Bottom right: Efficiencies relative prompt non-resonant decay.

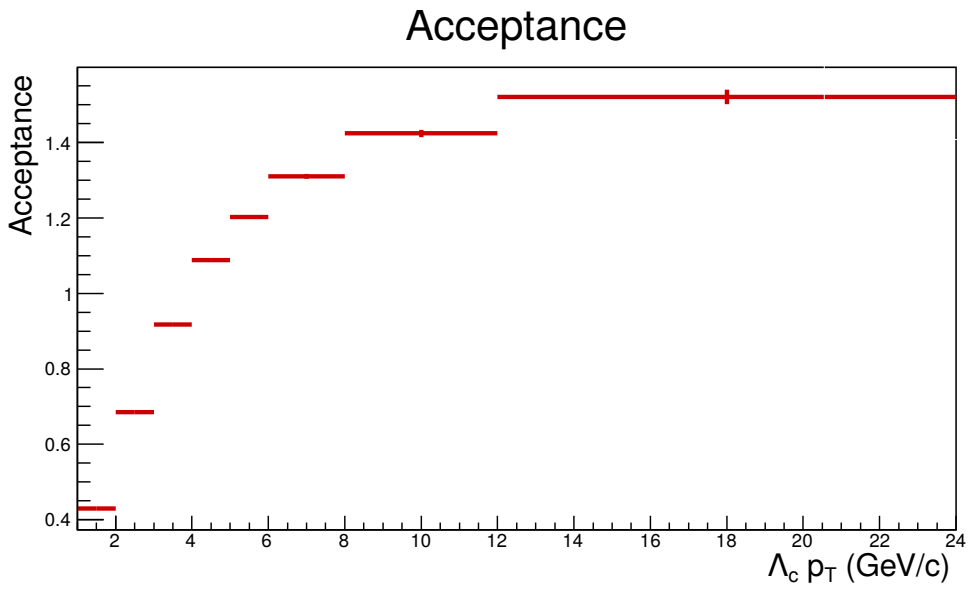

FIGURE 4.4: Acceptance factor as calculated in toy Monte Carlo generated with Pythia.

4.6.2 Feed-down correction

To extract the raw yield $N_{raw,prompt}^{\Lambda_c^+}$ corresponding to only prompt Λ_c^+, the contribution of feed-down $N_{raw}^{\Lambda_b^0 \to \Lambda_c^+ + X}$ from $\Lambda_b^0 \to \Lambda_c^+ + X$ decays is subtracted from the measured raw yield, $N_{raw}^{\Lambda_c^+}$:

$$N_{raw,prompt}^{\Lambda_c^+} = N_{raw}^{\Lambda_c^+} - N_{raw}^{\Lambda_b^0 \to \Lambda_c^+ + X} \tag{4.2}$$

,

$$N_{raw,prompt}^{\Lambda_c^+} = N_{raw}^{\Lambda_c^+} \cdot (1 - \frac{N_{raw}^{\Lambda_b^0 \to \Lambda_c^+ + X}}{N_{raw}^{\Lambda_c^+}}) = N_{raw}^{\Lambda_c^+} \cdot f_{prompt} \tag{4.3}$$

, where f_{prompt} is the relative fraction of Λ_c^+ not from the $\Lambda_b^0 \to \Lambda_c^+ + X$ decay. The method chosen to calculate the feed-down, referred to as the N_b method, uses the production cross section of Λ_b^0 calculated within FONLL multiplied by branching ratio to the decay channel $\Lambda_b^0 \to \Lambda_c^+ + X$, the correction factors for the acceptance and reconstruction efficiency $\epsilon_{\Lambda_b^0 \to \Lambda_c^+ + X}$ of non-prompt Λ_c^+, and the integrated Luminosity, $\mathcal{L}_{int}$.

$$f_{prompt} = 1 - \frac{1}{N_{raw}^{\Lambda_c^+}} \cdot \mathcal{L}_{int} \cdot BR_b \cdot \epsilon_{\Lambda_b^0 \to \Lambda_c^+ + X} \int_{\Delta y \Delta p_T} \frac{d\sigma_{FONLL}^{\Lambda_b^0}}{dy dp_T} \Delta y \Delta p_T \tag{4.4}$$

.

Figure 4.5 shows the prompt fraction, f_{prompt} determined using the method described in Section 3.7.2.

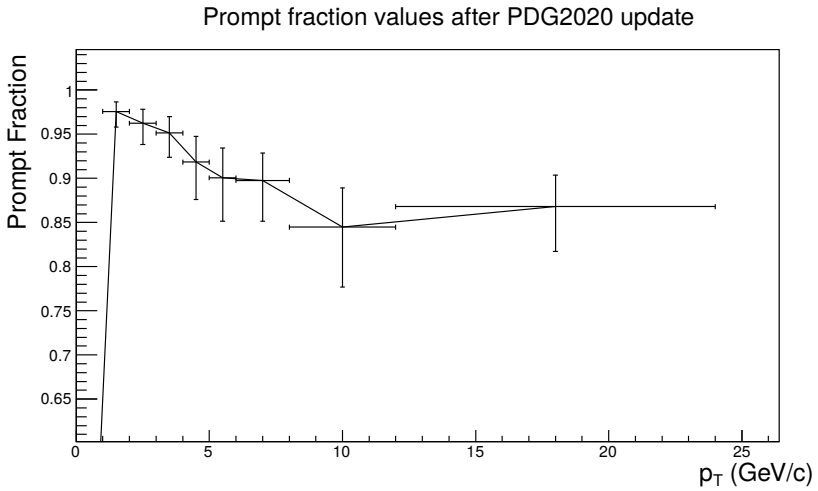

FIGURE 4.5: f_{prompt} for the $\Lambda_c^+ \rightarrow pK^-\pi^+$ analysis after an update with respect to data in PDG 2020.

4.7 Systematic uncertainties

This Section summarizes the steps taken into account to determine the systematic errors present in the analysis.

4.7.1 Signal extraction

The systematic uncertainty on the extraction of the raw yield can be estimated by varying the various fitting and histogram parameters from the default used in the central cross section calculation. This is done in a loop, and the following fit and histogram parameters are changed from the default (defined in **bold** below):

- The function used to fit background. Four functions were used an exponential, linear, **2nd order polynomial** and a 3rd order polynomial.
- The mass window. Five upper limits were chosen (2.40, 2.39, **2.38**, 2.37 and 2.36 GeV/c) and five lower limits were chosen(2.17, 2.18, **2.19**, 2.20, 2.21 GeV).
- Three rebin steps: 2, **4** and 6 GeV/c.
- Four combinations of either free or fixed standard deviation and free or fixed mean. The default was fixed sigma and free mean. The standard deviation values are fixed to values in the Monte Carlo.

For the p_T intervals from $2 < p_T < 8$ GeV/c it was found that the exponential and linear fit functions for the background did not describe the background well and thus lead to a very high χ^2/NDF for the overall fit. For this reason these fit functions were discarded from the trials. In total, 600 trials were performed for the p_T intervals $2 < p_T < 3$ GeV/c, $3 < p_T < 4$ GeV/c, $4 < p_T < 6$ GeV/c and $6 < p_T < 8$ GeV/c, and 1200 trials for $8 < p_T < 12$ GeV/c and $12 < p_T < 24$ GeV/c.

In all cases, it was found that almost all trials have a reasonable χ^2/NDF around 1, and that the peak width when leaving the width as a free parameter of the fit is in reasonable agreement with the MC expectation. A systematic uncertainty of the RMS of the distribution divided by the mean of the distribution in each p_T interval is assigned, ranging from $3-10\%$ depending on the p_T interval.

Systematics for split 4-5 and 5-6 GeV/c bins

For the splitting of the 4-6 GeV/c bin, the same raw yield variation study was extended to the 4-5 GeV/c and 5-6 GeV/c bins A systematic uncertainty of 6% and 9% was assigned, respectively.

4.7.2 Topological selection

The production cuts (which were the loosest possible) had been chosen as a result of the cut optimisation investigation. Due to this, the usual method of varying the cuts to be both tighter and looser than the central cut could only be done for tighter variations.

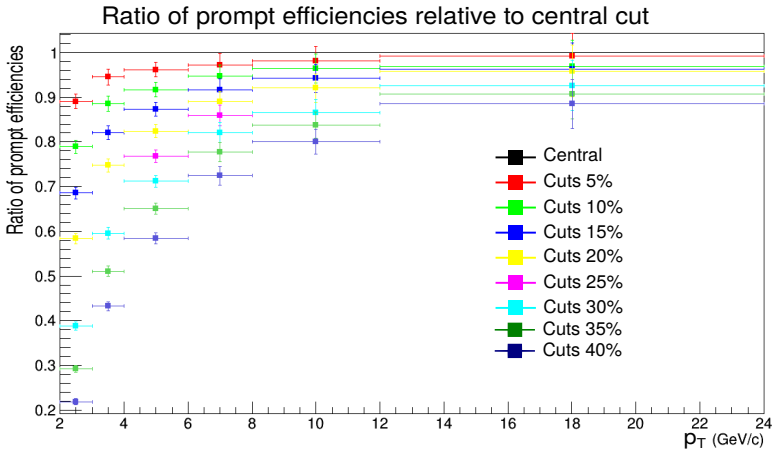

FIGURE 4.6: Ratio of prompt Λ_c^+ efficiencies for the different topological cuts.

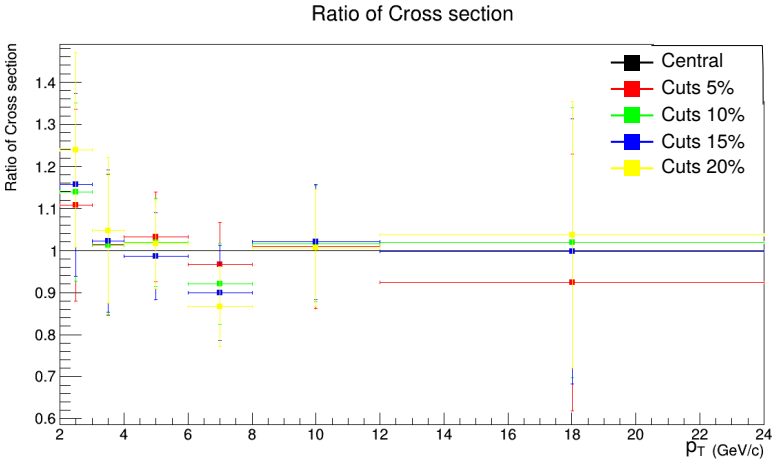

FIGURE 4.7: Ratio of Λ_c^+ cross section for the different topological cuts. Note that only the four loosest cuts where considered here as they covered up to 40% change in the efficiency.

Figure 4.6 shows the ratio of the prompt Λ_c^+ efficiencies for each topological variation relative to the central prompt Λ_c^+ efficiency and Figure 4.7 shows the ratio of the Λ_c^+ cross sections for each topological variation relative to the central cross section. It can be seen that in the 2-3 and 6-8 GeV/c bins that there is

an apparent shift with respect to the central cross section. After a cut variation study, where the cut parameters were varied individually, it was decided to set the uncertainty on the 2-3 GeV/c bin to 10% . This is based on the value of the RMS divided by the central value from Figure 4.8. The cut parameter driving the trend appears to be the p_{T}^{K} shown in Figure 4.9. An average value of 6% was assigned for bins 3-24 GeV/c to keep the systematic smooth with p_{T}.

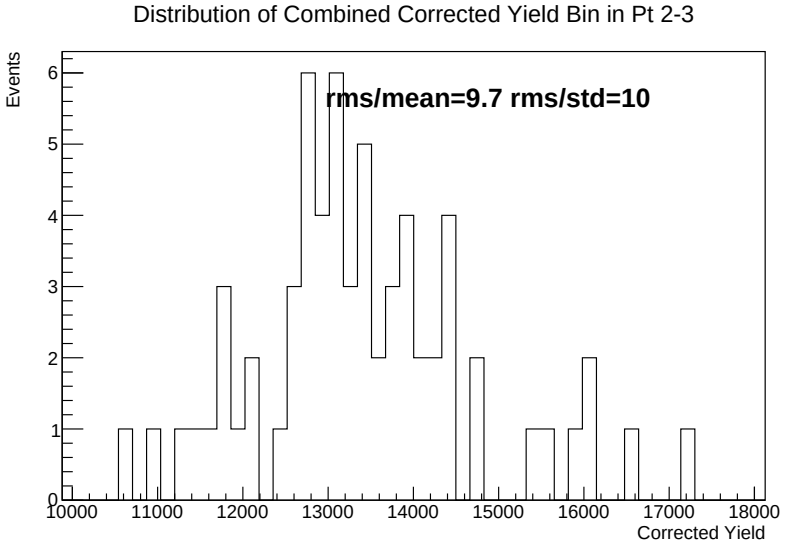

FIGURE 4.8: Distribution of the corrected yield for all 8 cut parameters varied up to a 40% difference in efficiency in 5% intervals for 2< p_{T} <3 GeV/c.

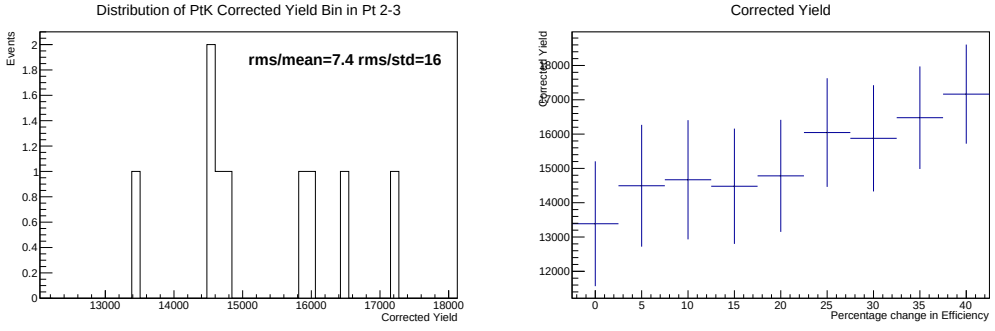

FIGURE 4.9: Variation of Λ_c^+ corrected yield with tighter cuts on the transverse momentum of the Kaon. Indicated in the figure on the right is the RMS/mean of the distribution and RMS divided by the 'central' cross section, given in a percentage of the overall corrected yield.

Systematics for split 4-5 and 5-6 GeV/c bins

The systematic variation of the split bins was determined to be lower than the flat 6% uncertainty that had been assigned previously for the 3-24 GeV/c bins. The flat 6% uncertainty will also be applied to these bins.

4.7.3 PID

This analysis used the Bayesian approach with the maximum probability criteria for the PID. To estimate the systematic uncertainty due to PID, a varying probability threshold cut was placed on the three decay species (p,K,π) using the values in Table 4.3.

Prob. Threshold	Proton	Kaon	Pion
	30	30	30
	40	40	40
	50	50	50
	60	60	60
	70	70	70
	80	80	80

TABLE 4.3: Probability thresholds used.

Figure 4.10 shows the efficiencies for each of the different PID thresholds relative to the efficiency corresponding to the maximum probability criteria. As can be seen in Figure 4.10, when the probability thresholds are high (50-80%) the efficiences fall as a function of p_{T} relative to the maximum probability criteria, and the opposite is true for low thresholds (30-40%). The corresponding Λ_c^+ cross sections for each PID threshold variation are shown relative to the 'central' cross section in Figure 4.11. A large variation seen in the cross section for the 12-24 GeV/c bin is due to low significance in the corresponding invariant mass distribution for that variation, and therefore is ignored when estimating a flat uncertainty. The average of the RMS/mean values for the remaining p_{T} bins gave a flat uncertainty of 5%.

Systematics for split 4-5 and 5-6 GeV/c bins

The systematic variation of the split bins is lower or similar to the flat 5% systematic uncertainty previously assigned for the 4-6 GeV/c p_{T} bin. The 5% unceratainty is also applied to these bins.

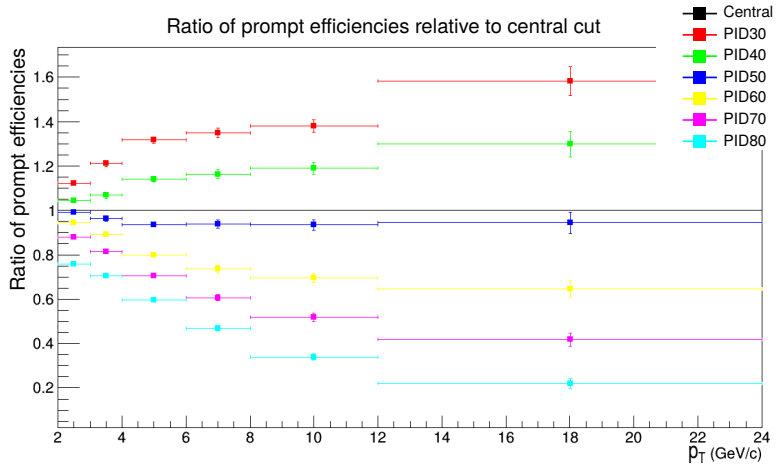

FIGURE 4.10: Ratio of prompt Λ_c^+ PID efficiencies for the different probability thresholds.

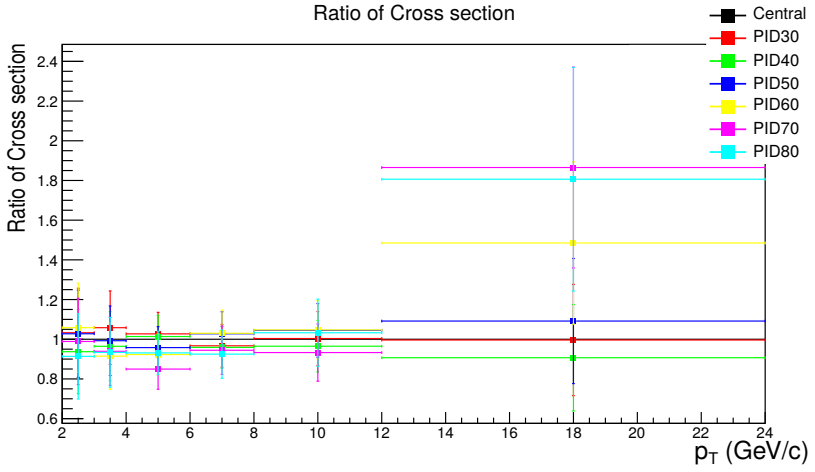

FIGURE 4.11: Ratio of Λ_c^+ cross section for the different PID probability thresholds.

4.7.4 MC p_T shape

Λ_c^+ generated in MC productions are generated with a certain p_T shape, given in PYTHIA. A discrepancy between the shape generated and the true shape of Λ_c^+ p_T shape will produce a systematic error in the calculated efficiences. To estimate this, the efficiency is calculated with the weights determined from different p_T hypotheses as predicted in FONLL. The two weights used are the generated Λ_c^+ p_T shape in MC production LHC13d3 divided by the p_T shape of D mesons in FONLL, and a flat p_T. Note that LHC13d3 is a Monte Carlo production anchored to Run 1 p-Pb collisions at $\sqrt{s_{NN}} = 5.02$ TeV, but since the weights are determined purely from generator-level information, and this analysis is at the same collision energy and in the same acceptance region, the generated Λ_c^+ p_T shape is identical in the Monte Carlo production used for the efficiency correction in this analysis, and thus the weights from the run 1 analysis can be used in this analysis.

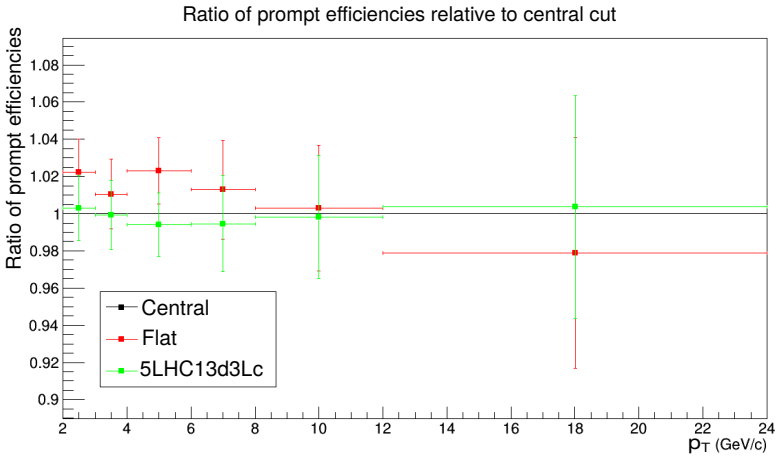

FIGURE 4.12: Ratio of prompt Λ_c^+ efficiencies for the different MC shapes.

Figure 4.12 shows the ratio of these efficiencies calculated using both weights. The variation between the default p_T shape vs the weighted p_T shape is minimal, and changes up to 1%. Even in the extreme case of the flat p_T shape, the variation was never larger than 3%. The variation between 5LHC13d3Lc and the default case was selected as the final systematic uncertainty, and is chosen to be 1% over all p_T.

Systematics for split 4-5 and 5-6 GeV/c bins

The systematic uncertainties shown in Figure 4.13 for the split bins are in agreement with the 1% uncertainty that had been previously assigned for the 4-6 GeV/c bin.

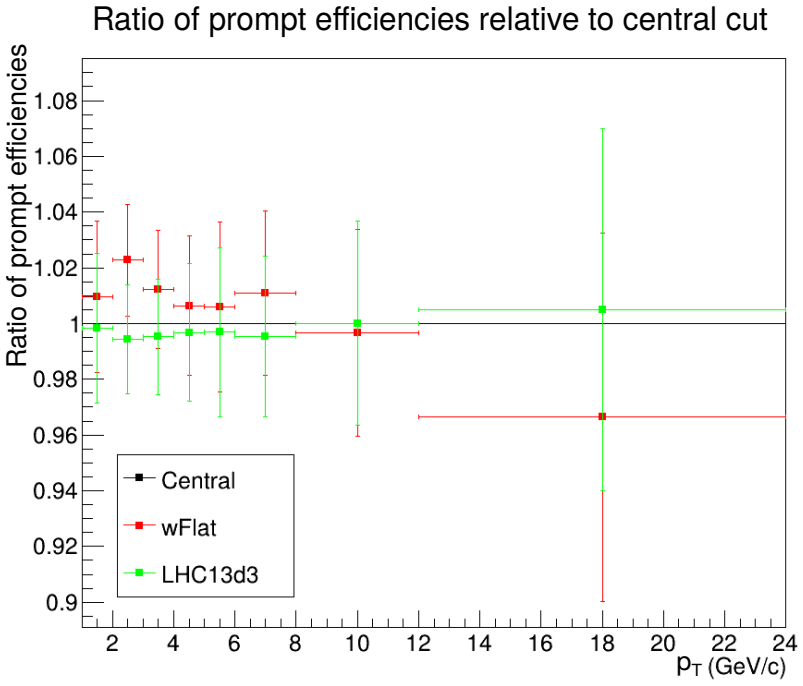

FIGURE 4.13: Ratio of prompt Λ_c^+ efficiencies for the different MC shapes.

4.7.5 Feed-down

The contribution to the uncertainties coming from the subtraction of Λ_c^+ baryons from Λ_b^0 was calculated taking into account the uncertainties in FONLL and the fragmentation fraction.

The method to calculate the feed-down fraction has been updated since the previous measurement of the Λ_b^0, which used a fragmentation fraction determined from e^+e^- collisions, and included a factor of two in the uncertainty to account for measurements of Λ_b^0 production in pp collisions. At that time, fragmentation fractions of beauty hadrons had not been measured at the LHC, but we now take advantage of the recent LHCb measurements [4, 5] to parameterise Λ_b^0 fragmentation in pp collisions. The $b \to \Lambda_b^0$ fragmentation was derived from the LHCb measurements of Λ_b^0-production fraction relative to $\overline{B}^0$ and B^- mesons in pp collisions at $\sqrt{s} = 13$ TeV [4], which indicates that the fraction of b quarks hadronising into a Λ_b^0 baryon is strongly p_T-dependent in the measured range of $4 < p_T < 25$ GeV/c. The method is described in more detail in Section 3.7.2.

The relative fraction of Λ_c^+ (also named f_{prompt}) is given in Figure 4.14. The green band indicates the full uncertainty, which takes into account the uncertainties on both FONLL and fragmentation fraction. The uncertainties range from $+1.1, -1.5\%$ at low p_T to $+1.8, -2.7\%$ at high p_T.

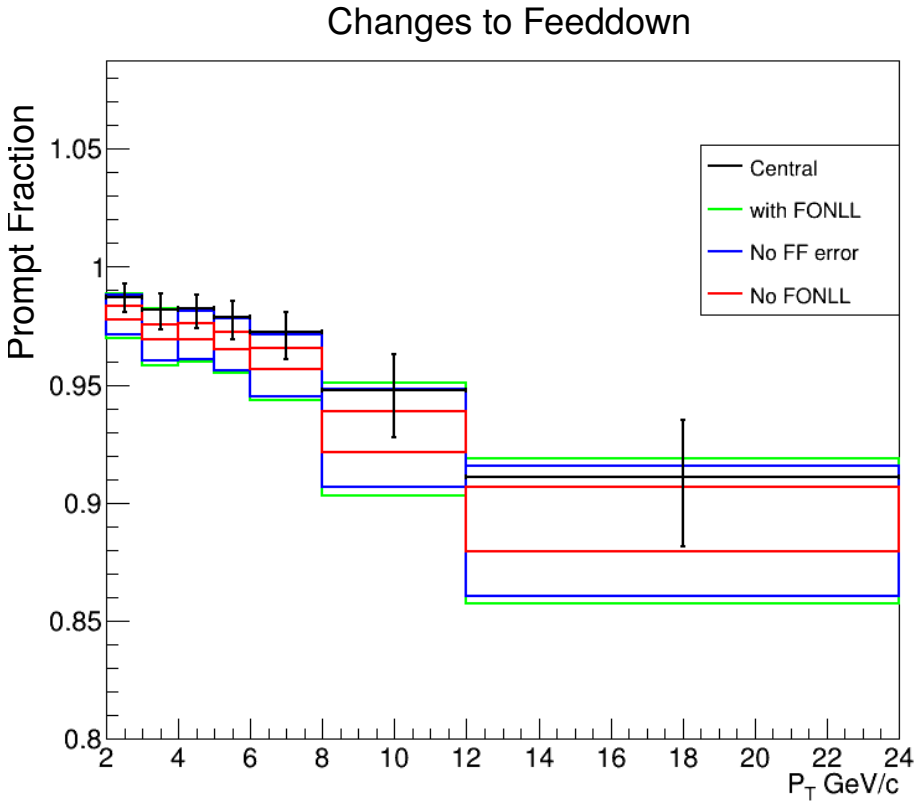

FIGURE 4.14: Relative fraction of Λ_c^+ estimated to be present in the the raw yield using N_b method. the 'Central' points are the values calculated using the Run 1 method, the boxes show the uncertainties of the new method including or not including the uncertainties from FONLL and the fragmentation fraction.

4.7.6 Tracking

Track selection variation

The Λ_c^+ raw yields, efficiency and corrected yields were evaluated with four different sets of track selections. Each variation was compared to the standard value.

1. p_T dependent cut: number of TPC crossed rows > 120 - $(5/p_T)$
2. number of TPC clusters > 0.65 × number of TPC crossed rows
3. number of clusters with TPC dE/dx signal > 0.5 × number of TPC crossed rows
4. ratio of crossed rows over findable clusters in the TPC > 0.9

Matching efficiency

The values for the matching efficiency were previously determined as part of a previous D meson measurement. The systematics from both the track selection variation and matching efficiency were combined taking into account the decay kinematics of the Λ_c^+ to give the values shown in Figure 4.15.

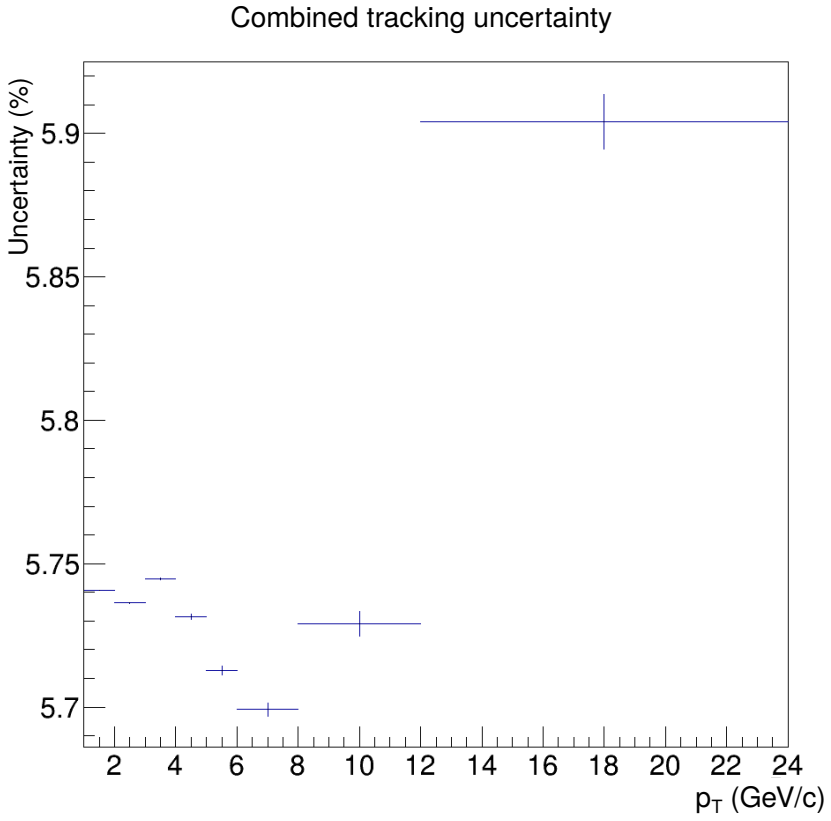

FIGURE 4.15: Combined tracking uncertainties vs p_T.

4.7.7 Summary

The total systematic uncertainties are summarized in Table 4.4, and include:

- Yield extraction: ranged 3-10%
- Cut efficiency: ranged 1-15%
- PID efficiency: considered flat at 5%
- Tracking: flat at 6%
- MC p_{T} Shape: ranged 0-1%
- Feed-down: asymmetric

p_T interval (GeV/c)	2-3	3-4	4-5	5-6	6-8	8-12	12-24
Yield extraction (%)	8	6	6	10	6	6	10
Cut efficiency (%)	10	6	6	6	6	6	6
PID (%)	5 (flat uncertainty)						
Tracking (%)	6	6	6	6	6	6	6
MC p_T Shape (%)	1	1	1	1	1	1	1
Feed-down (%)	+0.9 -1.3	+1.1 -1.6	+1.5 -2.0	+1.9 -2.7	+2.2 -3.4	+2.9 -3.9	+1.8 -2.7
Branching fraction (%)	+5.1						
Luminosity (%)	3.7						

TABLE 4.4: Summary of the systematic uncertainties assigned to each source.

References

[1] *ALISW/AliPhysics: Alice Analysis Repository.* URL: https://github.com/alisw/AliPhysics.

[2] Jaroslav Adam et al. "Particle identification in ALICE: a Bayesian approach". In: *Eur. Phys. J. Plus* 131.5 (2016), p. 168. DOI: 10.1140/epjp/i2016-16168-5. arXiv: 1602.01392 [physics.data-an].

[3] Andreas Hoecker et al. "TMVA: Toolkit for Multivariate Data Analysis". In: *PoS* ACAT (2007), p. 040. arXiv: physics/0703039.

[4] Roel Aaij et al. "Measurement of b hadron fractions in 13 TeV pp collisions". In: *Phys. Rev.* D100.3 (2019), p. 031102. DOI: 10.1103/PhysRevD.100.031102. arXiv: 1902.06794 [hep-ex].

[5] R. Aaij et al. "Study of the production of Λ_b^0 and $\overline{B}^0$ hadrons in pp collisions and first measurement of the $\Lambda_b^0 \to J/\psi p K^-$ branching fraction". In: *Chin. Phys.* C40.1 (2016), p. 011001. DOI: 10.1088/1674-1137/40/1/011001. arXiv: 1509.00292 [hep-ex].

Chapter 5

Λ_{c}^{+} production in pp and in p–Pb collisions at $\sqrt{s_{\mathrm{NN}}} = 5.02$ TeV

5.1 Declaration

This published work has been included in the place of a standard format chapter. My specific contribution to this work was the analysis of the $\Lambda_{\mathrm{c}}^{+} \rightarrow \mathrm{pK}^{-}\pi^{+}$ channel in pp and p–Pb collisions at $\sqrt{s_{\mathrm{NN}}} = 5.02$ TeV using data taken during LHC Run 2. I was part of the paper commitee who wrote the paper on behalf of the ALICE collaboration. The paper commitee was comprised of the same five analysers who wrote the analysis notes.

Permission to include this journal article [1] entitled "Λ_{c}^{+} production in pp and p–Pb collisions at $\sqrt{s_{\mathrm{NN}}} = 5.02$ TeV", published in Physical Review C, CERN-EP-2020-218, arXiv:2011.06079, was given on behalf of the ALICE Collaboration co-authors by the Physics Coordinator and Editorial Board co-chairs. Their consent declaration can be found in Appendix A.

5.1.1 APS Statement of Copyright

5.2 Abstract

The production cross section of prompt Λ_c^+ charm baryons was measured with the ALICE detector at the LHC at midrapidity in proton-proton (pp) and proton-lead (p–Pb) collisions at a centre-of-mass energy per nucleon pair of $\sqrt{s_{\rm NN}} = 5.02$ TeV. The Λ_c^+ and $\overline{\Lambda}_c^-$ baryons were reconstructed in the hadronic decay channels $\Lambda_c^+ \rightarrow {\rm pK}^-\pi^+$ and $\Lambda_c^+ \rightarrow {\rm pK}_S^0$ and respective charge conjugates. The measured differential cross sections as a function of transverse momentum ($p_{\rm T}$) and the $p_{\rm T}$-integrated Λ_c^+ production cross section in pp and in p–Pb collisions are presented. The Λ_c^+ nuclear modification factor ($R_{\rm pPb}$), calculated from the cross sections in pp and in p–Pb collisions, is presented and compared with the $R_{\rm pPb}$ of D mesons. The $\Lambda_c^+/{\rm D}^0$ ratio is also presented and compared with the light-flavour baryon-to-meson ratios ${\rm p}/\pi$ and $\Lambda/{\rm K}_S^0$, and measurements from other LHC experiments. The results are compared to predictions from model calculations and Monte Carlo event generators.

5.3 Introduction

In hadronic collisions, heavy quarks (charm and beauty) are created predominantly in hard scattering processes, and therefore the measurement of charm and beauty hadron production is a powerful test of perturbative quantum chromodynamics (pQCD) calculations. Theoretical predictions based on the QCD factorisation approach describe the heavy-flavour hadron production cross section as a convolution of parton distribution functions, parton hard-scattering cross sections, and fragmentation functions. The measurements of D- and B-meson production cross sections in pp collisions at centre-of-mass energies between 200 GeV and 13 TeV at RHIC [2], Tevatron [3, 4, 5], and the LHC [6, 7, 8, 9, 10] are generally described within uncertainties by perturbative calculations at next-to-leading order with next-to-leading-log resummation, such as the general-mass variable-flavour-number scheme (GM-VFNS [11, 12]) and fixed-order next-to-leading-log (FONLL [13, 14]), over a wide range of transverse momentum ($p_{\rm T}$).

The measurement of the relative production of different heavy-flavour hadron species is also sensitive to the charm- and beauty-quark fragmentation and heavy-flavour hadron formation processes. In particular, measurements of the Λ_c^+ production cross section relative to D mesons provide insight into the hadronisation

of charm quarks into baryons. A measurement of Λ_c^+ baryon production at midrapidity in pp collisions at $\sqrt{s} = 7$ TeV was reported by the ALICE Collaboration in [15]. The Λ_c^+/D^0 ratio was found to be substantially higher than previous measurements at lower energies in electron-positron (e^+e^-) [16, 17, 18, 19] and electron-proton (e^-p) [20, 21, 22] collisions, challenging the assumption that the probabilities for a charm quark to hadronise into a specific charm hadron (fragmentation fractions) are universal among different collision systems [23]. In addition, the Λ_c^+/D^0 ratio was compared with predictions from several Monte Carlo (MC) generators, which implement different fragmentation processes, such as the formation of strings (PYTHIA[24, 25]), ropes (DIPSY[26, 27]), or baryonic clusters (HERWIG[28]), where the fragmentation parameters for these simulations are tuned to previous e^+e^- and e^-p collision measurements. These predictions significantly underestimate the Λ_c^+/D^0 ratio, although the prediction from PYTHIA 8 that includes additional colour reconnection mechanisms [25] shows a p_T trend that is qualitatively similar to the measured trend. The CMS Collaboration has measured the Λ_c^+/D^0 ratio in pp collisions at $\sqrt{s} = 5.02$ TeV [29], which is consistent with predictions from PYTHIA 8 with additional colour reconnection mechanisms. Λ_c^+ production was also measured by the LHCb Collaboration in pp collisions at $\sqrt{s} = 7$ TeV at forward rapidity [30], and the Λ_c^+/D^0 ratio was found to be lower than that measured by ALICE at midrapidity [15]. Calculations of the charm-hadron production cross section based on the k_T-factorisation approach with gluon distributions obtained on the basis of novel collinear gluon distribution functions and Peterson fragmentation functions [31] are unable to simultaneously describe the ALICE and LHCb measurements using the same set of input parameters, suggesting that the measurements are difficult to explain within the independent parton fragmentation scheme. It is also important to note here that the magnitude of the relative production of Λ_b^0 baryons and beauty mesons in pp collisions measured by LHCb [32, 33, 34] and CMS [35] offer further hints that fragmentation fractions in the beauty sector differ between pp and e^+e^-/e^-p collisions.

Measurements in pp collisions also provide a necessary reference for studies in heavy-ion collisions, where the study of charm production is a powerful tool to investigate the quark–gluon plasma (QGP)[36, 37, 38], the deconfined state of matter created under extreme energy densities. In particular, the charm baryon-to-meson ratio in heavy-ion collisions is sensitive to the charm hadronisation mechanisms after the QGP phase. It is expected that a significant fraction of

low- and intermediate-momentum charm quarks hadronise via recombination (coalescence) with light (anti) quarks from the medium[39, 40], which would manifest as an enhancement of the Λ_c^+/D^0 ratio with respect to pp collisions. The Λ_c^+/D^0 ratio has been measured by STAR [41] in Au–Au collisions at $\sqrt{s_{NN}} = 200$ GeV, and by ALICE [42] and CMS [29] in Pb–Pb collisions at $\sqrt{s_{NN}} = 5.02$ TeV. These measurements offer constraints to different model calculations which implement contributions to hadronisation via quark recombination [43, 44, 45, 46].

The interpretation of the results obtained in heavy-ion collisions also requires detailed studies in p–Pb collisions in order to assess so-called cold nuclear matter (CNM) effects in the initial and final states, which could modify the production of heavy-flavour hadrons. In the initial state, the quark and gluon distributions are modified in bound nucleons compared to free nucleons, depending on the fractional longitudinal parton momentum x and the atomic mass number [47, 48]. The most relevant CNM effect at LHC energies is shadowing, i.e. a decrease of the parton densities in the small-x region. This effect is due to high phase-space densities of low-x partons and can be described in collinear pQCD by means of parametrisations of the modification of the nuclear parton distribution functions (nPDFs) [49, 50]. In the case of saturation of the parton phase-space, the Colour Glass Condensate (CGC) effective theory [51, 52, 53, 54, 55] offers an appropriate theoretical framework to describe the modification of the nPDFs. Moreover, partons can lose energy in the initial stages of the collisions due to initial-state radiation [56], or experience transverse momentum broadening due to multiple soft collisions before the heavy-quark pair is created in the hard scattering [57, 58, 59]. The modification of parton distributions in the nucleus and energy loss in the initial state can affect the yields and the momentum distributions of the produced hadrons, mainly at low momenta. In addition to initial-state effects, final-state effects such as hadronic rescattering [60] or the possible formation of a small QGP droplet [61, 62] can also modify the hadron yields and momentum distributions. Several measurements in high-multiplicity pp and p–Pb collisions, such as long-range correlations of charged hadrons [63, 64, 65, 66], and the enhancement of baryon-to-meson ratios in the light-flavour sector (p/π and Λ/K) [67, 68, 69], exhibit a similar behaviour as that observed in Pb–Pb collisions, suggesting that these findings may have similar physical origins in pp, p–A, and A–A collisions [70]. Λ_c^+ production was previously measured at midrapidity by ALICE in p–Pb collisions at $\sqrt{s_{NN}} = 5.02$ TeV [15]. The Λ_c^+/D^0 ratio was found to be compatible within the uncertainties with that measured in pp collisions at

$\sqrt{s} = 7$ TeV. The nuclear modification factor, $R_{\rm pPb}$, was found to be compatible with unity, as well as with models that implement cold nuclear matter effects via nPDF calculations [71] or assume the production of a deconfined medium in p–Pb collisions [61]. The LHCb Collaboration has measured the Λ_c^+/D^0 ratio at forward rapidity in p–Pb collisions at $\sqrt{s_{\rm NN}} = 5.02$ TeV [72] to be larger than that in pp collisions at forward rapidity [30] but smaller than the ALICE measurements in pp and p–Pb collisions at midrapidity [15].

Recent attempts have been made to model charm-baryon production in pp and p–Pb collisions. A framework based on a statistical hadronisation model [73], which takes into account an increased set of charm-baryon states beyond those listed by the Particle Data Group (PDG), is able to reproduce the Λ_c^+/D^0 ratios measured by ALICE in the pp and p–Pb collision systems, although it overestimates the LHCb measurement in pp collisions. A model implementing hadronisation via recombination [74, 75], where the $p_{\rm T}$ distributions of light and charm quarks and antiquarks are inputs of the model and the relative production of single-charm baryons to single-charm mesons is treated as a free parameter, is able to reproduce the $p_{\rm T}$ dependence of the Λ_c^+/D^0 ratio measured by ALICE at central rapidity in pp and p–Pb collisions, and by LHCb at forward rapidity in p–Pb collisions. While models implementing different approaches to Λ_c^+ production are effective in describing the measured Λ_c^+/D^0 ratio and $R_{\rm pPb}$, the large statistical and systematic uncertainties of the current measurements do not provide the discriminating power needed to differentiate between the various models. Therefore, more precise measurements are crucial in order to constrain predictions.

This paper presents the measurement of the $p_{\rm T}$-differential production cross section of charm Λ_c^+ baryons in pp collisions in the rapidity interval $|y| < 0.5$ and in p–Pb collisions in $-0.96 < y < 0.04$ at $\sqrt{s_{\rm NN}} = 5.02$ TeV, performed with the ALICE detector at the LHC. The rapidity y here and throughout this paper is defined in the centre-of-mass system, and in p–Pb collisions the rapidity sign is positive in the p-going direction. The ratio of the production cross sections of Λ_c^+ baryons and D^0 mesons, Λ_c^+/D^0, and the nuclear modification factor $R_{\rm pPb}$ are also presented. Finally, the Λ_c^+ production cross section per unit of rapidity at midrapidity is computed by integrating the $p_{\rm T}$-differential Λ_c^+ production cross section after extrapolating down to $p_{\rm T} = 0$, and the $p_{\rm T}$-integrated Λ_c^+/D^0 ratios are presented. Two hadronic decay channels of Λ_c^+ were studied: $\Lambda_c^+ \rightarrow pK^-\pi^+$ and $\Lambda_c^+ \rightarrow pK_S^0$. Different analysis strategies were implemented, taking advantage

of the methods used in previous analyses for the hadronic decays of D mesons [76, 77, 78, 79, 80, 81] and Λ_c^+ baryons [15]. With respect to our previous measurement of Λ_c^+ production [15], the p_T reach was extended, the overall uncertainties of the measurements were reduced, and the analysis was performed in finer p_T intervals. The precision of the measurement of the nuclear modification factor R_{pPb} was improved with respect to the previously published result thanks to the larger data samples as well as a pp reference measured at the same centre-of-mass energy.

The measurements are performed as the average of the particle and antiparticle cross sections, and so both Λ_c^+ and $\overline{\Lambda}_c^-$ baryons are referred to collectively as Λ_c^+ in the following. In all measurements the production cross section of prompt Λ_c^+ is reported, i.e. Λ_c^+ from direct hadronisation of a charm quark or from decays of directly produced excited charm states. For the centre-of-mass energy of pp collisions the simplified notation $\sqrt{s}$ is used throughout this paper.

It is noted that the Λ_c^+/D^0 baryon-to-meson ratio is the focus of a dedicated letter [82], and this document presents a more detailed description of the analysis procedure as well as supplementary results.

5.4 Experimental setup and data samples

The ALICE apparatus is composed of a central barrel, consisting of a set of detectors for particle reconstruction and identification covering the midrapidity region, a muon spectrometer at forward rapidity and various forward and backward detectors for triggering and event characterisation. The central barrel detectors cover the full azimuth in the pseudorapidity interval $|\eta| < 0.9$ and are embedded in a large solenoidal magnet that provides a $B = 0.5$ T field parallel to the beam direction (z-axis in the ALICE reference frame). A comprehensive description and overview of the typical performance of the detectors in pp and p–Pb collisions can be found in [83, 84].

The tracking and particle identification capabilities of the ALICE central barrel detectors were exploited to reconstruct the Λ_c^+ decay products at midrapidity. The Inner Tracking System (ITS), consisting of three subdetectors, the Silicon Pixel Detector (SPD), the Silicon Drift Detector (SDD), and the Silicon Strip Detector (SSD), each made of two concentric layers, allows for a precise determination of the track impact parameter (the distance of closest approach between the track and the primary vertex of the collision) in the transverse plane with

a resolution better than 75 μm for tracks with $p_T > 1$ GeV/c [85]. The Time Projection Chamber (TPC) is the main tracking detector of the experiment [86]. It provides up to 159 space points to reconstruct the charged-particle trajectory, and provides charged-particle identification (PID) via the measurement of the specific energy loss dE/dx. The particle identification capabilities are extended by the Time-of-Flight (TOF) detector, which is used to measure the flight time of charged particles from the interaction point. The TOF detector is an array of Multi-gap Resistive Plate Chambers. It measures the particle arrival time at the detector with a resolution of about 80 ps. The start time of the collision is obtained for each event either using the TOF detector, the T0 detector, or a combination of the two [87]. The T0 detector consists of two arrays of Cherenkov counters, located on both sides of the interaction point, covering the pseudo-rapidity regions $4.61 < \eta < 4.92$ and $-3.28 < \eta < -2.97$, respectively. The time resolution of the T0 detector in pp and p–Pb collisions is about 50 ps for events in which a measurement is made on both sides of the interaction point [87]. The V0 detector system, used for triggering and event selection, consists of two scintillator arrays covering the full azimuth in the pseudorapidity intervals $2.8 < \eta < 5.1$ and $-3.7 < \eta < -1.7$ ([83], Section 5.1). The Zero Degree Calorimeter (ZDC), used for offline event rejection in p–Pb collisions, consists of two sets of neutron and proton calorimeters positioned along the beam axis on both sides of the ALICE apparatus, about 110 m from the interaction point ([83], Section 5.4).

The results presented in this paper were obtained from the analysis of the LHC Run 2 data samples collected from pp collisions at $\sqrt{s} = 5.02$ TeV in 2017 and p–Pb collisions at $\sqrt{s_{NN}} = 5.02$ TeV in 2016. The proton–nucleon centre-of-mass system in p–Pb collisions is shifted in rapidity by $\Delta y = 0.465$ in the Pb-going direction (negative rapidity) due to the asymmetric beam energies of 4 TeV for protons and 1.59 TeV per nucleon for Pb nuclei. The analyses used events recorded with a minimum bias (MB) trigger, which was based on coincident signals from the V0 detectors in both pp and p–Pb collisions. In order to remove background from beam–gas collisions and other machine-induced backgrounds, in pp collisions the events were further selected offline based on the correlation between the numbers of clusters and track segments reconstructed in the SPD, and V0 timing information. The latter was also used for the p–Pb analysis, together with the timing from the ZDC. In order to maintain a uniform ITS acceptance in pseudorapidity, only events with a z-coordinate of the reconstructed vertex position within 10 cm from the nominal interaction point were analysed.

Events with multiple interaction vertices due to pileup from several collisions were removed using an algorithm based on tracks reconstructed with the TPC and ITS detectors [84]. Using these selection criteria, approximately one billion MB-triggered pp events were analysed, corresponding to an integrated luminosity of $\mathcal{L}_{\rm int} = 19.5$ nb^{-1}($\pm$2.1% [88]), while approximately 600 million MB-triggered p–Pb events were selected, corresponding to $\mathcal{L}_{\rm int} = 287$ μb^{-1} ($\pm$3.7% [89]).

5.5 Λ_c^+ analysis overview and methods

The analysis was performed using similar techniques to those reported in [15]. Λ_c^+ baryons were reconstructed in two hadronic decay channels: $\Lambda_c^+ \rightarrow {\rm pK}^-\pi^+$ (branching ratio, BR = 6.28 ± 0.33%), and $\Lambda_c^+ \rightarrow {\rm pK}^0_{\rm S}$ (BR = 1.59 ± 0.08%), followed by the subsequent decay ${\rm K}^0_{\rm S} \rightarrow \pi^+\pi^-$ (BR = 69.2 ± 0.05%) [90]. For the former, the Λ_c^+ decays to the ${\rm pK}^-\pi^+$ final state via four channels: $\Lambda_c^+ \rightarrow {\rm p}\overline{\rm K}^{*0}(892)$, $\Lambda_c^+ \rightarrow \Delta^{++}(1232){\rm K}^-$, $\Lambda_c^+ \rightarrow \Lambda(1520)\pi^+$, and the non-resonant $\Lambda_c^+ \rightarrow {\rm pK}^-\pi^+$ decay. As these channels are indistinguishable in the analysis, all four are considered together.

The selection of candidates was performed using a combination of kinematical, geometrical, and PID selections. The selection criteria were tuned on Monte Carlo simulations in order to maximise the statistical significance in each $p_{\rm T}$ interval. Λ_c^+ candidates were reconstructed by combining reconstructed tracks with $|\eta| < 0.8$ and at least 70 reconstructed space points in the TPC. For all decay products in the $\Lambda_c^+ \rightarrow {\rm pK}^-\pi^+$ analysis and for the proton-candidate tracks in the $\Lambda_c^+ \rightarrow {\rm pK}^0_{\rm S}$ analysis, at least one cluster was required in either of the two SPD layers. The PID selections for all analyses were performed utilising the Bayesian method for combining the TPC and TOF signals, as described in [91]. The Bayesian method entails the use of priors, an *a priori* probabilitiy of measuring a given particle species, which are determined using measured particle abundances. Where possible, the TPC and TOF signals were combined; however, if the TOF signal was absent for a given track, the TPC signal alone was used. For the $\Lambda_c^+ \rightarrow {\rm pK}^0_{\rm S}$ analysis in p–Pb collisions, a machine learning approach with Boosted Decision Trees (BDTs) was applied to select Λ_c^+ candidates, using the Toolkit for Multivariate Data Analysis (TMVA) [92].

The detector acceptance for Λ_c^+ baryons varies as a function of rapidity, in particular falling steeply to zero for $|y| > 0.5$ at low $p_{\rm T}$, and $|y| > 0.8$ for $p_{\rm T} >$

$5\,\mathrm{GeV}/c$. For this reason, a fiducial acceptance selection was applied on the rapidity of candidates, $|y_{\mathrm{lab}}| < y_{\mathrm{fid}}(p_{\mathrm{T}})$, where y_{fid} increases smoothly from 0.5 to 0.8 in $0 < p_{\mathrm{T}} < 5$ GeV/c and $y_{\mathrm{fid}} = 0.8$ for $p_{\mathrm{T}} > 5\,\mathrm{GeV}/c$ [76].

For the $\Lambda_c^+ \to \mathrm{pK}^-\pi^+$ analysis, candidates were formed by combining triplets of tracks with the correct configuration of charge sign. For this decay channel, the high-resolution tracking and vertexing information provided by the ITS and TPC allows the interaction point (primary vertex) and the reconstructed decay point of the Λ_c^+ candidate (secondary vertex) to be distinguished from one another, despite the short decay length of the Λ_c^+ ($c\tau = 60.7\,\mu$m [90]). Once the secondary vertex was computed from the three tracks forming the Λ_c^+ candidate, selections were applied on variables related to the kinematic properties of the decay, the quality of the reconstructed vertex, and the displaced decay-vertex topology. These variables comprise the transverse momenta of the decay products; the quadratic sum of the distance of closest approach of each track to the secondary vertex; the decay length of the Λ_c^+ candidate (separation between the primary and secondary vertices); and the cosine of the pointing angle between the Λ_c^+ candidate flight line (the vector that connects the primary and secondary vertices) and the reconstructed momentum vector of the candidate. Pions, kaons, and protons were identified using the *maximum-probability* Bayesian PID approach [91], where a probability is assigned to each track for every possible species based on the TPC and TOF signals and the identity of the track is taken to be the species with the highest probability value. This approach allows for a higher-purity sample to be selected, reducing the large level of combinatorial background and facilitating the signal extraction.

The $\Lambda_c^+ \to \mathrm{pK}_S^0$ analysis started from a $\mathrm{K}_S^0 \to \pi^+\pi^-$ candidate, which is reconstructed as a pair of opposite-sign charged tracks forming a neutral decay vertex displaced from the primary vertex (a V^0 candidate). This V^0 candidate was paired with a proton-candidate track originating from the primary vertex to form a Λ_c^+ candidate. Two strategies were then used to select Λ_c^+ candidates in pp and p–Pb collisions. In pp collisions, the analysis was based on rectangular selection criteria. The V^0 candidate was required to have an invariant mass compatible with the K_S^0 mass from the PDG [90] within 8 (20) MeV/c^2 at low (high) p_{T}, corresponding to one or two times the resolution of the K_S^0 invariant mass, depending on the p_{T} interval and the collision system. The V^0 candidates were selected based on the p_{T} and impact parameter of the decay pions to the K_S^0 decay vertex, and the cosine of the pointing angle between the V^0 flight line and its

reconstructed momentum. Proton-candidate tracks were selected based on their p_T, their impact parameter to the primary vertex, the number of reconstructed TPC clusters, and a cluster being present on at least one of the two SPD layers. Particle identification was performed on the proton-candidate track, first using a loose $|n_\sigma| < 3$ pre-selection on the TPC response, where n_σ corresponds to the difference between the measured and expected dE/dx for a given particle species, in units of the resolution. This was followed by a strict requirement that the Bayesian posterior probability for the track to be a proton must be greater than 80%.

In p–Pb collisions, an approach using BDTs was used for the $\Lambda_c^+ \to pK_S^0$ decay. The BDT algorithm provides a classification tree that maps simulated Λ_c^+ candidates to a single BDT response variable aiming to maximise the separation between signal and background candidates. The mapping function is then applied on a real data sample in which the true identities of particles are unknown, followed by the application of selections on the BDT response. Candidates were initially filtered using an $|n_\sigma{}^{\mathrm{TPC}}| < 3$ PID selection on the proton candidate. Independent BDTs were trained for each p_T interval in the analysis. The training was performed on samples of simulated events including a detailed description of the experimental apparatus and the detector response. The training sample for signal candidates was taken from a simulation of pp events containing charm hadrons generated using PYTHIA 6.4.25 [93] with the Perugia2011 tune [94], embedded into an underlying p–Pb collision generated with HIJING 1.36 [95]. The background candidates were taken from the HIJING simulation. The variables that were used in the training were the Bayesian PID probability of the proton-candidate track to be a proton, the p_T of the proton candidate, the invariant mass and $c\tau$ of the K_S^0 candidate, and the impact parameters of the V^0 and the proton-candidate track with respect to the primary vertex. The MC samples used for the efficiency calculation were different from those used in the training. The selection on the BDT response was tuned in each p_T interval to maximise the expected statistical significance, which is estimated using i) the signal obtained from the generated Λ_c^+ yield multiplied by the selection efficiency of the trained model and ii) the background estimated from preselected data multiplied by the background rejection factor from the BDT. The BDT analysis was cross checked with an independent analysis using rectangular selection criteria, and the two results were found to be fully consistent within the experimental uncertainties.

Signal extraction for all analyses was performed by means of a fit to the invariant mass distributions of candidates in each p_T interval under study. A Gaussian function was used to model the signal peak and an exponential function was used to model the background. Due to the small signal-to-background ratio, the standard deviation of the Gaussian signal function was fixed to the value obtained from simulations in order to improve the fit stability. In pp collisions, a Λ_c^+ signal could be extracted for the $\Lambda_c^+ \to pK^-\pi^+$ and $\Lambda_c^+ \to pK_S^0$ analyses in the range $1 < p_T < 12$ GeV. In p–Pb collisions a Λ_c^+ signal was extracted for the $\Lambda_c^+ \to pK_S^0$ analysis in the range $1 < p_T < 24$ GeV/c, and for the $\Lambda_c^+ \to pK^-\pi^+$ analysis in the range $2 < p_T < 24$ GeV/c, as the larger combinatorial background in the $\Lambda_c^+ \to pK^-\pi^+$ channel limits the low-p_T reach. A selection of the invariant mass distributions with their corresponding fit functions is displayed in Fig. 5.1 for different p_T intervals, decay channels, and collision systems.

5.6 Corrections

The p_T-differential cross section of prompt Λ_c^+-baryon production was obtained for each decay channel as

$$\frac{d^2\sigma^{\Lambda_c^+}}{dp_T dy} = \frac{1}{2c_{\Delta y} \times \Delta p_T} \times \frac{1}{BR} \times \frac{f_{prompt} \times N^{\Lambda_c}_{|y|<y_{fid}}}{(A \times \varepsilon)_{prompt}} \times \frac{1}{\mathcal{L}_{int}}, \tag{5.1}$$

where N^{Λ_c} is the raw yield (sum of particles and antiparticles) in a given p_T interval with width Δp_T, f_{prompt} is the fraction of the raw yield from prompt Λ_c^+, BR is the branching ratio for the considered decay mode, and $\mathcal{L}_{int}$ is the integrated luminosity. $(A \times \varepsilon)$ is the product of detector acceptance and efficiency for prompt Λ_c^+ baryons, where ϵ accounts for the reconstruction of the collision vertex, the reconstruction and selection of the tracks of the Λ_c^+ decay products, and the Λ_c^+-candidate selection. The correction factor for the rapidity coverage, $c_{\Delta y}$, was computed as the ratio between the generated Λ_c^+-baryon yield in $|y_{lab}| < y_{fid}(p_T)$ and that in $|y_{lab}| < 0.5$, where the Λ_c^+-baryon rapidity shape was taken from FONLL pQCD calculations. The factor 2 in the denominator of Eq. 5.1 takes into account that the raw yield includes both particles and antiparticles, while the cross section is given for particles only and is computed as the average of Λ_c^+ and $\overline{\Lambda}_c^-$.

The correction factor $(A \times \varepsilon)$ was obtained following the same approach as discussed in [79]. The correction factors were obtained from simulations in which

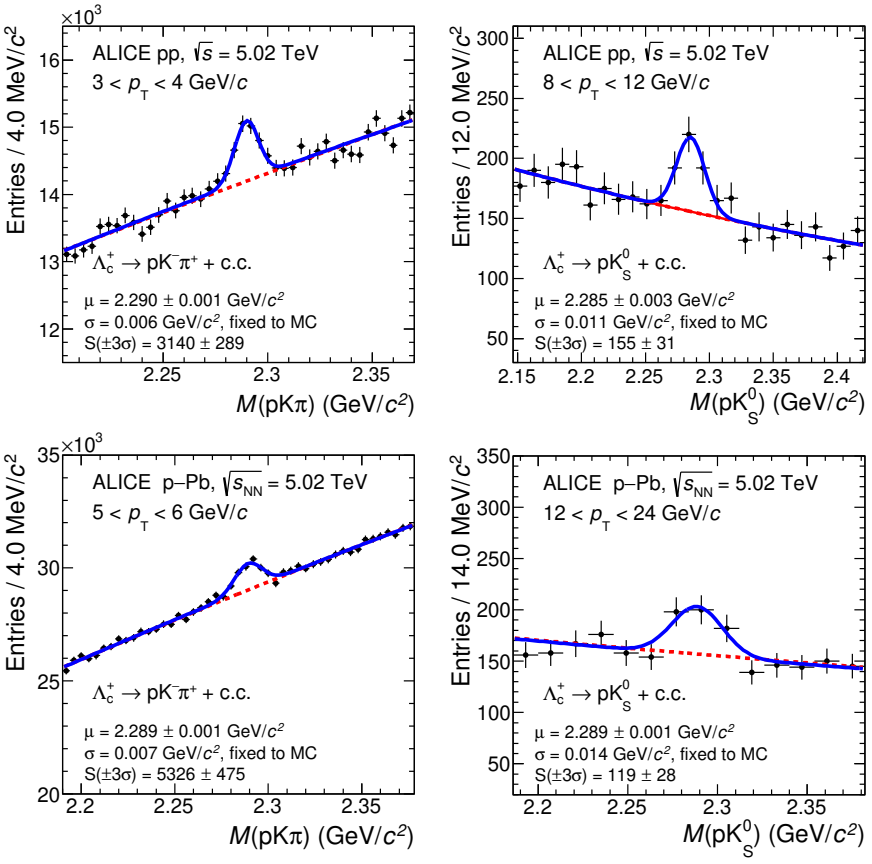

FIGURE 5.1: Invariant mass distributions of Λ_c^+ candidates in different p_T intervals, collision systems, and decay channels, with the corresponding fit functions. Top-left: $\Lambda_c^+ \to pK^-\pi^+$ for $3 < p_T < 4$ GeV/c in pp collisions; top-right: $\Lambda_c^+ \to pK_S^0$ for $8 < p_T < 12$ GeV/c in pp collisions; bottom-left: $\Lambda_c^+ \to pK^-\pi^+$ for $5 < p_T < 6$ GeV/c in p–Pb collisions; bottom-right: $\Lambda_c^+ \to pK_S^0$ with BDT analysis in $12 < p_T < 24$ GeV/c in p–Pb collisions. The dashed lines represent the fit to the background and the solid lines represent the total fit function.

the detector and data taking conditions of the corresponding data samples were reproduced. PYTHIA 6.4.25 and PYTHIA 8.243 [96] were used to simulate pp collisions. For p–Pb collisions, a pp event containing heavy-flavour signals was generated with PYTHIA 6 and HIJING was used to simulate the underlying background event.

The $(A \times \varepsilon)$ was computed separately for prompt and non-prompt Λ_c^+. The $\Lambda_c^+ \to pK^-\pi^+$ decay channel includes not only the direct (non-resonant) decay mode, but also three resonant channels, as explained in Section 5.5. Due to the kinematical properties of these decays, the acceptance and efficiency of each decay mode is different and the final correction was determined as a weighted average

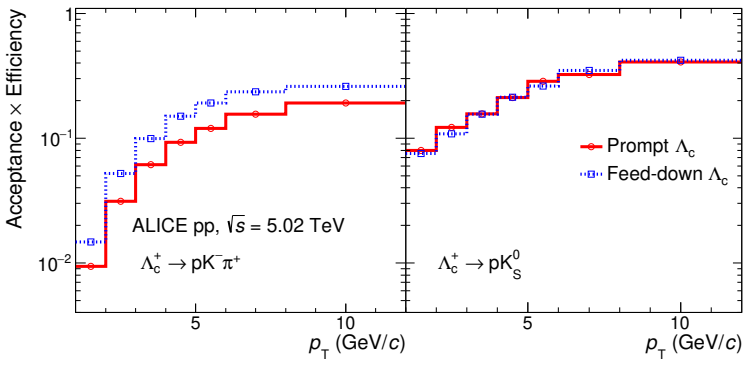

FIGURE 5.2: Product of detector acceptance and efficiency for Λ_c^+ baryons in pp collisions at $\sqrt{s} = 5.02$ TeV, as a function of p_T. From left to right: $\Lambda_c^+ \to pK^-\pi^+$ and $\Lambda_c^+ \to pK_S^0$. The solid lines correspond to the $(A \times \varepsilon)$ for prompt Λ_c^+, while the dotted lines represent $(A \times \epsilon)$ for Λ_c^+ baryons originating from beauty-hadron decays. The statistical uncertainties are smaller than the marker size.

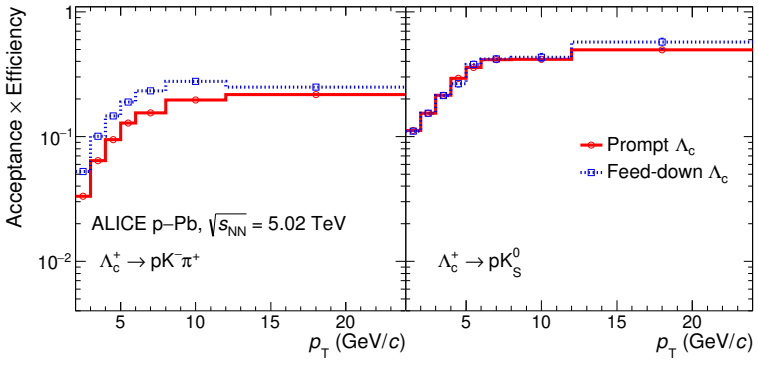

FIGURE 5.3: Product of detector acceptance and efficiency for Λ_c^+ baryons in p–Pb collisions at $\sqrt{s_{NN}} = 5.02$ TeV, as a function of p_T. From left to right: $\Lambda_c^+ \to pK^-\pi^+$ and $\Lambda_c^+ \to pK_S^0$. The solid lines correspond to the $(A \times \varepsilon)$ for prompt Λ_c^+, while the dotted lines represent $(A \times \epsilon)$ for Λ_c^+ baryons originating from beauty-hadron decays. The statistical uncertainties are smaller than the marker size.

of the $(A \times \varepsilon)$ values of the four decay channels with the relative branching ratios as weights.

Figures 5.2 and 5.3 show the product of $(A \times \varepsilon)$ for Λ_c^+ baryons with $|y| < y_{\text{fid}}$ in pp and p–Pb collisions as a function of p_T for the $\Lambda_c^+ \to pK^-\pi^+$ (left panel) and $\Lambda_c^+ \to pK_S^0$ (right panel) decay channels. The higher $(A \times \varepsilon)$ for Λ_c^+ from beauty-hadron decays in the $\Lambda_c^+ \to pK^-\pi^+$ decay channel is due to the geometrical selections on the displaced decay-vertex topology, which enhance the non-prompt component because of the relatively longer lifetime of the beauty

hadrons compared to prompt Λ_c^+. For the $\Lambda_c^+ \to pK_S^0$ analyses, the $(A \times \varepsilon)$ of prompt and non-prompt Λ_c^+ are compatible, as selections based on the displaced decay-vertex topology are not applied.

Contrary to pp collisions, where the charged-particle multiplicity in data is well described by the simulation, in p–Pb collisions a weighting procedure based on the event multiplicity was used in the calculation of the reconstruction efficiency from the simulated events. This approach accounts for the dependence of the reconstruction efficiency on the event multiplicity, which is due to the fact that the resolutions of the primary-vertex position and of the variables used in the geometrical selections of displaced decay vertices improve with increasing multiplicity. The event multiplicity was defined here using the number of tracklets, where a tracklet is defined as a track segment joining the reconstructed primary vertex with a space point on each SPD layer within the pseudorapidity range $|\eta| < 1.0$.

The factor $f_{\rm prompt}$ was calculated as in [15]:

$$f_{\rm prompt} = 1 - \frac{N^{\Lambda_c \text{feed-down}}}{N^{\Lambda_c}} = 1 - \frac{(A \times \epsilon)_{\text{feed-down}}\ c_{\Delta y}\ \Delta p_{\rm T}\ \text{BR}\ \mathcal{L}_{\rm int}}{N^{\Lambda_c}/2} \times \left(\frac{{\rm d}^2\sigma}{{\rm d}p_{\rm T}{\rm d}y}\right)^{\rm FONLL}_{\text{feed-down}}, \tag{5.2}$$

where $N^{\Lambda_c}/2$ is the raw yield divided by a factor of two to account for particles and antiparticles. The production cross section of Λ_c^+ from beauty-hadron decays, $\left(\frac{{\rm d}^2\sigma}{{\rm d}p_{\rm T}{\rm d}y}\right)^{\rm FONLL}_{\rm feed-down}$, was calculated using the b-quark $p_{\rm T}$-differential cross section from FONLL calculations [13, 14], the fraction of beauty quarks that fragment into beauty hadrons H_b estimated from LHCb measurements [34], and the $H_b \to \Lambda_c^+ + X$ decay kinematics and branching ratios of $f(H_b \to \Lambda_c^+ + X)$ modelled using PYTHIA 8 simulations [96].

The beauty-hadron fragmentation was derived from the LHCb measurements of the $\overline{B}_s^0$- and Λ_b^0-production fraction relative to $\overline{B}^0$ and B^- mesons in pp collisions at $\sqrt{s} = 13$ TeV [34], which indicates that the fraction of b quarks hadronising into a Λ_b^0 baryon is strongly $p_{\rm T}$-dependent in the measured range of $4 < p_{\rm T} < 25$ GeV/c. The fits to the production fractions of $\overline{B}_s^0$ and Λ_b^0 hadrons normalised to the sum of B^- and $\overline{B}^0$ hadrons are presented in [34] as a function of the beauty-hadron $p_{\rm T}$ as

$$\frac{f_s}{f_u + f_d}(p_{\rm T}) = A[p_1 + p_2 \times (p_{\rm T} - < p_{\rm T} >)] = X, \tag{5.3}$$

$$\frac{f_{\Lambda_b^0}}{f_u + f_d}(p_T) = C[q_1 + \exp(q_2 + q_3 \times p_T)] = Y, \tag{5.4}$$

where f_u, f_d, f_s, and $f_{\Lambda_b^0}$ are the fractions of b quarks that hadronise into $\overline{B}^0$, B^-, $\overline{B}_s^0$, and Λ_b^0, respectively, and A, p_1, p_2, $< p_T >$, C, q_1, q_2 and q_3 are free parameters of the fits to the measured ratios. The beauty hadron fragmentation fractions are defined assuming $f_u = f_d$ and $f_u + f_d + f_s + f_{\Lambda_b^0} = 1$. Around 90% of the feed-down Λ_c^+ comes from $\Lambda_b^0 \to \Lambda_c^+ + X$ decays, and the Λ_b^0 fragmentation fraction can be defined as

$$f_{\Lambda_b^0}(p_T) = \frac{Y}{(X + Y + 1)}. \tag{5.5}$$

For $p_T = 5$ GeV/c, $f_{\Lambda_b^0}$ is around 0.2, and it decreases to a value of around 0.09 for $p_T > 20$ GeV/c. For $p_T < 5$ GeV/c it was assumed that $f_{\Lambda_b^0} = 0.2$, since measurements of the ratio $\Lambda_b^0/\overline{B}^0$ in pp collisions at $\sqrt{s} = 7$ TeV and 8 TeV [33] are flat as a function of p_T in this interval within the experimental uncertainties. It was assumed that there is no rapidity dependence of $f_{\Lambda_b^0}$ since the LHCb measurements of beauty-production ratios are flat as a function of rapidity in $2 < y < 5$ within the experimental uncertainties [33, 34].

For p–Pb collisions, a hypothesis on the nuclear modification factor $R_{pPb}^{\text{feed-down}}$ of Λ_c^+ from beauty-hadron decays was included as an additional factor in the last term of Eq. 5.2. As in the D-meson analyses [77], it was assumed that the R_{pPb} of prompt and feed-down Λ_c^+ are equal. The values of f_{prompt} in both collision systems range between 87% and 98% for the $\Lambda_c^+ \to pK_S^0$ decay channel and between 84% and 98% for the $\Lambda_c^+ \to pK^-\pi^+$ decay channel.

5.7 Evaluation of systematic uncertainties

This section describes the various sources of systematic uncertainties of the measured cross section in each analysis, and the methods used to estimate them. A summary of the systematic uncertainties is shown in Tab. 5.1 and Tab. 5.2 for the pp and p–Pb analyses, respectively. The different sources of systematic uncertainty are assumed to be uncorrelated, and their contributions are added in quadrature to calculate the overall systematic uncertainty in each p_T interval.

The systematic uncertainty on the yield extraction was estimated by repeating the fits to the invariant mass distributions several times, varying i) the lower and upper limits of the fit interval, and ii) the functional form of the background

(linear, exponential, and second-order polynomial functions were used). For each of the above trials, the fit was repeated with different hypotheses on the signal peak width and mean, with variations including a) treating both the Gaussian width and mean as free parameters, b) fixing the peak width to the MC expectation and leaving the mean free, c) fixing the mean to the MC expectation and leaving the peak width free, and d) fixing both the peak width and mean to the MC expectation. The systematic uncertainty was defined as the RMS of the distribution of the raw yield values extracted from these trials.

The systematic uncertainty on the tracking efficiency was estimated by i) comparing the probability of prolonging a track from the TPC to the ITS ("matching efficiency") in data and simulation, and ii) by varying track selection criteria in the analyses. The matching efficiency in simulation was determined after re-weighting the relative abundance of primary and secondary particles to match that in data. The uncertainty on the matching efficiency was defined as the relative difference in the matching efficiency between simulation and data. It is species-dependent and therefore it was determined individually for protons, kaons, and pions. In the $\Lambda_c^+ \to \mathrm{pK}_S^0$ analysis only the proton matching efficiency uncertainty was included since no ITS condition was required for the pion tracks from the K_S^0 decay. The per-track uncertainty on the matching efficiency is p_T dependent and it was propagated to the Λ_c^+ taking into account the decay kinematics and treating the uncertainty as correlated among the tracks. The second contribution to the track reconstruction uncertainty was estimated by repeating the analysis varying the TPC track selection criteria. The uncertainty was defined as the RMS of the Λ_c^+ cross section values obtained with the different track selections. The total uncertainty on the tracking efficiency was defined as the quadratic sum of these two contributions.

The uncertainty on the Λ_c^+ selection efficiency due to imperfections in the simulated kinematical and geometrical variables used to select Λ_c^+ candidates was estimated by varying the selection criteria. For the BDT analysis in the $\Lambda_c^+ \to \mathrm{pK}_S^0$ channel, variations were made on the selection of the BDT response. The systematic uncertainty was estimated in each p_T interval as the RMS of the distribution of the corrected cross section values resulting from these variations.

Systematic uncertainties can arise from discrepancies in the PID efficiency between simulation and data. In the case of the $\Lambda_c^+ \to \mathrm{pK}_S^0$ analysis in pp collisions, the systematic uncertainty associated with the PID efficiency was estimated by

varying the minimum probability threshold required to identify a track as a proton. For the $\Lambda_c^+ \to pK^-\pi^+$ analysis, the systematic uncertainty was estimated by applying a minimum threshold selection on the Bayesian probability to assign the track identity, with the threshold varying between 30% and 80%. The systematic uncertainty in both cases was defined based on the variation of the corrected cross section. For the $\Lambda_c^+ \to pK_S^0$ analysis in p–Pb collisions, the PID variables were included as part of the BDT, and therefore the PID uncertainty is already accounted for by varying the selection on the BDT response. The contribution due to the 3σ PID preselection was found to be negligible.

An additional source of systematic uncertainty was assigned due to the dependence of the efficiencies on the generated p_T distribution of Λ_c^+ in the simulation ("MC p_T shape" in Tab. 5.1 and 5.2). To estimate this effect the efficiencies were evaluated after reweighting the p_T shape of the PYTHIA 6 simulations to match the p_T spectrum of D mesons from FONLL pQCD calculations. An uncertainty was assigned in each p_T interval based on the difference between the central and reweighted efficiencies.

The relative statistical uncertainty on $(A \times \varepsilon)$ was considered as an additional systematic uncertainty source, originating from the finite statistics in the simulation used to calculate the efficiency.

The systematic uncertainty on the prompt fraction ("Beauty feed-down" in Tab. 5.1 and 5.2) was estimated by varying independently i) the production cross section of beauty quarks within the theoretical uncertainties in FONLL [14], and ii) the function describing the fragmentation fraction $f_{\Lambda_b^0}$. For the variation of ii), the free parameters defined in [34] were varied independently within their uncertainties. For $p_T(\Lambda_b^0) < 5$ GeV/c, the lower uncertainty bound of $f_{\Lambda_b^0}$ was taken to be equal to the lower bound of the fit at $p_T(\Lambda_b^0) = 5$ GeV/c, independent of p_T, while the upper uncertainty bound was taken to be equal to the p_T-dependent upper bound of the fit. In order to account for a possible $\sqrt{s}$ dependence of the fragmentation fractions, an additional reduction of the lower bound of $f_{\Lambda_b^0}$ was considered based on the spread of the LHCb measurements at different values of $\sqrt{s}$. In the p–Pb analyses the uncertainty on the hypothesis of the nuclear modification factor of Λ_c^+ from beauty-hadron decays was estimated by varying the ratio $R_{\rm pPb}^{\rm feed\text{-}down}/R_{\rm pPb}^{\rm prompt}$ in the range $0.9 < R_{\rm pPb}^{\rm feed\text{-}down}/R_{\rm pPb}^{\rm prompt} < 1.3$. This range was chosen based on theoretical calculations of charm and beauty hadron production in p–Pb collisions as explained in [77]. The overall uncertainty on the

prompt fraction was defined as the envelope of these variations, which leads to an asymmetric uncertainty.

The uncertainty on the luminosity measurement is 2.1% for pp collisions [88] and 3.7% for p–Pb collisions [89]. The uncertainty on the branching fractions are 5.1% for the $\Lambda_c^+ \to pK^-\pi^+$ channel, and 5.0% for the $\Lambda_c^+ \to pK_S^0$ channel [90].

	$\Lambda_c^+ \to pK^-\pi^+$		$\Lambda_c^+ \to pK_S^0$	
	lowest p_T	highest p_T	lowest p_T	highest p_T
Yield extraction (%)	10	8	8	7
Tracking efficiency (%)	6	7	3	5
Selection efficiency (%)	6	6	3	3
PID efficiency (%)	5	5	2	4
MC p_T shape (%)	negl.	negl.	negl.	negl.
$(A \times \varepsilon)$ stat. unc. (%)	1.7	1.8	1.7	3.5
Beauty feed-down (%)	$^{+1.1}_{-1.8}$	$^{+5.3}_{-8.0}$	$^{+0.8}_{-1.3}$	$^{+2.6}_{-4.0}$
Branching ratio (%)	5.1		5.0	
Luminosity (%)	2.1			

TABLE 5.1: Summary of the systematic uncertainties for the two Λ_c^+ decay modes in pp collisions at $\sqrt{s} = 5.02$ TeV. The uncertainty sources found to be $< 1\%$ were considered negligible ("negl." in the table).

	$\Lambda_c^+ \to pK^-\pi^+$		$\Lambda_c^+ \to pK_S^0$	
	lowest p_T	highest p_T	lowest p_T	highest p_T
Yield extraction (%)	8	10	10	8
Tracking efficiency (%)	6	6	6	5
Selection efficiency (%)	10	6	15	8
PID efficiency (%)	5	5	negl.	negl.
MC p_T shape (%)	1	1	1	1
$(A \times \varepsilon)$ stat. unc. (%)	1.1	4.0	0.5	3.0
Beauty feed-down (%)	$^{+1.8}_{-3.0}$	$^{+4.2}_{-6.7}$	$^{+0.9}_{-1.5}$	$^{+4.6}_{-7.0}$
Branching ratio (%)	5.1		5.0	
Luminosity (%)	3.7			

TABLE 5.2: Summary of the systematic uncertainties for the two Λ_c^+ decay modes in p–Pb collisions at $\sqrt{s_{NN}} = 5.02$ TeV. The uncertainty sources found to be $< 1\%$ were considered negligible ("negl." in the table).

5.8 Results

5.8.1 p_T-differential cross sections

The p_T-differential cross section of prompt Λ_c^+-baryon production in pp collisions at $\sqrt{s} = 5.02$ TeV, measured in the rapidity interval $|y| < 0.5$ and p_T interval $1 < p_T < 12$ GeV/c, is shown in Fig. 5.4 (left) for the two decay channels $\Lambda_c^+ \rightarrow pK^-\pi^+$ and $\Lambda_c^+ \rightarrow pK_S^0$. Figure 5.4 (right) shows the p_T-differential cross section of prompt Λ_c^+-baryon production in p–Pb collisions at $\sqrt{s_{NN}} = 5.02$ TeV, measured in the rapidity interval $-0.96 < y < 0.04$ and p_T interval $1 < p_T < 24\,\text{GeV}/c$ for the two decay channels $\Lambda_c^+ \rightarrow pK^-\pi^+$ and $\Lambda_c^+ \rightarrow pK_S^0$. The measurements in the different decay channels agree within statistical and uncorrelated systematic uncertainties, with the largest discrepancies among the measured values being smaller than 1.4σ.

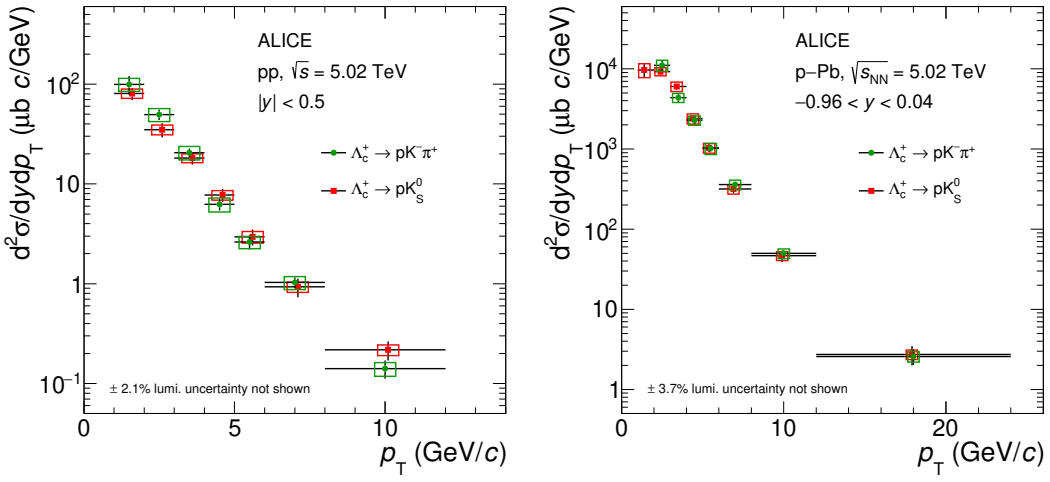

FIGURE 5.4: Left: p_T-differential prompt Λ_c^+-baryon cross section in pp collisions at $\sqrt{s} = 5.02$ TeV in the interval $1 < p_T < 12$ GeV/c. Right: p_T-differential prompt Λ_c^+-baryon cross section in p–Pb collisions at $\sqrt{s_{NN}} = 5.02$ TeV in the interval $1 < p_T < 24$ GeV/c. The statistical uncertainties are shown as vertical bars and the systematic uncertainties are shown as boxes. Horizontal position of points are shifted to provide better visibility.

To obtain a more precise measurement of the p_T-differential Λ_c^+-baryon production cross section, the results from the two decay channels were combined, taking into account the correlation between the statistical and systematic uncertainties. The systematic uncertainties treated as uncorrelated between the different decay channels ($\Lambda_c^+ \rightarrow pK^-\pi^+$ and $\Lambda_c^+ \rightarrow pK_S^0$) include those due to the

raw-yield extraction, the Λ_c^+-selection efficiency, and the $(A \times \epsilon)$ statistical uncertainties. The systematic uncertainties due to the tracking efficiency, the PID efficiency, the generated Λ_c^+ p_T spectrum, the beauty feed-down, and the luminosity were treated as correlated between the two decay channels. The branching ratio uncertainties were considered to be partially correlated, as described in [90]. A weighted average of the cross section values obtained from the different analyses was calculated, using the inverse of the quadratic sum of the relative statistical and uncorrelated systematic uncertainties as weights.

Figure 5.5 shows the measured production cross section (average of the two decay channels) in pp collisions compared to predictions from MC generators and pQCD calculations. The left panel shows the comparison with predictions from different tunes of the PYTHIA 8 generator, including the Monash tune [24], and tunes that implement colour reconnection (CR) beyond the leading-colour approximation [25]. These additional colour reconnection topologies include 'junctions' which fragment into baryons, leading to increased baryon production. For the CR tunes, three modes are considered (Mode 0, 2, and 3), as described in [25], which apply different constraints on the allowed reconnection, taking into account causal connection of dipoles involved in a reconnection and time-dilation effects caused by relative boosts between string pieces. It is noted that Mode 2 is recommended in [25] as the standard tune, and contains the strictest constraints on the allowed reconnection. In the simulations with the three CR modes, all soft QCD processes are switched on. All PYTHIA 8 tunes underestimate the measured p_T-differential prompt Λ_c^+ cross section. The Monash tune significantly underestimates the cross section by a factor ∼12 for $1 < p_T < 2$ GeV/c, and around a factor 2–3 for $p_T > 5$ GeV/c. All three CR modes yield a similar magnitude and shape of the Λ_c^+ cross section, and predict a significantly larger Λ_c^+ production cross section with respect to the Monash tune. However, for all three CR modes, the measured Λ_c^+ production cross section is underestimated by a factor of about two for $1 < p_T < 2$ GeV/c. For $p_T > 5$ GeV/c, Mode 2 and Mode 3 provide a good description of the data, while Mode 0 underestimates the data by 15–20%. All tunes exhibit a harder p_T distribution than observed in data.

The right panel of Fig. 5.5 shows a comparison with a NLO pQCD calculation obtained with the POWHEG framework [97], matched with PYTHIA 6 to generate the parton shower, and the CT14NLO parton distribution functions [98]. The nominal factorisation and renormalisation scales, μ_F and μ_R, were taken to be equal to the transverse mass of the quark, $\mu_0 = \sqrt{m^2 + p_T^2}$, and

the charm-quark mass was set to $m_c = 1.5$ GeV/c^2. The theoretical uncertainties were estimated by varying these scales in the range $0.5\mu_0 < \mu_{R,F} < 2.0\mu_0$, with $0.5\mu_0 < \mu_R/\mu_F < 2.0\mu_0$. Results are also compared with recent GM-VFNS pQCD calculations [99]. With respect to previous GM-VFNS calculations [11, 12], a new fragmentation function for Λ_c^+ has been used, obtained from a fit to OPAL data [100] and measurements from Belle at $\sqrt{s} = 10.52$ GeV [101]. The measured p_T-differential cross section is significantly underestimated by the POWHEG prediction, by a factor of up to 15 in the lowest p_T interval of the measurements, and around a factor 2.5 in the highest. While the discrepancy between the data and calculation decreases as the p_T increases, the measured cross section at $8 < p_T < 12$ GeV/c is still ∼50% larger than the upper edge of the POWHEG uncertainty band. The discrepancy between the data and POWHEG is similar to what was observed in pp collisions at $\sqrt{s} = 7$ TeV [15]. The GM-VFNS predictions also significantly underestimate the data, by about a factor of 3–4 at low p_T and by about a factor of 1.5 at high p_T.

In Fig. 5.6, the Λ_c^+-production cross section in pp collisions at $\sqrt{s} = 5.02$ TeV is compared with the measurement at $\sqrt{s} = 7$ TeV [15]. For a direct comparison, the intervals $4 < p_T < 5$ GeV/c and $5 < p_T < 6$ GeV/c of the $\sqrt{s} = 5.02$ TeV analysis have been merged. When merging, the systematic uncertainties were propagated considering the uncertainty due to the raw-yield extraction as fully uncorrelated and all the other sources as fully correlated between p_T intervals. In the lower panel of the same figure, the ratio of the cross sections is shown. In this case, the systematic uncertainties on feed-down, p_T shape, and branching ratio were assumed to be fully correlated, while all the other sources were considered as uncorrelated between the results at the two collision energies. The relative statistical uncertainties in the measurement at $\sqrt{s} = 5.02$ TeV are on average smaller than those in the measurement at $\sqrt{s} = 7$ TeV by a factor ∼1.5. As expected, a lower Λ_c^+-production cross section is observed at the lower collision energy. The difference between the cross sections at the two $\sqrt{s}$ values increases with increasing p_T, indicating a harder p_T shape at the higher collision energy. This behaviour is consistent with that observed for the D-meson cross section ratios at $\sqrt{s} = 7$ TeV and $\sqrt{s} = 5.02$ TeV, which is described by pQCD calculations [10].

Figure 5.7 shows the p_T-differential cross section averaged among the decay channels and analysis techniques in p–Pb collisions. The cross section is compared to the POWHEG event generator, where the generator settings, the parton

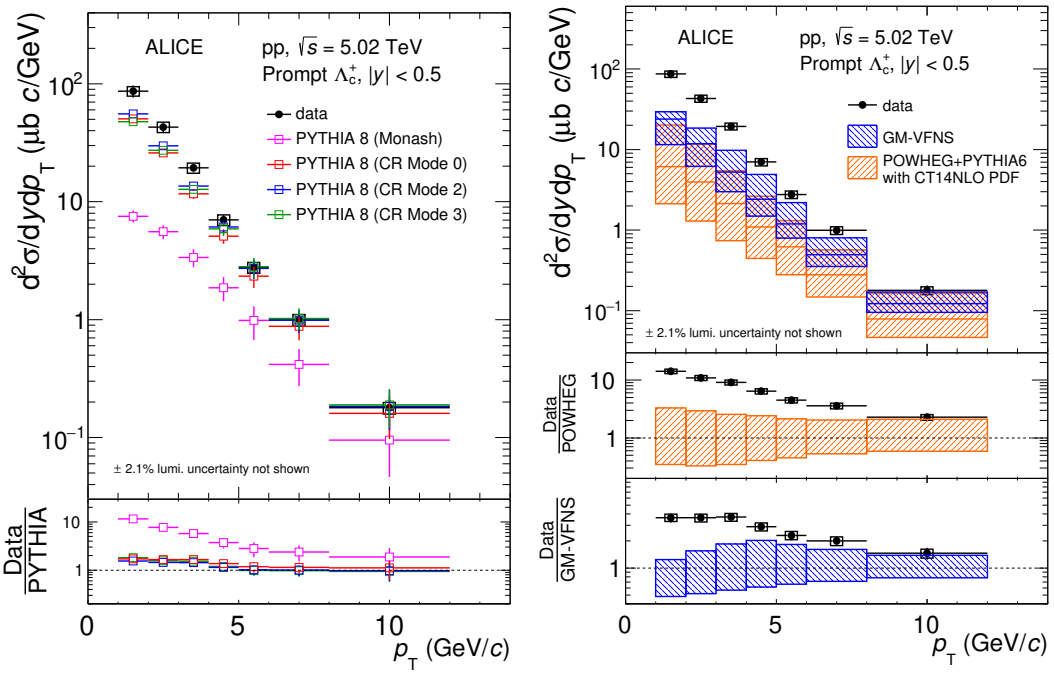

FIGURE 5.5: Prompt Λ_c^+-baryon p_T-differential production cross section in pp collisions at $\sqrt{s} = 5.02$ TeV in the interval $1 < p_T < 12$ GeV/c. The statistical uncertainties are shown as vertical bars and the systematic uncertainties are shown as boxes. Left: Comparison to predictions from different tunes of the PYTHIA 8 event generator [24] [25]. The vertical bars on the PYTHIA 8 predictions represent the statistical uncertainty from the simulation, and the vertical bars on the ratios in the bottom panel also include the statistical uncertainties from the data. Right: Comparison to predictions from the POWHEG event generator [97] and GM-VFNS calculations [99]. The orange(blue) boxes represent the uncertainties of POWHEG(GM-VFNS) due to the choice of pQCD scales. See text for details on the PYTHIA 8 and POWHEG event generator settings.

shower, and the set of parton distribution functions are the same as used in the calculations for pp collisions, and the nuclear modification of the parton distribution functions is modelled with the EPPS16 nPDF parameterisation [49]. The theoretical uncertainty includes the uncertainty on the factorisation and renormalisation scales (estimated as done for POWHEG predictions for pp collisions), while the uncertainties on the parton distribution functions and EPPS16 nPDF are not included in the calculation as they are smaller than the scale uncertainties. The cross section is underestimated by the POWHEG prediction by a factor of up to 15 in the lowest p_T intervals, similar to what is observed for pp collisions. The difference between the POWHEG predictions and the measured cross section

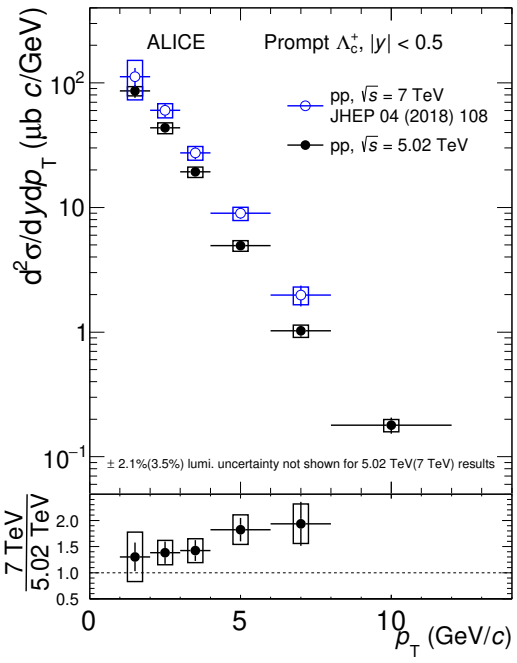

FIGURE 5.6: Comparison between the p_T-differential production cross section of prompt Λ_c^+ baryons in pp collisions at $\sqrt{s} = 7$ TeV [15] and $\sqrt{s} = 5.02$ TeV. The ratio between the cross sections is shown in the lower panel. The statistical uncertainties are shown as vertical bars and the systematic uncertainties are shown as boxes.

decreases with increasing p_T and in the highest p_T interval of the measurement ($12 < p_T < 24$ GeV/c) the data point lies on the upper edge of the POWHEG uncertainty band. The Run 2 p–Pb results are compatible with our previous results from the sample of p–Pb collisions at $\sqrt{s_{NN}} = 5.02$ TeV collected in LHC Run 1 [15]. The statistical uncertainties have been reduced by approximately a factor of two for all p_T intervals, and the systematic uncertainties improved by approximately 30% at low p_T and 10% at high p_T.

5.8.2 Nuclear modification factor

The nuclear modification factor R_{pPb} was calculated as the p_T-differential Λ_c^+ cross section in p–Pb collisions divided by the reference measurement of the p_T-differential Λ_c^+ cross section in pp collisions scaled by the lead mass number $A = 208$

$$R_{pPb} = \frac{1}{A} \frac{d\sigma_{pPb}/dp_T}{d\sigma_{pp}/dp_T} \tag{5.6}$$

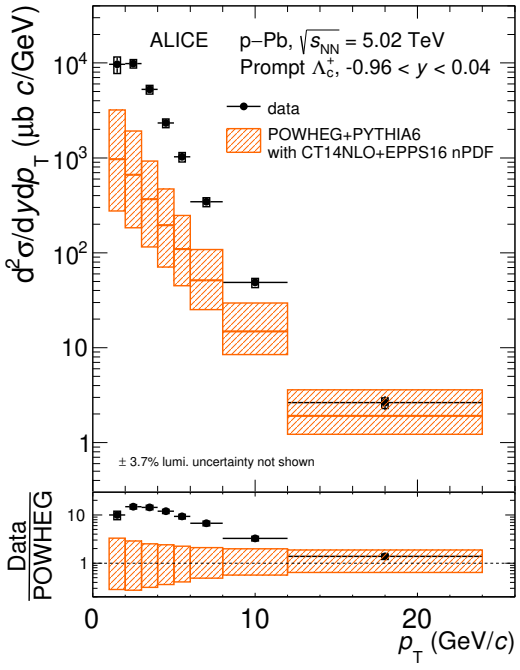

FIGURE 5.7: p_T-differential prompt Λ_c^+-baryon production cross section in p–Pb collisions at $\sqrt{s_{NN}} = 5.02$ TeV in the interval $1 < p_T < 24$ GeV/c compared to predictions from the POWHEG event generator [97]. The statistical uncertainties are shown as vertical bars and the systematic uncertainties are shown as boxes. The orange boxes represent the uncertainties of POWHEG due to the choice of pQCD scales. See text for details on the POWHEG event generator settings.

where $d\sigma_{pp}/dp_T$ was obtained from the cross section measured in pp collisions in $|y| < 0.5$ applying a correction factor to account for the different rapidity coverage of the pp and p–Pb measurements. The correction factor is calculated with FONLL and ranges from 0.995 (in $1 < p_T < 2$ GeV/c) to 0.983 (in $8 < p_T < 12$ GeV/c). Figure 5.8 (left) shows the R_{pPb} of Λ_c^+ baryons in the p_T interval $1 < p_T < 12$ GeV/c compared to the R_{pPb} of non-strange D mesons from [102]. With respect to the previous measurement of the Λ_c^+-baryon R_{pPb} [15], the p_T reach has been extended to higher and lower p_T. In addition, the pp reference at the same per-nucleon centre-of-mass energy as the p–Pb sample eliminates the uncertainty originating from the $\sqrt{s}$-scaling of the pp cross section measured at $\sqrt{s} = 7$ TeV that was present in the previous results. These improvements, along with the increased statistical precision, have allowed for a reduction of the overall uncertainty of the R_{pPb} by a factor of 1.7–2 compared with the previous measurement. The result is consistent with the D-meson R_{pPb}

within the uncertainties in the p_T regions $1 < p_T < 4$ GeV/c and $p_T > 8$ GeV/c, but larger than the D-meson R_{pPb} in $4 < p_T < 8$ GeV/c with a maximum deviation of 1.9σ in $5 < p_T < 6$ GeV/c, where σ is defined as the quadratic sum of the statistical and the lower(upper) systematic uncertainties for Λ_c^+ baryons (D mesons). For $p_T > 2$ GeV/c the Λ_c^+-baryon R_{pPb} is systematically above unity, with a maximum deviation from $R_{pPb} = 1$ reaching 2.2σ in the p_T interval $5 < p_T < 6$ GeV/c, where σ is defined as the quadratic sum of the statistical and the upper systematic uncertainty. In the p_T interval $1 < p_T < 2$ GeV/c the R_{pPb} is lower than unity by 2.6σ. This hints that Λ_c^+ production is suppressed at low p_T and is enhanced at mid-p_T in p–Pb collisions with respect to pp collisions. In Fig. 5.8 (right) the measured Λ_c^+-baryon R_{pPb} is compared to model calculations. The POWHEG+PYTHIA 6 simulations use the POWHEG event generator with PYTHIA 6 parton shower and EPPS16 parameterisation of the nuclear modification of the PDFs [49]. The uncertainty band includes the uncertainties on the nuclear PDFs and on the choice of the pQCD scales. The POWLANG model [61] assumes that a hot deconfined medium is formed in p–Pb collisions, and the transport of heavy quarks through an expanding QGP is computed utilising the Langevin approach and Hard Thermal Loop (HTL) transport coefficients. The POWLANG model does not implement specific differences in hadronisation mechanisms for baryons and mesons, and the same prediction holds for all charm hadron species. The two models capture some features of the data, but neither of them can quantitatively reproduce the observed Λ_c^+-baryon R_{pPb} in the measured p_T interval.

5.8.3 p_T-integrated Λ_c^+ cross sections

The visible Λ_c^+ cross section was computed by integrating the p_T-differential cross section in its measured range. In the integration, the systematic uncertainties were propagated considering the uncertainty due to the raw-yield extraction as fully uncorrelated and all the other sources as fully correlated between p_T intervals. The visible Λ_c^+ cross section in pp collisions at $\sqrt{s} = 5.02$ TeV is

$$\begin{aligned} \mathrm{d}\sigma^{\Lambda_c^+}_{\mathrm{pp,\ 5.02\ TeV}}/\mathrm{d}y|^{1<p_T<12\ \mathrm{GeV}/c}_{|y|<0.5} = 161 \pm 11\ (\mathrm{stat.}) \pm 14\ (\mathrm{syst.}) \\ \pm 3\ (\mathrm{lumi.})\ \mu\mathrm{b}. \end{aligned} \tag{5.7}$$

The visible Λ_c^+ cross section in p–Pb collisions is

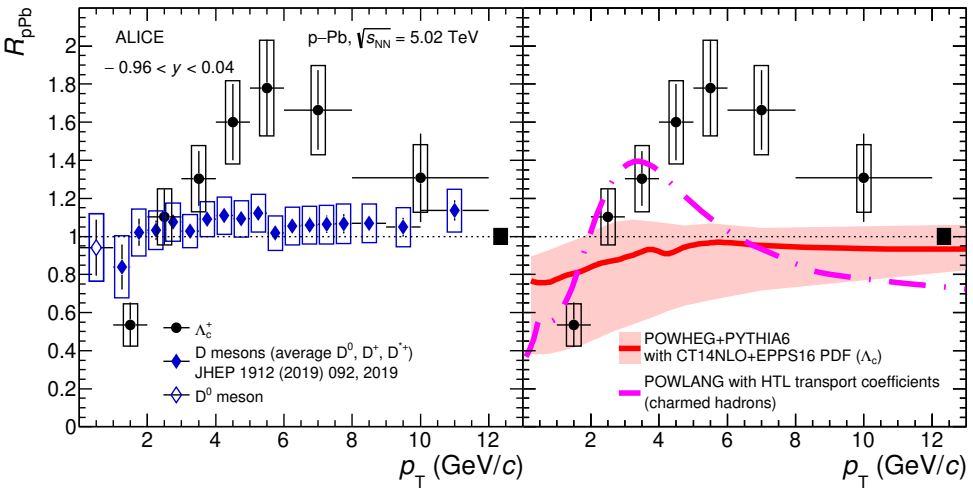

FIGURE 5.8: The nuclear modification factor $R_{\rm pPb}$ of prompt Λ_c^+ baryons in p–Pb collisions at $\sqrt{s_{\rm NN}} = 5.02$ TeV as a function of $p_{\rm T}$, compared to the $R_{\rm pPb}$ of D mesons [102] (average of $\rm D^0$, $\rm D^+$, and $\rm D^{*+}$ in the range $1 < p_{\rm T} < 12$ GeV/c and $\rm D^0$ in $0 < p_{\rm T} < 1$ GeV/c) (left), as well as to POWHEG+PYTHIA 6 [97] with EPPS16 [49] simulations, and POWLANG [61] predictions (right). The black-filled box at $R_{\rm pPb} = 1$ represents the normalisation uncertainty.

$$\mathrm{d}\sigma^{\Lambda_c^+}_{\mathrm{pPb},\ 5.02\ \mathrm{TeV}}/\mathrm{d}y\big|^{1<p_{\rm T}<24\ \mathrm{GeV}/c}_{-0.96<y<0.04} = 29.0 \pm 2.0\ (\mathrm{stat.}) \pm 3.6\ (\mathrm{syst.}) \pm 1.1\ (\mathrm{lumi.})\ \mathrm{mb}. \tag{5.8}$$

The $p_{\rm T}$-integrated Λ_c^+ production cross section at midrapidity was obtained by extrapolating the visible cross sections to the full $p_{\rm T}$ range. The extrapolation approach used for D mesons [76], based on the $p_{\rm T}$-differential cross sections predicted by FONLL calculations, is not applicable here because FONLL does not have predictions for Λ_c^+ baryons. For pp collisions, PYTHIA 8 predictions with specific tunes implementing CR mechanisms were used for the extrapolation. The $p_{\rm T}$-differential Λ_c^+ cross section values in $0 < p_{\rm T} < 1$ GeV/c and for $p_{\rm T} \geq 12$ GeV/c were obtained by scaling the measured Λ_c^+ cross section in $1 < p_{\rm T} < 12$ GeV/c for the fractions of cross section given by PYTHIA in $0 < p_{\rm T} < 1$ GeV/c and for $p_{\rm T} \geq 12$ GeV/c respectively. The PYTHIA 8 simulation with Mode 2 CR tune [25] including soft QCD processes, which gives the best description of both the magnitude and shape of the Λ_c^+ cross section and $\Lambda_c^+/\rm D^0$ ratio, was used to calculate the central value of the extrapolation factors. The procedure was repeated considering the three modes defined in [25], with the envelopes of

the corresponding results assigned as the extrapolation uncertainty. A second extrapolation method was also implemented as a cross check. This consisted of multiplying the measured D^0 cross section value in $0 < p_\mathrm{T} < 1$ GeV/c by the Λ_c^+/D^0 ratio estimated with PYTHIA 8 (CR Mode 2) in the same p_T interval to get an estimate of the Λ_c^+ cross section value in $0 < p_\mathrm{T} < 1$ GeV/c, and then integrating in p_T. The results obtained with the two methods were found to be compatible within the uncertainties.

The resulting p_T-integrated cross section of the Λ_c^+ baryon in pp collisions at $\sqrt{s} = 5.02$ TeV is

$$\begin{aligned} \mathrm{d}\sigma^{\Lambda_c^+}_{\mathrm{pp},\ 5.02\ \mathrm{TeV}}/\mathrm{d}y|_{|y|<0.5} = \ & 230 \pm 16\ (\mathrm{stat.})\ \pm 20\ (\mathrm{syst.}) \\ & \pm 5\ (\mathrm{lumi.})\,^{+5}_{-10}\ (\mathrm{extrap.})\ \mu\mathrm{b}. \end{aligned} \tag{5.9}$$

In p–Pb collisions, the p_T-integrated Λ_c^+-production cross section was obtained using a different approach, since the p_T spectrum of Λ_c^+ is not well described by PYTHIA or other event generators. In this case, the cross sections in $0 < p_\mathrm{T} < 1$ GeV/c and $p_\mathrm{T} > 24$ GeV/c were calculated as the product of the pp cross sections in these p_T intervals obtained from the extrapolation of the measured p_T-differential cross section, as described above; the Pb mass number; a correction factor to account for the different rapidity interval covered in pp and p–Pb collisions; and an assumption on the nuclear modification factor R_pPb as described hereafter. For $0 < p_\mathrm{T} < 1$ GeV/c, the R_pPb was taken as $R_\mathrm{pPb} = 0.5$ as in the $1 < p_\mathrm{T} < 2$ GeV/c interval, under the hypothesis that the trend of the Λ_c^+ R_pPb at low p_T is similar to that of D mesons. The uncertainty was estimated by varying the hypothesis in the range $0.35 < R_\mathrm{pPb} < 0.8$, which incorporates the envelope of the available models (see Fig. 5.8) and the range defined by the combination of the statistical and systematic uncertainties of the Λ_c^+ R_pPb in $1 < p_\mathrm{T} < 2$ GeV/c. For $p_\mathrm{T} > 24$ GeV/c, the R_pPb was assumed to be equal to unity, with the range $0.8 < R_\mathrm{pPb} < 1.2$ used to define the uncertainty.

The resulting p_T-integrated cross section of prompt Λ_c^+ in p–Pb collisions at $\sqrt{s_\mathrm{NN}} = 5.02$ TeV is

$$\begin{aligned} \mathrm{d}\sigma^{\Lambda_c^+}_{\mathrm{pPb},\ 5.02\ \mathrm{TeV}}/\mathrm{d}y|_{-0.96<y<0.04} = \ & 36.2 \pm 2.5\ (\mathrm{stat.})\ \pm 4.5\ (\mathrm{syst.}) \\ & \pm 1.3\ (\mathrm{lumi.})^{+4.4}_{-2.7}\ (\mathrm{extrap.})\ \mathrm{mb}. \end{aligned} \tag{5.10}$$

The visible cross sections make up 70% and 80% of the integrated cross sections

in pp and p–Pb collisions, respectively. The p_T-integrated Λ_c^+ cross sections in pp and p–Pb collisions can be used for the comparison of fragmentation fractions of charm quarks in different collision systems and rapidity intervals. They can also be used in the calculation of the $c\bar{c}$ cross section together with the cross sections of D mesons and higher-mass charm baryons that do not decay into Λ_c^+. Due to the lack of measurements of higher-mass charm baryons ($\Xi_c^{+,0}, \Omega_c$) at $\sqrt{s} = 5.02$ TeV, which contribute to the $c\bar{c}$ cross section, a calculation of the $c\bar{c}$ cross section is beyond the scope of this work.

5.8.4 Λ_c^+/D^0 ratios

The ratios between the yields of Λ_c^+ baryons and D^0 mesons were calculated using the D^0 cross sections reported in [10] for pp collisions and [102] for p–Pb collisions, respectively. The uncertainty sources assumed to be uncorrelated between the Λ_c^+ and D^0 production cross sections include those due to the raw-yield extraction, the selection efficiency, the PID efficiency, the generated p_T shape, the $(A \times \epsilon)$ statistical uncertainties, and the branching ratios. The uncertainties assumed to be correlated include those due to the tracking, the beauty feed-down and the luminosity. The D^0 cross section was measured in finer p_T intervals than the Λ_c^+, so it was rebinned such that the p_T intervals match between the two species.

The Λ_c^+/D^0 ratio as a function of p_T in pp and p–Pb collisions is shown in Fig. 5.9. A clear decreasing trend with increasing p_T is seen in both pp and p–Pb collisions for $p_T > 2$ GeV/c, and at high p_T the ratio reaches a value of about 0.2. The ratios measured in pp and p–Pb collisions are qualitatively consistent with each other, although a larger Λ_c^+/D^0 ratio in $3 < p_T < 8$ GeV/c and a lower ratio in $1 < p_T < 2$ GeV/c are measured in p–Pb collisions with respect to pp collisions.

The values of the p_T-integrated Λ_c^+/D^0 ratios are reported in Tab. 5.3 along with the values measured in e^+e^- and e^-p collisions by other experiments. The Λ_c^+/D^0 ratios in pp and p–Pb collisions are consistent with each other within the experimental uncertainties. Comparing to previous measurements in other collision systems, the Λ_c^+/D^0 ratio is significantly enhanced by a factor of about 3–5 in pp collisions and a factor of about 2–4 in p–Pb collisions, indicating that the fragmentation fractions of charm quarks into baryons are different with

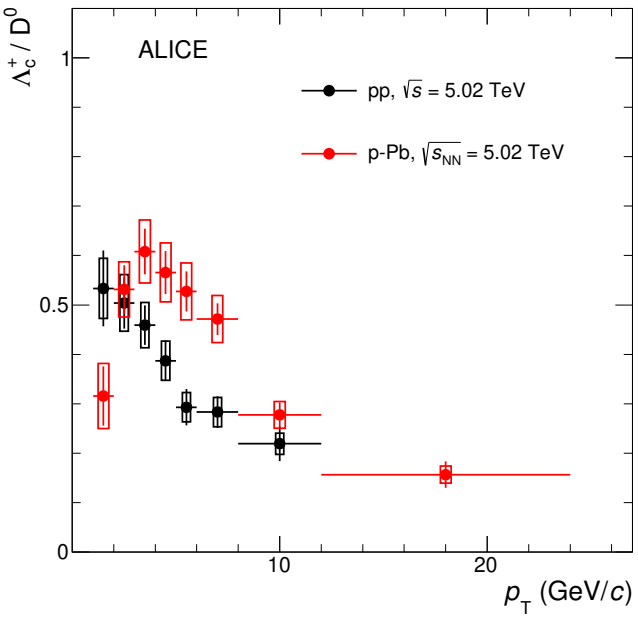

FIGURE 5.9: The Λ_c^+/D^0 ratio as a function of p_T measured in pp collisions at $\sqrt{s} = 5.02$ TeV and in p–Pb collisions at $\sqrt{s_{NN}} = 5.02$ TeV.

respect to e^+e^- and e^-p collisions. This is consistent with the previous ALICE measurements [15], where the p_T-integrated Λ_c^+/D^0 ratios were restricted to $1 < p_T < 8$ GeV/c in pp collisions, and to $2 < p_T < 12$ GeV/c in p–Pb collisions.

Figure 5.10 shows the Λ_c^+/D^0 ratio in pp collisions compared with models from MC generators, and a statistical hadronisation model. The MC generators include PYTHIA 8 with Monash tune and colour reconnection tunes as described above; PYTHIA 8 with colour reconnection plus rope hadronisation [103, 25] where colour charges can act coherently to form a rope, increasing the effective string tension; HERWIG 7.2 [28] where hadronisation is implemented via clusters; and POWHEG pQCD generator matched to PYTHIA 6 to generate the parton shower, as described above. The measured points are also compared to predictions from GM-VFNS pQCD calculations, which were computed as the ratios of the Λ_c^+ and D^0 cross sections obtained with the same choice of pQCD scales [99]. The left panel shows the predictions of the Λ_c^+/D^0 ratio from PYTHIA 8 (Monash tune), HERWIG 7, POWHEG, and GM-VFNS, which all implement fragmentation processes tuned on charm production measurements in e^+e^- collisions, and therefore all predict a value of the Λ_c^+/D^0 ratio around 0.1, with a very mild p_T dependence. These predictions significantly underestimate the data at low p_T by a factor of about 5–10, while at high p_T the discrepancy is reduced to a factor

Experiment	$\Lambda_c^+/D^0 \pm$ stat. $\pm$ syst.	System	$\sqrt{s}$ (GeV)	Notes
ALICE	$0.51 \pm 0.04 \pm 0.04\ ^{+0.01}_{-0.02}$	pp	5020	$p_T > 0, \|y\| < 0.5$
ALICE	$0.42 \pm 0.03 \pm 0.06^{+0.05}_{-0.03}$	p–Pb	5020	$p_T > 0, -0.96 < y < 0.04$
CLEO [17]	$0.119 \pm 0.021 \pm 0.019$	e^+e^-	10.55	
ARGUS [16, 18]	0.127 ± 0.031	e^+e^-	10.55	
LEP average [19]	$0.113 \pm 0.013 \pm 0.006$	e^+e^-	91.2	
ZEUS DIS [22]	$0.124 \pm 0.034^{+0.025}_{-0.022}$	e^-p	320	$1 < Q^2 < 1000$ GeV^2, $0 < p_T < 10$ GeV/c, $0.02 < y < 0.7$
ZEUS γp, HERA I [20]	$0.220 \pm 0.035^{+0.027}_{-0.037}$	e^-p	320	$130 < W < 300$ GeV, $Q^2 < 1$ GeV^2, $p_T > 3.8$ GeV/c, $\|\eta\| < 1.6$
ZEUS γp, HERA II [21]	$0.107 \pm 0.018^{+0.009}_{-0.014}$	e^-p	320	$130 < W < 300$ GeV, $Q^2 < 1$ GeV^2, $p_T > 3.8$ GeV/c, $\|\eta\| < 1.6$

TABLE 5.3: Comparison of the p_T-integrated Λ_c^+/D^0 ratio measured in pp and p–Pb collisions, and the same ratios in e^+e^- and e^-p collisions (reproduced from [15]). Statistical and systematic uncertainties are reported (from references [16, 18] it was not possible to separate systematics and statistical uncertainties). The ALICE measurements report an additional uncertainty source from the extrapolation procedure.

of about 2. The right panel shows models which include processes that enhance baryon production. A significant enhancement of the Λ_c^+/D^0 ratio is observed with PYTHIA 8 simulations including CR beyond the leading-colour approximation, with respect to the Monash tune. The results of these PYTHIA 8 tunes are consistent with the measured Λ_c^+/D^0 ratio in pp collisions, also reproducing the decreasing trend of Λ_c^+/D^0 with increasing p_T. Including rope hadronisation in addition to colour reconnection induces a small modification in the Λ_c^+/D^0 ratio, suggesting that the increased string tension does not significantly affect the relative production of baryons with respect to mesons. The data is also compared with a statistical hadronisation model [73] where the underlying charm baryon spectrum is either taken from the PDG, or augmented to include additional excited baryon states, which have not yet been observed but are predicted by the Relativistic Quark Model (RQM) [104]. For the former case, the model underpredicts the data at low p_T. For the latter case, the additional charm baryon states decay strongly to Λ_c^+ baryons, contributing to the prompt Λ_c^+ spectrum. This increases the Λ_c^+/D^0 ratio and allows the model to describe both the magnitude and the p_T dependence of the measured ratio. Finally, the Catania model [105] is also presented, which assumes that a QGP is formed in pp collisions and that the hadronisation occurs via coalescence as well as fragmentation. The light quark p_T spectrum is determined with a blast wave model, while the heavy quark p_T spectrum is determined with FONLL pQCD predictions, and coalescence is implemented via the Wigner formalism. Contrary to the implementation in Pb–Pb collisions [106], jet quenching mechanisms are not included in pp collisions. The model predicts that hadronisation via coalescence is dominant at low p_T, while fragmentation dominates at high p_T. Both the magnitude and the p_T shape of the measured Λ_c^+/D^0 ratio are described well by this model.

Figure 5.11 (left) shows the Λ_c^+/D^0 ratio in pp collisions at $\sqrt{s} = 5.02$ TeV compared with the previous measurement at $\sqrt{s} = 7$ TeV, and with predictions from PYTHIA 8 simulations. The Λ_c^+/D^0 ratio is found to be consistent between the two collision energies, within the experimental uncertainties; however, the wider p_T coverage and the improved statistical and systematic uncertainties on the new measurement reveal a clear decreasing trend in the Λ_c^+/D^0 ratio in pp collisions at $\sqrt{s} = 5.02$ TeV, which was not clearly visible in the result at $\sqrt{s} = 7$ TeV. The predictions of PYTHIA 8 with Monash tune do not show a $\sqrt{s}$-dependence, while those with CR Mode 2 indicate a slight $\sqrt{s}$-dependence, where the Λ_c^+/D^0 ratio is slightly larger at low p_T at $\sqrt{s} = 7$ TeV than at $\sqrt{s} =$

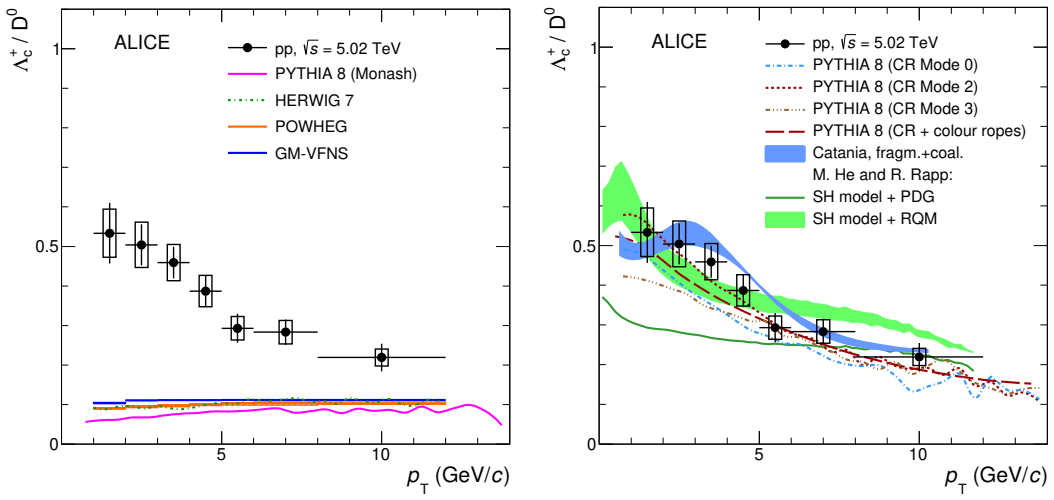

FIGURE 5.10: The Λ_c^+/D^0 ratio measured in pp collisions at $\sqrt{s} = 5.02$ TeV, compared to theoretical predictions. The measurement is compared with predictions from MC generators (PYTHIA 8 [24, 25], HERWIG 7 [28], POWHEG [97]), GM-VFNS [99], a statistical hadronisation model [73] ('SH model' in the legend) and a model which implements hadronisation via coalescence and fragmentation [105]. See text for model details.

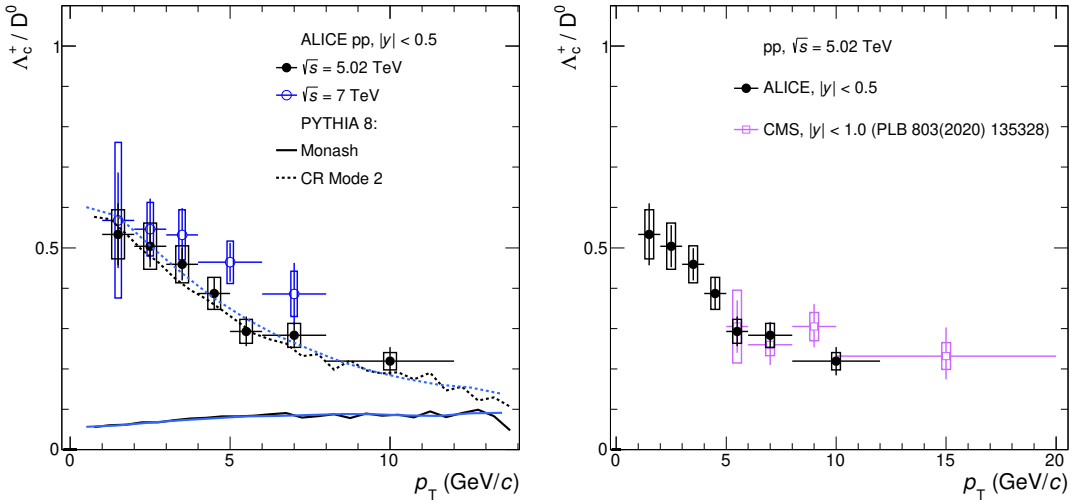

FIGURE 5.11: Left: The Λ_c^+/D^0 ratio measured in pp collisions at $\sqrt{s} = 5.02$ TeV, compared to the measurement at $\sqrt{s} = 7$ TeV [15]. PYTHIA 8 predictions are shown at both energies, for the Monash tune (solid lines) and with the Mode 2 CR tune (dotted lines). Right: the Λ_c^+/D^0 ratio at $\sqrt{s} = 5.02$ TeV compared with the measurement by the CMS Collaboration at $|y| < 1$ [29].

5.02 TeV. The right panel shows the Λ_c^+/D^0 ratio in pp collisions, compared with the measurement by the CMS Collaboration in $5 < p_T < 20$ GeV/c and

$|y| < 1$ [29]. In the p_T region covered by both experiments, the results are found to be consistent with one another.

In Fig. 5.12, the Λ_c^+/D^0 ratio in p–Pb collisions at midrapidity ($-0.96 < y < 0.04$) is compared with the measurements by the LHCb Collaboration at forward ($1.5 < y < 4$) and backward ($-4.5 < y < -2.5$) rapidities [72]. The left panel shows the comparison of the Λ_c^+/D^0 ratios in the different rapidity intervals as a function of p_T. For $p_T < 8\,\mathrm{GeV}/c$ the ratio measured at midrapidity is higher than the ones measured at forward and backward rapidities, whereas at higher p_T the measurements are consistent within uncertainties. The right panel shows the p_T-integrated Λ_c^+/D^0 ratio as a function of rapidity. The p_T range of the integration of the ALICE data ($2 < p_T < 12\,\mathrm{GeV}/c$) is chosen to be similar to the reported LHCb integrated p_T range ($2 < p_T < 10\,\mathrm{GeV}/c$). The results suggest an enhancement of the ratio at midrapidity with respect to forward and backward rapidities. The difference between the Λ_c^+/D^0 ratio at mid and forward (backward) rapidities is less pronounced in p–Pb collisions compared to the one observed in pp collisions at 7 TeV [30, 15].

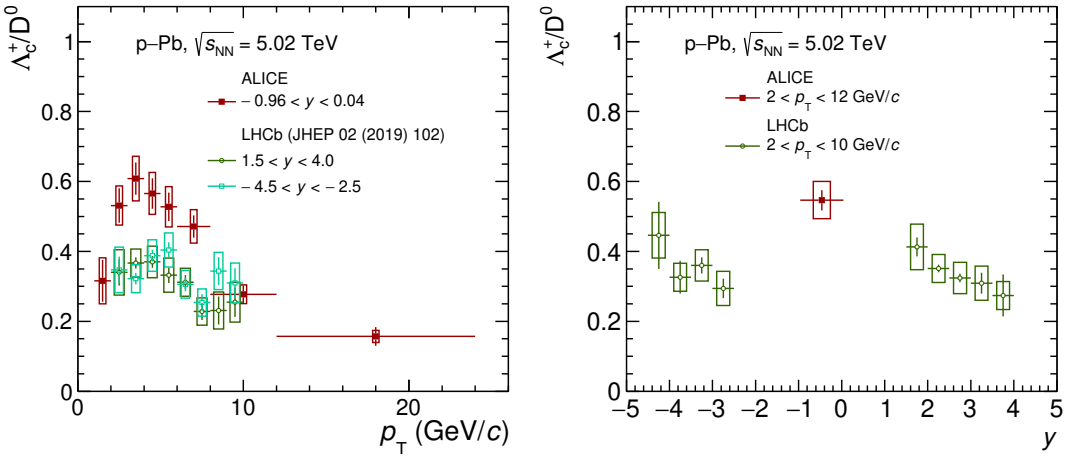

FIGURE 5.12: The Λ_c^+/D^0 ratio measured in p–Pb collisions at $\sqrt{s_{NN}} = 5.02$ TeV, compared with the measurement at forward and backward rapidity [72] by the LHCb collaboration. The measurements are shown as a function of p_T (left) and as a function of y (right).

Figure 5.13 shows the Λ_c^+/D^0 ratio in pp and p–Pb collisions, compared to the baryon-to-meson ratios in the light flavour sector, p/π [69, 107] and Λ/K_S^0 [108, 109]. The p/π ratio in pp collisions is shown at centre-of-mass energies of 7 TeV and 5.02 TeV, and both results are fully consistent with each other. The Λ/K_S^0 ratio in pp collisions is shown at $\sqrt{s} = 7$ TeV. Comparing the Λ_c^+/D^0 ratio to the

light-flavour ratios, similar characteristics can be seen. All the baryon-to-meson ratios decrease with increasing p_T for $p_T > 3$ GeV/c. In addition, the light-flavour hadron ratios show a distinct peak at intermediate p_T (around 3 GeV/c), while the Λ_c^+/D^0 ratio shows a hint of a peak at $2 < p_T < 4$ GeV/c in p–Pb collisions, though a higher precision measurement would be needed to confirm this. Also shown in Fig. 5.13 are predictions from PYTHIA 8 with Monash and CR Mode 2 tunes. The PYTHIA 8 predictions for the light-flavour baryon-to-meson ratios are calculated at $\sqrt{s} = 7$ TeV. It can be observed that the behaviours of the PYTHIA 8 predictions for light-flavour and charm baryon-to-meson ratios are similar. The measured Λ/K_S^0 ratio in pp collisions is underestimated by the Monash tune, while for the CR Mode 2 tune both the magnitude and trend of the ratio are closer to data, despite predicting a slightly flatter trend with p_T. The p/π ratio ratio is underestimated by PYTHIA 8 (Monash) at low p_T but overestimated at high p_T, while CR Mode 2 improves the agreement with data at low p_T but still overestimates the data at high p_T. Overall, the colour reconnection modes in PYTHIA 8 generally provide for a better description of the baryon-to-meson ratios in both the light-flavour and charm sector.

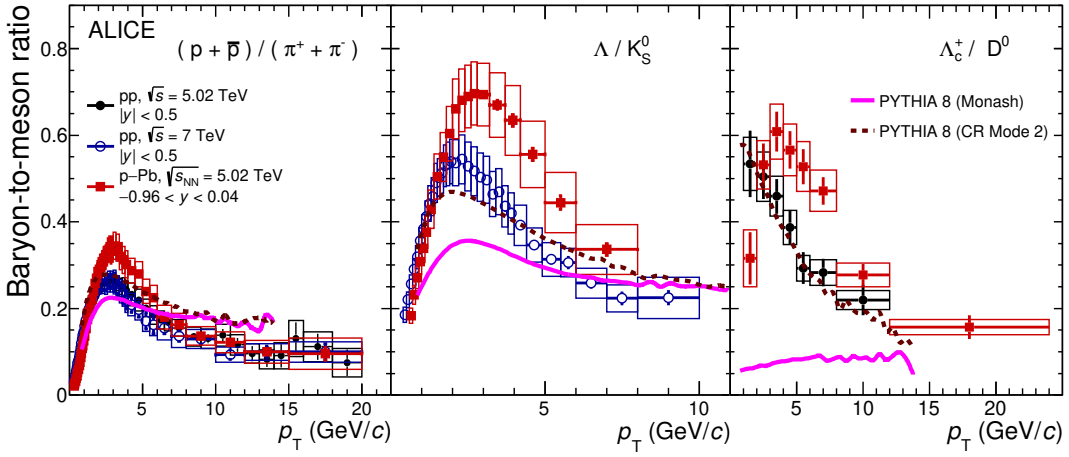

FIGURE 5.13: The baryon-to-meson ratios in the light-flavour and charm sector; p/π in pp collisions at $\sqrt{s} = 5.02$ TeV and 7 TeV and p–Pb collisions at $\sqrt{s_{NN}} = 5.02$ TeV [69] (left), Λ/K_S^0 in pp collisions at $\sqrt{s} = 7$ TeV and p–Pb collisions at $\sqrt{s_{NN}} = 5.02$ TeV [108, 109] (middle), and Λ_c^+/D^0 in pp collisions at $\sqrt{s} = 5.02$ TeV and p–Pb collisions at $\sqrt{s_{NN}} = 5.02$ TeV (right). The data are compared to predictions from PYTHIA 8 [24, 25]. See text for model details.

5.9 Summary and conclusions

The measurements of the production of prompt Λ_c^+ baryons at midrapidity in pp collisions at $\sqrt{s} = 5.02$ TeV and in p–Pb collisions at $\sqrt{s_{NN}} = 5.02$ TeV with the ALICE detector at the LHC have been reported. The measurement in pp collisions, in particular, was performed at a different centre-of-mass energy with respect to the previous work in which Λ_c^+-baryon production was measured in pp collisions at $\sqrt{s} = 7$ TeV [15]. The pp data sample at $\sqrt{s} = 5.02$ TeV is the natural reference for measurements in p–Pb and Pb–Pb collisions at the same centre-of-mass energy per nucleon pair. Moreover, with respect to [15], the uncertainties were significantly reduced, and the p_T range and the p_T granularity of the measurements were improved in both collision systems. The analysis was performed using two different decay channels, $\Lambda_c^+ \rightarrow pK^-\pi^+$ and $\Lambda_c^+ \rightarrow pK_S^0$. The results were reported for pp collisions in the rapidity interval $|y| < 0.5$ and the transverse-momentum interval $1 < p_T < 12$ GeV/c and for p–Pb collisions in $-0.96 < y < 0.04$ and $1 < p_T < 24$ GeV/c. The p_T-differential production cross sections were obtained averaging the results from different hadronic decay channels.

The p_T-differential cross section was measured to be larger than predictions given by pQCD calculations in both pp and p–Pb collisions. The nuclear modification factor R_{pPb} of Λ_c^+ baryons was found to be below unity in the interval $1 < p_T < 2$ GeV/c and to peak above unity around 5 GeV/c. It is consistent with the R_{pPb} of D mesons in the p_T regions $1 < p_T < 4$ GeV/c and $p_T > 8$ GeV/c and larger than the D-meson R_{pPb} in $4 < p_T < 8$ GeV/c. The current precision of the measurement is not enough to draw conclusions on the role of different CNM effects and the possible presence of hot-medium effects. As already observed in [15], the Λ_c^+/D^0 baryon-to-meson ratio in pp collisions is larger than previous measurements obtained in e^+e^- and e^-p collision systems at lower centre-of-mass energies. The increase of precision in this paper allowed to observe, for the first time, a clear decreasing trend as a function of transverse momentum in the Λ_c^+/D^0 ratio. The Λ_c^+/D^0 ratio was compared to pp event generators and models that implement different particle production and hadronisation mechanisms: qualitative agreement with the measurement is obtained with PYTHIA 8 tunes including string formation beyond the leading-colour approximation; a prediction based on the statistical hadronisation model which includes unobserved charm baryon states that strongly decay to Λ_c^+; and a prediction which assumes

the formation of a QGP and implements hadronisation via coalescence and fragmentation. The Λ_c^+/D^0 ratio measured in pp collisions is consistent with the results by CMS at midrapidity in the common p_T regions of both measurements. The ratio in p–Pb collisions at midrapidity is higher than the one measured by LHCb at forward and backward rapidities in $2 < p_T < 8$ GeV/c, while for $p_T > 8$ GeV/c the measurements at central, forward and backward rapidities are consistent within uncertainties. The measured Λ_c^+/D^0 ratio was also compared with baryon-to-meson ratios measured in the light-flavour sector. The measured Λ/K_S^0 ratio can also be described by PYTHIA 8 when including string formation beyond the leading-colour approximation, although this PYTHIA 8 tune slightly overestimates the measured p/π ratio. The increased precision of this measurement with respect to the measurements made with the Run 1 data is crucial for providing further insight into charm baryon production in pp and p–Pb collisions. A more precise measurement is expected to be obtained during the LHC Run 3 and Run 4 after the upgrade of the ALICE apparatus [110].

References

[1] S. Acharya et al. "Λ_c^+ production in pp and in p-Pb collisions at $\sqrt{s_{NN}} =$ 5.02 TeV". In: *Phys. Rev. C* 104 (5 2021), p. 054905. DOI: 10.1103/PhysRevC.104.054905. URL: https://link.aps.org/doi/10.1103/PhysRevC.104.054905.

[2] L. Adamczyk et al. "Measurements of D^0 and D^* Production in $p + p$ Collisions at $\sqrt{s} = 200$ GeV". In: *Phys. Rev. D* 86 (2012), p. 072013. DOI: 10.1103/PhysRevD.86.072013. arXiv: 1204.4244 [nucl-ex].

[3] D. Acosta et al. "Measurement of prompt charm meson production cross sections in $p\bar{p}$ collisions at $\sqrt{s} = 1.96$ TeV". In: *Phys. Rev. Lett.* 91 (2003), p. 241804. DOI: 10.1103/PhysRevLett.91.241804. arXiv: hep-ex/0307080.

[4] D. Acosta et al. "Measurement of the J/ψ meson and $b-$hadron production cross sections in $p\bar{p}$ collisions at $\sqrt{s} = 1960$ GeV". In: *Phys. Rev. D* 71 (2005), p. 032001. DOI: 10.1103/PhysRevD.71.032001. arXiv: hep-ex/0412071.

[5] A. Abulencia et al. "Measurement of the B+ production cross-section in p anti-p collisions at s**(1/2) = 1960-GeV". In: *Phys. Rev. D* 75 (2007), p. 012010. DOI: 10.1103/PhysRevD.75.012010. arXiv: hep-ex/0612015.

[6] A. Andronic et al. "Heavy-flavour and quarkonium production in the LHC era: from protonâĂŞproton to heavy-ion collisions". In: *Eur. Phys. J.* C76.3 (2016), p. 107. DOI: 10.1140/epjc/s10052-015-3819-5. arXiv: 1506.03981 [nucl-ex].

[7] Roel Aaij et al. "Measurements of prompt charm production cross-sections in pp collisions at $\sqrt{s} = 13$ TeV". In: *JHEP* 03 (2016). [Erratum: JHEP09,013(2016); Erratum: JHEP05,074(2017)], p. 159. DOI: 10.1007/JHEP03(2016)159, 10.1007/JHEP09(2016)013, 10.1007/JHEP05(2017)074. arXiv: 1510.01707 [hep-ex].

[8] Vardan Khachatryan et al. "Measurement of the total and differential inclusive B^+ hadron cross sections in pp collisions at $\sqrt{s} = 13$ TeV". In: *Phys. Lett.* B771 (2017), pp. 435–456. DOI: 10.1016/j.physletb.2017.05.074. arXiv: 1609.00873 [hep-ex].

[9] Roel Aaij et al. "Measurement of the $B^{\pm}$ production cross-section in pp collisions at $\sqrt{s} = 7$ and 13 TeV". In: *JHEP* 12 (2017), p. 026. DOI: 10.1007/JHEP12(2017)026. arXiv: 1710.04921 [hep-ex].

[10] Shreyasi Acharya et al. "Measurement of D^0 , D^+ , D^{*+} and D_s^+ production in pp collisions at $\sqrt{s} = 5.02$ TeV with ALICE". In: *Eur. Phys. J.* C79.5 (2019), p. 388. DOI: 10.1140/epjc/s10052-019-6873-6. arXiv: 1901.07979 [nucl-ex].

[11] B. A. Kniehl et al. "Collinear subtractions in hadroproduction of heavy quarks". In: *Eur. Phys. J. C* 41 (2005), pp. 199–212. DOI: 10.1140/epjc/s2005-02200-7. arXiv: hep-ph/0502194.

[12] B. A. Kniehl et al. "Inclusive Charmed-Meson Production at the CERN LHC". In: *Eur. Phys. J.* C72 (2012), p. 2082. DOI: 10.1140/epjc/s10052-012-2082-2. arXiv: 1202.0439 [hep-ph].

[13] Matteo Cacciari, Mario Greco, and Paolo Nason. "The P(T) spectrum in heavy flavor hadroproduction". In: *JHEP* 05 (1998), p. 007. DOI: 10.1088/1126-6708/1998/05/007. arXiv: hep-ph/9803400.

[14] Matteo Cacciari et al. "Theoretical predictions for charm and bottom production at the LHC". In: *JHEP* 10 (2012), p. 137. DOI: 10.1007/JHEP10(2012)137. arXiv: 1205.6344 [hep-ph].

[15] Shreyasi Acharya et al. "Λ_c^+ production in pp collisions at $\sqrt{s} = 7$ TeV and in p–Pb collisions at $\sqrt{s_{\rm NN}} = 5.02$ TeV". In: *JHEP* 04 (2018), p. 108. DOI: 10.1007/JHEP04(2018)108. arXiv: 1712.09581 [nucl-ex].

[16] H. Albrecht et al. "Observation of the charmed baryon Λ_c in e^+e^- annihilation at 10-GeV". In: *Phys. Lett.* B207 (1988), pp. 109–114. DOI: 10.1016/0370-2693(88)90896-9.

[17] P. Avery et al. "Inclusive production of the charmed baryon Λ_c from e^+e^- annihilations at $\sqrt{s} = 10.55$ GeV". In: *Phys. Rev.* D43 (1991), pp. 3599–3610. DOI: 10.1103/PhysRevD.43.3599.

[18] H. Albrecht et al. "Inclusive production of D^0, D^+ and $D^*(2010)^+$ mesons in B decays and nonresonant e^+e^- annihilation at 10.6 GeV". In: *Z. Phys.* C52 (1991), pp. 353–360. DOI: 10.1007/BF01559430.

[19] Leonid Gladilin. "Fragmentation fractions of c and b quarks into charmed hadrons at LEP". In: *Eur. Phys. J. C* 75.1 (2015), p. 19. DOI: 10.1140/epjc/s10052-014-3250-3. arXiv: 1404.3888 [hep-ex].

[20] S. Chekanov et al. "Measurement of charm fragmentation ratios and fractions in photoproduction at HERA". In: *Eur. Phys. J.* C44 (2005), pp. 351–366. DOI: 10.1140/epjc/s2005-02397-3. arXiv: hep-ex/0508019 [hep-ex].

[21] H. Abramowicz et al. "Measurement of charm fragmentation fractions in photoproduction at HERA". In: *JHEP* 09 (2013), p. 058. DOI: 10.1007/JHEP09(2013)058. arXiv: 1306.4862 [hep-ex].

[22] H. Abramowicz et al. "Measurement of D^+ and Λ_c^+ production in deep inelastic scattering at HERA". In: *JHEP* 11 (2010), p. 009. DOI: 10.1007/JHEP11(2010)009. arXiv: 1007.1945 [hep-ex].

[23] Mykhailo Lisovyi, Andrii Verbytskyi, and Oleksandr Zenaiev. "Combined analysis of charm-quark fragmentation-fraction measurements". In: *Eur. Phys. J. C* 76.7 (2016), p. 397. DOI: 10.1140/epjc/s10052-016-4246-y. arXiv: 1509.01061 [hep-ex].

[24] Peter Skands, Stefano Carrazza, and Juan Rojo. "Tuning PYTHIA 8.1: the Monash 2013 Tune". In: *Eur. Phys. J.* C74.8 (2014), p. 3024. DOI: 10.1140/epjc/s10052-014-3024-y. arXiv: 1404.5630 [hep-ph].

[25] Jesper R. Christiansen and Peter Z. Skands. "String Formation Beyond Leading Colour". In: *JHEP* 08 (2015), p. 003. DOI: 10.1007/JHEP08(2015)003. arXiv: 1505.01681 [hep-ph].

[26] Christian Bierlich and Jesper Roy Christiansen. "Effects of color reconnection on hadron flavor observables". In: *Phys. Rev.* D92.9 (2015), p. 094010. DOI: 10.1103/PhysRevD.92.094010. arXiv: 1507.02091 [hep-ph].

[27] Christoffer Flensburg, Gosta Gustafson, and Leif Lonnblad. "Inclusive and Exclusive Observables from Dipoles in High Energy Collisions". In: *JHEP* 08 (2011), p. 103. DOI: 10.1007/JHEP08(2011)103. arXiv: 1103.4321 [hep-ph].

[28] Johannes Bellm et al. "Herwig 7.0/Herwig++ 3.0 release note". In: *Eur. Phys. J. C* 76.4 (2016), p. 196. DOI: 10.1140/epjc/s10052-016-4018-8. arXiv: 1512.01178 [hep-ph].

[29] Albert M Sirunyan et al. "Production of Λ_c^+ baryons in proton-proton and lead-lead collisions at $\sqrt{s_{NN}} = 5.02$ TeV". In: *Phys. Lett. B* 803 (2020), p. 135328. DOI: 10.1016/j.physletb.2020.135328. arXiv: 1906.03322 [hep-ex].

[30] R Aaij et al. "Prompt charm production in pp collisions at $\sqrt{s} = 7$ TeV". In: *Nucl. Phys.* B871 (2013), pp. 1–20. DOI: 10.1016/j.nuclphysb.2013.02.010. arXiv: 1302.2864 [hep-ex].

[31] RafaÅĆ MaciuÅĆa and Antoni Szczurek. "Production of Λ_c baryons at the LHC within the k_T-factorization approach and independent parton fragmentation picture". In: *Phys. Rev.* D98.1 (2018), p. 014016. DOI: 10.1103/PhysRevD.98.014016. arXiv: 1803.05807 [hep-ph].

[32] R. Aaij et al. "Measurement of b-hadron production fractions in 7 TeV pp collisions". In: *Phys. Rev.* D85 (2012), p. 032008. DOI: 10.1103/PhysRevD.85.032008. arXiv: 1111.2357 [hep-ex].

[33] R. Aaij et al. "Study of the production of Λ_b^0 and $\overline{B}^0$ hadrons in pp collisions and first measurement of the $\Lambda_b^0 \to J/\psi p K^-$ branching fraction". In: *Chin. Phys.* C40.1 (2016), p. 011001. DOI: 10.1088/1674-1137/40/1/011001. arXiv: 1509.00292 [hep-ex].

[34] Roel Aaij et al. "Measurement of b hadron fractions in 13 TeV pp collisions". In: *Phys. Rev.* D100.3 (2019), p. 031102. DOI: 10.1103/PhysRevD.100.031102. arXiv: 1902.06794 [hep-ex].

[35] Serguei Chatrchyan et al. "Measurement of the Λ_b cross section and the $\overline{\Lambda}_b$ to Λ_b ratio with $J/\Psi\Lambda$ decays in pp collisions at $\sqrt{s} = 7$ TeV". In: *Phys. Lett.* B714 (2012), pp. 136–157. DOI: 10.1016/j.physletb.2012.05.063. arXiv: 1205.0594 [hep-ex].

[36] John Adams et al. "Experimental and theoretical challenges in the search for the quark gluon plasma: The STAR Collaboration's critical assessment of the evidence from RHIC collisions". In: *Nucl. Phys.* A757 (2005), pp. 102–183. DOI: 10.1016/j.nuclphysa.2005.03.085. arXiv: nucl-ex/0501009 [nucl-ex].

[37] K. Adcox et al. "Formation of dense partonic matter in relativistic nucleus-nucleus collisions at RHIC: Experimental evaluation by the PHENIX collaboration". In: *Nucl. Phys.* A757 (2005), pp. 184–283. DOI: 10.1016/j.nuclphysa.2005.03.086. arXiv: nucl-ex/0410003 [nucl-ex].

[38] I. Arsene et al. "Quark gluon plasma and color glass condensate at RHIC? The Perspective from the BRAHMS experiment". In: *Nucl. Phys.* A757 (2005), pp. 1–27. DOI: 10.1016/j.nuclphysa.2005.02.130. arXiv: nucl-ex/0410020 [nucl-ex].

[39] V. Greco, C. M. Ko, and R. Rapp. "Quark coalescence for charmed mesons in ultrarelativistic heavy ion collisions". In: *Phys. Lett.* B595 (2004), pp. 202–208. DOI: 10.1016/j.physletb.2004.06.064. arXiv: nucl-th/0312100 [nucl-th].

[40] Yongseok Oh et al. "Heavy baryon/meson ratios in relativistic heavy ion collisions". In: *Phys. Rev.* C79 (2009), p. 044905. DOI: 10.1103/PhysRevC.79.044905. arXiv: 0901.1382 [nucl-th].

[41] Jaroslav Adam et al. "Observation of enhancement of charmed baryon-to-meson ratio in Au+Au collisions at $\sqrt{s_{\mathrm{NN}}} = 200$ GeV". In: *Phys. Rev. Lett.* 124.17 (2020), p. 172301. DOI: 10.1103/PhysRevLett.124.172301. arXiv: 1910.14628 [nucl-ex].

[42] Shreyasi Acharya et al. "Λ_c^+ production in Pb–Pb collisions at $\sqrt{s_{\mathrm{NN}}} = 5.02$ TeV". In: *Phys. Lett.* B793 (2019), pp. 212–223. DOI: 10.1016/j.physletb.2019.04.046. arXiv: 1809.10922 [nucl-ex].

[43] Su Houng Lee et al. "Λ_c enhancement from strongly coupled quark-gluon plasma". In: *Phys. Rev. Lett.* 100 (2008), p. 222301. DOI: 10.1103/PhysRevLett.100.222301. arXiv: 0709.3637 [nucl-th].

[44] Jiaxing Zhao et al. "Sequential Coalescence with Charm Conservation in High Energy Nuclear Collisions". In: (2018). arXiv: 1805.10858 [hep-ph].

[45] Sungtae Cho et al. "Charmed hadron production in an improved quark coalescence model". In: (2019). arXiv: 1905.09774 [nucl-th].

[46] Min He and Ralf Rapp. "Hadronization and Charm-Hadron Ratios in Heavy-Ion Collisions". In: *Phys. Rev. Lett.* 124.4 (2020), p. 042301. DOI: 10.1103/PhysRevLett.124.042301. arXiv: 1905.09216 [nucl-th].

[47] Michele Arneodo. "Nuclear effects in structure functions". In: *Physics Reports* 240.5 (1994), pp. 301 –393. ISSN: 0370-1573. DOI: https://doi.org/10.1016/0370-1573(94)90048-5.

[48] Simona Malace et al. "The Challenge of the EMC Effect: existing data and future directions". In: *Int. J. Mod. Phys.* E23.08 (2014), p. 1430013. DOI: 10.1142/S0218301314300136. arXiv: 1405.1270 [nucl-ex].

[49] Kari J. Eskola et al. "EPPS16: Nuclear parton distributions with LHC data". In: *Eur. Phys. J.* C77.3 (2017), p. 163. DOI: 10.1140/epjc/s10052-017-4725-9. arXiv: 1612.05741 [hep-ph].

[50] K. Kovarik et al. "nCTEQ15 - Global analysis of nuclear parton distributions with uncertainties in the CTEQ framework". In: *Phys. Rev. D* 93.8 (2016), p. 085037. DOI: 10.1103/PhysRevD.93.085037. arXiv: 1509.00792 [hep-ph].

[51] Francois Gelis et al. "The Color Glass Condensate". In: *Ann. Rev. Nucl. Part. Sci.* 60 (2010), pp. 463–489. DOI: 10.1146/annurev.nucl.010909.083629. arXiv: 1002.0333 [hep-ph].

[52] Prithwish Tribedy and Raju Venugopalan. "QCD saturation at the LHC: Comparisons of models to p + p and A + A data and predictions for p + Pb collisions". In: *Phys. Lett.* B710 (2012). [Erratum: Phys. Lett.B718,1154(2013)], pp. 125–133. DOI: 10.1016/j.physletb.2012.02.047, 10.1016/j.physletb.2012.12.004. arXiv: 1112.2445 [hep-ph].

[53] Javier L. Albacete et al. "CGC predictions for p + Pb collisions at the LHC". In: *Nucl. Phys.* A897 (2013), pp. 1–27. DOI: 10.1016/j.nuclphysa.2012.09.012. arXiv: 1209.2001 [hep-ph].

[54] Amir H. Rezaeian. "CGC predictions for p+A collisions at the LHC and signature of QCD saturation". In: *Phys. Lett.* B718 (2013), pp. 1058–1069. DOI: 10.1016/j.physletb.2012.11.066. arXiv: 1210.2385 [hep-ph].

[55] Hirotsugu Fujii and Kazuhiro Watanabe. "Heavy quark pair production in high energy pA collisions: Open heavy flavors". In: *Nucl. Phys.* A920 (2013), pp. 78–93. DOI: 10.1016/j.nuclphysa.2013.10.006. arXiv: 1308.1258 [hep-ph].

[56] Ivan Vitev. "Non-Abelian energy loss in cold nuclear matter". In: *Phys. Rev.* C75 (2007), p. 064906. DOI: 10.1103/PhysRevC.75.064906. arXiv: hep-ph/0703002 [hep-ph].

[57] M. Lev and B. Petersson. "Nuclear Effects at Large Transverse Momentum in a QCD Parton Model". In: *Z. Phys.* C21 (1983), p. 155. DOI: 10.1007/BF01648792.

[58] Xin-Nian Wang. "Systematic study of high p_T hadron spectra in pp, p A and A A collisions from SPS to RHIC energies". In: *Phys. Rev.* C61 (2000), p. 064910. DOI: 10.1103/PhysRevC.61.064910. arXiv: nucl-th/9812021 [nucl-th].

[59] B. Z. Kopeliovich et al. "Cronin effect in hadron production off nuclei". In: *Phys. Rev. Lett.* 88 (2002), p. 232303. DOI: 10.1103/PhysRevLett.88.232303. arXiv: hep-ph/0201010 [hep-ph].

[60] Christian Bierlich, Torbjörn Sjöstrand, and Marius Utheim. "Hadronic Rescattering in pA and AA Collisions". In: (Mar. 2021). arXiv: 2103.09665 [hep-ph].

[61] Andrea Beraudo et al. "Heavy-flavour production in high-energy d-Au and p–Pb collisions". In: *JHEP* 03 (2016), p. 123. DOI: 10.1007/JHEP03(2016)123. arXiv: 1512.05186 [hep-ph].

[62] Yingru Xu et al. "Heavy-flavor dynamics in relativistic p–Pb collisions at $\sqrt{s_{\mathrm{NN}}} = 5.02$ TeV". In: *Nucl. Part. Phys. Proc.* 276-278 (2016), pp. 225–228. DOI: 10.1016/j.nuclphysbps.2016.05.050. arXiv: 1510.07520 [nucl-th].

[63] Serguei Chatrchyan et al. "Observation of long-range near-side angular correlations in proton-lead collisions at the LHC". In: *Phys. Lett.* B718 (2013), pp. 795–814. DOI: 10.1016/j.physletb.2012.11.025. arXiv: 1210.5482 [nucl-ex].

[64] Betty Abelev et al. "Long-range angular correlations on the near and away side in p–Pb collisions at $\sqrt{s_{\mathrm{NN}}} = 5.02$ TeV". In: *Phys. Lett.* B719 (2013), pp. 29–41. DOI: 10.1016/j.physletb.2013.01.012. arXiv: 1212.2001 [nucl-ex].

[65] Betty Abelev et al. "Long-range angular correlations of π, K and p in p–Pb collisions at $\sqrt{s_{\mathrm{NN}}} = 5.02$ TeV". In: *Phys. Lett.* B726 (2013), pp. 164–177. DOI: 10.1016/j.physletb.2013.08.024. arXiv: 1307.3237 [nucl-ex].

[66] Jaroslav Adam et al. "Forward-central two-particle correlations in p–Pb collisions at $\sqrt{s_{\mathrm{NN}}} = 5.02$ TeV". In: *Phys. Lett.* B753 (2016), pp. 126–139. DOI: 10.1016/j.physletb.2015.12.010. arXiv: 1506.08032 [nucl-ex].

[67] Shreyasi Acharya et al. "Multiplicity dependence of light-flavor hadron production in pp collisions at $\sqrt{s} = 7$ TeV". In: *Phys. Rev. C* 99.2 (2019), p. 024906. DOI: 10.1103/PhysRevC.99.024906. arXiv: 1807.11321 [nucl-ex].

[68] Shreyasi Acharya et al. "Multiplicity dependence of π, K, and p production in pp collisions at $\sqrt{s} = 13$ TeV". In: *Eur. Phys. J. C* 80.8 (2020), p. 693. DOI: 10.1140/epjc/s10052-020-8125-1. arXiv: 2003.02394 [nucl-ex].

[69] Jaroslav Adam et al. "Multiplicity dependence of charged pion, kaon, and (anti)proton production at large transverse momentum in p–Pb collisions at $\sqrt{s_{\rm NN}} = 5.02$ TeV". In: *Phys. Lett. B* 760 (2016), pp. 720–735. DOI: 10.1016/j.physletb.2016.07.050. arXiv: 1601.03658 [nucl-ex].

[70] James L. Nagle and William A. Zajc. "Small System Collectivity in Relativistic Hadronic and Nuclear Collisions". In: *Ann. Rev. Nucl. Part. Sci.* 68 (2018), pp. 211–235. DOI: 10.1146/annurev-nucl-101916-123209. arXiv: 1801.03477 [nucl-ex].

[71] K. J. Eskola, H. Paukkunen, and C. A. Salgado. "EPS09: A New Generation of NLO and LO Nuclear Parton Distribution Functions". In: *JHEP* 04 (2009), p. 065. DOI: 10.1088/1126-6708/2009/04/065. arXiv: 0902.4154 [hep-ph].

[72] Roel Aaij et al. "Prompt Λ_c^+ production in pPb collisions at $\sqrt{s_{\rm NN}} = 5.02$ TeV". In: *JHEP* 02 (2019), p. 102. DOI: 10.1007/JHEP02(2019)102. arXiv: 1809.01404 [hep-ex].

[73] Min He and Ralf Rapp. "Charm-Baryon Production in Proton-Proton Collisions". In: *Phys. Lett.* B795 (2019), pp. 117–121. DOI: 10.1016/j.physletb.2019.06.004. arXiv: 1902.08889 [nucl-th].

[74] Jun Song, Hai-hong Li, and Feng-lan Shao. "New feature of low p_T charm quark hadronization in pp collisions at $\sqrt{s} = 7$ TeV". In: *Eur. Phys. J.* C78.4 (2018), p. 344. DOI: 10.1140/epjc/s10052-018-5817-x. arXiv: 1801.09402 [hep-ph].

[75] Hai-Hong Li et al. "Production of single-charm hadrons by quark combination mechanism in p-Pb collisions at $\sqrt{s_{\rm NN}} = 5.02$ TeV". In: *Phys. Rev.* C97.6 (2018), p. 064915. DOI: 10.1103/PhysRevC.97.064915. arXiv: 1712.08921 [hep-ph].

[76] Shreyasi Acharya et al. "Measurement of D-meson production at mid-rapidity in pp collisions at $\sqrt{s} = 7$ TeV". In: *Eur. Phys. J.* C77.8 (2017), p. 550. DOI: 10.1140/epjc/s10052-017-5090-4. arXiv: 1702.00766 [hep-ex].

[77] Jaroslav Adam et al. "D-meson production in p–Pb collisions at $\sqrt{s_{\rm NN}} = 5.02$ TeV and in pp collisions at $\sqrt{s} = 7$ TeV". In: *Phys. Rev.* C94.5 (2016), p. 054908. DOI: 10.1103/PhysRevC.94.054908. arXiv: 1605.07569 [nucl-ex].

[78] S. Acharya et al. "Measurement of $\rm D^0$, $\rm D^+$, $\rm D^{*+}$ and $\rm D_s^+$ production in Pb–Pb collisions at $\sqrt{\rm s_{NN}} = 5.02$ TeV". In: *JHEP* 10 (2018), p. 174. DOI: 10.1007/JHEP10(2018)174. arXiv: 1804.09083 [nucl-ex].

[79] B. Abelev et al. "Measurement of charm production at central rapidity in proton-proton collisions at $\sqrt{s} = 7$ TeV". In: *JHEP* 01 (2012), p. 128. DOI: 10.1007/JHEP01(2012)128. arXiv: 1111.1553 [hep-ex].

[80] Betty Abelev et al. "D_s^+ meson production at central rapidity in proton–proton collisions at $\sqrt{s} = 7$ TeV". In: *Phys. Lett.* B718 (2012), pp. 279–294. DOI: 10.1016/j.physletb.2012.10.049. arXiv: 1208.1948 [hep-ex].

[81] Betty Abelev et al. "Measurement of charm production at central rapidity in proton-proton collisions at $\sqrt{s} = 2.76$ TeV". In: *JHEP* 07 (2012), p. 191. DOI: 10.1007/JHEP07(2012)191. arXiv: 1205.4007 [hep-ex].

[82] Shreyasi Acharya et al. "Λ_c^+ production and baryon-to-meson ratios in pp and p-Pb collisions at $\sqrt{s_{\rm NN}} = 5.02$ TeV at the LHC". In: (Nov. 2020). arXiv: 2011.06078 [nucl-ex].

[83] K. Aamodt et al. "The ALICE experiment at the CERN LHC". In: *JINST* 3 (2008), S08002. DOI: 10.1088/1748-0221/3/08/S08002.

[84] Betty Abelev et al. "Performance of the ALICE Experiment at the CERN LHC". In: *Int. J. Mod. Phys.* A29 (2014), p. 1430044. DOI: 10.1142/S0217751X14300440. arXiv: 1402.4476 [nucl-ex].

[85] K Aamodt et al. "Alignment of the ALICE Inner Tracking System with cosmic-ray tracks". In: *JINST* 5 (2010), P03003. DOI: 10.1088/1748-0221/5/03/P03003. arXiv: 1001.0502 [physics.ins-det].

[86] J. Alme et al. "The ALICE TPC, a large 3-dimensional tracking device with fast readout for ultra-high multiplicity events". In: *Nucl. Instrum. Meth. A* 622 (2010), pp. 316–367. DOI: 10.1016/j.nima.2010.04.042. arXiv: 1001.1950 [physics.ins-det].

[87] Jaroslav Adam et al. "Determination of the event collision time with the ALICE detector at the LHC". In: *Eur. Phys. J. Plus* 132.2 (2017), p. 99. DOI: 10.1140/epjp/i2017-11279-1. arXiv: 1610.03055 [physics.ins-det].

[88] S. Acharya et al. "ALICE 2017 luminosity determination for pp collisions at $\sqrt{s} = 5$ TeV". In: (2018). ALICE-PUBLIC-2018-014. URL: https://cds.cern.ch/record/2648933.

[89] Betty Abelev et al. "Measurement of visible cross sections in proton-lead collisions at $\sqrt{s_{\mathrm{NN}}} = 5.02$ TeV in van der Meer scans with the ALICE detector". In: *JINST* 9.11 (2014), P11003. DOI: 10.1088/1748-0221/9/11/P11003. arXiv: 1405.1849 [nucl-ex].

[90] P A Zyla et al. "Review of Particle Physics". In: *Progress of Theoretical and Experimental Physics* 2020 (). 083C01 (2020). ISSN: 2050-3911. DOI: 10.1093/ptep/ptaa104.

[91] Jaroslav Adam et al. "Particle identification in ALICE: a Bayesian approach". In: *Eur. Phys. J. Plus* 131.5 (2016), p. 168. DOI: 10.1140/epjp/i2016-16168-5. arXiv: 1602.01392 [physics.data-an].

[92] Andreas Hoecker et al. "TMVA: Toolkit for Multivariate Data Analysis". In: *PoS* ACAT (2007), p. 040. arXiv: physics/0703039.

[93] Torbjorn Sjöstrand, Stephen Mrenna, and Peter Z. Skands. "PYTHIA 6.4 Physics and Manual". In: *JHEP* 05 (2006), p. 026. DOI: 10.1088/1126-6708/2006/05/026. arXiv: hep-ph/0603175 [hep-ph].

[94] Peter Z. Skands. "The Perugia Tunes". In: *Proceedings, 1st International Workshop on Multiple Partonic Interactions at the LHC (MPI08): Perugia, Italy, October 27-31, 2008*. 2009, pp. 284–297. arXiv: 0905.3418 [hep-ph].

[95] Xin-Nian Wang and Miklos Gyulassy. "HIJING: A Monte Carlo model for multiple jet production in p p, p A and A A collisions". In: *Phys. Rev.* D44 (1991), pp. 3501–3516. DOI: 10.1103/PhysRevD.44.3501.

[96] Torbjorn Sjöstrand, Stephen Mrenna, and Peter Z. Skands. "A Brief Introduction to PYTHIA 8.1". In: *Comput. Phys. Commun.* 178 (2008), pp. 852–867. DOI: 10.1016/j.cpc.2008.01.036. arXiv: 0710.3820 [hep-ph].

[97] Stefano Frixione, Paolo Nason, and Giovanni Ridolfi. "A Positive-weight next-to-leading-order Monte Carlo for heavy flavour hadroproduction". In: *JHEP* 09 (2007), p. 126. DOI: 10.1088/1126-6708/2007/09/126. arXiv: 0707.3088 [hep-ph].

[98] Sayipjamal Dulat et al. "New parton distribution functions from a global analysis of quantum chromodynamics". In: *Phys. Rev.* D93.3 (2016), p. 033006. DOI: 10.1103/PhysRevD.93.033006. arXiv: 1506.07443 [hep-ph].

[99] B.A. Kniehl et al. "$\Lambda_c^\pm$ production in pp collisions with a new fragmentation function". In: *Phys. Rev. D* 101 (2020), p. 114021. DOI: 10.1103/PhysRevD.101.114021. arXiv: 2004.04213 [hep-ph].

[100] G. Alexander et al. "A Study of charm hadron production in $Z^0 \to c\bar{c}$ and $Z^0 \to b\bar{b}$ decays at LEP". In: *Z. Phys.* C72 (1996), pp. 1–16. DOI: 10.1007/s002880050218.

[101] M. Niiyama et al. "Production cross sections of hyperons and charmed baryons from e^+e^- annihilation near $\sqrt{s} = 10.52$˜GeV". In: *Phys. Rev. D* 97.7 (2018), p. 072005. DOI: 10.1103/PhysRevD.97.072005. arXiv: 1706.06791 [hep-ex].

[102] Shreyasi Acharya et al. "Measurement of prompt D^0, D^+, D^{*+}, and D_S^+ production in pâĂŞPb collisions at $\sqrt{s_{NN}} = 5.02$ TeV". In: *JHEP* 12 (2019), p. 092. DOI: 10.1007/JHEP12(2019)092. arXiv: 1906.03425 [nucl-ex].

[103] Christian Bierlich et al. "Effects of Overlapping Strings in pp Collisions". In: *JHEP* 03 (2015), p. 148. DOI: 10.1007/JHEP03(2015)148. arXiv: 1412.6259 [hep-ph].

[104] D. Ebert, R.N. Faustov, and V.O. Galkin. "Spectroscopy and Regge trajectories of heavy baryons in the relativistic quark-diquark picture". In: *Phys. Rev. D* 84 (2011), p. 014025. DOI: 10.1103/PhysRevD.84.014025. arXiv: 1105.0583 [hep-ph].

[105] Vincenzo Minissale, Salvatore Plumari, and Vincenzo Greco. "Charm Hadrons in pp collisions at LHC energy within a Coalescence plus Fragmentation approach". In: (Dec. 2020). arXiv: 2012.12001 [hep-ph].

[106] Salvatore Plumari et al. "Charmed Hadrons from Coalescence plus Fragmentation in relativistic nucleus-nucleus collisions at RHIC and LHC". In: *Eur. Phys. J.* C78.4 (2018), p. 348. DOI: 10.1140/epjc/s10052-018-5828-7. arXiv: 1712.00730 [hep-ph].

[107] Shreyasi Acharya et al. "Production of charged pions, kaons and (anti-)protons in Pb-Pb and inelastic pp collisions at $\sqrt{s_{\rm NN}}$ = 5.02 TeV". In: *Phys. Rev. C* 101.4 (2020), p. 044907. DOI: 10.1103/PhysRevC.101.044907. arXiv: 1910.07678 [nucl-ex].

[108] Betty Bezverkhny Abelev et al. "$\rm K^0_S$ and Λ production in Pb–Pb collisions at $\sqrt{s_{\rm NN}}$ = 2.76 TeV". In: *Phys. Rev. Lett.* 111 (2013), p. 222301. DOI: 10.1103/PhysRevLett.111.222301. arXiv: 1307.5530 [nucl-ex].

[109] Betty Bezverkhny Abelev et al. "Multiplicity Dependence of Pion, Kaon, Proton and Lambda Production in p–Pb Collisions at $\sqrt{s_{\rm NN}}$ = 5.02 TeV". In: *Phys. Lett. B* 728 (2014), pp. 25–38. DOI: 10.1016/j.physletb.2013.11.020. arXiv: 1307.6796 [nucl-ex].

[110] B Abelev et al. "Upgrade of the ALICE Experiment: Letter Of Intent". In: *J. Phys.* G41 (2014), p. 087001. DOI: 10.1088/0954-3899/41/8/087001.

Chapter 6

Λ_{c}^{+} production and baryon-to-meson ratios in pp and p–Pb collisions at $\sqrt{s_{\mathrm{NN}}} = 5.02$ TeV at the LHC

6.1 Declaration

This published work has been included in the place of a standard format chapter. My specific contribution to this work was the analysis of the $\Lambda_{\mathrm{c}}^{+} \rightarrow \mathrm{pK}^{-}\pi^{+}$ channel in pp and p–Pb collisions at $\sqrt{s_{\mathrm{NN}}} = 5.02$ TeV using data taken during LHC Run 2. I was part of the paper commitee who wrote the paper on behalf of the ALICE collaboration. The paper commitee was comprised of the same five analysers who wrote the analysis notes.

Permission to include this journal article [1] entitled "Λ_{c}^{+} production and baryon-to-meson ratios in pp and p–Pb collisions at $\sqrt{s_{\mathrm{NN}}} = 5.02$ TeV at the LHC", published in Physical Review Letters, CERN-EP-2020-217, arXiv:2011.06078, was given on behalf of the ALICE Collaboration co-authors by the Physics Co-ordinator and Editorial Board co-chairs. Their consent declaration can be found in Appendix A.

6.1.1 APS Statement of Copyright

6.2 Abstract

The prompt production of the charm baryon Λ_c^+ and the Λ_c^+/D^0 production ratios were measured at midrapidity with the ALICE detector in pp and p–Pb collisions at $\sqrt{s_{NN}} = 5.02$ TeV. These new measurements show a clear decrease of the Λ_c^+/D^0 ratio with increasing transverse momentum (p_T) in both collision systems in the range $2 < p_T < 12$ GeV/c, exhibiting similarities with the light-flavour baryon-to-meson ratios p/π and Λ/K_S^0. At low p_T, predictions that include additional colour-reconnection mechanisms beyond the leading-colour approximation; assume the existence of additional higher-mass charm-baryon states; or include hadronisation via coalescence can describe the data, while predictions driven by charm-quark fragmentation processes measured in e^+e^- and e^-p collisions significantly underestimate the data. The results presented in this letter provide significant evidence that the established assumption of universality (colliding-system independence) of parton-to-hadron fragmentation is not sufficient to describe charm-baryon production in hadronic collisions at LHC energies.

6.3 Introduction

Heavy-flavour hadron production in hadronic collisions occurs through the fragmentation of a charm or beauty quark, created in hard parton-parton scattering processes, into a given meson or baryon. Theoretical calculations of heavy-flavour production generally utilise the QCD factorisation theorem [2], which describes the hadron cross section as the convolution of three terms: the parton distribution functions, the parton hard-scattering cross sections, and the fragmentation functions. It is generally assumed that the fragmentation functions are universal between collision systems and energies, and the measurement of the relative production of different heavy-flavour hadron species is sensitive to fragmentation functions used in pQCD-based calculations. While perturbative calculations at next-to-leading order with next-to-leading-log resummation [3, 4, 5, 6] generally describe the D- and B-meson cross-section measurements [7, 8, 9, 10, 11] and the ratios of strange and non-strange D mesons [7, 11] within uncertainties, heavy-flavour baryon production is less well understood.

The Λ_c^+ production cross section in pp collisions at $\sqrt{s} = 7$ TeV and p–Pb collisions at $\sqrt{s_{NN}} = 5.02$ TeV was reported by ALICE [12]. It was shown that in both collision systems the p_T-differential Λ_c^+ production cross section is higher

than predictions from pQCD calculations with charm fragmentation tuned on previous e^+e^- and e^-p measurements [3, 4]. The Λ_c^+/D^0 ratio in pp and p–Pb collisions is consistent in both collision systems and also significantly underestimated by several Monte Carlo (MC) generators implementing different charm-quark fragmentation processes [13, 14, 15, 16], suggesting that the fragmentation fractions of charm quarks into different hadronic states are non-universal with respect to collision system and centre-of-mass energy. The production of charm baryons has recently been calculated within the k_T-factorisation approach using unintegrated gluon distribution functions and the Peterson fragmentation functions [17], and with the GM-VFNS scheme using updated fragmentation functions from OPAL and Belle [18]. These approaches are unable to simultaneously describe ALICE and LHCb data with the same set of parameters, suggesting that the independent parton fragmentation scheme is insufficient to fully describe the results. An alternative explanation has been offered by a statistical hadronisation model, taking into account an augmented list of charm-baryon states based on guidance from the Relativistic Quark Model (RQM) [19] and lattice QCD [20], which is able to reproduce the Λ_c^+/D^0 ratio measured by ALICE. The magnitude of the relative yields of Λ_b^0 baryons and beauty mesons in pp collisions measured by LHCb [21, 22, 23] and CMS [24] offers further evidence that the fragmentation fractions in the beauty sector also vary between collision systems.

The measurement of baryon production has also been important in heavy-ion collisions, where the high energy density and temperature create a colour-deconfined state of matter [25]. A measured enhancement of the light-flavour [26, 27] and charm [28, 29, 30] baryon-to-meson ratio at the LHC and RHIC can be explained via an additional mechanism of hadronisation known as coalescence (or recombination), where soft quarks from the medium recombine to form a meson or baryon [31], in addition to hydrodynamical radial flow. Measurements in p–Pb collisions are crucial to provide an 'intermediate' collision system where the generated particle multiplicities and energy densities are between those generated in pp and A–A collisions. ALICE and CMS reported an enhancement of the baryon-to-meson ratios in the light-flavour sector (p/π and Λ/K_S^0) at intermediate p_T ($2 < p_T < 10$ GeV/c) in high-multiplicity pp and p–Pb collisions, similar to that observed in heavy-ion collisions [32, 33]. This adds to the evidence that small systems also exhibit collective behaviour, which may have similar physical origins in pp, p–A, and A–A collisions [34]. It has been suggested that hadronisation of

charm quarks via coalescence may also occur in pp and p–Pb collisions [35, 36, 37].

In this letter, the measurements of the prompt production of the charm baryon Λ_c^+ in pp collisions at $\sqrt{s} = 5.02$ TeV in $|y| < 0.5$ and in p–Pb collisions at $\sqrt{s_{NN}} = 5.02$ TeV in $-0.96 < y < 0.04$ are presented, with a focus on the Λ_c^+/D^0 production ratios. The measurement is performed as an average of the Λ_c^+ and its charge conjugate $\overline{\Lambda}_c^-$, collectively referred to as Λ_c^+ in the following. Two hadronic decay channels were measured: $\Lambda_c^+ \to pK^-\pi^+$ (branching ratio BR $= 6.28 \pm 0.33\%$), and $\Lambda_c^+ \to pK_S^0$ (BR $= 1.59 \pm 0.08\%$)[38], which were reconstructed exploiting the topology of the weakly-decaying Λ_c^+ ($c\tau = 60.7\mu m$) [38]. The results from both decay channels were averaged to obtain more precise production cross sections. With respect to the results presented in [12], this work studies a different centre-of-mass energy for pp collisions, and the cross section is measured in finer p_T intervals and over a wider p_T range. The overall precision of the measurements is significantly improved, by a factor of 1.5–2, depending on p_T, for both pp and p–Pb collisions. For a detailed description of the analysis techniques, corrections, systematic uncertainty determination, and supplementary measurements, the reader is referred to [39].

6.4 Experimental setup and data Samples

A description of the ALICE detector and its performance are reported in [40, 41]. The pp data sample was collected in 2017 and the p–Pb data sample was collected in 2016 during the LHC Run 2. Both pp and p–Pb collisions were recorded using a Minimum Bias (MB) trigger, which required coincident signals in the two V0 scintillator detectors located on either side of the interaction vertex. Further offline selection was applied in order to remove background from beam–gas collisions and other machine-induced backgrounds. To reduce superposition of more than one interaction within the colliding bunches (pile-up), events with multiple reconstructed primary vertices were rejected. Only events with a z-coordinate of the reconstructed vertex position within 10 cm from the nominal interaction point were used. With these requirements, approximately one billion MB-triggered pp events were selected, corresponding to an integrated luminosity of $\mathcal{L}_{int} = 19.5$ nb^{-1}($\pm$ 2.1% [42]). Approximately 600 million MB-triggered p–Pb events were selected, corresponding to $\mathcal{L}_{int} = 287$ μb^{-1} ($\pm$ 3.7% [43]).

6.5 Λ_c^+ analysis overview and methods

The analysis techniques used for the results presented here are described in detail in [39]. Charged-particle tracks and particle decay vertices are reconstructed in the central barrel using the Inner Tracking System (ITS) and the Time Projection Chamber (TPC), which are located inside a solenoid magnet of field strength 0.5 T. In order to reduce the large combinatorial background, selections on the Λ_c^+ candidates were made based on the particle identification (PID) signals and the displacement of the decay tracks from the collision point. The PID was performed using information on the specific energy loss of charged particles as they pass through the gas of the TPC and, where available, with flight-time measurements given by the Time-Of-Flight detector (TOF).

For the $\Lambda_c^+ \to pK^-\pi^+$ analysis, candidates were built by reconstructing triplets of tracks with the correct configuration of charges. For this analysis, the high-resolution tracking provided by the detectors meant that the decay vertex of the Λ_c^+ candidates could be resolved from the interaction point. To identify each of the p, K, and π daughter tracks, information from the TPC and TOF was combined using the 'maximum-probability' Bayesian approach described in [44]. Kinematic selections were made on the p_T of the decay products of the Λ_c^+, and geometrical selections were made on topological properties related to the displaced vertex of the Λ_c^+ decay.

The reconstruction of $\Lambda_c^+ \to pK_S^0$ candidates relied on reconstructing the V-shaped decay of the K_S^0 meson into two pions, which was then combined with a proton track (bachelor). In pp collisions, candidates were further selected using criteria related to PID and properties of the $\Lambda_c^+ \to pK_S^0$ decay. The Bayesian probability of the combined TPC and TOF response for the bachelor track to be a proton was required to be above 80%. The selection criteria on kinematical and geometrical variables included the distance of closest approach between the decay daughters, the invariant mass, and the cosine of the pointing angle of the neutral decay vertex (K_S^0) to the primary vertex.

For the $\Lambda_c^+ \to pK_S^0$ decay channel in p–Pb collisions, the analysis was performed using a multivariate technique based on the Boosted Decision Tree (BDT) algorithm provided by the Toolkit for Multivariate Data Analysis (TMVA) [45]. The BDT algorithm was trained using signal and background $\Lambda_c^+ \to pK_S^0$ decay candidates simulated using PYTHIA 6.4.25 [46] with the Perugia2011 tune [47], and the underlying p–Pb event simulated with HIJING 1.36 [48]. Candidates

obtained with the same reconstruction strategy previously described were preselected using loose geometrical selections and PID selection on the bachelor proton track. The model was trained independently for each p_T interval analysed, with input variables comprising the p_T and Bayesian PID probability of the proton track, the $c\tau$ and invariant mass of the K_S^0, and the impact parameters of the Λ_c^+ decay tracks to the primary vertex. This model was then applied on data, and a selection on the output response was chosen based on the expected maximum significance determined from simulations.

For both decay channels the yield of Λ_c^+ baryons was extracted in each p_T interval via fits to the candidate invariant-mass distributions. The fitting function consisted of a Gaussian to estimate the signal and an exponential or polynomial function to estimate the background. The width of the Gaussian was fixed in each p_T interval to values obtained from Monte Carlo simulations, and the mean was treated as a free parameter. A statistical significance higher than 4 standard deviations was achieved in all p_T intervals.

6.6 Corrections

Several corrections were applied to the measurement of the Λ_c^+ cross section. The geometrical acceptance of the detector as well as the selection and reconstruction efficiencies for prompt Λ_c^+ were taken into account. These correction factors were determined from pp collisions generated with PYTHIA 6 and PYTHIA 8.243 [49], with each event including either a $c\bar{c}$ or a $b\bar{b}$ pair. For p–Pb collisions, this was supplemented with an underlying event from the HIJING event generator. In p–Pb collisions the efficiency was calculated after reweighting the events based on their charged particle multiplicity. This accounts for the fact that the event multiplicity in simulation does not reproduce the one in data, and the efficiency depends on the multiplicity of the event as a consequence of the improvement of the resolution of the primary vertex and thus of the performance of the topological selections at higher multiplicities. The fraction of the Λ_c^+ yield originating from beauty decays (feed-down) was obtained using the beauty-quark production cross section from FONLL [5, 6], the fraction of beauty quarks that fragment into beauty hadrons H_b from LHCb measurements [23], and $H_b \to \Lambda_c^+ + X$ decay kinematics from PYTHIA 8, as well as the selection and reconstruction efficiency of Λ_c^+ from beauty-hadron decays. The fraction of the Λ_c^+ yield from beauty decays

was found to be 2% at low p_T and up to 16% at high p_T, and was subtracted from the measured yield. As done in the D-meson analysis [50], the possible modification of beauty-hadron production in p–Pb collisions was included in the feed-down calculation by scaling the beauty-quark production by a nuclear modification factor $R_{pPb}^{feed\text{-}down}$, where it was assumed that $R_{pPb}^{feed\text{-}down} = R_{pPb}^{prompt}$ with their ratio varied in the range $0.9 < R_{pPb}^{feed\text{-}down}/R_{pPb}^{prompt} < 1.3$ to evaluate the systematic uncertainties.

6.7 Evaluation of systematic uncertainties

Systematic uncertainties on the Λ_c^+ cross sections were estimated considering the same sources as described in [12]. The contributions from the raw-yield extraction were evaluated by repeating the fits varying the fit interval and the functional form of the background fit function. For each of these variations the four combinations of free and fixed Gaussian mean and width parameters of the fit were considered. Overall, the relative uncertainty ranged from 4% to 11% depending on the p_T and analysis. The uncertainties on the track reconstruction efficiency were estimated by adding in quadrature the uncertainty due to track quality selection and the uncertainty due to the TPC-ITS matching efficiency (from 3% to 7%). The former is estimated by varying the track-quality selection criteria and the latter is estimated by comparing the probability to match the tracks from the TPC to the ITS hits in data and simulation. The uncertainty on the Λ_c^+ selection efficiency was estimated by varying the selection on the kinematical and topological properties of the Λ_c^+ decays, or the selection on the BDT response (from 3% to 15%). The uncertainty on the PID efficiency was estimated by varying the selection on the Bayesian probability variables (from 2% to 5%). The systematic effect on the efficiencies due to the shape of the simulated Λ_c^+ p_T distribution was evaluated by reweighting the generated Λ_c^+ from PYTHIA 6 to match the p_T distribution obtained from FONLL calculations for D mesons (maximum 1% uncertainty). The relative statistical uncertainty on the acceptance and efficiency correction was considered as an additional systematic uncertainty source (from 1–2% at low p_T to 3–5% at high p_T). The uncertainties on f_{prompt} were estimated by varying the hypothesis on the production of Λ_c^+ from B-hadron decays to account for the theoretical uncertainties of b-quark production within FONLL and experimental uncertainties on B-hadron fragmentation (around 2% at low p_T, and

from 4% to 7% at high p_T, depending on the analysis). Global uncertainties of the measurement include those from the luminosity and Λ_c^+ branching ratios. The raw-yield extraction uncertainty source are considered to be uncorrelated across p_T bins, while all other sources are considered to be correlated.

The results in each collision system from the two Λ_c^+ decay channels were averaged to obtain the final results. A weighted average of the results was calculated, with weights defined as the inverse of the quadratic sum of the relative statistical and uncorrelated systematic uncertainties. The sources of systematic uncertainty assumed to be uncorrelated between different decay channels were those due to the raw-yield extraction, the statistical uncertainties on the efficiency and acceptance, and those related to the Λ_c^+ selection. The remaining uncertainties were assumed to be correlated, except the branching ratio uncertainties, which were treated as partially correlated among the hadronic-decay modes as defined in [38].

6.8 Results

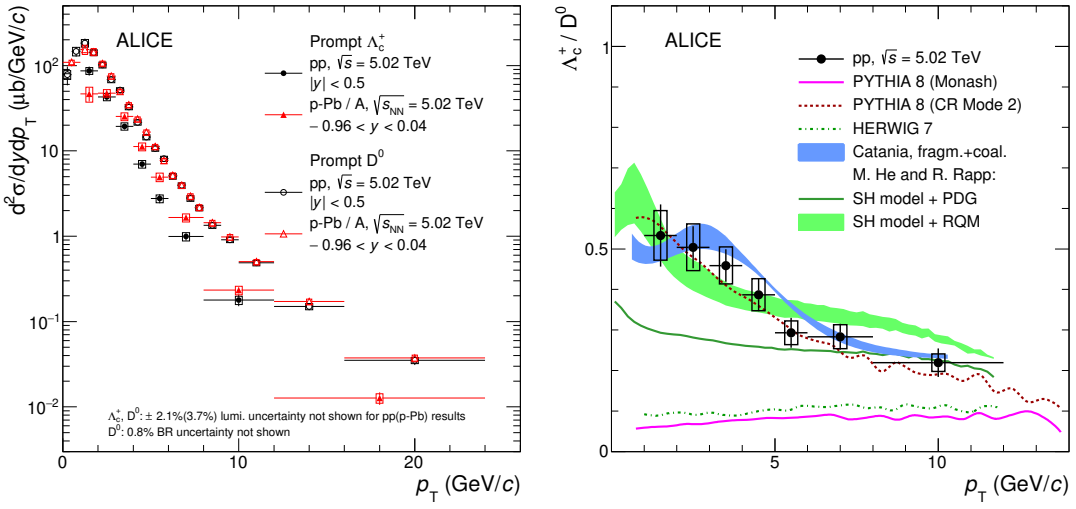

FIGURE 6.1: Left: Prompt Λ_c^+ and D^0 p_T-differential cross section in pp collisions and in p–Pb collisions at $\sqrt{s_{NN}} = 5.02$ TeV. The results in p–Pb collisions are scaled with the atomic mass number A of the Pb nucleus. Right: the Λ_c^+/D^0 ratio as a function of p_T measured in pp collisions at $\sqrt{s} = 5.02$ TeV compared with theoretical predictions (see text for details). Statistical uncertainties are shown as vertical bars, while systematic uncertainties are shown as boxes, and the bin widths are shown as horizontal bars.

Figure 6.1 (left) shows a comparison of the Λ_c^+ p_T-differential cross sections in pp and in p–Pb collisions at $\sqrt{s_{NN}} = 5.02$ TeV. The D^0 p_T-differential cross

sections measured in the same collision systems and at the same centre-of-mass energy during the same data taking periods [11, 51] are also shown. In order to compare the spectral shapes in the two different collision systems at the same energy, the results in p–Pb collisions are scaled by the atomic mass number of the lead nucleus. For Λ_c^+ baryons the spectral shape in p–Pb collisions is slightly harder than in pp collisions, while for D^0 mesons the spectral shapes are fully consistent within uncertainties.

Figure 6.1 (right) shows the baryon-to-meson ratio Λ_c^+/D^0 measured in pp collisions at $\sqrt{s} = 5.02$ TeV as a function of p_T, compared to theoretical predictions. The uncertainty on the luminosity cancels in the ratio. The Λ_c^+/D^0 ratio is measured to be 0.4–0.5 at low p_T, and decreases to around 0.2 at high p_T. The previous results at $\sqrt{s} = 7$ TeV hinted at a decrease of the Λ_c^+/D^0 ratio with p_T, although the precision was not enough to confirm this [12]. The results in pp collisions at $\sqrt{s} = 5.02$ TeV, with much higher precision than $\sqrt{s} = 7$ TeV results, show a clear decrease with increasing p_T. The strong p_T-dependence of the Λ_c^+/D^0 ratio is in contrast with the ratios of strange and non-strange D mesons in pp collisions at $\sqrt{s} = 5.02$ TeV and $\sqrt{s} = 7$ TeV [11, 52] and in p–Pb collisions at $\sqrt{s_{NN}} = 5.02$ TeV [51], which do not show a significant p_T dependence within uncertainties and thus indicate that there are no large differences between fragmentation functions of charm quarks to charm mesons. The result presented here instead provides strong indications that the fragmentation functions of baryons and mesons differ significantly.

The measured Λ_c^+/D^0 ratios in pp collisions are compared with predictions from several MC generators and models in which different hadronisation processes are implemented. The PYTHIA 8 predictions include the Monash tune [13] and a tune that implements colour reconnection beyond the leading-colour approximation, corresponding to CR Mode 2 as defined in [14]. Hadronisation in PYTHIA is built on the Lund string fragmentation model [53, 54], where quarks and gluons connected by colour strings fragment into hadrons, and colour reconnection allows for partons created in the collision to interact via colour strings. The latter tune introduces new colour reconnection topologies beyond the leading-colour approximation, including 'junctions' that fragment into baryons, leading to increased baryon production. As a technical point, the PYTHIA 8 simulations are generated with all soft QCD processes switched on [49]. The PYTHIA 8 Monash tune and HERWIG 7.2 [16] predictions are driven by the fragmentation fraction

$f(c \to \Lambda_c^+)$ implemented in these generators, which all suggest a relatively constant Λ_c^+/D^0 ratio versus p_T of about 0.1, significantly underestimating the data at low p_T. At high p_T, the data approach the predictions from these generators, although the measurement in $8 < p_T < 12$ GeV/c is still underestimated by about a factor of 2. A significant enhancement of the Λ_c^+/D^0 ratio is seen with colour reconnection beyond the leading-colour approximation (PYTHIA 8 CR Mode 2). This prediction is consistent with the measured Λ_c^+/D^0 ratio in pp collisions, also reproducing the downward p_T trend. The statistical hadronisation model ('SH model' in the legend) [20] uses either an underlying charm-baryon spectrum taken from the PDG, or includes additional excited charm baryons that have not yet been observed but are predicted by the RQM. These additional states decay strongly to Λ_c^+ baryons, which contribute to the prompt Λ_c^+ spectrum. The RQM predictions include a source of uncertainty related to the branching ratios of the excited baryon states into Λ_c^+ final states, which is estimated by varying the branching ratios between 50% and 100%. With the PDG charm-baryon spectrum the model underpredicts the data. With the additional baryon states the model instead gives a good description of the pp data, both in the magnitude of the ratio, and the decreasing trend with p_T. The Catania model [37] assumes that a colour-deconfined state of matter is formed and hadronisation can occur via coalescence in addition to fragmentation. Coalescence is implemented through the Wigner formalism, where a blast wave model is used to determine the p_T spectrum of light quarks and FONLL pQCD calculations are used for heavy quarks. Hadronisation via coalescence is predicted to dominate at low p_T, while fragmentation dominates at high p_T. This model provides a good description of both the magnitude and shape of the data over the full p_T range.

Figure 6.2 shows the Λ_c^+/D^0 baryon-to-meson ratio measured in pp collisions at $\sqrt{s} = 5.02$ TeV (left) and in p–Pb collisions at $\sqrt{s_{NN}} = 5.02$ TeV (right) as a function of p_T, compared to baryon-to-meson ratios in the light-flavour sector, Λ/K_S^0 [26, 55] and p/π [32, 56] (calculated as the sum of both charged particles and antiparticles, $(p + \bar{p})/(\pi^+ + \pi^-)$). The p/π ratio in pp collisions is shown at both $\sqrt{s} = 5.02$ TeV and $\sqrt{s} = 7$ TeV, displaying consistent results at both centre-of-mass energies, while the Λ/K_S^0 ratio in pp collisions is shown only at $\sqrt{s} = 7$ TeV. Unlike heavy-flavour hadron production, which occurs primarily through the fragmentation of a charm quark produced in the initial hard scattering, light-flavour hadrons have a significant contribution from gluon fragmentation. Low-p_T light-flavour hadrons also primarily originate from soft scattering

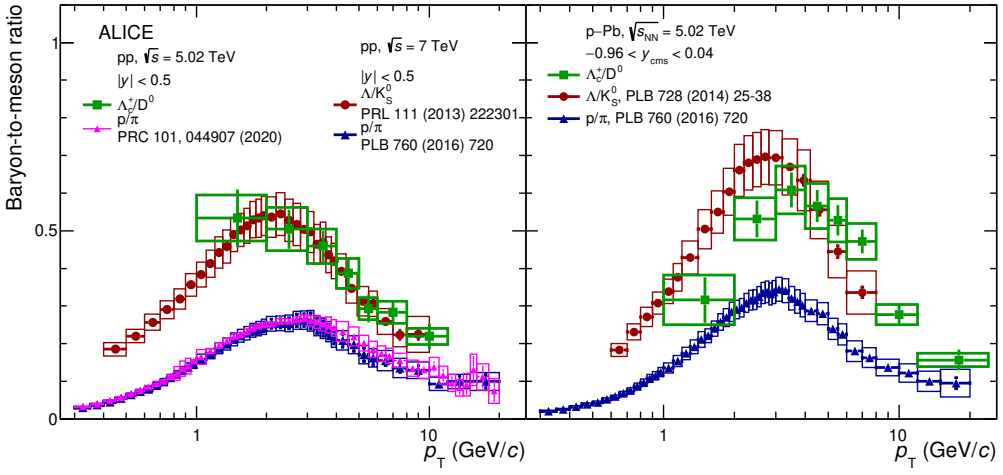

FIGURE 6.2: The charm baryon-to-meson ratio Λ_c^+/D^0 in pp collisions (left), and p–Pb collisions (right) at $\sqrt{s_{NN}} = 5.02$ TeV, compared to the light-flavour baryon-to-meson ratios Λ/K_S^0 and p/π. Statistical uncertainties are shown as vertical bars, while systematic uncertainties are shown as boxes, and the bin widths are shown as horizontal bars.

processes involving small momentum transfers. All particle yields in these ratios were corrected for feed-down from weak decays, although the pion spectrum is expected to have significant feed-down contributions also from the strong decays of other particle species, primarily ρ and ω mesons. Despite these differences, the three ratios, Λ_c^+/D^0, Λ/K_S^0, and p/π demonstrate some remarkably similar characteristics in both collision systems. All ratios exhibit a decreasing trend after $p_T \gtrsim 2$–3 GeV/c. The Λ_c^+/D^0 and Λ/K_S^0 ratios are consistent, in terms of both shape and magnitude, within uncertainties. The light-flavour ratios both peak at ∼2–3 GeV/c in both pp and p–Pb collisions, and there is an indication of a peak at $2 < p_T < 4$ GeV/c in the Λ_c^+/D^0 ratio in p–Pb collisions. These similarities between heavy-flavour and light-flavour measurements hint at a potential common mechanism for light- and charm-baryon formation in pp and p–Pb collisions at LHC energies. It is interesting to note that all baryon-to-meson ratios also indicate a shift toward higher momenta in p–Pb collisions, which for light-flavour particle production is often attributed to radial flow [55]. However, while flow effects in the charm sector (D^0 and heavy-flavour decay leptons) have been observed in high-multiplicity p–Pb collisions [57, 58], these effects are expected to be smaller at lower multiplicities, and also smaller for charm than for light-flavour hadrons.

6.9 Conclusions

In summary, Λ_c^+-baryon production was measured in pp collisions at midrapidity ($|y| < 0.5$) and in p–Pb collisions in the rapidity interval $-0.96 < y < 0.04$ at $\sqrt{s_{\rm NN}} = 5.02$ TeV. A clear $p_{\rm T}$-dependence of the $\Lambda_c^+/{\rm D}^0$ ratio is reported, with the ratio decreasing as the $p_{\rm T}$ increases. This trend is similar to that of baryon-to-meson ratios measured in the light-flavour sector in pp and p–Pb collisions, suggesting common mechanisms for light- and charm-baryon formation. While models incorporating fragmentation parameters from $\rm e^+e^-$ and $\rm e^-p$ collisions significantly underestimate the $\Lambda_c^+/{\rm D}^0$ ratio, three models can reproduce the measurements. The first is a tune of PYTHIA 8 which considers that, in pp collisions at high energy, multi-parton interactions produce a rich hadronic environment that requires an extension of colour reconnection in hadronisation processes beyond the leading-colour approximation. The second method is the SH+RQM model, which relies on the presence of a large set of yet-unobserved higher-mass charm-baryon states with relative yields following the Statistical Hadronisation model. The third relies on hadronisation via coalescence and fragmentation after the formation of a colour-deconfined state of matter. All three models imply a substantially different description of the charm-baryon production in pp collisions with respect to $\rm e^+e^-$ and $\rm e^-p$ collisions, indicating that the assumption of universal parton-to-hadron fragmentation between collision systems is not sufficient to describe charm-baryon production.

References

[1] S. Acharya et al. "Λ_c^+ Production and Baryon-to-Meson Ratios in *pp* and *p*-Pb Collisions at $\sqrt{s_{\rm NN}} = 5.02$ TeV at the LHC". In: *Phys. Rev. Lett.* 127 (20 2021), p. 202301. DOI: 10.1103/PhysRevLett.127.202301. URL: https://link.aps.org/doi/10.1103/PhysRevLett.127.202301.

[2] John C. Collins, Davison E. Soper, and George F. Sterman. "Factorization of Hard Processes in QCD". In: *Adv. Ser. Direct. High Energy Phys.* 5 (1989), pp. 1–91. DOI: 10.1142/9789814503266_0001. arXiv: hep-ph/0409313.

[3] B. A. Kniehl et al. "Collinear subtractions in hadroproduction of heavy quarks". In: *Eur. Phys. J. C* 41 (2005), pp. 199–212. DOI: 10.1140/epjc/s2005-02200-7. arXiv: hep-ph/0502194.

[4] B. A. Kniehl et al. "Inclusive Charmed-Meson Production at the CERN LHC". In: *Eur. Phys. J.* C72 (2012), p. 2082. DOI: 10.1140/epjc/s10052-012-2082-2. arXiv: 1202.0439 [hep-ph].

[5] Matteo Cacciari, Mario Greco, and Paolo Nason. "The P(T) spectrum in heavy flavor hadroproduction". In: *JHEP* 05 (1998), p. 007. DOI: 10.1088/1126-6708/1998/05/007. arXiv: hep-ph/9803400.

[6] Matteo Cacciari et al. "Theoretical predictions for charm and bottom production at the LHC". In: *JHEP* 10 (2012), p. 137. DOI: 10.1007/JHEP10(2012)137. arXiv: 1205.6344 [hep-ph].

[7] A. Andronic et al. "Heavy-flavour and quarkonium production in the LHC era: from protonâĂŞproton to heavy-ion collisions". In: *Eur. Phys. J.* C76.3 (2016), p. 107. DOI: 10.1140/epjc/s10052-015-3819-5. arXiv: 1506.03981 [nucl-ex].

[8] Roel Aaij et al. "Measurements of prompt charm production cross-sections in *pp* collisions at $\sqrt{s} = 13$ TeV". In: *JHEP* 03 (2016). [Erratum: JHEP09,013(2016); Erratum: JHEP05,074(2017)], p. 159. DOI: 10.1007/JHEP03(2016)159, 10.1007/JHEP09(2016)013, 10.1007/JHEP05(2017)074. arXiv: 1510.01707 [hep-ex].

[9] Vardan Khachatryan et al. "Measurement of the total and differential inclusive B^+ hadron cross sections in pp collisions at $\sqrt{s} = 13$ TeV". In: *Phys. Lett.* B771 (2017), pp. 435–456. DOI: 10.1016/j.physletb.2017.05.074. arXiv: 1609.00873 [hep-ex].

[10] Roel Aaij et al. "Measurement of the $B^\pm$ production cross-section in pp collisions at $\sqrt{s} = 7$ and 13 TeV". In: *JHEP* 12 (2017), p. 026. DOI: 10.1007/JHEP12(2017)026. arXiv: 1710.04921 [hep-ex].

[11] Shreyasi Acharya et al. "Measurement of D^0 , D^+ , D^{*+} and D_s^+ production in pp collisions at $\sqrt{s} = 5.02$ TeV with ALICE". In: *Eur. Phys. J.* C79.5 (2019), p. 388. DOI: 10.1140/epjc/s10052-019-6873-6. arXiv: 1901.07979 [nucl-ex].

[12] Shreyasi Acharya et al. "Λ_c^+ production in pp collisions at $\sqrt{s} = 7$ TeV and in p–Pb collisions at $\sqrt{s_{\rm NN}} = 5.02$ TeV". In: *JHEP* 04 (2018), p. 108. DOI: 10.1007/JHEP04(2018)108. arXiv: 1712.09581 [nucl-ex].

[13] Peter Skands, Stefano Carrazza, and Juan Rojo. "Tuning PYTHIA 8.1: the Monash 2013 Tune". In: *Eur. Phys. J.* C74.8 (2014), p. 3024. DOI: 10.1140/epjc/s10052-014-3024-y. arXiv: 1404.5630 [hep-ph].

[14] Jesper R. Christiansen and Peter Z. Skands. "String Formation Beyond Leading Colour". In: *JHEP* 08 (2015), p. 003. DOI: 10.1007/JHEP08(2015)003. arXiv: 1505.01681 [hep-ph].

[15] Christian Bierlich and Jesper Roy Christiansen. "Effects of color reconnection on hadron flavor observables". In: *Phys. Rev.* D92.9 (2015), p. 094010. DOI: 10.1103/PhysRevD.92.094010. arXiv: 1507.02091 [hep-ph].

[16] Johannes Bellm et al. "Herwig 7.0/Herwig++ 3.0 release note". In: *Eur. Phys. J. C* 76.4 (2016), p. 196. DOI: 10.1140/epjc/s10052-016-4018-8. arXiv: 1512.01178 [hep-ph].

[17] RafaÅĆ MaciuÅĆa and Antoni Szczurek. "Production of Λ_c baryons at the LHC within the k_T-factorization approach and independent parton fragmentation picture". In: *Phys. Rev.* D98.1 (2018), p. 014016. DOI: 10.1103/PhysRevD.98.014016. arXiv: 1803.05807 [hep-ph].

[18] B.A. Kniehl et al. "$\Lambda_c^\pm$ production in pp collisions with a new fragmentation function". In: *Phys. Rev. D* 101 (2020), p. 114021. DOI: 10.1103/PhysRevD.101.114021. arXiv: 2004.04213 [hep-ph].

[19] D. Ebert, R.N. Faustov, and V.O. Galkin. "Spectroscopy and Regge trajectories of heavy baryons in the relativistic quark-diquark picture". In: *Phys. Rev. D* 84 (2011), p. 014025. DOI: 10.1103/PhysRevD.84.014025. arXiv: 1105.0583 [hep-ph].

[20] Min He and Ralf Rapp. "Charm-Baryon Production in Proton-Proton Collisions". In: *Phys. Lett.* B795 (2019), pp. 117–121. DOI: 10.1016/j.physletb.2019.06.004. arXiv: 1902.08889 [nucl-th].

[21] R. Aaij et al. "Measurement of b-hadron production fractions in 7 TeV pp collisions". In: *Phys. Rev.* D85 (2012), p. 032008. DOI: 10.1103/PhysRevD.85.032008. arXiv: 1111.2357 [hep-ex].

[22] R. Aaij et al. "Study of the production of Λ_b^0 and $\overline{B}^0$ hadrons in pp collisions and first measurement of the $\Lambda_b^0 \to J/\psi p K^-$ branching fraction". In: *Chin. Phys.* C40.1 (2016), p. 011001. DOI: 10.1088/1674-1137/40/1/011001. arXiv: 1509.00292 [hep-ex].

[23] Roel Aaij et al. "Measurement of b hadron fractions in 13 TeV pp collisions". In: *Phys. Rev.* D100.3 (2019), p. 031102. DOI: 10.1103/PhysRevD.100.031102. arXiv: 1902.06794 [hep-ex].

[24] Serguei Chatrchyan et al. "Measurement of the Λ_b cross section and the $\overline{\Lambda}_b$ to Λ_b ratio with $J/\Psi\Lambda$ decays in pp collisions at $\sqrt{s} = 7$ TeV". In: *Phys. Lett.* B714 (2012), pp. 136–157. DOI: 10.1016/j.physletb.2012.05.063. arXiv: 1205.0594 [hep-ex].

[25] Wit Busza, Krishna Rajagopal, and Wilke van der Schee. "Heavy Ion Collisions: The Big Picture, and the Big Questions". In: *Ann. Rev. Nucl. Part. Sci.* 68 (2018), pp. 339–376. DOI: 10.1146/annurev-nucl-101917-020852. arXiv: 1802.04801 [hep-ph].

[26] Betty Bezverkhny Abelev et al. "K_S^0 and Λ production in Pb–Pb collisions at $\sqrt{s_{NN}} = 2.76$ TeV". In: *Phys. Rev. Lett.* 111 (2013), p. 222301. DOI: 10.1103/PhysRevLett.111.222301. arXiv: 1307.5530 [nucl-ex].

[27] John Adams et al. "Measurements of identified particles at intermediate transverse momentum in the STAR experiment from Au + Au collisions at $\sqrt{s_{NN}} = 200$ GeV". In: (Jan. 2006). arXiv: nucl-ex/0601042.

[28] Shreyasi Acharya et al. "Λ_c^+ production in Pb–Pb collisions at $\sqrt{s_{NN}} = 5.02$ TeV". In: *Phys. Lett.* B793 (2019), pp. 212–223. DOI: 10.1016/j.physletb.2019.04.046. arXiv: 1809.10922 [nucl-ex].

[29] Jaroslav Adam et al. "Observation of enhancement of charmed baryon-to-meson ratio in Au+Au collisions at $\sqrt{s_{NN}} = 200$ GeV". In: *Phys. Rev. Lett.* 124.17 (2020), p. 172301. DOI: 10.1103/PhysRevLett.124.172301. arXiv: 1910.14628 [nucl-ex].

[30] Albert M Sirunyan et al. "Production of Λ_c^+ baryons in proton-proton and lead-lead collisions at $\sqrt{s_{NN}} = 5.02$ TeV". In: *Phys. Lett. B* 803 (2020), p. 135328. DOI: 10.1016/j.physletb.2020.135328. arXiv: 1906.03322 [hep-ex].

[31] Rainer J. Fries, Vincenzo Greco, and Paul Sorensen. "Coalescence Models For Hadron Formation From Quark Gluon Plasma". In: *Ann. Rev. Nucl. Part. Sci.* 58 (2008), pp. 177–205. DOI: 10.1146/annurev.nucl.58.110707.171134. arXiv: 0807.4939 [nucl-th].

[32] Jaroslav Adam et al. "Multiplicity dependence of charged pion, kaon, and (anti)proton production at large transverse momentum in p–Pb collisions at $\sqrt{s_{NN}} = 5.02$ TeV". In: *Phys. Lett. B* 760 (2016), pp. 720–735. DOI: 10.1016/j.physletb.2016.07.050. arXiv: 1601.03658 [nucl-ex].

[33] Vardan Khachatryan et al. "Multiplicity and rapidity dependence of strange hadron production in pp, pPb, and PbPb collisions at the LHC". In: *Phys. Lett.* B768 (2017), pp. 103–129. DOI: 10.1016/j.physletb.2017.01.075. arXiv: 1605.06699 [nucl-ex].

[34] James L. Nagle and William A. Zajc. "Small System Collectivity in Relativistic Hadronic and Nuclear Collisions". In: *Ann. Rev. Nucl. Part. Sci.* 68 (2018), pp. 211–235. DOI: 10.1146/annurev-nucl-101916-123209. arXiv: 1801.03477 [nucl-ex].

[35] Jun Song, Hai-hong Li, and Feng-lan Shao. "New feature of low p_T charm quark hadronization in pp collisions at $\sqrt{s} = 7$ TeV". In: *Eur. Phys. J.* C78.4 (2018), p. 344. DOI: 10.1140/epjc/s10052-018-5817-x. arXiv: 1801.09402 [hep-ph].

[36] Hai-Hong Li et al. "Production of single-charm hadrons by quark combination mechanism in p-Pb collisions at $\sqrt{s_{NN}} = 5.02$ TeV". In: *Phys. Rev.* C97.6 (2018), p. 064915. DOI: 10.1103/PhysRevC.97.064915. arXiv: 1712.08921 [hep-ph].

[37] Vincenzo Minissale, Salvatore Plumari, and Vincenzo Greco. "Charm Hadrons in pp collisions at LHC energy within a Coalescence plus Fragmentation approach". In: (Dec. 2020). arXiv: 2012.12001 [hep-ph].

[38] P A Zyla et al. "Review of Particle Physics". In: *Progress of Theoretical and Experimental Physics* 2020 (). 083C01 (2020). ISSN: 2050-3911. DOI: 10.1093/ptep/ptaa104.

[39] Shreyasi Acharya et al. "Λ_c^+ production in pp and in p-Pb collisions at $\sqrt{s_{NN}} = 5.02$ TeV". In: (Nov. 2020). arXiv: 2011.06079 [nucl-ex].

[40] K. Aamodt et al. "The ALICE experiment at the CERN LHC". In: *JINST* 3 (2008), S08002. DOI: 10.1088/1748-0221/3/08/S08002.

[41] Betty Abelev et al. "Performance of the ALICE Experiment at the CERN LHC". In: *Int. J. Mod. Phys.* A29 (2014), p. 1430044. DOI: 10.1142/S0217751X14300440. arXiv: 1402.4476 [nucl-ex].

[42] "ALICE 2017 luminosity determination for pp collisions at $\sqrt{s} = 5$ TeV". In: (2018). ALICE-PUBLIC-2018-014. URL: http://cds.cern.ch/record/2648933.

[43] Betty Abelev et al. "Measurement of visible cross sections in proton-lead collisions at $\sqrt{s_{NN}} = 5.02$ TeV in van der Meer scans with the ALICE detector". In: *JINST* 9.11 (2014), P11003. DOI: 10.1088/1748-0221/9/11/P11003. arXiv: 1405.1849 [nucl-ex].

[44] Jaroslav Adam et al. "Particle identification in ALICE: a Bayesian approach". In: *Eur. Phys. J. Plus* 131.5 (2016), p. 168. DOI: 10.1140/epjp/i2016-16168-5. arXiv: 1602.01392 [physics.data-an].

[45] Andreas Hoecker et al. "TMVA: Toolkit for Multivariate Data Analysis". In: *PoS* ACAT (2007), p. 040. arXiv: physics/0703039.

[46] Torbjorn Sjöstrand, Stephen Mrenna, and Peter Z. Skands. "PYTHIA 6.4 Physics and Manual". In: *JHEP* 05 (2006), p. 026. DOI: 10.1088/1126-6708/2006/05/026. arXiv: hep-ph/0603175 [hep-ph].

[47] Peter Z. Skands. "The Perugia Tunes". In: *Proceedings, 1st International Workshop on Multiple Partonic Interactions at the LHC (MPI08): Perugia, Italy, October 27-31, 2008*. 2009, pp. 284–297. arXiv: 0905.3418 [hep-ph].

[48] Xin-Nian Wang and Miklos Gyulassy. "HIJING: A Monte Carlo model for multiple jet production in p p, p A and A A collisions". In: *Phys. Rev.* D44 (1991), pp. 3501–3516. DOI: 10.1103/PhysRevD.44.3501.

[49] Torbjorn Sjöstrand, Stephen Mrenna, and Peter Z. Skands. "A Brief Introduction to PYTHIA 8.1". In: *Comput. Phys. Commun.* 178 (2008), pp. 852–867. DOI: 10.1016/j.cpc.2008.01.036. arXiv: 0710.3820 [hep-ph].

[50] Jaroslav Adam et al. "D-meson production in p–Pb collisions at $\sqrt{s_{NN}} = 5.02$ TeV and in pp collisions at $\sqrt{s} = 7$ TeV". In: *Phys. Rev.* C94.5 (2016), p. 054908. DOI: 10.1103/PhysRevC.94.054908. arXiv: 1605.07569 [nucl-ex].

[51] Shreyasi Acharya et al. "Measurement of prompt D^0, D^+, D^{*+}, and D_S^+ production in pâĂŞPb collisions at $\sqrt{s_{NN}} = 5.02$ TeV". In: *JHEP* 12 (2019), p. 092. DOI: 10.1007/JHEP12(2019)092. arXiv: 1906.03425 [nucl-ex].

[52] Shreyasi Acharya et al. "Measurement of D-meson production at mid-rapidity in pp collisions at $\sqrt{s} = 7$ TeV". In: *Eur. Phys. J.* C77.8 (2017), p. 550. DOI: 10.1140/epjc/s10052-017-5090-4. arXiv: 1702.00766 [hep-ex].

[53] B. Andersson et al. "Parton fragmentation and string dynamics". In: *Physics Reports* 97.2 (1983), pp. 31 –145. ISSN: 0370-1573. DOI: https://doi.org/10.1016/0370-1573(83)90080-7.

[54] Bo Andersson. *The Lund model*. Vol. 7. Cambridge University Press, July 2005. ISBN: 978-0-521-01734-3, 978-0-521-42094-5, 978-0-511-88149-7.

[55] Betty Bezverkhny Abelev et al. "Multiplicity Dependence of Pion, Kaon, Proton and Lambda Production in p–Pb Collisions at $\sqrt{s_{NN}} = 5.02$ TeV". In: *Phys. Lett. B* 728 (2014), pp. 25–38. DOI: 10.1016/j.physletb.2013.11.020. arXiv: 1307.6796 [nucl-ex].

[56] Shreyasi Acharya et al. "Production of charged pions, kaons and (anti-)protons in Pb-Pb and inelastic pp collisions at $\sqrt{s_{NN}} = 5.02$ TeV". In: *Phys. Rev. C* 101.4 (2020), p. 044907. DOI: 10.1103/PhysRevC.101.044907. arXiv: 1910.07678 [nucl-ex].

[57] A. M. Sirunyan et al. "Elliptic flow of charm and strange hadrons in high-multiplicity pPb collisions at $\sqrt{s_{NN}} = 8.16$ TeV". In: *Phys. Rev. Lett.* 121.8 (2018), p. 082301. DOI: 10.1103/PhysRevLett.121.082301. arXiv: 1804.09767 [hep-ex].

[58] Shreyasi Acharya et al. "Azimuthal Anisotropy of Heavy-Flavor Decay Electrons in p-Pb Collisions at $\sqrt{s_{\rm NN}} = 5.02$ TeV". In: *Phys. Rev. Lett.* 122.7 (2019), p. 072301. DOI: 10.1103/PhysRevLett.122.072301. arXiv: 1805.04367 [nucl-ex].

Chapter 7

Conclusion and Future Perspectives

The p_{T}-differential cross section for the charmed baryon Λ_{c}^{+}, in the $\Lambda_{\mathrm{c}}^{+} \rightarrow \mathrm{pK}^{-}\pi^{+}$ decay channel, has been measured in the transverse momentum ranges $1 < p_{\mathrm{T}} < 12$ GeV/c in pp collisions and $2 < p_{\mathrm{T}} < 24$ GeV/c in p–Pb collisions at $\sqrt{s_{\mathrm{NN}}} = 5.02$ TeV with the ALICE detector. These new measurements improve upon the previous measurements performed with the LHC Run 1 data by extending the measured p_{T} range, using finer p_{T} intervals, and confirming trends previously hinted at by the RUN 1 analysis.

The measured cross sections in both pp and p-Pb collisions are shown to be underestimated by predictions given by Monte Carlo generators or calculated with perturbative QCD. In pp collisions, the predictions that implement colour reconnection [1] give a better description than the prediction based on $\mathrm{e}^{+}\mathrm{e}^{-}$ data [2], which strongly underestimates the cross section (by a factor of 12 at low p_{T}). The POWHEG [3] and GM-VFNS [4] predictions similarly underestimate the data, but the GM-VFNS prediction offers a better description. All predictions give worsening descriptions with decreasing p_{T}.

The measured baryon-to-meson ratio $\Lambda_{\mathrm{c}}^{+}/\mathrm{D}^{0}$, obtained from the measured production cross sections, for both pp and p–Pb collisions is seen to have a clear decreasing trend for $p_{\mathrm{T}} > 2$ GeV/c, where at high p_{T} the ratio becomes equal to 0.2. The baryon-to-meson ratio in p–Pb collisions is lower in the $1 < p_{\mathrm{T}} < 2$ GeV/c range and higher in the $3 < p_{\mathrm{T}} < 8$ GeV/c relative to pp collisions. The baryon-to-meson ratio $\Lambda_{\mathrm{c}}^{+}/\mathrm{D}^{0}$ is found to be larger than previous measurements in $\mathrm{e}^{+}\mathrm{e}^{-}$ and $\mathrm{e}^{-}\mathrm{p}$ experiments and underestimated by any predictions tuned on $\mathrm{e}^{+}\mathrm{e}^{-}$ data [2]. This is an indication that the fragmentation fractions of charm quarks into charmed baryons differs between collision systems. A better description is

given by models that include an additional enhancement mechanism (colour reconnection [1], additional excited baryon states [5], or coalescence [6]) for charmed baryon production, although greater precision is needed to discriminate between the models. Comparisons between the results in p-Pb and results from LHCb [7] indicate an enhancement at midrapidity with respect to forward and backward rapidities. In comparisons with light-flavour baryon-to-meson ratios [8, 9, 10] similar qualitative characteristics are observed.

The nuclear modification factor $R_{\rm pPb}$ of $\Lambda_{\rm c}^{+}$ baryons, obtained from the measured production cross sections in both pp and p–Pb collisions, can be seen to be lower than unity in the $1 < p_{\rm T} < 2$ GeV/c range and higher at $p_{\rm T} > 2$ GeV/c, peaking in the $5 < p_{\rm T} < 6$ GeV/c region. The nuclear modification factor $R_{\rm pPb}$ of $\Lambda_{\rm c}^{+}$ baryons was also compared against D-meson measurements and theory predictions. The $\Lambda_{\rm c}^{+}$ $R_{\rm pPb}$ is largely consistent with the D-meson measurement [11], although the $\Lambda_{\rm c}^{+}$ measurement is notably larger in the $4 < p_{\rm T} < 8$ GeV/c range. Greater precision is needed to determine the contribution of cold nuclear matter effects [3] or hot-medium effects [12] described by theoretical models.

In LHC Run 2, there have been a number of other charmed baryons that have been measured with the ALICE detector. These include measurements of the Ξ_c^- [13], Ξ_c^0 [14], and $\Sigma_c^{0,+,++}$ [15]. These measurements all show a similar enhanced production with respect to e^+e^- and e^-p measurements. These additional measurements complement the measurements detailed in this thesis, introducing additional constraints by the measuring the contribution to feed-down into the $\Lambda_{\rm c}^{+}$ state from the decay of the Σ_c, or by studying the production of charmed baryons containing an additional strange component, such as in the case of the Ξ_c. The $p_{\rm T}$-integrated charm fragmentation fractions and the total $c\bar{c}$ cross section at mid-rapidity have recently been measured [16], combining the measurement of $\Lambda_{\rm c}^{+}$ production presented in this thesis with measurements of the Ξ_c baryons and D-mesons at $\sqrt{s} = 5.02$ TeV. The most recent measurement of the $c\bar{c}$ cross section is about 40% higher than the previous measurement [17] where it had been previously assumed that fragmentation fractions in $\rm e^+e^-$ and $\rm e^-p$ matched those in hadronic collisions and that the Ξ_c contribution to the $c\bar{c}$ cross section was small.

Future measurements of the $\Lambda_{\rm c}^{+}$ baryon and other charmed baryons planned during the upcoming Run 3 data taking period of the LHC will hopefully provide further insight into charmed baryon production with the enhanced precision of the newly upgraded ALICE detector [18]. Improvements made to the vertexing

and tracking at low p_{T} by the upgrades during LHC Long Shutdown 2 will be needed to investigate model predictions for the thermalisation, energy loss, and azimuthal-flow anisotropy of charmed particles.

References

[1] Jesper R. Christiansen and Peter Z. Skands. "String Formation Beyond Leading Colour". In: *JHEP* 08 (2015), p. 003. DOI: 10.1007/JHEP08(2015)003. arXiv: 1505.01681 [hep-ph].

[2] Peter Skands, Stefano Carrazza, and Juan Rojo. "Tuning PYTHIA 8.1: the Monash 2013 Tune". In: *Eur. Phys. J.* C74.8 (2014), p. 3024. DOI: 10.1140/epjc/s10052-014-3024-y. arXiv: 1404.5630 [hep-ph].

[3] Stefano Frixione, Paolo Nason, and Giovanni Ridolfi. "A Positive-weight next-to-leading-order Monte Carlo for heavy flavour hadroproduction". In: *JHEP* 09 (2007), p. 126. DOI: 10.1088/1126-6708/2007/09/126. arXiv: 0707.3088 [hep-ph].

[4] B.A. Kniehl et al. "$\Lambda_c^{\pm}$ production in pp collisions with a new fragmentation function". In: *Phys. Rev. D* 101 (2020), p. 114021. DOI: 10.1103/PhysRevD.101.114021. arXiv: 2004.04213 [hep-ph].

[5] Min He and Ralf Rapp. "Charm-Baryon Production in Proton-Proton Collisions". In: *Phys. Lett.* B795 (2019), pp. 117–121. DOI: 10.1016/j.physletb.2019.06.004. arXiv: 1902.08889 [nucl-th].

[6] Salvatore Plumari et al. "Charmed Hadrons from Coalescence plus Fragmentation in relativistic nucleus-nucleus collisions at RHIC and LHC". In: *Eur. Phys. J.* C78.4 (2018), p. 348. DOI: 10.1140/epjc/s10052-018-5828-7. arXiv: 1712.00730 [hep-ph].

[7] Roel Aaij et al. "Prompt Λ_c^+ production in pPb collisions at $\sqrt{s_{\mathrm{NN}}} = 5.02$ TeV". In: *JHEP* 02 (2019), p. 102. DOI: 10.1007/JHEP02(2019)102. arXiv: 1809.01404 [hep-ex].

[8] Serguei Chatrchyan et al. "Study of the production of charged pions, kaons, and protons in pPb collisions at $\sqrt{s_{\mathrm{NN}}} = 5.02$ TeV". In: *Eur. Phys. J.* C74.6 (2014), p. 2847. DOI: 10.1140/epjc/s10052-014-2847-x. arXiv: 1307.3442 [hep-ex].

[9] Shreyasi Acharya et al. "Production of charged pions, kaons and (anti-)protons in Pb-Pb and inelastic pp collisions at $\sqrt{s_{\mathrm{NN}}} = 5.02$ TeV". In: *Phys. Rev. C* 101.4 (2020), p. 044907. DOI: 10.1103/PhysRevC.101.044907. arXiv: 1910.07678 [nucl-ex].

[10] Betty Bezverkhny Abelev et al. "Multiplicity Dependence of Pion, Kaon, Proton and Lambda Production in p–Pb Collisions at $\sqrt{s_{\mathrm{NN}}} = 5.02$ TeV". In: *Phys. Lett. B* 728 (2014), pp. 25–38. DOI: 10.1016/j.physletb.2013.11.020. arXiv: 1307.6796 [nucl-ex].

[11] Shreyasi Acharya et al. "Measurement of prompt D^0, D^+, D^{*+}, and $\mathrm{D}_{\mathrm{S}}^+$ production in pâĂŞPb collisions at $\sqrt{\mathrm{s_{NN}}} = 5.02$ TeV". In: *JHEP* 12 (2019), p. 092. DOI: 10.1007/JHEP12(2019)092. arXiv: 1906.03425 [nucl-ex].

[12] Andrea Beraudo et al. "Heavy-flavour production in high-energy d-Au and p–Pb collisions". In: *JHEP* 03 (2016), p. 123. DOI: 10.1007/JHEP03(2016)123. arXiv: 1512.05186 [hep-ph].

[13] Shreyasi Acharya et al. "Measurement of the cross sections of Ξ_{c}^0 and Ξ_{c}^+ baryons and branching-fraction ratio $\mathrm{BR}(\Xi_{\mathrm{c}}^0 \to \Xi^-\mathrm{e}^+\nu_{\mathrm{e}})/\mathrm{BR}(\Xi_{\mathrm{c}}^0 \to \Xi^-\pi^+)$ in pp collisions at 13 TeV". In: (May 2021). arXiv: 2105.05187 [nucl-ex].

[14] Shreyasi Acharya et al. "Measurement of the production cross section of prompt Ξ_{c}^0 baryons at midrapidity in pp collisions at $\sqrt{s} = 5.02$ TeV". In: *JHEP* 10 (2021), p. 159. DOI: 10.1007/JHEP10(2021)159. arXiv: 2105.05616 [nucl-ex].

[15] Shreyasi Acharya et al. "Measurement of prompt D^0, Λ_c^+, and $\Sigma_c^{0,++}(2455)$ production in pp collisions at $\sqrt{s} = 13$ TeV". In: (June 2021). arXiv: 2106.08278 [hep-ex].

[16] Shreyasi Acharya et al. "Charm-quark fragmentation fractions and production cross section at midrapidity in pp collisions at the LHC". In: (May 2021). arXiv: 2105.06335 [nucl-ex].

[17] Mykhailo Lisovyi, Andrii Verbytskyi, and Oleksandr Zenaiev. "Combined analysis of charm-quark fragmentation-fraction measurements". In: *Eur. Phys. J. C* 76.7 (2016), p. 397. DOI: 10.1140/epjc/s10052-016-4246-y. arXiv: 1509.01061 [hep-ex].

[18] B Abelev et al. "Upgrade of the ALICE Experiment: Letter Of Intent". In: *J. Phys.* G41 (2014), p. 087001. DOI: 10.1088/0954-3899/41/8/087001.

Chapter 8

Appendix A

8.1 Permissions to include published content

Co-author Consent Declaration

The undersigned give Christopher Hills their consent to include in his PhD thesis the contents of their co-authored material published in two ALICE Analysis Notes, with internal identification references ALICE-ANA-844 and ALICE-ANA-811, and entitled respectively "Measurement of prompt Λ_c^+ production via hadronic decay channels, in pp collisions at $\sqrt{s}$ = 5.02 TeV (Run 2 data)" and "Measurement of prompt Λ_c^+ production via hadronic decay channels, in p-Pb collisions at $\sqrt{s_{NN}}$ = 5.02 TeV (Run 2 data)".

Co-authors:

A. De Caro Date: 26/10/2021 Signature: Annalisa De Caro

E. Mennino Date: 27/10/2021 Signature: Elisa Mennino

J. Norman Date: 26/10/2021 Signature:

J. Wilkinson Date: 26/10/2021 Signature:

ALICE Physics Coordinator:

A. Dainese Date: 25/10/2021 Signature:

ALICE Editorial Board Chairs:

Y. Pachmayer Date: 25.10.21 Signature: Y. Pachmayer

J. Castillo Castellanos Date: 25/10/2021 Signature: J. CASTILLO

Co-author Consent Declaration

The undersigned give Christopher Hills their consent on behalf of the ALICE Collaboration co-authors to include in his PhD thesis the contents of two APS journal articles recently accepted for publication:

"Λ_c^+ production in pp and p-Pb collisions at $\sqrt{s_{NN}}$ = 5.02 TeV", accepted in Physical Review C, CERN-EP-2020-218, arXiv:2011.06079.

"Λ_c^+ production and baryon-to-meson ratios in pp and p-Pb collisions at $\sqrt{s_{NN}}$ = 5.02 TeV at the LHC", accepted in Physical Review Letters, CERN-EP-2020-217, arXiv:2011.06078.

ALICE Physics Coordinator:

A. Dainese Date: 25/10/2021 Signature: 

ALICE Editorial Board Chairs:

Y. Pachmayer Date: 25.10.21 Signature: 

J. Castillo Castellanos Date: Signature: 

Illustrations

List of Figures

List of Tables